Novel Features in Quantum Synchronization and Quantum Simulation Using Superconducting Qudits

Inauguraldissertation
zur
Erlangung der Würde eines Doktors der Philosophie
vorgelegt der
Philosophisch-Naturwissenschaftlichen Fakultät
der Universität Basel

von

Tobias Maurice Kehrer

2025

Genehmigt von der Philosophisch-Naturwissenschaftlichen Fakultät
auf Antrag von

Erstbetreuer: Prof. Dr. Christoph Bruder
Zweitbetreuer: Prof. Dr. Stefan Goedecker
Externer Experte: Prof. Dr. Rosario Fazio

Basel, den 16. September 2025

Prof. Dr. Heiko Schuldt, Dekan

The important thing is not to stop questioning.

Albert Einstein, 1879 – 1955

Summary

About a century after the genesis of quantum mechanics, continuous development in many directions of theory and engineering persists. Several open questions like the quantum theory of gravity tested by macroscopic quantum states, the realization of a fault-tolerant quantum computer, or the discovery of new unique quantum effects in general remain to be answered. In this thesis, aspects of the latter two of these topics are studied in more detail. The common ground on which they meet is the quantum simulation of open quantum systems.

The first part of the thesis focuses on quantum computing. In particular, the extension of the standard two-level bit-like qubit, on which standard quantum computers rely, is studied: the qudit. Qudits are multilevel quantum systems whose larger Hilbert space can provide advantages in quantum computation. To profit from the additional degrees of freedom of a qudit, its individual states have to be properly discriminated during readout. Two measurement strategies, based on a readout model of a superconducting transmon qudit, are proposed and compared by their theoretical performance. We implement the measurement of the four lowest eigenstates on state-of-the-art quantum computing hardware and employ higher-order gate operations realized as two-photon transitions. Moreover, we investigate a way of simulating open quantum systems by engineering adjustable effective gain using echo-sequence-like gate operations.

In the second part of this thesis, the quantum analogue of synchronization of oscillators, i.e., the alignment of features like frequency and phase, is studied. The building blocks of quantum synchronization are limit-cycle states. These states are stabilized by incoherent gain and damping and feature a free phase of oscillation that can be locked to an external signal or to the phases of other limit-cycle oscillators. We investigate spin-1 and harmonic-oscillator-like models by a refined operator representation of common synchronization measures. In particular, we show that in a system of spins 1 synchronization through interference blockades, that suppress synchronization effects, is possible. Furthermore, for harmonic-oscillator-like limit-cycle states, we find that the interplay of three independent synchronization mechanisms leads to active states induced by nonreciprocal interactions. The phase diagrams for both the quantum and classical version are analyzed. Finally, a new avenue of quantum synchronization is identified: quantum oscillators that host multiple limit cycles. Here, one phenomenon is the coexistence of both the occurrence and the absence of quantum synchronization in a single quantum state.

This thesis combines the theoretical study of new quantum features of synchronization with proposals of potential realizations on quantum simulators and quantum computers, especially, with a focus on superconducting transmon qudits and trapped ions.

Acknowledgments

I am extremely grateful for all the support I received throughout the period of my PhD studies.

First, I would like to thank my supervisor Christoph Bruder. I feel very fortunate to be a part of his academic family. As a PhD student in his group, I have experienced great team spirit, a fair working environment, strong work ethics, and an impressive gathering of minds. As a supervisor, he is asking the right questions to drive creativity which in combination with great freedom allowed me to perfectly shape my academic journey. By always being available to discuss physics but also art, language, and architecture, I was feeling to be at the right place during the whole time of my PhD studies. Furthermore, I am extraordinary thankful for all the granted opportunities to travel to conferences as well as for the freedom to co-design teaching blockcourses.

Second, I am grateful for my second supervisor Stefan Goedecker whose feedback in the PhD committee meetings fine-tuned the journey of my PhD.

Third, I would like to thank Rosario Fazio for agreeing to referee my thesis as the external expert as well as Tomasz Smoleński for chairing my PhD defense.

I owe special thanks to my two PhD colleagues Julian Arnold and Tobias Nadolny. I would like to thank my first fellow PhD student Julian, among other things, for his contributions to my warm welcome to the group, the joint Computerverantwortlicher work, and the co-organization of the blockcourses. I highly appreciate the daily discussions about physics and the almost daily discussions about colors with Tobias. As the inventor of the “cake day”, he brightened up the group’s afternoons. Thank you both for your companionship!

I furthermore want to thank Niels Lörch for his inspiring discussions about physics and economics and Parvinder Solanki for his intuition to identify fascinating innovative projects. I would like to acknowledge Frank Schäfer for guiding Julian and me as the predecessor of the group’s Computerverantwortlicher.

Moreover, I want to express my gratitude to the not yet mentioned current, temporary, and former group members: Ryan Tan, Gaomin Tang, Martin Koppenhöfer, Petr Zapletal, Markus Hoffmann, Susanne Schaub, Heinz Krummenacher, and Benjamin Senn. I would also like to thank my Master students Jan Neuser and Brennan Hughes for the joint study of interesting projects. The group’s administration assistants Tatsiana Dolmat and Dominique Zbinden deserve special recognition for their support in administrative tasks.

I am extremely grateful to the IBM Quantum team for granting (pulse level) access to their quantum computers as well as for the possibility to attend the quantum developers conference at the IBM Thomas J. Watson Research Center in November 2024. In particular, I want to express my gratitude to Sieglinde Pfaendler, Daniel

Egger, and Will Shanks. I furthermore want to thank Machiel Blok and his amazing group members, especially Zihao Wang, Rayleigh Parker, and Elizabeth Champion, for their heartfelt hospitality during my research visit and their impressive qudit research.

I owe special thanks to Björn Trauzettel, who introduced me to quantum information and quantum computing and nurtured my fascination.

Last, I would like to express my utmost gratitude to my family and my boyfriend. Their unlimited love and support enabled me to overcome all the difficulties that arose during the time of my PhD.

Publications

The main content of this thesis is based on the following peer-reviewed publications:

1. *Improving transmon qudit measurement on IBM Quantum hardware*,
   T. Kehrer, T. Nadolny, and C. Bruder,
   Physical Review Research **6**, 013050 (2024)

2. *Quantum synchronization through the interference blockade*,
   T. Kehrer, T. Nadolny, and C. Bruder,
   Physical Review A **110**, 042203 (2024)

3. *Quantum synchronization blockade induced by nonreciprocal coupling*,
   T. Kehrer and C. Bruder,
   Physical Review A **112**, 012223 (2025)

4. *Quantum Synchronization of Twin Limit-Cycle Oscillators*,
   T. Kehrer, C. Bruder, and P. Solanki,
   Physical Review Letters **135**, 063601 (2025)

Contents

Abbreviations and Symbols

A selection of relevant abbreviations and symbols used in this thesis is listed below.

Abbreviation	Meaning	Introduced in
MDE	**M**aximum **D**istance **E**stimator	Sec. 4.5.1
MLE	**M**aximum **L**ikelihood **E**stimator	Sec. 4.5.1
NISQ	**N**oisy **I**ntermediate-**S**cale **Q**uantum	Ch. 4
qubit	**qu**antum **bit**	Sec. 3.1.1
qudit	**qu**antum **dit**	Sec. 3.1.1
TLC	**T**win **L**imit **C**ycle	Sec. 10.1
vdP	**v**an **d**er **P**ol	Sec. 6.2.1

Symbol	Meaning	Defined in
$a^{(\dagger)}$	annihilation (creation) operator	Eq. (2.1.8)
$\Gamma(z)$	Gamma function	Eq. (7.2.9)
$\left\vert\mathcal{C}_\alpha^{l,n}\right\rangle$	l-legged cat state	Eq. (3.3.13)
$\vert\alpha\rangle$	coherent state	Eq. (2.1.11)
$D(\beta, s)$	generalized displacement operator	Eq. (2.4.3)
$\mathcal{D}[L](\rho)$	Lindblad dissipator	Eq. (2.3.16)
I_ν	modified Bessel function of the first kind	Eq. (6.1.10)
J_ν	Bessel function of the first kind	Eq. (6.1.11)
L_n^k	Laguerre polynomial	Eq. (3.3.12)
P_N	Synchronization measures of N quantum vdP oscillators	Eq. (9.2.15)
S_N	Synchronization measures of N spins	Eq. (8.2.9)
$S^\pm$	spin ladder operator	Eq. (2.2.11)
$\mathrm{SU}(N)$	special unitary group	Eq. (2.2.2)

Chapter 1

Introduction

The year 2025 marks the 100th anniversary of the famous “Umdeutung” paper by Werner Heisenberg [Heisenberg (1925)]. For this reason, on the 7th June of 2024, the year 2025 was officially declared to be the *International Year of Quantum Science and Technology* by the U.N. General Assembly following the resolution by the nation of Ghana in May 2024 [UNESCO (2025)].

In the last century, quantum mechanics became one of the most relevant theories not only for fundamental research but also for human daily life: it is the foundation of, e.g., semiconductors [Bardeen and Brattain (1948)], solar cells [Chapin et al. (1954)], atomic clocks [Essen and Parry (1955)], lasers [Maiman (1960)], light-emitting diodes [Holonyak and Bevacqua (1962)], and medical imaging [Lauterbur (1973), Hounsfield (2014)]. In return, these technological inventions like the computer or the laser became essential tools for subsequent scientific research.

A selection of famous contributors to quantum mechanics besides Heisenberg are Max Planck [Planck (1901)], Albert Einstein [Einstein (1905), Einstein (1917)], Niels Bohr [Bohr (1913a), Bohr (1913b), Bohr (1913c)], Arnold Sommerfeld [Sommerfeld (1916a), Sommerfeld (1916b)], Paul Dirac [Dirac and Fowler (1925), Dirac and Fowler (1927)], De Broglie [De Broglie (1925)], and Erwin Schrödinger [Schrödinger (1926a), Schrödinger (1926b), Schrödinger (1926c), Schrödinger (1926d), Schrödinger (1926e)]. A historical overview of the early developments of quantum mechanics is presented in [Duncan and Janssen (2019), Janssen and Duncan (2023)].

Another architect of quantum mechanics is John von Neumann, mainly known for his contributions to classical computing [Neumann (1993)], who introduced the density-matrix representation of ensembles of quantum systems in a Hilbert space formalism [Neumann (1927a), Neumann (1927b), Neumann (1927c)]. Considering von Neumann, the “personification of the combination of computing and quantum mechanics”, as an inspiration, we arrive at the first topic of this thesis: *quantum computing*. Innovative suggestions to consider a quantum description of computers [Benioff (1980)] and to utilize quantum systems as platforms for computation [Feynman (1982)] have been made in the 1980s. Following these proposals, first prototypical problems were solved by quantum algorithms [Deutsch and Penrose (1985), Deutsch and Jozsa (1992), Simon (1997), Bernstein and Vazirani (1997)]. Subsequently, more practical algorithms like Grover’s search algorithm [Grover (1996)] and Shor’s prime-factorization algorithm

[Shor (1997)] have been published.

These quantum algorithms rely on fault-tolerant quantum computers that do not yet exist. However, in the current noisy intermediate-scale quantum era [Preskill (2018)], we have access to a variety of quantum computing platforms that are candidates for future quantum computers. Examples of these platforms are superconducting circuits [Blais et al. (2021)], trapped ions [Bruzewicz et al. (2019)], cold atoms and Rydberg atoms [Saffman (2016)], electron spins in quantum dots [Burkard et al. (2023)], magnetic racetracks [Zou et al. (2023)], photonic circuits [Slussarenko and Pryde (2019)], and topological states [Nayak et al. (2008)]. In the last years, many quantum computing companies focusing on hardware and/or software have been founded. One of the early competitors with a substantial history in classical computing is IBM. The evolution of the superconducting-qubit hardware of IBM Quantum involves an increase in the number of qubits from 1 to 100+ [Kandala et al. (2017), Kim et al. (2023), Miessen et al. (2024), Mandelbaum et al. (2024)] and a reduction of the error rates of single and two-qubit gates to the orders $\mathcal{O}(10^{-3})$ and $\mathcal{O}(10^{-4})$ [McKay et al. (2023), IBM Quantum. (2025)]. Note that in 2022 a 433-qubit chip[1] and in 2023 a 1121-qubit chip[2] were released.

A common feature among many quantum computing platforms is that the qubit Hilbert space is realized as a two-level subspace of a larger physical Hilbert space. Quantum systems that exhibit d states are called qudits [Wang et al. (2020)]. In the example of the transmon qudit [Koch et al. (2007)], an anharmonic superconducting oscillator, the qubit is formed by the ground state and first excited state. The higher-excited states of qudits can provide advantages in a passive way by improving, e.g., qubit readout [Elder et al. (2020)], the implementation of multiqubit gates [Fedorov et al. (2012)], or qubit reset [Zeytinoğlu et al. (2015), Egger et al. (2018)]. Moreover, the full potential of qudits can be unleashed by taking advantage of higher-excited states in an active way by, e.g., using them as ancillas [Fischer et al. (2022)], logical states [Cervera-Lierta et al. (2022)], or for quantum simulation [Ciavarella et al. (2021), Champion et al. (2025)]. One of the main limiting factors of superconducting qubits is their readout [Dumas et al. (2024)]. The default readout scheme for qubits optimizes the distinguishability between the qubit states. Since this scheme is not necessarily optimal for distinguishing all qudit states, we propose different measurement strategies based on a qudit readout model.

In the first part of this thesis, this project, together with the description of an echo-sequence-like model that can be used to simulate effective gain and damping on quantum hardware, will be discussed. Simulating open quantum systems, i.e., including incoherent processes like decay, on quantum hardware is of great interest [Weimer et al. (2010), Barreiro et al. (2011)], especially on quantum computers [Sweke et al. (2015), Schlimgen et al. (2021), Leppäkangas et al. (2023)].

In the second part of this thesis, we will focus on open quantum systems. In

---

[1] https://newsroom.ibm.com/2022-11-09-IBM-Unveils-400-Qubit-Plus-Quantum-Processor-and-Next-Generation-IBM-Quantum-System-Two [Accessed: August 10, 2025]

[2] https://www.ibm.com/quantum/blog/quantum-roadmap-2033 [Accessed: August 10, 2025]

the scenarios we will present, gain and damping are essential to stabilize particular quantum states that feature a free phase that can be synchronized. Synchronization, i.e., the alignment of features of oscillators like their frequency and phase of oscillations, has been initially studied in 1665 by Christiaan Huygues [Huygens (1893)] in the setup of two coupled pendulum clocks. In many scientific domains like biology [Buck (1938)] or civil engineering [Strogatz et al. (2005)], synchronization has been observed. In the research domain called *quantum synchronization*, people usually aim at identifying unique quantum effects of synchronization of quantum oscillators [Lee et al. (2014), Lörch et al. (2017), Roulet and Bruder (2018b)]. In recent years, quantized classical oscillators [Lee and Sadeghpour (2013)] (top-down approach) and inherently quantum spin-like oscillators [Roulet and Bruder (2018a)] (bottom-up approach) have been studied. Quantum synchronization is in some aspects related to quantum sensing [Vaidya et al. (2025)], quantum thermodynamics [Jaseem et al. (2020b)], and time-crystals [Hajdušek et al. (2022)].

In this second part, we will present publications on both spin-oscillator models and harmonic-oscillator-like models. We will discuss the synchronization of indirectly coupled spin-1 oscillators in the presence of synchronization blockades [Solanki et al. (2023)] that simultaneously suppress synchronization of directly coupled spin-1 oscillators. Moreover, in a setup of two harmonic-oscillator-like oscillators, we will consider an effective nonreciprocal interaction realized by coherent and dissipative couplings and find, e.g., quantum analogues of traveling-wave states [Fruchart et al. (2021)] that are related to active matter [Vrugt and Wittkowski (2025)].

Finally, we identify a new direction of quantum synchronization: multi-limit-cycle oscillators. Here, multiple limit cycles coexist in the same steady state of a single oscillator. We will present refined synchronization measures to access the locking information of the individual limit cycles and discuss the basic quantum synchronization features of a model that features two coexisting limit cycles. The study of multi-limit-cycle oscillators provides a multitude of research possibilities by exploring how well-known quantum synchronization effects manifest in this class of models as well as by finding exclusive unique quantum features.

Overview

This thesis is structured as follows:

Chapter 2 We will start by a recap of the theoretical foundations of the building blocks of most models considered in this thesis: the quantum harmonic oscillator and spins. In addition to their unitary time evolution, we want to describe nonunitary processes like decay and incoherent pumping of open quantum systems. Thus, we will briefly derive the Lindblad master equation in the Born-Markov approximation.

Part I: Quantum Computing on Superconducting Hardware

Chapter 3 In the first chapter of the first part of this thesis, we will introduce the basic elements of universal quantum computing. We will build intuition for why the universal gate set is universal by constructing approximations for noncommuting rotations of states on the Bloch sphere around two linear independent axes. These operations can be used to generate any unitary operator with a desired level of error. After introducing the quantum circuit as the representation of the gate sequences of a quantum algorithm, we will briefly learn how to use fault-tolerant quantum computers as a digital quantum simulator.

A more promising way of using quantum hardware at the moment is analog quantum simulation. We will understand the basic modeling aspects of superconducting transmon qudits like their level structure and driving of (higher-order) transitions. In contrast to the previously described qubits of standard universal quantum computing, qudits feature more than two states.

The mathematical description of a second quantum platform, viz., trapped ions, will be outlined. Trapped ions are often the prime candidate for implementing setups considered in Chs. 8 to 10 in the second part of the thesis.

Chapter 4 In this chapter presenting the publication [Kehrer et al. (2024a)], we will learn about the readout model of transmon qudits. In contrast to the standard readout scheme for qubits that optimizes the discrimination of both qubit states, measurement strategies for qudits have to provide sufficient distinguishability of multiple states simultaneously. We will present two measurement strategies that are based on the readout-drive-dependent model. The first one features a single readout frequency whereas the second one splits the total number of measurement runs into experiments at different readout frequencies. We will present actual data of a ququart implemented on an IBM Quantum device. By the realization of two-photon transitions, higher-order X gates are used to prepare the ququart states.

Chapter 5 Having learned how to improve the readout of qudit states, in this chapter, we will study an echo-sequence-like model that mimics the simulation of effective incoherent gain and damping on a quantum computer. Despite being designed for unitary operations, state-of-the-art quantum computers still feature loss. On the contrary, native decay can be viewed as a source for quantum simulation of open quantum systems. We will present a sequence of operations involving gates and decay periods that enables the generation of mixed states by the realization of tunable gain and damping rates. Extending this model to qutrits will potentially be interesting regarding the implementation of spin-1-like setups, e.g., the ones discussed in Ch. 8.

Part II: Quantum Synchronization of Oscillating Systems

Chapter 6 The second part of this thesis focuses on a particular family of open quantum systems that we would like to implement on a quantum simulator of platforms like the ones presented in Sec. 3.3 using methods that might have evolved from Ch. 5. This family is called "quantum synchronization". Its classical analogue has been established in 1665 by Christiaan Huygens. In this chapter, we will give a broad overview of relevant models an their features that will be reference points for the studies of quantum synchronization in Chs. 8 to 10. We will begin with the Kuramoto model of phase oscillators, meaning oscillators that exhibit only one free parameter, viz. their phase of oscillation. With this model, we will understand the basics of synchronization, i.e., the alignment of oscillator properties like their frequency or phase of oscillation. Next, we will define the building block of further models of synchronization: the limit cycle. It is a stabilized, closed, and isolated trajectory in the phase space of an oscillator that exhibits a phase and an amplitude. We will introduce the van der Pol and the Stuart-Landau oscillator and begin to study frequency and phase synchronization. Furthermore, we will understand synchronization blockades whose quantum analogues will play a significant role in Chs. 8 to 10.

Chapter 7 After having established the tools for analyzing classical synchronization, in this chapter, we will introduce quantum synchronization, the main topic of the second part of this thesis. We will introduce two typical setups and their measures of quantum synchronization that will be relevant for Chs. 9 and 10. The first one is the harmonic-oscillator-like "quantum van der Pol" oscillator. For a single coherently driven oscillator and for two coherently coupled oscillators, we will review the basic synchronization effects. For the second setup, spin-1 oscillators that will be studied in Ch. 8, we will recall similar basics of synchronization properties.

Chapter 8 In this chapter, in which the work published in [Kehrer et al. (2024b)] will be discussed, two scenarios of coherently coupled spin-1 oscillators will be considered: (i) two oscillators, one of which is driven, and (ii) a chain of three oscillators. Quantum synchronization interference blockades, like the ones introduced in Sec. 7.2, between pairs of coupled oscillators as well as between the driven spin and its coherent drive exist. The surprising quantum feature is that even if both types of blockades persist, the undriven spin synchronizes with the external drive as well as both spins at the ends of the three-oscillator chain. We will define an operator representation of the common synchronization measure that reduces its calculation complexity and increases its interpretability.

Chapter 9 This chapter based on the publication [Kehrer and Bruder (2025)], will present a phase diagram of three competing independent quantum synchronization mechanisms. A coherent drive and a coherent coupling, that will be presented individually in Sec. 7.1, will be combined together with a dissipative interaction in a model of two quantum van der Pol oscillators. Effective nonreciprocal interactions arise and induce quantum analogues of traveling-wave states. We will see that tuning these interactions to become unidirectional, a synchronization blockade between the undriven oscillator and the coherent drive, that acts only on the other oscillator, emerges. At the end of this chapter we will furthermore investigate the rich phase diagrams of the classical analogues of two and three such oscillators and will show examples of highly nontrivial active states.

Chapter 10 The last publication [Kehrer et al. (2025)] presented in this thesis will be discussed in this chapter. We will consider a quantum Liénard system whose classical analogue features two concentric limit cycles and call it a “twin limit cycle”. This creates the avenue of quantum synchronization of multi-limit-cycle oscillators. We will provide its foundations by showing the coexistence of quantum synchronization behavior in the cases of a single coherently driven twin limit cycle and two coherently coupled twin limit-cycle oscillators. By defining refined measures of quantum synchronization we will be able to access the individual phase-locking information of the two limit cycles of one oscillator. For both cases, we will find intriguing synchronization effects: the limit cycles of the driven oscillator lock to distinct phases and the steady state of the two-oscillator model features both synchronization and synchronization blockades.

Part III: Conclusion

Chapter 11 In the final chapter, we summarize the main findings presented in this thesis and propose several directions of future research. By relating the thesis to other works, further projects are identified.

Chapter 2

Theoretical Background

In this chapter, theoretical foundations that are relevant for both parts of this thesis are presented.

2.1 Quantum Harmonic Oscillator

The *harmonic oscillator* is probably one of the most considered approximations in physics. One reason might be the fact that in many domains of physics local minima of potentials can be approximated by a quadratic function. Another reason might be their simple analytical solutions. Moreover, it is the standard example of canonical quantization leading to the *quantum harmonic oscillator* that is relevant for Chs. 4, 9 and 10. The following section is based on [Schwabl (2007)].

The classical harmonic oscillator is given by the Hamiltonian

$$H = \frac{p^2}{2m} + \frac{m\omega^2}{2}x^2\,, \tag{2.1.1}$$

which corresponds to the total energy of a nonrelativistic particle with momentum p, position x, and mass m moving in a quadratic potential with curvature $\partial_x^2 H/m = \omega^2$. As canonical quantization, we understand replacing position and momentum by quantum mechanical operators as well as replacing the Poisson bracket $\{x, p\} = 1$ of the classical system with the commutator $[x, p] = xp - px = \mathrm{i}\hbar$. The system can be transformed into a different set of operators a and $a^\dagger$,

$$x = \sqrt{\frac{\hbar}{2m\omega}}(a^\dagger + a), \quad p = \mathrm{i}\sqrt{\frac{\hbar m\omega}{2}}(a^\dagger - a)\,, \tag{2.1.2}$$

called the annihilation and creation operators that obey $[a, a^\dagger] = 1$. Using these operators the Hamiltonian of the quantum harmonic oscillator reads

$$H = \hbar\omega\left(a^\dagger a + \frac{1}{2}\right)\,. \tag{2.1.3}$$

Here, eigenstates of the Hamiltonian are eigenstates of the number operator $n = a^\dagger a$. These states are called Fock states $a^\dagger a\,|n\rangle = n\,|n\rangle$ and obey $\langle n|m\rangle = \delta_{nm}$, where δ_{nm}

is the Kronecker delta. Using $[n, a^\dagger] = a^\dagger$ and $[n, a] = -a$, the action of $a^\dagger$ and a on these states can be derived,

$$\begin{aligned} n a^\dagger |n\rangle &= (a^\dagger n + [n, a^\dagger]) |n\rangle = (n+1) a^\dagger |n\rangle = (n+1) c_1 |n+1\rangle \ , && (2.1.4) \\ n a |n\rangle &= (a^\dagger n + [n, a]) |n\rangle = (n-1) a |n\rangle = (n-1) c_2 |n-1\rangle \ , && (2.1.5) \\ \langle n| a a^\dagger |n\rangle &= \langle n+1| c_1^* c_1 |n+1\rangle = \langle n| (a^\dagger a + 1) |n\rangle = |c_1|^2 = n+1 \, , && (2.1.6) \\ \langle n| a^\dagger a |n\rangle &= \langle n-1| c_2^* c_2 |n-1\rangle = |c_2|^2 = n \, , && (2.1.7) \end{aligned}$$

leading to $c_1 = \sqrt{n+1}$ and $c_2 = \sqrt{n}$. The Fock-state representation of both operators is

$$a^\dagger = \sum_{n=0}^{\infty} \sqrt{n+1}\, |n+1\rangle\langle n| \, , \quad a = \sum_{n=0}^{\infty} \sqrt{n+1}\, |n\rangle\langle n+1| \ . \tag{2.1.8}$$

The eigenstates $|\alpha\rangle$[3] of the annihilation operator a are also well known as *coherent states* [Glauber (1963)]. Using a superposition of Fock states as an ansatz,

$$a |\alpha\rangle = \alpha |\alpha\rangle = a \sum_{n=0}^{\infty} d_n |n\rangle = \sum_{n=0}^{\infty} d_n \sqrt{n} |n-1\rangle = \sum_{n=0}^{\infty} d_{n+1} \sqrt{n+1} |n\rangle = \alpha \sum_{n=0}^{\infty} d_n |n\rangle \ , \tag{2.1.9}$$

results in a recursion relation $d_{n+1}\sqrt{n+1} = d_n \alpha$ that is solved by $d_n = d_0 \alpha^n / \sqrt{n!}$. The normalization

$$\langle \alpha | \alpha \rangle = \sum_{n,m=0}^{\infty} |d_0|^2 \frac{\alpha^{*n} \alpha^m}{\sqrt{n! m!}} \langle n | m \rangle = |d_0|^2 \sum_{n,m=0}^{\infty} \frac{|\alpha|^n}{n!} = |d_0|^2 \mathrm{e}^{|\alpha|^2} = 1 \tag{2.1.10}$$

is guaranteed by $d_0 = \mathrm{e}^{-|\alpha|^2/2}$,

$$|\alpha\rangle = \mathrm{e}^{-|\alpha|^2/2} \sum_{n=0}^{\infty} \frac{\alpha^n}{\sqrt{n!}} |n\rangle \ . \tag{2.1.11}$$

Remembering the relation between a and position and momentum operators, see Eq. (2.1.2), we see that the real part of α can be related to position and the imaginary part of α can be related to momentum,

$$x |\alpha\rangle = \sqrt{\frac{2\hbar}{m\omega}} \mathrm{Re}[\alpha] |\alpha\rangle \, , \quad p |\alpha\rangle = \sqrt{2\hbar m \omega}\, \mathrm{Im}[\alpha] |\alpha\rangle \ . \tag{2.1.12}$$

Moreover, the position and momentum expectation values of coherent states obey the classical equations of motion. These states might therefore be interpreted as the “most classical quantum states”.

In systems with multiple harmonic oscillators, annihilation operators of oscillator A, B, C, … are often denoted by $a_A = a$, $a_B = b$, $a_C = c$, …. Studying unitary time

---

[3] Note that the same symbol $|\cdot\rangle$ as for Fock states is used even if $\alpha = n$ does not imply $|\alpha\rangle = |n\rangle$.

evolutions, transforming between different reference frames is relevant. A transformation $|\psi\rangle \to U|\phi\rangle$, with $U = \exp\big(-\mathrm{i}\omega a^\dagger a t\big)$, of a system given by a Hamiltonian H leads to

$$\mathrm{i}\hbar\frac{\mathrm{d}}{\mathrm{d}t}|\psi\rangle = H|\psi\rangle \to \mathrm{i}\hbar\frac{\mathrm{d}}{\mathrm{d}t}(U|\phi\rangle) = \mathrm{i}\hbar\dot{U}|\phi\rangle + \mathrm{i}\hbar U\frac{\mathrm{d}}{\mathrm{d}t}|\phi\rangle = HU|\phi\rangle\ , \tag{2.1.13}$$

and the effective Hamiltonian for $|\phi\rangle$

$$\mathrm{i}\hbar\frac{\mathrm{d}}{\mathrm{d}t}|\phi\rangle = H_{\text{eff}}|\phi\rangle = U^\dagger(HU - \mathrm{i}\hbar\dot{U})|\phi\rangle = (U^\dagger HU - \hbar\omega a^\dagger a)|\phi\rangle\ . \tag{2.1.14}$$

Since U extracted the time evolution induced by $H_0 = \hbar\omega a^\dagger a$, the effective Hamiltonian H_{eff} for $|\phi\rangle$ is missing exactly this term in comparison to H for $|\psi\rangle$. This frame is also called the “rotating frame”. Note that in the majority of the thesis $\hbar = 1$ is chosen.

2.2 Spin

Another highly important quantum model are spins [Pauli (1925)] that will be considered in Ch. 8. A spin state $|s, m_s\rangle$ is defined by its quantum numbers $s \in \{\frac{n}{2}\,|\, n \in \mathbb{N}\}$ and $m_s = -s, -s+1\ldots, s$. In contrast to the infinite-dimensional creation and annihilation operators of the quantum harmonic oscillator, vector representations $(s, s-1, \ldots, -s)$ of spins are $(2s+1)$-dimensional. Spin-s operators S^j correspond to the $(2s+1)$-dimensional representation of the $\mathfrak{su}(2)$ Lie algebra elements. The traceless Hermitian elements T^a of $\mathfrak{su}(N)$ [Duistermaat and Kolk (2000)],

$$\mathfrak{su}(N) = \{T^a \in \mathrm{L}_{\mathbb{C}}(\mathbb{C}^N, \mathbb{C}^N)\,|\, T^{a\dagger} = T^a \text{ and } \mathrm{Tr}[T^a] = 0\}\,, \tag{2.2.1}$$

are the generators of the Lie group

$$\mathrm{SU}(N) = \{U \in \mathrm{U}(N)\,|\,\det(U) = 1\}\,, \tag{2.2.2}$$

called the special unitary group. Here, $U = \exp(\mathrm{i}\sum_a x_a T^a)$ with $x_a \in \mathbb{R}$ are elements of a subset of the unitary group [Duistermaat and Kolk (2000)]

$$\mathrm{U}(N) = \{U \in \mathrm{L}_{\mathbb{C}}(\mathbb{C}^N, \mathbb{C}^N)\,|\, U^\dagger U = \mathbb{1}\}\,, \tag{2.2.3}$$

where $\mathrm{L}_{\mathbb{C}}(\mathbb{C}^N, \mathbb{C}^N)$ is the space of complex-linear maps $\mathbb{C}^N \to \mathbb{C}^N$. The Spin-$s$ operators S^j obey[4]

$$[S^i, S^j] = \mathrm{i}\sum_k \epsilon_{ijk} S^k\,. \tag{2.2.4}$$

---

[4] Note that we neglect factors of $\hbar$, i.e., we measure spin in multiples of $\hbar$.

Here,

$$\epsilon_{ijk} = \begin{cases} 1 & \text{for even permutations } (i,j,k) \text{ of } (x,y,z)\,, \\ -1 & \text{for odd permutations } (i,j,k) \text{ of } (x,y,z)\,, \\ 0 & \text{else}\,, \end{cases} \tag{2.2.5}$$

is the Levi-Civita symbol. The spin operators are defined by their nonvanishing matrix elements [Landau and Lifshitz (1977)]

$$\langle s, m_s| S^x |s, m_s - 1\rangle = \langle s, m_s - 1| S^x |s, m_s\rangle = \frac{1}{2}\sqrt{(s+m_s)(s-m_s+1)}\,, \tag{2.2.6}$$

$$\langle s, m_s| S^y |s, m_s - 1\rangle = -\langle s, m_s - 1| S^y |s, m_s\rangle = \frac{1}{2\mathrm{i}}\sqrt{(s+m_s)(s-m_s+1)}\,, \tag{2.2.7}$$

$$\langle s, m_s| S^z |s, m_s\rangle = m_s\,. \tag{2.2.8}$$

The quantum numbers mentioned in the beginning are the eigenvalues of the following operators

$$\vec{S}^2 |s, m_s\rangle = \sum_j S^{j2} |s, m_s\rangle = s(s+1) |s, m_s\rangle\ , \tag{2.2.9}$$

$$S^z |s, m_s\rangle = m_s |s, m_s\rangle\ . \tag{2.2.10}$$

Spin ladder operators are defined as $S^{\pm} = S^x \pm \mathrm{i}S^y$ and raise and lower the m_s quantum number,

$$\begin{aligned} S^{\pm} |s, m_s\rangle &= \sqrt{(s \mp m_s)(s \pm m_s + 1)}\, |s, m_s \pm 1\rangle \\ &= \sqrt{s(s+1) - m_s(m_s \pm 1)}\, |s, m_s \pm 1\rangle\ . \end{aligned} \tag{2.2.11}$$

Since the m_s quantum number is bounded, $S^+ |s, s\rangle = S^- |s, -s\rangle = 0$ and $S^{\pm(2s+1)} = 0$.

The smallest but somewhat trivial spin is $s = 0$ which has only one state $m_s = 0$, i.e., it is a scalar. Since here $\vec{S}^2 |0, 0\rangle = 0$, the spin vector has zero length and $S^j = 0$. Therefore, a spin-0 object does not define a particular reference frame in the three-dimensional spin space, i.e., it is spherically symmetric.

2.2.1 Spin-1/2

The smallest half-integer spin is $s = 1/2$ which has two states $m_s = \pm 1/2$. The most famous examples and applications are, e.g., electrons and qubits. The spin-1/2 operators

$$S^x = \frac{1}{2}\begin{pmatrix} 0 & 1 \\ 1 & 0 \end{pmatrix}, \quad S^y = \frac{1}{2}\begin{pmatrix} 0 & -\mathrm{i} \\ \mathrm{i} & 0 \end{pmatrix}, \quad S^z = \frac{1}{2}\begin{pmatrix} 1 & 0 \\ 0 & -1 \end{pmatrix}, \tag{2.2.12}$$

obey $S^{j2} = \mathbb{1}/4$, $\mathrm{Tr}[\mathbb{1}] = 2$, and

$$S^i S^j = \frac{1}{4}\delta_{ij}\mathbb{1} + \frac{\mathrm{i}}{2}\sum_k \epsilon_{ijk} S^k\,, \tag{2.2.13}$$

$$\mathrm{Tr}\big[S^j\big] = 0, \quad \mathrm{Tr}\big[S^i S^j\big] = \frac{1}{2}\delta_{ij}, \quad \mathrm{Tr}\Big[S^i S^j S^k\Big] = \frac{\mathrm{i}}{4}\epsilon_{ijk}\,. \tag{2.2.14}$$

A spin-1/2 density matrix

$$\rho = \frac{1}{2}\mathbb{1} + \vec{n}\vec{S} \tag{2.2.15}$$

exhibits three real-valued degrees of freedom $\vec{n} \in \mathbb{R}^3$. Purity, i.e., $\mathrm{Tr}\big[\rho^2\big] = 1/2 + \mathrm{Tr}\Big[(\vec{n}\vec{S})^2\Big] = (1 + |\vec{n}|^2)/2 = 1$ is provided by unit length vectors $\vec{n}$. These $\vec{n}$ correspond to states that lie on the so-called Bloch sphere. See Fig. 3.1 in the next chapter for a visualization.

2.2.2 Spin-1

The next larger spin is $s = 1$ and has three states $m_s = -1, 0, 1$. Its spin operators

$$S^x = \frac{1}{\sqrt{2}}\begin{pmatrix} 0 & 1 & 0 \\ 1 & 0 & 1 \\ 0 & 1 & 0 \end{pmatrix}, \quad S^y = \frac{1}{\sqrt{2}}\begin{pmatrix} 0 & -\mathrm{i} & 0 \\ \mathrm{i} & 0 & -\mathrm{i} \\ 0 & \mathrm{i} & 0 \end{pmatrix}, \quad S^z = \begin{pmatrix} 1 & 0 & 0 \\ 0 & 0 & 0 \\ 0 & 0 & -1 \end{pmatrix}, \tag{2.2.16}$$

obey $S^{j3} = S^j$, $\mathrm{Tr}[\mathbb{1}] = 3$, and

$$\mathrm{Tr}\big[S^j\big] = 0, \quad \mathrm{Tr}\big[S^i S^j\big] = 2\delta_{ij}, \quad \mathrm{Tr}\Big[S^i S^j S^k\Big] = \mathrm{i}\epsilon_{ijk}, \quad \mathrm{Tr}\Big[S^i S^j S^k S^l\Big] = \delta_{ij}\delta_{kl} + \delta_{il}\delta_{jk}\,. \tag{2.2.17}$$

The density matrix exhibits $3^2 - 1 = 8$ (hermiticity and purity $\mathrm{Tr}[\rho] = 1$) free parameters that are restricted to guarantee positive semidefiniteness. One choice of parameters are the expectation values of S^j, S^{x2}, S^{z2}, $S^x S^y$, $S^y S^z$, and $S^z S^x$,

$$\rho = \frac{1}{3}\mathbb{1} + \frac{\vec{n}}{2}\vec{S} + \sum_{ij} n_{ij} S^{ij}\,, \tag{2.2.18}$$

where [Band and Park (1971)]

$$S^{xx} = \begin{pmatrix} 0 & 0 & 1 \\ 0 & 0 & 0 \\ 1 & 0 & 0 \end{pmatrix}, \quad S^{zz} = \begin{pmatrix} 1 & 0 & 0 \\ 0 & -2 & 0 \\ 0 & 0 & 1 \end{pmatrix}, \tag{2.2.19}$$

$$S^{xy} = \begin{pmatrix} 0 & 0 & -\mathrm{i} \\ 0 & 0 & 0 \\ \mathrm{i} & 0 & 0 \end{pmatrix}, \quad S^{yz} = \frac{1}{\sqrt{2}}\begin{pmatrix} 0 & -\mathrm{i} & 0 \\ \mathrm{i} & 0 & \mathrm{i} \\ 0 & -\mathrm{i} & 0 \end{pmatrix}, \quad S^{zx} = \frac{1}{\sqrt{2}}\begin{pmatrix} 0 & 1 & 0 \\ 1 & 0 & -1 \\ 0 & -1 & 0 \end{pmatrix}. \tag{2.2.20}$$

2.3 Open Quantum Systems

Unitary time evolution originates from a Hamiltonian H and the Schrödinger equation

$$\mathrm{i}\hbar\frac{\mathrm{d}}{\mathrm{d}t}\left|\psi\right\rangle = H\left|\psi\right\rangle \,, \tag{2.3.1}$$

where $\left|\psi\right\rangle = U\left|\psi_0\right\rangle$ with $U = \exp(-\mathrm{i}Ht/\hbar)$ solves the equation for time-independent H. Some crucial features of unitary time evolutions are the preserving of norm, linearity, and time reversibility. The last feature is a clear indication that the description of nonreversible processes like decay is not included. In this section, which is based on [Wiseman and Milburn (2009)], the *quantum master equation* of systems including dissipative processes will be presented. This framework is highly relevant for the main part of this thesis. In the following, we set $\hbar = 1$.

2.3.1 Lindblad Master Equation

To move from unitary time evolution of "closed quantum systems" to nonunitary time evolutions of "open quantum systems", we start by breaking the total Hilbert space apart in the system S of interest and its environment E. The aim is to consider the environment as a large reservoir, i.e., not significantly influenced by state changes in the system, that couples to the system. The unitary time evolution of the density matrix of the total system is

$$\frac{\mathrm{d}}{\mathrm{d}t}\rho_{\mathrm{tot}} = -\mathrm{i}[H_S + H_E + H_{\mathrm{int}}, \rho_{\mathrm{tot}}] \,. \tag{2.3.2}$$

Here, H_S and H_E are the individual Hamiltonians of the system and its environment and H_{int} describes the interaction between both. In the rotating frame of the free Hamiltonians $H_S + H_E$,

$$\rho_{\mathrm{tot}} = \mathrm{e}^{-\mathrm{i}(H_S+H_E)t}\rho_{\mathrm{tot,int}}\mathrm{e}^{\mathrm{i}(H_S+H_E)t} \,, \tag{2.3.3}$$

the time evolution obeys

$$\frac{\mathrm{d}}{\mathrm{d}t}\rho_{\mathrm{tot,int}} = -\mathrm{i}[\mathrm{e}^{\mathrm{i}(H_S+H_E)t}H_{\mathrm{int}}\mathrm{e}^{-\mathrm{i}(H_S+H_E)t}, \rho_{\mathrm{tot,int}}] = -\mathrm{i}[V, \rho_{\mathrm{tot,int}}] \,. \tag{2.3.4}$$

Similar to Eq. (2.1.14), this unitary transformation of the density matrix leads to the subtraction of $-\mathrm{i}[H_S + H_E, \rho_{\mathrm{tot,int}}]$ from Eq. (2.3.2). The formal solution

$$\rho_{\mathrm{tot,int}}(t) = \rho_{\mathrm{tot,int}}(0) - \mathrm{i}\int_0^t \mathrm{d}t_1[V(t_1), \rho_{\mathrm{tot,int}}(t_1)] \,, \tag{2.3.5}$$

is used to find the equation of motion of the total system in the rotating frame by inserting it back into Eq. (2.3.4),

$$\frac{\mathrm{d}}{\mathrm{d}t}\rho_{\mathrm{tot,int}}(t) = -\mathrm{i}[V(t),\rho_{\mathrm{tot,int}}(0)] - \int_0^t \mathrm{d}t_1 [V(t),[V(t_1),\rho_{\mathrm{tot,int}}(t_1)]]\,. \tag{2.3.6}$$

In the so-called *Born approximation*, a system that is initialized in an uncorrelated state

$$\rho_{\mathrm{tot,int}}(0) = \rho_{S,\mathrm{int}}(0)\otimes\rho_{E,\mathrm{int}}(0)\,, \tag{2.3.7}$$

is assumed to stay uncorrelated,

$$\rho_{\mathrm{tot,int}}(t) \approx \rho_{S,\mathrm{int}}(t)\otimes\rho_{E,\mathrm{int}}(0)\,, \tag{2.3.8}$$

if the system-environment coupling is weak. In this case, the state of the large environment is approximately unchanged when the system state evolves. The second term in Eq. (2.3.6) still depends on the full solution of the system state. To turn this equation into a local-in-time differential equation, we have to assume that the integrand is small except around $t_1 \approx t$. This, together with replacing the lower time limit by $-\infty$ is so-called *Markov approximation*,

$$\frac{\mathrm{d}}{\mathrm{d}t}\rho_{\mathrm{tot,int}}(t) = -\mathrm{i}[V(t),\rho_{\mathrm{tot,int}}(0)] - \int_{-\infty}^t \mathrm{d}t_1 [V(t),[V(t_1),\rho_{S,\mathrm{int}}(t)\otimes\rho_{E,\mathrm{int}}(0)]]\,. \tag{2.3.9}$$

The Markov approximation is often interpreted as “the state does not have a memory”, i.e., meaning the derivative of the state at time t should not depend on the full history of the previous state evolution.

The Hamiltonian of the environment, also called bath or reservoir, is now assumed to be a collection of many harmonic oscillators,

$$H_E = \sum_k \omega_k b_k^\dagger b_k\,, \tag{2.3.10}$$

where the annihilation operators b_k are commuting with each other $[b_j, b_k^\dagger] = \delta_{jk}$ and the system annihilation operator $[a, b_k^{(\dagger)}] = 0$. The coupling is set to the Jaynes-Cummings type [Jaynes and Cummings (1963)]

$$H_{\mathrm{int}} = \sum_k g_k (a^\dagger + a)(b_k^\dagger + b_k)\,, \tag{2.3.11}$$

also called a dipole-dipole interaction. In the rotating frame of $H_S + H_E$, where $\exp(\mathrm{i}H_S t)a\exp(-\mathrm{i}H_S t) = a\mathrm{e}^{-\mathrm{i}\omega_S t}$ is assumed, two options arise. Either the sum $\omega_S + \omega_k$ of system and environment frequencies is large compared to their difference $\omega_S - \omega_k$ or vice versa. In the case $\omega_S + \omega_k \gg \omega_S - \omega_k$, in the rotating-wave approximation, the rapidly oscillating terms proportional to ab_k and $a^\dagger b_k^\dagger$ average to zero on smaller time scales than the evolution of the system. The resulting terms of the interaction Hamiltonian in the rotating frame are

$$V = \sum_k g_k (a^\dagger b_k \mathrm{e}^{-\mathrm{i}(\omega_k - \omega_S)t} + a b_k^\dagger \mathrm{e}^{\mathrm{i}(\omega_k - \omega_S)t}) \,. \tag{2.3.12}$$

To obtain an equation of motion for $\rho_{S,\mathrm{int}}$, we have to take the partial trace over the environment of Eq. (2.3.6). In the Born approximation, see Eq. (2.3.8), and initializing the environment $\rho_{E,\mathrm{int}}(0)$ in the vacuum state, leads to

$$\begin{aligned} \frac{\mathrm{d}}{\mathrm{d}t}\rho_{S,\mathrm{int}}(t) =& -\mathrm{i}\,\mathrm{Tr}_E[[V(t), \rho_{S,\mathrm{int}}(t) \otimes \rho_{E,\mathrm{int}}(0)]] \\ & - \int_0^t \mathrm{d}t_1\, \mathrm{Tr}_E[[V(t), [V(t_1), \rho_{S,\mathrm{int}}(t_1) \otimes \rho_{E,\mathrm{int}}(0)]]] \\ =& - \int_0^t \mathrm{d}t_1 \sum_k g_k^2 \mathrm{e}^{-\mathrm{i}(\omega_k - \omega_S)(t-t_1)} (a^\dagger a \rho_{S,\mathrm{int}}(t_1) - a\rho_{S,\mathrm{int}}(t_1) a^\dagger) + \mathrm{H.c.}\,. \end{aligned} \tag{2.3.13}$$

Here, the terms in the first line vanish since $\mathrm{Tr}_E[b_k^{(\dagger)}\rho_{E,\mathrm{int}}(0)] = 0$. In the second line, we additionally use $\mathrm{Tr}_E[b_j^\dagger b_k^\dagger \rho_{E,\mathrm{int}}(0)] = \mathrm{Tr}_E[\rho_{E,\mathrm{int}}(0) b_j b_k] = 0$ and $\mathrm{Tr}_E[b_j^\dagger \rho_{E,\mathrm{int}}(0) b_k] = \delta_{jk}$. The sum over k of the many coupling strengths g_k^2 weighted by the complex phase factor $\mathrm{e}^{-\mathrm{i}(\omega_k - \omega_S)(t-t_1)}$ can be expected to be sharply located at $t \approx t_1$ due to destructive interference of the many phase factors for $t \neq t_1$. This motivates the Markov approximation $\rho_{S,\mathrm{int}}(t_1) \approx \rho_{S,\mathrm{int}}(t)$. The value of the t_1 integral over this factor will feature a real part and an imaginary part,

$$- \int_0^t \mathrm{d}t_1 \sum_k g_k^2 \mathrm{e}^{-\mathrm{i}(\omega_k - \omega_S)(t-t_1)} \rho_{S,\mathrm{int}}(t_1) \approx \left(\mathrm{i}\Delta - \frac{\kappa}{2}\right) \rho_{S,\mathrm{int}}(t)\,. \tag{2.3.14}$$

The final result back in the nonrotating frame is the well-known *Lindblad master equation*

$$\frac{\mathrm{d}}{\mathrm{d}t}\rho_S = \frac{\mathrm{d}}{\mathrm{d}t}\rho = -\mathrm{i}[H_S + \Delta a^\dagger a, \rho] + \kappa \mathcal{D}[a](\rho)\,. \tag{2.3.15}$$

Here, the state ρ of the system is evolving under its Hamiltonian H_S and a correction $\Delta a^\dagger a$ and now additionally exhibits a decay with rate κ described by the *Lindblad dissipator*

$$\mathcal{D}[L](\rho) = L\rho L^\dagger - \frac{1}{2}(L^\dagger L + \rho L^\dagger L)\,. \tag{2.3.16}$$

The operators L are called *Lindblad operators*. Note that

$$\mathcal{D}[L](U\rho U^\dagger) = U\mathcal{D}[U^\dagger L U](\rho)U^\dagger \tag{2.3.17}$$

and

$$\mathcal{D}[\lambda L](\rho) = |\lambda|^2\mathcal{D}[L](\rho) \tag{2.3.18}$$

were used to go back from the rotating to the nonrotating frame.

In the above derivation of the Lindblad master equation, we used the fact that the interaction Hamiltonian of Eq. (2.3.11) is of the form

$$H_{\text{int}} = \sum_k g_k(l^\dagger(a,a^\dagger) + l(a,a^\dagger))(b_k^\dagger + b_k)\,, \tag{2.3.19}$$

where $l(a,a^\dagger)$ transforms like $\exp(\mathrm{i}H_S t)l(a,a^\dagger)\exp(-\mathrm{i}H_S t) = l(a,a^\dagger)\mathrm{e}^{-\mathrm{i}\omega_{S,l}t}$ such that a rotating-wave approximation can be made, see Eq. (2.3.12). Similar to the case $l(a,a^\dagger) = a$ discussed above, the resulting Lindblad operator in the effective master equation of the system, see Eq. (2.3.15), is $L = l(a,a^\dagger)$ and the Hamiltonian correction is $\Delta L^\dagger L$. In, e.g., Sec. 7.1.2 as well as Chs. 8 to 10, different choices of Lindblad operators like $L = a^n$ and $L = a^{\dagger m}$ are considered.

Since in general $\mathcal{D}[L_1 + L_2](\rho) \neq \mathcal{D}[L_1](\rho) + \mathcal{D}[L_2](\rho)$, the realization of multiple Lindblad dissipation terms $\mathcal{D}[L_j]$ requires independent baths, e.g., consider the interaction Hamiltonian

$$H_{\text{int}} = \sum_{j=1}^{J}\sum_{k\in\mathcal{K}_j} g_k(L_j^\dagger + L_j)(b_k^\dagger + b_k)\,, \tag{2.3.20}$$

where J is the number of Lindblad dissipators and $\mathcal{K}_j$ are the disjoint sets of bath-mode indices.

2.3.2 Engineered Dissipation

In experiments, decay is almost always present. Despite its negative connotation, it can be used to engineer particular Lindblad dissipators as presented below, see [Poyatos et al. (1996)]. Consider the total master equation

$$\frac{\mathrm{d}}{\mathrm{d}t}\rho = -\mathrm{i}[H_S + H_{\text{int}}, \rho] + \kappa\mathcal{D}[c](\rho)\,, \tag{2.3.21}$$

of a mode a of interest and a rapidly decaying mode c ($\kappa \gg g, \omega_S$, where ω_S is the energy scale of H_S), e.g., a lossy cavity or an ion transition starting from a short-lived state. Both are coupled by the interaction Hamiltonian $H_{\text{int}} = g\,l(a,a^\dagger)c^\dagger + \text{H.c.}$. The time evolution of c is given by the Heisenberg equation of motion [Wiseman and

Milburn (2009)]

$$\frac{\mathrm{d}}{\mathrm{d}t}c = \mathrm{i}g[l(a,a^\dagger)c^\dagger + l^\dagger(a,a^\dagger)c, c] + \kappa\left(c^\dagger cc - \frac{1}{2}(c^\dagger cc + cc^\dagger c)\right) = -\mathrm{i}gl(a,a^\dagger) - \frac{\kappa}{2}c\,. \tag{2.3.22}$$

If this mode is rapidly decaying in comparison to the time evolution of the system mode a, it can be assumed to be in its steady state $\dot{c} = 0$ during the time evolution of a. The steady state solution

$$c = -2\mathrm{i}\frac{g}{\kappa}l(a,a^\dagger) \tag{2.3.23}$$

can be used to simplify the total time evolution of Eq. (2.3.21) to an effective time evolution

$$\frac{\mathrm{d}}{\mathrm{d}t}\rho = -\mathrm{i}[H_S,\rho] + 4\frac{g^2}{\kappa}\mathcal{D}[l(a,a^\dagger)](\rho)\,, \tag{2.3.24}$$

where $H_{\mathrm{int}} \to 0$ and Eq. (2.3.18) is used. This method can be used to realize the Lindblad operators $L = a^n$ and $L = a^{\dagger m}$ mentioned at the end of the previous section.

Moreover, coupling multiple modes a_j of interest to the same lossy mode c leads to a dissipative interaction, see [Metelmann and Clerk (2015)]. This is used in Ch. 9 to engineer the collective decay of two modes: $\mathcal{D}[a_A + a_B]$.

2.4 State Representations

To compress the information about a state ρ stored in its many degrees of freedom, e.g., for visualization, a particular state representation with fewer or more accessible degrees of freedom has to be chosen. An overview of common examples is given in the following. This section is based on Chapters 3 and 4 of [Carmichael (1999)] and Chapter 3 of [Gerry and Knight (2004)].

2.4.1 Glauber-Sudarshan P Representation

The Glauber-Sudarshan P representation is defined as a quasi probability distribution of coherent states forming a density matrix

$$\rho = \int \mathrm{d}^2\alpha\, |\alpha\rangle\langle\alpha|\, P(\alpha,\alpha^*)\,, \tag{2.4.1}$$

or vice versa,

$$P(\alpha,\alpha^*) = \frac{1}{\pi^2}\int \mathrm{d}^2\beta\, \mathrm{e}^{\beta^*\alpha-\beta\alpha^*}\, \mathrm{Tr}[D(\beta,1)\rho]\,, \tag{2.4.2}$$

where

$$D(\beta, s) = \mathrm{e}^{\beta a^\dagger - \beta^* a + s|\beta|^2/2} = \mathrm{e}^{(s-1)|\beta|^2/2} \mathrm{e}^{\beta a^\dagger} \mathrm{e}^{-\beta^* a} \tag{2.4.3}$$

is a generalization of the standard displacement operator $D(\beta) = D(\beta, 0)$. A coherent state $|\alpha\rangle$, see Eq. (2.1.11), can be generated by applying $D(\alpha)$ to the ground state,

$$|\alpha\rangle = \mathrm{e}^{-|\alpha|^2/2} \sum_{n=0}^{\infty} \frac{\alpha^n}{\sqrt{n!}} |n\rangle = \mathrm{e}^{-|\alpha|^2/2} \mathrm{e}^{\alpha a^\dagger} |0\rangle = D(\alpha) |0\rangle \ . \tag{2.4.4}$$

Further useful identities of the displacement operator are

$$\begin{aligned} D^\dagger(\alpha) &= D(-\alpha)\,, && (2.4.5) \\ aD(\alpha) &= D(\alpha)(a+\alpha)\,, && (2.4.6) \\ D(\alpha)a^\dagger &= (a^\dagger - \alpha^*)D(\alpha)\,, && (2.4.7) \\ D(\beta)|\alpha\rangle &= \mathrm{e}^{(\beta\alpha^* - \beta^*\alpha)/2} |\alpha + \beta\rangle \ . && (2.4.8) \end{aligned}$$

Given a Lindblad Master equation, that defines the time evolution of ρ, the corresponding equation of motion of the state representation function $P(\alpha, \alpha^*, t)$ can be obtained as follows. The creation and annihilation operators that act on $|\alpha\rangle\langle\alpha|$ can be expressed by derivatives with respect to α and α^* using

$$\begin{aligned} \partial_\alpha |\alpha\rangle\langle\alpha| &= \partial_\alpha (\mathrm{e}^{-|\alpha|^2} \mathrm{e}^{\alpha a^\dagger} |0\rangle\langle 0| \mathrm{e}^{\alpha^* a}) = (a^\dagger - \alpha^*) |\alpha\rangle\langle\alpha| \ , && (2.4.9) \\ \partial_{\alpha^*} |\alpha\rangle\langle\alpha| &= \partial_{\alpha^*} (\mathrm{e}^{-|\alpha|^2} \mathrm{e}^{\alpha a^\dagger} |0\rangle\langle 0| \mathrm{e}^{\alpha^* a}) = |\alpha\rangle\langle\alpha| (a - \alpha)\,. && (2.4.10) \end{aligned}$$

By inserting Eq. (2.4.1) in the Lindblad master equation, terms of the form

$$\begin{aligned} f(a^\dagger, a)\rho &= \int \mathrm{d}^2\alpha\, P(\alpha, \alpha^*, t) f(a^\dagger, a) |\alpha\rangle\langle\alpha| \ , && (2.4.11) \\ \rho\, g(a^\dagger, a) &= \int \mathrm{d}^2\alpha\, P(\alpha, \alpha^*, t) |\alpha\rangle\langle\alpha| g(a^\dagger, a)\,, && (2.4.12) \end{aligned}$$

can be identified and replaced using Eqs. (2.4.9) and (2.4.10). By partial integration, the derivatives that act on $|\alpha\rangle\langle\alpha|$ can be moved to act on $P(\alpha, \alpha^*, t)$.

A state that exhibits negative values of its corresponding P is defined to be *non-classical*.

2.4.2 Husimi Q Function

Another famous probability distribution is the Husimi Q function [Husimi (1940)] which will be relevant in, e.g., Secs. 7.1.1 and 7.2.1 as well as Ch. 8. Its definition

$$\begin{aligned} Q(\alpha, \alpha^*) &= \frac{1}{\pi^2} \int \mathrm{d}^2\beta\, \mathrm{e}^{\beta^*\alpha - \beta\alpha^*} \,\mathrm{Tr}[D(\beta, -1)\rho] = \frac{1}{\pi} \int \mathrm{d}^2\beta\, \mathrm{e}^{-|\alpha-\beta|^2} P(\beta, \beta^*) \\ &= \frac{1}{\pi} \langle\alpha| \rho |\alpha\rangle \ , && (2.4.13) \end{aligned}$$

note the similarity to Eq. (2.4.2), can be written as the projection of a state ρ onto coherent states $|\alpha\rangle$. The exponential in the second equation in the first line of Eq. (2.4.13) can be interpreted as a Gaussian filter leading to smoothing of P. The last line of Eq. (2.4.13) together with $\int \mathrm{d}^2\alpha\, |\alpha\rangle\langle\alpha| = \pi\mathbb{1}$ shows that Q is a proper probability distribution, i.e., normalized to one and nonnegative.

2.4.3 Wigner Function

Maybe the most famous quasi probability distribution is the Wigner function,

$$W(\alpha,\alpha^*) = \frac{1}{\pi^2}\int \mathrm{d}^2\beta\, \mathrm{e}^{\beta^*\alpha-\beta\alpha^*}\,\mathrm{Tr}[D(\beta,0)\rho] = \frac{2}{\pi}\int \mathrm{d}^2\beta\, \mathrm{e}^{-2|\alpha-\beta|^2}P(\beta,\beta^*)\,. \tag{2.4.14}$$

Note the similarity to Eqs. (2.4.2) and (2.4.13). It will be the standard function to visualize states in this thesis.

As an example, the Wigner function of a coherent state,

$$W(\alpha,\alpha^*) = \frac{2}{\pi}\mathrm{e}^{-2|\alpha-\beta|^2}\,, \tag{2.4.15}$$

is nonnegative. In contrast, the Wigner function of the Fock state $|n\rangle$,

$$W(\alpha,\alpha^*) = (-1)^n\frac{2}{\pi}L_n^0(4|\alpha|^2)\mathrm{e}^{-2|\alpha|^2}\,, \tag{2.4.16}$$

where L_n^0 is a Laguerre polynomial, see Eq. (3.3.12), features negative values. The definition of nonclassical states given in Sec. 2.4.1 partially applies to the Wigner function: if the Wigner function features negative values, the state is nonclassical. An example for which the other direction is not true are squeezed states [Gerry and Knight (2004)],

$$|\zeta\rangle = \mathrm{e}^{(\zeta^* a^2-\zeta a^{\dagger 2})/2}\,|0\rangle\;, \tag{2.4.17}$$

with Wigner function

$$W(\alpha,\alpha^*) = \frac{2}{\pi}\exp\left(-\frac{\mathrm{Re}[\alpha]^2\mathrm{e}^{-2|\zeta|}+\mathrm{Im}[\alpha]^2\mathrm{e}^{2|\zeta|}}{2}\right). \tag{2.4.18}$$

In comparison to Eq. (2.4.3), the squeezing operator can be interpreted as a generalization of the displacement operator to higher-orders of a. Squeezing of even higher orders is visualized in Fig. 7.3.

Part I

Quantum Computing on Superconducting Hardware

Chapter 3

Quantum Computing and Quantum Simulation

In the 1980s, inspirational suggestions have been made to consider a quantum description of computers [Benioff (1980)], or vice versa, quantum systems as platforms for computation [Feynman (1982)]. Shortly thereafter, a handful of elementary algorithms [Deutsch and Penrose (1985), Deutsch and Jozsa (1992), Simon (1997), Bernstein and Vazirani (1997)] as well as more advanced algorithms like Grover's algorithm [Grover (1996)] and Shor's algorithm [Shor (1997)] have been published

3.1 Universal Quantum Computing

These quantum algorithms mentioned above, rely on quantum computation and quantum information. The terms quantum computing and quantum computation will be mostly used as synonyms, similar for quantum information and quantum information processing. This section is based on [Nielsen and Chuang (2010)].

3.1.1 Qubits and Quantum Gates

The fundamental building block of a classical computer is a bit c which can take two values $c \in \{0, 1\}$. Similarly, the fundamental building block of a quantum computer and quantum information is called a *quantum bit* (qubit). It is a quantum mechanical two-level system, i.e., a spin-1/2, whose states are most often defined as

$$|0\rangle \leftrightarrow \begin{pmatrix} 1 \\ 0 \end{pmatrix}, \quad |1\rangle \leftrightarrow \begin{pmatrix} 0 \\ 1 \end{pmatrix}. \tag{3.1.1}$$

The state space of an arbitrary pure qubit state $|\psi\rangle = \alpha |0\rangle + \beta |1\rangle$ with $\alpha, \beta \in \mathbb{C}$ is limited due to the normalization condition

$$\langle\psi|\psi\rangle = (\alpha^* \langle 0| + \beta^* \langle 1|)(\alpha |0\rangle + \beta |1\rangle) = |\alpha|^2 + |\beta|^2 = 1\,, \tag{3.1.2}$$

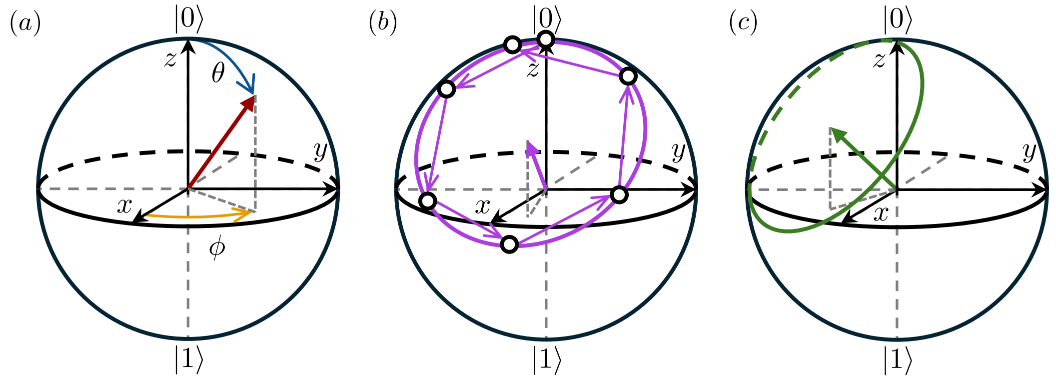

Figure 3.1: Bloch sphere state representations. (a) A pure state (red arrow) can be described by two angles θ and ϕ. (b) Arbitrary rotations (purple circle) of $|0\rangle$ around $\vec{n}^* = (\cos(\pi/8), \sin(\pi/8), \cos(\pi/8))$ (purple arrow with solid head), see Eq. (3.1.12), can be approximated by R^{*n}. The dots correspond to $R^{*n}\,|0\rangle$ for $n = 0, 1, 2, 3, 4, 5, 6$. Note that $R^{*6}\,|0\rangle \neq |0\rangle$. (c) Arbitrary rotations (green circle) of $|0\rangle$ around $\vec{m}^* = (\cos(\pi/8), -\sin(\pi/8), \cos(\pi/8))$ (green arrow with solid head), see Eq. (3.1.13), can be approximated by $(HR^*H)^n$.

which is used to fix the magnitude of the coefficients. A common parametrization is

$$|\psi\rangle = \cos(\theta/2)\,|0\rangle + \mathrm{e}^{\mathrm{i}\phi}\sin(\theta/2)\,|1\rangle\ , \tag{3.1.3}$$

where $\theta \in [0, \pi]$ and $\phi \in [0, 2\pi]$. The state can be visualized as a three-dimensional real-valued vector connecting the origin with a point on the so-called *Bloch sphere* of unit radius, see Fig. 3.1(a).

In the qubit Hilbert space, arbitrary transformations that preserve the norm of the state are described by unitary SU(2) operators

$$U = \mathrm{e}^{\mathrm{i}\eta}\exp\left(-\frac{\mathrm{i}}{2}\vec{n}\vec{\sigma}\right) = \mathrm{e}^{\mathrm{i}\eta}\cos\left(\frac{|\vec{n}|}{2}\right)\mathbb{1} - \mathrm{i}\mathrm{e}^{\mathrm{i}\eta}\sin\left(\frac{|\vec{n}|}{2}\right)\frac{\vec{n}}{|\vec{n}|}\vec{\sigma}\,, \tag{3.1.4}$$

where $\vec{\sigma}$ is the vector of Pauli matrices

$$\sigma^x = X = |1\rangle\langle 0| + |0\rangle\langle 1| \leftrightarrow \begin{pmatrix} 0 & 1 \\ 1 & 0 \end{pmatrix}\ , \tag{3.1.5}$$

$$\sigma^y = Y = \mathrm{i}\,|1\rangle\langle 0| - \mathrm{i}\,|0\rangle\langle 1| \leftrightarrow \begin{pmatrix} 0 & -\mathrm{i} \\ \mathrm{i} & 0 \end{pmatrix}\ , \tag{3.1.6}$$

$$\sigma^z = Z = |0\rangle\langle 0| - |1\rangle\langle 1| \leftrightarrow \begin{pmatrix} 1 & 0 \\ 0 & -1 \end{pmatrix}\ . \tag{3.1.7}$$

The unitary operator in Eq. (3.1.4) can be interpreted as a SO(3) rotation of states on the Bloch sphere with angle $|\vec{n}|$ around the axis $\vec{n}/|\vec{n}|$. Rotations around the individual axes are defined as

$$RX(\phi) = \exp\left(-\frac{\mathrm{i}}{2}\phi X\right),\quad RY(\phi) = \exp\left(-\frac{\mathrm{i}}{2}\phi Y\right),\quad RZ(\phi) = \exp\left(-\frac{\mathrm{i}}{2}\phi Z\right)\ . \tag{3.1.8}$$

On actual quantum hardware, not all of these operations, called “gates” like in classical computing, have to implemented physically. For example, since RZ can be realized virtually [McKay et al. (2017)], a rotation around the x-axis can be realized effectively by a fixed rotation around the x-axis, i.e., the Hardamard gate $H = (X + Z)/\sqrt{2} = -\mathrm{i}RZ(\pi/2)RX(\pi/2)RZ(\pi/2)$, and virtual rotations around the z-axis,

$$RX(\theta) = HRZ(\theta)H\,. \tag{3.1.9}$$

In general, the less gates that need to be calibrated the better. However, this approach of replacing a single parametrized gate by a sequence of few calibrated gates is only preferable if the few gates have low error. An alternative way of expressing the general single-qubit gate U of Eq. (3.1.4) using the elementary rotations defined in Eq. (3.1.8) is

$$U = \mathrm{e}^{\mathrm{i}\eta}RZ(\phi)RY(\theta)RZ(\gamma) = \mathrm{e}^{\mathrm{i}\eta}RZ(\phi + \pi/2)RX(\theta)RZ(\gamma - \pi/2)\,. \tag{3.1.10}$$

Other relevant gates are the S and T gate that obey $Z = S^2 = T^4$,

$$S = \begin{pmatrix} 1 & 0 \\ 0 & \mathrm{i} \end{pmatrix}, \quad T = \begin{pmatrix} 1 & 0 \\ 0 & \mathrm{e}^{\mathrm{i}\pi/4} \end{pmatrix}. \tag{3.1.11}$$

Using only T and H gates, a rotation around $\vec{n}^*/|\vec{n}^*|$, where

$$\vec{n}^* = (\cos(\pi/8), \sin(\pi/8), \cos(\pi/8))\,, \tag{3.1.12}$$

by an irrational rotation angle θ^*, that is implicitly defined by $\cos(\theta^*/2) = \cos^2(\pi/8)$, can be realized by the gate $R^* = THTH$. Since $3\theta^*/\pi \approx 1.046657$, R^{*6} almost matches $-\mathrm{i}\mathbb{1}$, i.e., since θ^* is irrational, an integer multiple of rotations R^* do not come back to the initial starting point, see Fig. 3.1(b). Thus, this small discrepancy leads to the fact that R^{*n} can approximate any rotation around the axis $\vec{n}^*/|\vec{n}^*|$. Since furthermore HR^*H corresponds to a rotation around a linearly independent axis $\vec{m}^*/|\vec{m}^*|$, where

$$\vec{m}^* = (\cos(\pi/8), -\sin(\pi/8), \cos(\pi/8))\,, \tag{3.1.13}$$

see Fig. 3.1(c), an arbitrary single-qubit gate can be realized by only using T and H gates,

$$U = R^{*k_1}(HR^*H)^{k_2}R^{*k_3}\,. \tag{3.1.14}$$

The exponents k_j have to be chosen such that U approximates the desired gate up to the required accuracy. In conclusion, if a quantum computer can apply a large number of gates efficiently enough, only two gates (T and H) have to be implemented physically to realize any single-qubit operation!

In a useful algorithm, more than one qubit is needed. Quantum states of n qubits, a so-called register, are defined by tensor products

$$|q_{n-1}q_{n-2}\dots q_1q_0\rangle = |q_{n-1}\rangle_{n-1} \otimes |q_{n-2}\rangle_{n-2} \otimes \cdots \otimes |q_1\rangle_1 \otimes |q_0\rangle_0 \leftrightarrow |z\rangle \ . \tag{3.1.15}$$

The symbol $|q_j\rangle_j$ denotes that the jth qubit is in state $q_j \in \{0,1\}$. Sometimes, the index j that indicates the difference between multiqubit and single-qubit states as well as $\otimes$ are omitted. Here, we use the standard convention of binary number representation $z = \sum_{j=0}^{n-1} q_j 2^j$ such that the multiqubit state can be written as $|z\rangle$.

A fundamental two-qubit gate is the CNOT gate,

$$\mathrm{CNOT}(1,0)\,|q_1\rangle_1 \otimes |q_0\rangle_0 = |q_1\rangle_1 \otimes |q_1 \oplus q_0\rangle_0 \ , \tag{3.1.16}$$

$$\mathrm{CNOT}(0,1)\,|q_1\rangle_1 \otimes |q_0\rangle_0 = |q_1 \oplus q_0\rangle_1 \otimes |q_0\rangle_0 \ , \tag{3.1.17}$$

where the first index corresponds to the control qubit and the second index to the target qubit. Here, $\oplus$ denotes a cyclical addition,

$$q_1 \oplus q_0 = (q_0 + q_1) \bmod 2\,. \tag{3.1.18}$$

Therefore, if the control qubit is in state $|0\rangle_i$, then the target qubit state remains unchanged. If the control qubit is in state $|1\rangle_i$, then an X gate is applied to the target state, i.e., $X\,|q_j\rangle_j = |q_j \oplus 1\rangle_j$. Note that this conditional behavior of applying an X gate on the target qubit or not does not involve a measurement. If the control qubit is in a superposition, the total state will also be in a superposition, e.g., for the maximally entangled Bell state

$$|B_{00}\rangle = \mathrm{CNOT}(1,0)(H\,|0\rangle_1) \otimes |0\rangle_0 = (|00\rangle + |11\rangle)/\sqrt{2}\,. \tag{3.1.19}$$

Here, entanglement is quantified by the von Neumann entropy [Neumann (1927c)]

$$S(\mathrm{Tr}_j[\rho]) = -\,\mathrm{Tr}[\mathrm{Tr}_j[\rho]\ln(\mathrm{Tr}_j[\rho])] = -\sum_k \lambda_k \ln(\lambda_k)\,, \tag{3.1.20}$$

where λ_k are the eigenvalues of the state reduced density matrix $\mathrm{Tr}_j[\rho]$. The partial trace Tr_j traces out only states of qubit j.

The H, S, and CNOT gate are elements of the so-called Clifford group. Together with the T gate, they form a set of universal quantum gates, meaning any unitary two-qubit operation can be represented as a sequence of these gates. Note the redundancy $S = T^2$. Furthermore, an n-qubit unitary operator can be decomposed into sequences of two-qubit unitaries [Barenco et al. (1995)].

3.1.2 Quantum Algorithms

Using the universal gate set $\{H, S, \mathrm{CNOT}, T\}$, any n-qubit unitary operation can be constructed. In general, quantum algorithms consist of sequences of many gates and are presented in a circuit diagram. The standard readout method is to measure every qubit in the Z basis at the end of the circuit. Here, the final state $|\psi\rangle = U_{\text{circuit}}\,|0\rangle^{\otimes n} =$

$U_{\text{circuit}} \left|0\right\rangle_{n-1} \otimes \cdots \otimes \left|0\right\rangle_0$ will be projected onto possible outcomes $q_{n-1} \dots q_0$ with the probability $|\left\langle q_{n-1} \dots q_0 | \psi \right\rangle|^2$. Here, we will look at some basic example circuits. The visualizations of the quantum circuits shown below are generated using Qiskit [Javadi-Abhari et al. (2024)].

The previously mentioned Bell state $\left|B_{00}\right\rangle$ is generated by the circuit

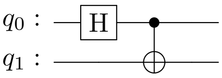

Each qubit in the register has its own timeline of gates that are applied to it and is initialize to $\left|0\right\rangle$. The “time” (order of operations) flows from left to right, i.e., the opposite direction of matrix multiplication. Single-qubit gates appear as boxes and multiqubit gates are connected to all qubit lines they are applied to. The CNOT gate is connected to the line of the control qubit with a solid dot and to the line of the target qubit with the $\oplus$ symbol, see Eq. (3.1.18). A solid (empty) dot means that the rest of the gate operation is active if the control qubit is in state $\left|1\right\rangle$ ($\left|0\right\rangle$). Another important two-qubit gate is the SWAP gate

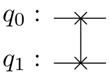

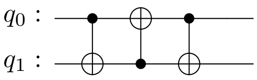

which can be constructed using three CNOTs. It swaps the state of the two connected qubits. Multiple swaps can be used to virtually move qubits around in the register such that two-qubit gates between distant qubits can be executed.

An example for a three-qubit gate is the Toffoli gate

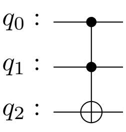

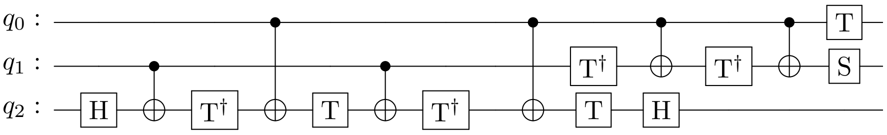

Here, an X gate is applied to the last qubit if both q_0 and q_1 are in the state $\left|1\right\rangle$. Note that $T^\dagger = T^3 Z$. Interestingly, applying an X gate to q_2 after the Toffoli gate, the classical NAND gate $q_2 = \neg(q_0 \wedge q_1)$ is realized. The NAND gate is the universal gate of classical computing [Mano and Ciletti (2013)], i.e., it can be used to implement any logical operation and therefore any algorithm. Thus, any classical algorithm can be implemented on a quantum computer.

The arguably most famous quantum algorithm is the Shor algorithm [Shor (1997)]. It can be used to speed up prime factorization, whose difficulty is essential for the security of RSA encryption [Rivest et al. (1978)], from exponential scaling to polynomial scaling. A detailed description can be found in Ch. 5 of [Nielsen and Chuang (2010)].

Another important class of gate sequences are error correction codes that provide protection against certain errors. Famous examples are the Shor code [Shor (1995)], the toric code [Kitaev (1997)], the color code [Bombin and Martin-Delgado (2006), Bombin and Martin-Delgado (2007)], low-density parity-check codes [Gottesman (2014)], the binomial code [Michael et al. (2016)], and the cat code [Ofek et al. (2016)].

3.2 Digital Quantum Simulation

A perfectly operating quantum computer can be used to simulate the unitary time evolution of a quantum system. The Suzuki-Trotter decomposition [Trotter (1959), Suzuki (1976)] can be used to split the time evolution of a Hamiltonian $H = \sum_j H_j$ into products of time evolutions of its constituents H_j. The unitaries describing the time evolutions of these constituents can be represented by quantum gates. The approximation can be performed in various orders of the small time step Δt [Nielsen and Chuang (2010)]

$$\mathrm{e}^{-\mathrm{i}(H_0+H_1)\Delta t} = \mathrm{e}^{-\mathrm{i}H_0\Delta t}\mathrm{e}^{-\mathrm{i}H_1\Delta t} + \mathcal{O}(\Delta t^2) = \mathrm{e}^{-\mathrm{i}H_0\Delta t/2}\mathrm{e}^{-\mathrm{i}H_1\Delta t}\mathrm{e}^{-\mathrm{i}H_0\Delta t/2} + \mathcal{O}(\Delta t^3). \tag{3.2.1}$$

The higher-order approximations can be interpreted as analogies to classical higher-order integration algorithms like the Runge-Kutta methods [Runge (1895), Kutta (1901)]. An example where such a decomposition has been used to simulate the effective time evolution of a spin-1 is presented in [Koppenhöfer et al. (2020)].

3.3 Quantum Computing Hardware

So far, we discussed the theoretical and abstract form of quantum computing and quantum gates. In this section, the focus will be on the physical implementation of qubits and gate operations. Similar to the various platforms of classical computing, e.g., silicon, spintronics [Wolf et al. (2006)], and carbon nanotubes [Shulaker et al. (2013)]), there exists a variety of platforms that are candidates for quantum computers. Examples include superconducting circuits [Blais et al. (2021)], trapped ions [Bruzewicz et al. (2019)], cold atoms and Rydberg atoms [Saffman (2016)], electron spins in quantum dots [Burkard et al. (2023)], and photonic circuits [Bourassa et al. (2021)]. In the following, the superconducting transmon [Koch et al. (2007)] and trapped ions [Leibfried et al. (2003)] will be presented in more detail.

As we will see below, physical implementations of two-level qubits often feature many more quantum states. A system with d available computational states is called a qudit. The higher-excited states of qudits can provide advantages in many ways, e.g., see the works [Fedorov et al. (2012), Zeytinoğlu et al. (2015), Egger et al. (2018), Elder et al. (2020)] or the review [Wang et al. (2020)].

3.3.1 Transmon Qudits

The superconducting circuits subgroup of quantum computing platforms itself is a zoo of different materials and architectures. Examples include the charge qubit [Shnirman et al. (1997)], fluxonium [Manucharyan et al. (2009)], the phase qubit [Martinis et al. (2002)], the Xmon [Barends et al. (2013)], and the blochnium [Pechenezhskiy et al. (2020)]. Reviews of superconducting architechtures are [Makhlin et al. (2001), Krantz et al. (2019)]. Several companies including IBM, Google, IQM, and Rigetti are building

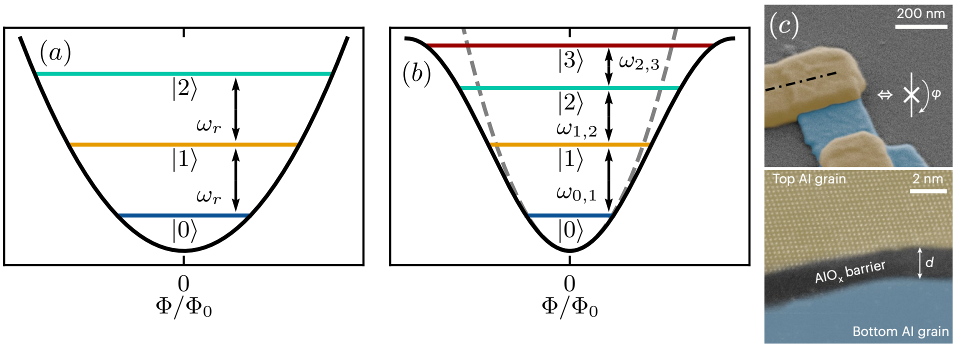

Figure 3.2: Schematic potentials of quantum oscillators and lower-excited Fock states. (a) Quantum harmonic oscillator, see Eqs. (3.3.1) and (3.3.3). (b) Quantum anharmonic oscillator, see Eq. (3.3.4). (c) False-colored scanning electron microscope (upper) and scanning transmission electron microscope (lower) images of an Al-AlO$_x$-Al Josephson junction. Adapted from [Willsch et al. (2024)] and used under CC BY 4.0 (https://creativecommons.org/licenses/by/4.0/).

commercial superconducting quantum computers. The following is based on [Blais et al. (2021)].

The arguably most famous quantum model is the quantum harmonic oscillator, see Sec. 2.1. A well-known example in classical electronics is the LC oscillator, an electronic circuit consisting of a coil with inductance L and a capacitor with capacitance C. The eigenfrequency of this resonator is $\omega_r = 1/\sqrt{LC}$ and the Hamiltonian reads

$$H_{LC} = \frac{Q^2}{2C} + \frac{\Phi^2}{2L} = \frac{Q^2}{2C} + \frac{C}{2}\omega_r^2\Phi^2 \,. \tag{3.3.1}$$

Here, Q is the charge stored on the capacitor and Φ is the magnetic flux in the inductance. The right-hand side can be identified as the electronic analogue of the mechanical harmonic oscillator where C corresponds to a mass m, Q to a momentum p, and Φ to a position x. Therefore, the canonical quantization procedure in this case corresponds to the following choice of creation and annihilation operators

$$\Phi = \sqrt{\frac{\hbar}{2\omega_r C}}(a^\dagger + a), \quad Q = \mathrm{i}\sqrt{\frac{\hbar\omega_r C}{2}}(a^\dagger - a)\,, \tag{3.3.2}$$

leading to

$$H_{LC} = \hbar\omega_r\left(a^\dagger a + \frac{1}{2}\right) . \tag{3.3.3}$$

Eigenstates of this Hamiltonian are Fock states $|n\rangle$, with $a^\dagger a\,|n\rangle = n\,|n\rangle$. Energy differences between neighboring states $|n\rangle$ and $|n+1\rangle$ are constant $\hbar\omega_r$, see Fig. 3.2(a). In Sec. 3.1, we saw that quantum computers should feature two quantum states that are perfectly addressable in the sense of quantum gate operations. However, since the energy spacing of the quantum harmonic oscillator is constant, a drive that is in resonance with the $|0\rangle \leftrightarrow |1\rangle$ transition will also drive all other transitions of the form $|j\rangle \leftrightarrow |j+1\rangle$.

This problem can be solved by introducing anharmonicity. One possibility is to replace the standard inductance with a Josephson junction [Josephson (1962)], see Fig. 3.2(c). The transmon Hamiltonian incorporating the capacitance, the Josephson junction, and an (i) external gate voltage or (ii) influence by quasi-particle tunneling [Ristè et al. (2013)] reads

$$H_T = 4E_C(n - n_g)^2 - E_J \cos\left(2\pi\frac{\Phi}{\Phi_0}\right). \tag{3.3.4}$$

Here, $n = Q/2e$ is the charge number operator of the Cooper pairs, the scalar n_g is the so-called offset charge, $\Phi_0 = h/2e$ the flux quantum, E_C the charging energy, and E_J the Josephson energy. The anharmonic cosine potential is depicted schematically in Fig. 3.2(b). It can be interpreted as an analogy to the gravitational potential of a pendulum or a rotor. Note that higher-order Josephson harmonics of the cosine potential can be relevant [Willsch et al. (2024), Wang et al. (2025)].

The quantized version of Eq. (3.3.4) can be written as [Vool and Devoret (2017)]

$$H_T = 4E_C \sum_n (n - n_g)^2 \left|n\middle\rangle\middle\langle n\right| - \frac{E_J}{2} \sum_n \left(|n\rangle\langle n+1| + |n+1\rangle\langle n|\right), \tag{3.3.5}$$

or in the $E_J \gg E_C$ limit as

$$H_T \overset{E_J \gg E_C}{\approx} \hbar\omega_q b^\dagger b - \frac{E_C}{2} b^\dagger b^\dagger b b\,. \tag{3.3.6}$$

Here, b is the annihilation operator of the transmon, $\omega_q = \sqrt{8E_JE_C} - E_C$ is the qubit energy between the ground state and the first excited state, and $-E_C$ is the anharmonicity. The resulting spectra for $E_J/E_C = 5$ and $E_J/E_C = 45$ are shown in Figs. 3.3(a) and 3.3(b). For $E_J/E_C = 45$, the anharmonicity of the levels is visible and enables driving transitions between $|j\rangle \leftrightarrow |j+1\rangle$ selectively. Especially, transitions in the qubit subspace $|0\rangle \leftrightarrow |1\rangle$, i.e., gates, can be realized. The number of addressable transmon levels can be estimated as the number of bound states in the Josephson potential. Assuming zero anharmonicity, it can be approximated by dividing the height of the potential $2E_J$ by the energy spacing between neighboring levels

$$N_\text{bound} \approx \frac{2E_J}{\sqrt{8E_JE_C} - E_C} \approx \sqrt{\frac{E_J}{2E_C}}\,, \tag{3.3.7}$$

see the dashed curve in Fig. 3.3(c). Taking a constant anharmonicity $-E_C$ into account, the approximation turns into $N_\text{bound} \approx (\sqrt{8} - 2)\sqrt{E_J/E_C}$, see the dotted curve in Fig. 3.3(c).

In the paragraphs above, we have seen that physical implementations of qubits, e.g., the superconducting transmon, feature more states than only the two qubit states. Therefore, it is natural to think about quantum information beyond two-level systems. Taking higher-excited states into account, the so-called quantum dit (*qudit*) is born. Here, the “d” stands for an integer number d larger than two and corresponds to the

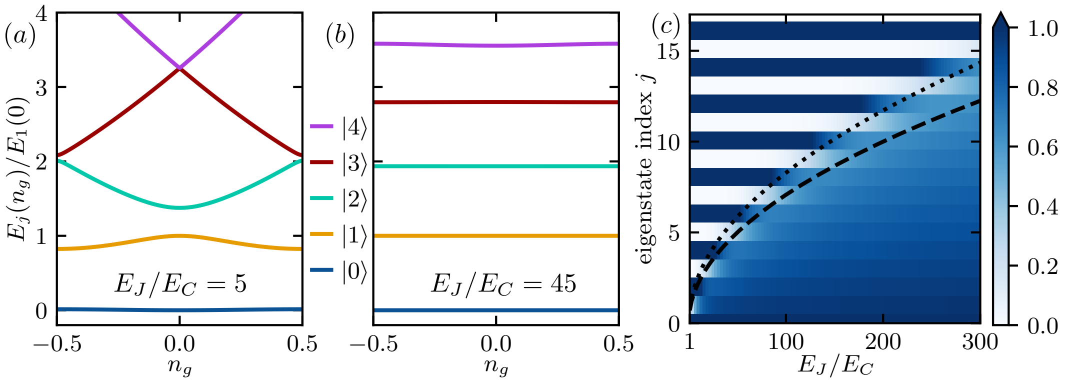

Figure 3.3: Schematic level structure based on the eigenenergies $E_j(n_g)$ of the transmon Hamiltonian Eq. (3.3.5). (a) Low E_J/E_C limit: strong dependence of the eigenenergies on n_g. (b) Large E_J/E_C limit, typical values for transmon qubits, see Fig. 4.1: less dependence of the eigenenergies on n_g. (c) The ratio $E_j(0)/E_0(0)$ which depends smoothly on j for bound states and jumps between zero and values above one for unbound states. The dashed curve corresponds to $\sqrt{E_J/2E_C}$ and the dotted curve corresponds to $(\sqrt{8}-2)\sqrt{E_J/E_C}$. Both are approximations of the number of bound states, see Eq. (3.3.7).

base of the number system we use for representing states. The case $d = 3$ is also known as the qutrit. In Ch. 4, that is based on [Kehrer et al. (2024a)], a measurement of a ququart (four states) on an IBM Quantum transmon will be presented. Qudits can be used to simulate large-spin systems more naturally [Champion et al. (2025)].

Using Qiskit [Javadi-Abhari et al. (2024)], the software development kit for quantum hardware of IBM and other companies, quantum algorithms can be programmed. On superconducting platforms, gates are implemented as microwave pulses of an external drive that acts on the qudit. The model Hamiltonian of qudit states $|j\rangle$ with eigenenergies ω_j in the rotating frame of the drive is

$$H = \sum_j (\omega_j - j\omega_d)\,|j\rangle\langle j| + \Omega_q(b^\dagger + b)\,, \tag{3.3.8}$$

where ω_d is the drive frequency and Ω_q is the drive strength. In Fig. 3.4, simulation data based on Rabi oscillations between $|j\rangle \leftrightarrow |j+k\rangle$ for $k = 1, 2, 3$ are shown. The qudit is prepared in the state $|j\rangle$ (corresponds to color) and a drive with frequency ω_d is applied, see Eq. (3.3.8). The height of the curve corresponds to the minimal population of this state in the time evolution of duration $t\omega_{0,1} = 4000$. A dip indicates a resonant transition. Solid, dashed and dotted lines correspond to the predictions of first, second, and third-order transitions. In Fig. 4.6, we will present measurement data of the implementation of a $|0\rangle \leftrightarrow |2\rangle$ and $|1\rangle \leftrightarrow |3\rangle$ transition.

In preparation for the publication [Kehrer et al. (2024a)] presented in Ch. 4, several experiments have been run on IBM Quantum hardware. Experimental data on up to second-order transitions is presented in Fig. 4.6. Preliminary data on the $|0\rangle \leftrightarrow |3\rangle$ transition on *ibmq_lima* as well as on the $|2\rangle \leftrightarrow |4\rangle$ transition on *ibmq_guadalupe* has been collected. A Ramsey measurement like in [Ristè et al. (2013)] has revealed the two background charge configurations $n_g = 0, 0.5$ indicated by two observed qubit

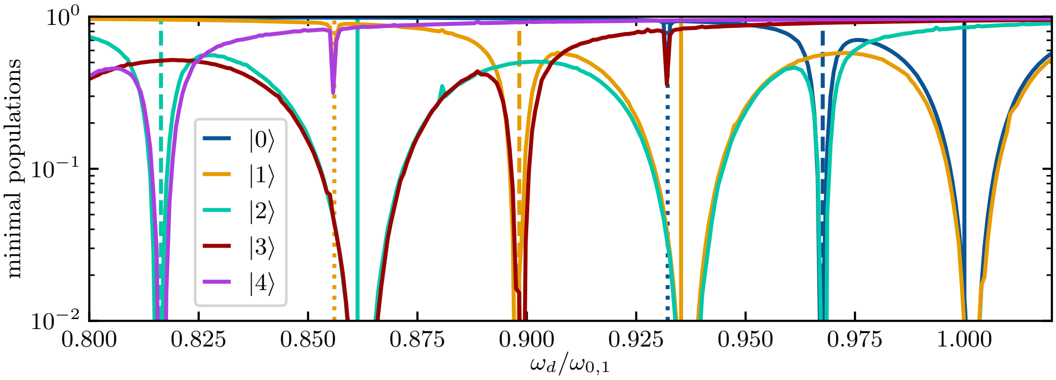

Figure 3.4: Simulated Rabi oscillations for $E_J/E_C = 45$ and $\Omega_q = 0.008\omega_{0,1}$ of duration $t\omega_{0,1} = 4000$ between states $|j\rangle \leftrightarrow |j+k\rangle$, see Eq. (3.3.8). The color of the curves corresponds to the state $|j\rangle$ in which the qudit is initialized and the height of the curves corresponds to the minimal population of $|j\rangle$ during the time evolution. Vertical lines of solid, dashed, and dotted (for $k = 1, 2, 3$) style indicate the prediction of the transition frequency $\omega_{j,j+k} = (E_{j+k} - E_j)/k$ between $|j\rangle \leftrightarrow |j+k\rangle$. The energy E_j is the average of $E_j(n_g)$ over $n_g \in [-0.5, 0.5]$, see Fig. 3.3(b). The choice of E_J/E_C is typical for IBM Quantum devices, see Fig. 4.1(b).

frequencies.

An overview of other retired devices with, e.g., $n_q = 1, 5, 7, 16, 27, 65, 127, 433$ qubits, can be found online[5]. For IBM's vision about the future of quantum computing, check out the roadmap[6] of IBM Quantum.

In Sec. 4.4, the model for reading out transmon qudit states is presented. Measurement data of a ququart on an IBM Quantum device can be found in Sec. 4.6.

3.3.2 Trapped Ions

Another promising physical platform for quantum computing are trapped ions. Here, some lower-energy levels in the electronic structure of single ions, e.g., of calcium, beryllium, strontium, or ytterbium, are used to encode the logical qubit states $|g\rangle$ (ground state) and $|e\rangle$ (excited state), see [Bruzewicz et al. (2019)]. Companies that are building commercial trapped-ion quantum computers are, e.g., AQT, IonQ, and Quantinuum. The following is based on [Leibfried et al. (2003)].

Single ions are mostly trapped in either Penning traps [Penning (1936)] or Paul traps [Paul (1990)]. The latter trap uses oscillating electromagnetic fields at radio-frequency. The effective trapping potential is often described as a quadratic harmonic potential. In so-called linear traps, ions are trapped strongly in the radial direction but less strong in the axial direction. The interaction between the motional degree of freedom along the trap axis and the electronic states is mediated by laser light propagating along the same trap axis. The so-called Lamb-Dicke parameter $\eta = kx_0 = k\sqrt{\hbar/2m\nu}$ depends on the effective wave vector k of the light, on the ion mass, and on the trap

---

[5] https://quantum.cloud.ibm.com/docs/de/guides/retired-qpus [Accessed: August 3, 2025]

[6] https://www.ibm.com/quantum/technology [Accessed: August 3, 2025]

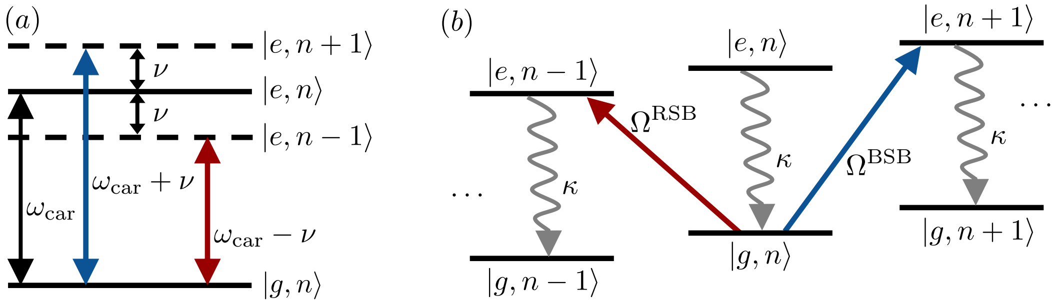

Figure 3.5: Blue and red sideband transitions. (a) The first blue sideband corresponds to $\delta = \nu$ and the first red sideband corresponds to $\delta = -\nu$. The surplus (missing) energy ν is compensated by (de)exciting the motion by one quanta $|n\rangle \to |n+1\rangle$ ($|n\rangle \to |n-1\rangle$). (b) Including the fast decay of the ion state $|e\rangle \to |g\rangle$ with rate κ, the sidebands with effective Rabi frequency Ω^{BSB} and Ω^{RSB} can be interpreted to heat and cool the ion motion.

frequency ν. Using η, the effective model Hamiltonian reads

$$H = \frac{\hbar}{2}\Omega_0 \sigma^+ \exp\Big(\mathrm{i}\eta(a\mathrm{e}^{-\mathrm{i}\nu t} + a^\dagger \mathrm{e}^{\mathrm{i}\nu t})\Big)\mathrm{e}^{\mathrm{i}(\phi - \delta t)} + \text{H.c.}\,. \tag{3.3.9}$$

Here, $\sigma^+ = |e\rangle\langle g|$ is the operator exciting the ion from state $|g\rangle$ to $|e\rangle$, δ is the detuning between the drive frequency and the ion frequency ω_{car} ("carrier"), and a is the annihilation operator of the quantum harmonic oscillator of motion.

In the so-called Lamb-Dicke regime, where $\eta \ll 1$ is small, the first exponential factor in Eq. (3.3.9) can be Taylor expanded. Choosing a detuning $\delta = s\nu$, with $s \in \mathbb{Z}$, the so-called $|s|$th blue (red) sideband transition is driven resonantly if $s > 0$ ($s < 0$), see Fig. 3.5(a). In the $|s|$th blue (red) sideband case, the surplus (missing) energy ν is compensated by (de)exciting the motion by $|s|$ quanta. Including the fast decay of the ion state $|e\rangle \to |g\rangle$ with rate κ, the blue (red) sideband heat (cool) the ion motion $|n\rangle \to |n+s\rangle$, see Fig. 3.5(b). Their effective Rabi frequency is Ω^{BSB} and Ω^{RSB}, where BSB (RSB) means blue (red) sideband. In [Behrle et al. (2023)], a red sideband is realized on a calcium ion and a blue sideband is driven on a beryllium ion simultaneously, both trapped in the same potential. In a certain parameter regime, this leads to a lasing state, also understood as a limit cycle, see Sec. 6.2. In contrast, if the sidebands are driven on the same electronic transition, e.g., squeezed states occur, [Rojkov et al. (2024)]. See Sec. 10.6 for a brief discussion about simultaneous driving of multiple higher-order sidebands.

In Sec. 10.6, another setup will be discussed: the operation of trapped ions outside the Lamb-Dicke regime of small η. Here, the higher orders of the first exponential in Eq. (3.3.9) lead to nonlinear effective Rabi frequencies [Leibfried et al. (2003)],

$$\Omega_{n,n+s} = \Omega_{n+s,n} = \Omega_0 |\langle n+s|\, \mathrm{e}^{\mathrm{i}\eta(a^\dagger + a)}\, |n\rangle\,| = \Omega_0 \eta^{|s|} \mathrm{e}^{-\eta^2/2} \sqrt{\frac{n_{\text{min}}!}{n_{\text{max}}!}} L^{|s|}_{n_{\text{min}}}(\eta^2)\,, \tag{3.3.10}$$

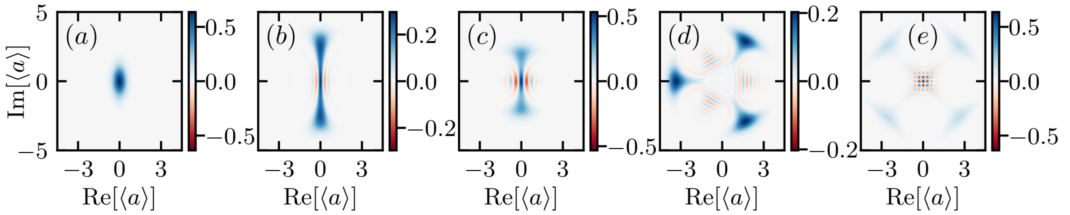

Figure 3.6: Blue and red sidebands driven on the same ion transition with $\Omega^{\mathrm{BSB}} = \Omega^{\mathrm{RSB}} = 0.2\kappa$. (a) Squeezed-like state for $\eta_{\mathrm{BSB}} = 0.1$. (b), (c) Squeezed-cat-like states for $\eta_{\mathrm{BSB}} = 0.4, 0.6$ (from left to right). For panels (a) to (c) $(s_{\mathrm{BSB}}, s_{\mathrm{RSB}}) = (1, -1)$ and $\eta_{\mathrm{RSB}} = 0.3$ is chosen. (d) State resembling a squeezed three-legged cat state for $(s_{\mathrm{BSB}}, s_{\mathrm{RSB}}) = (2, -1)$ and $\eta_{\mathrm{RSB}} = 0.1$. (e) State resembling a squeezed four-legged cat state for $(s_{\mathrm{BSB}}, s_{\mathrm{RSB}}) = (2, -2)$ and $\eta_{\mathrm{RSB}} = 0.2$. For panels (d) and (e) $\eta_{\mathrm{BSB}} = 0.6$ is chosen.

where

$$n_{\min} = \min(n, n+s), \quad n_{\max} = \max(n, n+s)\,, \tag{3.3.11}$$

and the generalized Laguerre polynomials are

$$L_n^k(x) = \sum_{m=0}^{n} (-1)^m \binom{n+k}{n-m} \frac{x^m}{m!}\,, \tag{3.3.12}$$

see Eq. (8.970.1) of [Gradshteyn and Ryzhik (2015)].

Applying a red and a blue sideband to the same electronic transition leads to squeezed states, see Fig. 3.6(a), and states that look like squeezed cat states, see Figs. 3.6(b) and 3.6(c). Moreover, choosing $(s_{\mathrm{BSB}}, s_{\mathrm{RSB}}) = (2, -1)$ or $(s_{\mathrm{BSB}}, s_{\mathrm{RSB}}) = (2, -2)$, states that resemble squeezed three-legged or four-legged cat states can be generated, see Figs. 3.6(d) and 3.6(e). An l-legged cat state is defined as [Haroche and Raimond (2006)]

$$\left|\mathcal{C}_\alpha^{l,n}\right\rangle = \frac{a^n}{\mathcal{N}} \sum_{k=0}^{l-1} \left|\mathrm{e}^{\mathrm{i}2\pi k/l}\alpha\right\rangle\,, \tag{3.3.13}$$

where $n \in [0, l-1]$ and $\mathcal{N}$ guarantees normalization $\left\langle \mathcal{C}_\alpha^{l,n} \middle| \mathcal{C}_\alpha^{l,m} \right\rangle = \delta_{nm}$. In [Rojkov et al. (2024)], the setup was studied with a focus on bosonic error-correction codes [Gottesman et al. (2001), Mirrahimi et al. (2014)]. Depending on the parameters $\Omega^{\mathrm{BSB/RSB}}$ and $\eta_{\mathrm{BSB/RSB}}$, a large phase diagram hosting interesting states might be explored in future research projects, e.g., in the context of dissipative phase transitions [Minganti et al. (2023), Beaulieu et al. (2025)].

Chapter 4

Resolving Transmon Qudit States on IBM Quantum Hardware

This chapter is based on the results published in:

T. Kehrer, T. Nadolny, and C. Bruder,
Improving transmon qudit measurement on IBM Quantum hardware,
Physical Review Research **6**, 013050 (2024)

4.1 Motivation

Conventional quantum computing is based on qubits which are realized on two-level subspaces of a larger physical Hilbert space. A number of physical realizations of qubits have been proposed and implemented on various platforms. These include superconducting qubits [Blais et al. (2021)], trapped ions [Bruzewicz et al. (2019)], cold atoms and Rydberg atoms [Saffman (2016)], as well as electron spins in quantum dots [Burkard et al. (2023)]. On all of these platforms, it is necessary to isolate the two-dimensional qubit space from the remaining states of the physical Hilbert space to avoid leakage out of the computation space. However, utilizing *qudits*, i.e., d-dimensional building blocks of quantum computation, can provide advantages [Fedorov et al. (2012), Zeytinoğlu et al. (2015), Jerger et al. (2016), Egger et al. (2018), Elder et al. (2020), Yurtalan et al. (2020), Wang et al. (2020), Ciavarella et al. (2021), Li et al. (2021), Tacchino et al. (2021), Cervera-Lierta et al. (2022), Fischer et al. (2022), Fischer et al. (2023)]. Examples include implementing an ancilla qubit within the second and third excited states of a qudit [Fischer et al. (2022)] that leads to a smaller number of physical qubits needed to realize the same algorithm. Another example is the so-called shelving [Elder et al. (2020)]: by transferring the population of the first excited state to the second excited state before final readout, the error of identifying the ground state decreases.

Superconducting qubits [Blais et al. (2004), Koch et al. (2007)] are prominent building blocks of noisy intermediate-scale quantum (NISQ) systems [Preskill (2018)]. The most promising example is the so-called *transmon* that can effectively be described as a quantum anharmonic electromagnetic oscillator. In this system, the two lowest-energy levels are identified as the qubit. Taking into account higher-lying transmon levels leads to a natural realization of a superconducting qudit. The smallest extension of the qubit is the qutrit, i.e., a three-level system. Qutrits have been used to implement a Toffoli gate [Fedorov et al. (2012)] with a significantly lower number of elementary gates compared with a realization based on two-level systems. Another interesting example is the recent experimental demonstration of a qutrit Greenberger–Horne–Zeilinger (GHZ) state [Cervera-Lierta et al. (2022)].

In general, if one is interested in measuring a qudit state, a proper classification of all levels involved is needed. In [Bianchetti et al. (2010)], the qubit state is determined by a fit of the time evolution of the system. In setups which do not provide time-resolved data, such as the current IBM Quantum [IBM Quantum. (2023)] devices, other methods of separating qudit states have to be employed [Wang et al. (2021), Chen et al. (2023), Miao et al. (2023)]. The strategies described in [Wang et al. (2021), Chen et al. (2023)] involve exciting the qudit-resonator system at readout drive frequencies other than the default frequency. At the default frequency, the distinguishability of the ground state and first excited state is maximized, whereas using the adapted frequencies aims at optimizing various distances between different pairs of qudit states.

In the work this chapter is based on, we propose and evaluate improvements of the measurement scheme of transmon qudit states by enhancing their distinguishability. To optimize the readout, we determine the measurement errors from the assignment matrix whose entries denote the probability to classify a measurement outcome to a state $|i\rangle$ even if state $|j\rangle$ was prepared. This assignment matrix is calculated using qudit-state dependent resonator steady-state amplitudes obtained from a model describing the readout of a transmon qudit by driving a coupled resonator. The default measurement schedule of most superconducting quantum hardware consists of a single-tone drive applied to the readout resonator. The frequency of the tone is chosen to maximally separate the ground and first excited states. The strategies we propose are based on modified readout resonator drive frequencies that take into account the separation of all qudit states. These strategies include a single-frequency as well as a multifrequency readout scheme. For a ququart, viz., the four lowest states of a qudit, we compare the proposed strategies in simulation and show that depending on hardware parameters, both strategies can be beneficial. We furthermore compare the model to a measurement of the drive-frequency-dependent resonator states on a current IBM Quantum device.

This chapter is organized as follows. After describing the level scheme of a typical IBM transmon qudit in Sec. 4.2, we present our model of a transmon qudit coupled to a harmonic readout resonator in Sec. 4.3. In Sec. 4.4, the mean-field model describing the readout sequence is discussed. Based on this model, we calculate the readout drive-frequency-dependent assignment errors between multiple states that in some limits can be expressed analytically. In Sec. 4.5, we analyze both proposed readout schemes that aim to minimize these errors. In Sec. 4.6, before we compare the data that we generated on current IBM Quantum hardware to the readout model and strategies discussed earlier, we present calibrations of relevant qudit gates. To improve the state preparation procedure, we propose to add two-photon transitions to the universal gate set of qudit gates [Fischer et al. (2023)] and show that this will reduce the execution time of certain qudit circuits and the duration of X-gate calibrations.

4.2 Transmon Energy Levels

To estimate resonance frequencies for various transitions of a transmon qudit, we numerically compute the energy levels of its Hamiltonian [Koch et al. (2007), Vool and Devoret (2017)],

$$H_{\mathrm{T}} = 4E_C \sum_n (n - n_g)^2 \left|n\right\rangle\!\left\langle n\right| - \frac{E_J}{2} \sum_n (\left|n\right\rangle\!\left\langle n+1\right| + \left|n+1\right\rangle\!\left\langle n\right|)\,, \tag{4.2.1}$$

depending on the offset charge n_g, the charging energy E_C, and the Josephson energy E_J. The relevant parameter is the ratio of the two energy scales E_J/E_C. The sorted eigenvalues $E_n(n_g)$ are shifted such that $E_0(0) = 0$. Using $\hbar = 1$ here and in the rest of the chapter, we define the average transition frequency $\omega_{i,j}$ between $|i\rangle$ and $|j\rangle$ of both configurations $n_g = 0, 1/2$ as

$$\omega_{i,j} = \frac{E_j(0) + E_j(1/2) - E_i(0) - E_i(1/2)}{2(j-i)}\,, \tag{4.2.2}$$

and the frequency difference $\Delta\omega_{i,j}$ as

$$\Delta\omega_{i,j} = \frac{E_j(0) - E_i(0) - E_j(1/2) + E_i(1/2)}{j-i}\,. \tag{4.2.3}$$

The anharmonicity α_j and the energy dispersion ϵ_j of the transmon qudit are defined by

$$\alpha_j = \omega_{j,j+1} - \omega_{j-1,j}\,, \tag{4.2.4}$$

$$\epsilon_j = E_j(0) - E_j(1/2)\,. \tag{4.2.5}$$

We numerically obtain the fundamental parameter E_J/E_C of a specific IBM Quantum backend by demanding that the qubit frequency $\omega_{0,1}$ and anharmonicity α_1 reported by the device match the values calculated using the equations above. In Fig. 4.1(a), we plot the dependence of E_n on n_g for the five lowest states. The values of the frequency difference vary from $\Delta\omega_{0,1}/2\pi = 25.1\,\mathrm{kHz}$ to $\Delta\omega_{3,4}/2\pi = -142\,\mathrm{MHz}$. In Fig. 4.1(b), the values ϵ_3 for a number of IBM Quantum devices are displayed. For large ϵ_j compared to $\omega_{j,j+1}$, the Wigner function of the state $|j\rangle$ effectively is smeared out in phase space since both configurations $n_g = 0, 1/2$ exhibit different resonance frequencies.

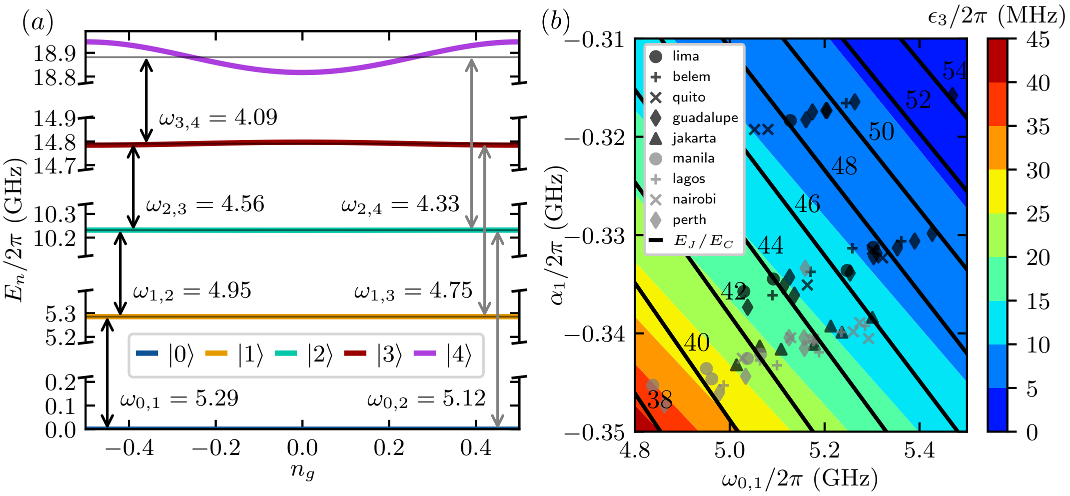

Figure 4.1: Transmon spectra. (a) Numerical prediction of the energy levels $E_n(n_g)$ of *ibm_lagos Q4* (July 7, 2023) based on Eq. (4.2.1) and $E_J/E_C \approx 45.6$. The transition frequencies $\omega_{i,j}$ are displayed in units of (2π) GHz. (b) Overview of the qubit resonance frequency $\omega_{0,1}$ and anharmonicity α_1 of the IBM Quantum devices listed in the legend. The energy dispersion ϵ_3 of the third excited state given in Eq. (4.2.5) follows from these device specifications that were accessed on May 23, 2023. The labeled straight black lines correspond to constant values of E_J/E_C.

4.3 Transmon-Resonator System

The fundamental building blocks of a superconducting quantum computer are a quantum anharmonic oscillator, i.e., the transmon qudit, coupled to a harmonic oscillator, i.e., the readout resonator. Following the notation of [Koch et al. (2007)], the Hamiltonian describing a transmon qudit and its readout resonator reads

$$H_q + H_r + H_{\text{int}} = \sum_j \omega_j |j\rangle\langle j| + \omega_r a^\dagger a + \sum_j g_{j,j+1}(a^\dagger |j\rangle\langle j+1| + a\,|j+1\rangle\langle j|)\,, \tag{4.3.1}$$

where ω_j is the energy (see Sec. 4.2) of the bare qudit state $|j\rangle$, ω_r is the energy of the readout resonator, and $a^{(\dagger)}$ is its annihilation (creation) operator. The parameters $g_{j,j+1}$ denote generalized Jaynes-Cummings coupling strengths between the qudit and the resonator. The approximation $g_{j,j+1} = g\sqrt{j+1}$ used in [Blais et al. (2004)] reduces the interaction Hamiltonian to $g(a^\dagger b + ab^\dagger)$, where $b^{(\dagger)}$ is the annihilation (creation) operator of the transmon qudit. The qudit and resonator Hamiltonians H_q and H_r denote two sets of commuting operators $|i\rangle\langle j|$ and $a^{(\dagger)}$. Each set can be visually interpreted as a block in the total Hamiltonian. The generalized Jaynes-Cummings interaction couples both blocks.

In general, a Hamiltonian of interest can be defined by

$$H = H_0 + \lambda H_1 + \lambda V\,. \tag{4.3.2}$$

Here, H_0 and H_1 are block diagonal in the subsystems, whereas V is block off diagonal.

To find an effective block-diagonal Hamiltonian, i.e., eliminate the block off-diagonal part V, the unitary transformation $U = \mathrm{e}^S$ is applied to H,

$$H_{\text{eff}} = UHU^\dagger = \mathrm{e}^S H \mathrm{e}^{-S} \,. \tag{4.3.3}$$

Expanding the anti-Hermitian operator $S = -S^\dagger$ as $S = \sum_{n=1}^{\infty} \lambda^n S^{(n)}$, H_{eff} can be expressed as

$$H_{\text{eff}} = H + [S, H] + \frac{1}{2}[S, [S, H]] + \cdots = \sum_{n=0}^{\infty} \frac{1}{n!}[S, H]^{(n)} = \sum_{n=0}^{\infty} \lambda^n H_{\text{eff}}^{(n)} \,, \tag{4.3.4}$$

where $[S, H]^{(0)} = H$ and

$$[S, H]^{(n+1)} = \left[S, [S, H]^{(n)}\right] \,. \tag{4.3.5}$$

The lowest order $H_{\text{eff}}^{(0)} = H_0$ is identical to the total Hamiltonian evaluated for $\lambda = 0$. The first-order contribution reads $H_{\text{eff}}^{(1)} = H_1 + V + \left[S^{(1)}, H_0\right]$. To eliminate the block off-diagonal V in this expression, we impose $\left[S^{(1)}, H_0\right] = -V$. Since H_0 is block diagonal, $S^{(1)}$ has to be block off diagonal. As a consequence, $\left[S^{(1)}, V\right]$ is block diagonal. The second-order contribution reads $H_{\text{eff}}^{(2)} = \frac{1}{2}\left[S^{(1)}, V\right] + \left[S^{(1)}, H_1\right] + \left[S^{(2)}, H_0\right]$, and imposing $\left[S^{(2)}, H_0\right] = -\left[S^{(1)}, H_1\right]$ guarantees the second order to be block diagonal. The second-order contribution to the effective block-diagonal Hamiltonian is then given by

$$H_{\text{eff}}^{(2)} = \frac{1}{2}\left[S^{(1)}, V\right] \,. \tag{4.3.6}$$

We choose a superposition of all operators appearing in V as an ansatz for $S^{(1)}$.

To compute the effective Hamiltonian of the Jaynes-Cummings interaction, we start with identifying the block-diagonal parts $H_0 = H_q + H_r$ and $H_1 = H_d$ as well as the block off-diagonal parts $V = H_{\text{int}}$ of Eq. (4.3.1). The ansatz for $S^{(1)}$ consists of a superposition of all operators appearing in V,

$$S^{(1)} = \sum_j \left(C_j a^\dagger |j\rangle\langle j+1| - C_j^* a |j+1\rangle\langle j|\right) \,. \tag{4.3.7}$$

The coefficients C_j are defined implicitly by the previously mentioned equation $[S^{(1)}, H_0] = -V$,

$$C_j = \frac{g_{j,j+1}}{\omega_j - \omega_{j+1} + \omega_r} \,. \tag{4.3.8}$$

Replacing C_j in Eq. (4.3.7) by this expression and using the definition $g_{-1,0} = 0$ as well as the sign convention of [Koch et al. (2007), Blais et al. (2021)] leads to

$$H_{\text{eff}}^{(2)} = \frac{1}{2}\left[S^{(1)}, V\right] = \sum_j \chi_{j-1,j} \left|j\middle\rangle\!\middle\langle j\right| + \sum_j \chi_j a^\dagger a \left|j\middle\rangle\!\middle\langle j\right| . \tag{4.3.9}$$

Here, corrections to the qudit energy are

$$\chi_{j,j+1} = \frac{g_{j,j+1}^2}{\omega_{j+1} - \omega_j - \omega_r} , \tag{4.3.10}$$

and corrections to the qudit-state-dependent resonator energies or the resonator-state-dependent qudit energies are

$$\chi_j = \chi_{j-1,j} - \chi_{j,j+1} = \frac{g_{j-1,j}^2}{\omega_j - \omega_{j-1} - \omega_r} - \frac{g_{j,j+1}^2}{\omega_{j+1} - \omega_j - \omega_r} . \tag{4.3.11}$$

We have neglected terms proportional to $(a^2 \left|j+2\middle\rangle\!\middle\langle j\right| + \text{H.c.})$. This is justified by the possibility to interpret these terms as perturbations that are eliminated by a second Schrieffer-Wolff transformation. This second transformation will lead to fourth-order terms proportional to $\left|j\middle\rangle\!\middle\langle j\right|$, $a^\dagger a \left|j\middle\rangle\!\middle\langle j\right|$, $(a^\dagger a)^2 \left|j\middle\rangle\!\middle\langle j\right|$, and also $(a^4 \left|j+4\right\rangle \left\langle j\right| + \text{H.c.})$. Importantly, for typical values of $g_{j,j+1}$, ω_j, and ω_r, the coefficients of all these terms are a factor of 10^4 smaller than the previous second-order contributions and can therefore safely be neglected. In Eq. (4.3.9), we arrived at corrections to the Hamiltonian that are diagonal in the qudit and resonator states. The shifts of the qudit and resonator energies are

$$\begin{aligned} \tilde{\omega}_j &= \omega_j + \chi_{j-1,j} , \\ \tilde{\omega}_{r,j} &= \omega_r + \chi_j . \end{aligned} \tag{4.3.12}$$

The resonance frequencies of the qudit transitions $|i\rangle \leftrightarrow |j\rangle$ can be estimated to

$$\tilde{\omega}_{i,j} = \frac{\tilde{\omega}_j - \tilde{\omega}_i}{j - i} . \tag{4.3.13}$$

The effective Hamiltonian of the transmon coupled to a readout resonator is

$$H_{\text{eff}} = \sum_j (\omega_j + \chi_{j-1,j} + \chi_j a^\dagger a) \left|j\middle\rangle\!\middle\langle j\right| + \omega_r a^\dagger a . \tag{4.3.14}$$

The parameter ω_j is the energy (see Sec. 4.2) of the bare qudit state $|j\rangle$, ω_r is the energy of the readout resonator, and $a^{(\dagger)}$ is its annihilation (creation) operator. The second-order corrections $\chi_{j-1,j}$ and χ_j to the qudit and resonator energies, are defined in Eqs. (4.3.10) and (4.3.11). Additionally, we describe a coherent driving of the resonator at frequency ω_d by [Blais et al. (2021)]

$$H_d = \frac{\Omega}{2}\left(\mathrm{e}^{\mathrm{i}\omega_d t - \mathrm{i}\phi} a + \mathrm{e}^{-\mathrm{i}\omega_d t + \mathrm{i}\phi} a^\dagger\right) , \tag{4.3.15}$$

which enables the readout of qudit states.

4.4 Readout of Qudit States

The readout of a transmon qudit, in short, consists of driving the readout resonator while recording the response signal. We model the time evolution of a general quantum state ρ comprised of a qudit and its readout resonator by the following Lindblad master equation:

$$\frac{\mathrm{d}}{\mathrm{d}t}\rho = -\mathrm{i}[H_{\text{eff}} + H_d, \rho] + \kappa\mathcal{D}[a](\rho)\,, \tag{4.4.1}$$

where $\mathcal{D}[L](\rho) = L\rho L^\dagger - (L^\dagger L\rho + \rho L^\dagger L)/2$ is the Lindblad dissipator and κ is the decay rate of the resonator. Using the effective Hamiltonian given by Eq. (4.3.14) and assuming the qudit to be in state $|j\rangle$, we arrive at the equation of motion of the mean-field amplitude $A \equiv \langle a\rangle = \mathrm{Tr}[a\rho]$

$$\frac{\mathrm{d}}{\mathrm{d}t}A = -\mathrm{i}(\omega_r + \chi_j)A - \mathrm{i}\frac{\Omega}{2}\mathrm{e}^{-\mathrm{i}\omega_d t + \mathrm{i}\phi} - \frac{\kappa}{2}A\,. \tag{4.4.2}$$

The fact that A depends on the qudit state $|j\rangle$ is used to discriminate different qudit states. If the qudit is in a mixture or superposition of states, this measurement procedure projects the qudit onto one of its Fock states [Blais et al. (2021)].

The general form of the complex value returned by an IBM Quantum device is

$$\bar{A} = \int_0^T \mathrm{d}t\, k(t)A\,, \tag{4.4.3}$$

where $k(t)$ encodes the so-called kernel integration instructions, see *meas_kernel* [McKay et al. (2018)] in QISKIT [Qiskit contributors (2023)], and T is the total duration of the measurement. The choice $k(t) = \exp(\mathrm{i}\omega_d t)$ corresponds to integrating the measurement signal in the rotating frame of the drive, see Sec. 4.4.1, whereas the choice $k(t) = \exp(\mathrm{i}\omega_m t)$ corresponds to a frame rotating at an arbitrary modulation frequency ω_m, see Sec. 4.4.2.

In the following, we mainly consider the offset charge configuration $n_g = 0$. The value of n_g influences the transmon qudit energy spectrum, see Sec. 4.2(a). Note that due to the significant dependence on n_g of the third and higher excited states, their corresponding readout-resonator states may be smeared out in phase space if charge noise is present. In Fig. 4.1(b) we present an overview of the energy dispersion ϵ_3 of the third excited state defined in Eq. (4.2.5) for several IBM Quantum devices. Since ϵ_3 decreases with increasing E_J/E_C, qudits that lie in the upper-right region are preferred in general.

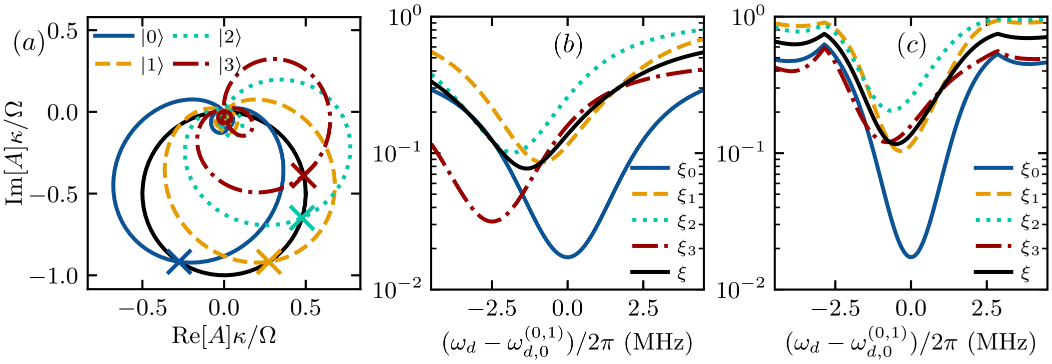

Figure 4.2: Theory prediction of the readout resonator amplitude. (a) Drive-frequency-dependent phase-space positions A_j^d and A_j^m of the coherent state of the resonator given the qudit prepared in $|j\rangle$, see Eqs. (4.4.4) and (4.4.9). For $\omega_m = \omega_d$, the trajectories of all states A_j^d match, denoted by the black circle. The colored lines correspond to A_j^m for $\omega_m = \omega_{d,0}^{(0,1)}$. Crosses indicate the positions at $\omega_d = \omega_m$ where both models match, $A_j^d = A_j^m$. (b), (c) Error measures ξ_j and ξ in the frame of ω_d and ω_m respectively, see Eqs. (4.5.5) and (4.5.6). Following Secs. 4.2 and 4.3, for these plots, we determine E_J/E_C by the qubit parameters $\omega_{0,1}$ and α_1 from *ibm_lagos Q4* (July 7, 2023). Moreover, we choose $g/2\pi = 100\,\mathrm{MHz}$, $\Omega/2\pi = 100\,\mathrm{MHz}$, $\kappa/2\pi = 5\,\mathrm{MHz}$, $T = 0.35\,\mathrm{\mu s}$, $\sigma_j = 0.13\Omega/\kappa$, $\phi = 0$, and $n_g = 0$.

4.4.1 Rotating Frame of Drive

In this section, we will work in the rotating frame of the drive. Quantities in this frame will be denoted by the superscript d. Since Eq. (4.4.2) is defined in the laboratory frame, we choose $k(t) = \exp(\mathrm{i}\omega_d t)$ to transform the signal into the rotating frame of the drive and obtain

$$\frac{\bar{A}^d}{T} \xrightarrow{\kappa T \gg 1} -\frac{\Omega}{2} \frac{\mathrm{e}^{\mathrm{i}\phi}}{\omega_r + \chi_j - \omega_d - \mathrm{i}\kappa/2} \equiv A_j^d \,. \tag{4.4.4}$$

Here, A_j^d is the complex-valued steady-state amplitude of the resonator when the qudit is in state $|j\rangle$ and defines a coherent state $\left|A_j^d\right\rangle$. Its dependence on the resonator drive frequency is presented in Fig. 4.2(a). Varying ω_d, the steady-state amplitudes A_j^d of the readout resonator move on a circle centered at $A_c = -\mathrm{i}\mathrm{e}^{\mathrm{i}\phi}\Omega/2\kappa$ with diameter Ω/κ. At resonance $\omega_{d,0}^{(j)} = \omega_r + \chi_j$, the states reach the maximum amplitude $2A_c$. For qudit readout, it is important that the distance $d_{i,j} = |A_i^d - A_j^d|$ between two qudit-state-dependent resonator states is large. We can identify two regimes of how the positions of the states in phase space depend on the readout drive frequency. For a large resonator decay rate $\kappa \gg |\chi_i - \chi_j|$, all states are close to the position of maximum amplitude within the same frequency range. In this case, $d_{i,j}$ exhibits only one maximum at

$$\omega_{d,0}^{(i,j)} = \omega_r + \frac{\chi_i + \chi_j}{2} \,, \tag{4.4.5}$$

$$d_{i,j}\left(\omega_{d,0}^{(i,j)}\right) = \frac{2\Omega|\chi_i - \chi_j|}{(\chi_i - \chi_j)^2 + \kappa^2} \,. \tag{4.4.6}$$

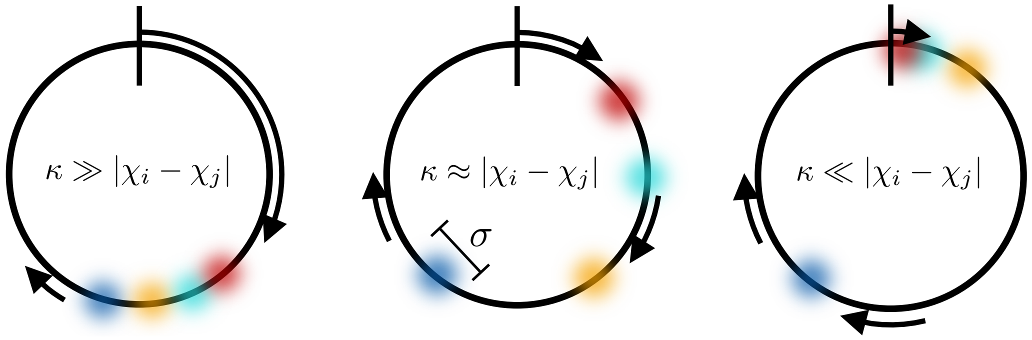

Figure 4.3: Visualization of the different regimes of steady-state movement in the complex plane of the readout-resonator amplitude. For a large resonator decay rate $\kappa \gg |\chi_i - \chi_j|$, all states are close to the position of maximum amplitude within the same frequency range. For a small resonator decay rate $\kappa \ll |\chi_i - \chi_j|$, the states hit the resonance maximum at distinct frequencies.

In contrast, for a small resonator decay rate $\kappa \ll |\chi_i - \chi_j|$, the frequency ranges where the state amplitudes A_j^d are close to the maximum amplitude do not match, i.e., A_j^d hit the resonance maximum at distinct frequencies. A visualization is given in Fig. 4.3. Here, two drive frequencies $\omega_d = \omega_{d,\pm}^{(i,j)}$ maximize the distance $d_{i,j}$,

$$\omega_{d,\pm}^{(i,j)} = \omega_{d,0}^{(i,j)} \pm \frac{1}{2}\sqrt{(\chi_i - \chi_j)^2 - \kappa^2}\,, \tag{4.4.7}$$

$$d_{i,j}\left(\omega_{d,\pm}^{(i,j)}\right) = \frac{\Omega}{\kappa} \equiv d_c\,, \tag{4.4.8}$$

where d_c denotes the diameter of the circle on which the states move. Thus, at $\omega_{d,\pm}^{(i,j)}$, both states are located on opposite sides of the circle, which is the maximum separation they can obtain.

If we set the drive frequency to $\omega_{d,0}^{(i,j)}$ or $\omega_{d,\pm}^{(i,j)}$, i.e., maximizing the distance between state $|i\rangle$ and $|j\rangle$, the distance between other pairs of states is in general reduced and hence not optimal for discrimination of these states. Therefore, in Sec. 4.5, we present two measurement strategies to mitigate this issue.

4.4.2 General Rotating Frame

In a frame of a general rotation frequency ω_m, i.e., choosing $k(t) = \exp(\mathrm{i}\omega_m t)$, the state reached in the long-time limit $\kappa T \gg 1$ is time dependent,

$$\frac{\bar{A}^m}{T} \xrightarrow{\kappa T \gg 1} \mathrm{e}^{\mathrm{i}((\omega_m - \omega_d)T/2)}\mathrm{sinc}\left((\omega_d - \omega_m)T/2\right) A_j^d \equiv A_j^m\,, \tag{4.4.9}$$

where $\mathrm{sinc}(x) = \sin(x)/x$ and the superscript m is used to denote quantities in this frame. The difference between Eqs. (4.4.4) and (4.4.9) is an additional factor of sinc peaking at $\omega_d = \omega_m$. These resonator-state amplitudes and their dependence on the drive frequency ω_d are also visualized in Fig. 4.2(a). The states A_j^d move on the black circle with diameter Ω/κ, whereas the motion of the states A_j^m follows a distorted circle (colored curves).

4.5 Measurement Strategies

In the previous section, we presented a model describing the readout on superconducting quantum hardware. The centers of the Wigner functions of the coherent readout-resonator states when the qudit is in state $|j\rangle$ are given by A_j. Due to intrinsic quantum noise and hardware limitations, the possible readout-resonator states for each qudit state overlap. This leads to potential misclassification and thus measurement errors when reading out the qudit states.

In the following of this section, we propose two strategies for improving qudit readout compared to the default measurement scheme that utilizes a single resonator drive frequency that optimizes the classification of $|0\rangle$ and $|1\rangle$. The first strategy consists of finding a single frequency that maximizes the distinguishability between all d qudit Fock states. In the second strategy, we allow for multiple different drive frequencies.

4.5.1 Assignment Matrix

To arrive at a measure of the distinguishability of states, we introduce the measurement assignment matrix M [Bravyi et al. (2021)]. The qudit-state-dependent resonator states are defined by their steady-state amplitude A_j. We assume their Wigner functions to follow a two-dimensional Gaussian distribution,

$$G(z, A_j, \sigma_j) = \frac{1}{2\pi\sigma_j^2} \exp\left(-\frac{|z - A_j|^2}{2\sigma_j^2}\right) , \tag{4.5.1}$$

centered at A_j with standard deviation σ_j larger than the intrinsic quantum noise. The elements of M are given by

$$M_{i,j} = \int \mathrm{d}^2 z \, G(z, A_j, \sigma_j) \prod_{k \neq i} \Theta_{i,k} \tag{4.5.2}$$

and define the probability to classify a measurement as state $|i\rangle$ even if state $|j\rangle$ was prepared. The region corresponding to each state $|i\rangle$ is defined by the maximum likelihood estimator (MLE) leading to

$$\Theta_{i,k} = \Theta\left(G(z, A_i, \sigma_i) - G(z, A_k, \sigma_k)\right) , \tag{4.5.3}$$

where Θ denotes the Heaviside function. For $\sigma_j = \sigma$ (valid assumption for the hardware setup studied later in this chapter, see the discussion about the distribution of σ of Gaussian fits in the second paragraph of Sec. 4.6), the MLE is equivalent to the minimum distance estimator (MDE) that implies

$$\Theta_{i,k} = \Theta(|z - A_k| - |z - A_i|) . \tag{4.5.4}$$

Using the MDE, a data point z is assigned to the region of state A_i if its Euclidean distance to all of the other states A_k is larger. In contrast, using the MLE, a data point z is assigned to the region of the state A_i that has the largest value of the probability density at that point. For simplicity and since in our measurements all σ_j are comparable, we choose the MDE throughout this chapter.

Ideally, $M_{i,j} = \delta_{i,j}$, meaning perfect measurement: a measurement outcome is assigned to $|i\rangle$ only if $|j\rangle$ was prepared. We define the error measures

$$\xi_j = 1 - M_{j,j}\,, \tag{4.5.5}$$

where ξ_j is the probability of misclassifying the qudit state $|j\rangle$, and their mean ξ over all d qudit states,

$$\xi = \frac{1}{d}\sum_{j=0}^{d-1} \xi_j\,. \tag{4.5.6}$$

The theoretical dependence of ξ_j and ξ on the readout resonator drive frequency is shown in Figs. 4.2(b) and 4.2(c). The measurement errors ξ_j achieve their minima at different readout resonator drive frequencies. If $\omega_m \neq \omega_d$, the locations of the minima cannot be distinguished as well as for $\omega_m = \omega_d$. In the current setup of IBM Quantum hardware, the frequency ω_m of the rotating frame cannot be changed. Therefore, the difference between the frequency dependencies of all ξ_j is less pronounced.

Note that for setups where $\sigma_j = \sigma$ and all qudit states lie on a circle centered at $A_c = x_c + \mathrm{i}y_c$, the assignment matrix $M_{i,j}$ can be expressed in terms of Owen's T function, that allows for a fast numerical calculation. Examples of such setups are qudit systems with $\omega_m = \omega_d$, see Sec. 4.4.1, or qutrit systems even with arbitrary ω_m. In the rotated coordinate system in which A_i and A_{i+1} are aligned along the real axis in phase space, Eq. (4.5.2) can be written as

$$\begin{aligned}
M_{i,j} &= \frac{1}{2\pi\sigma^2}\int_{-\infty}^{x_c} \mathrm{d}x \int_{-\infty}^{y(x)} \mathrm{d}y \exp\left(-\frac{(x-x_j)^2}{2\sigma^2} - \frac{(y-y_j)^2}{2\sigma^2}\right) \\
&= \frac{1}{2\sqrt{2\pi}\sigma}\int_{-\infty}^{x_c} \mathrm{d}x \exp\left(-\frac{(x-x_j)^2}{2\sigma^2}\right)\left(1 + \mathrm{erf}\left(\frac{y_c - y_j + a_i(x-x_c)}{\sqrt{2}\sigma}\right)\right) \\
&= \frac{1}{4}\left(1 - \mathrm{erf}\left(\frac{x_j - x_c}{\sqrt{2}\sigma}\right)\right) + T\left(\frac{x_j - x_c}{\sigma}, -a_i, \frac{y_c - y_j + a_i(x_j - x_c)}{\sigma}\right)\,,
\end{aligned} \tag{4.5.7}$$

where $y(x) = y_c + a_i(x - x_c)$ and a_i is the slope of the bisecting line between A_i and A_{i-1},

$$a_i = -\frac{x_i - x_{i-1}}{y_i - y_{i-1}}\,, \tag{4.5.8}$$

see the visualization in Fig. 4.4. The variables x_j and y_j are the real and imaginary

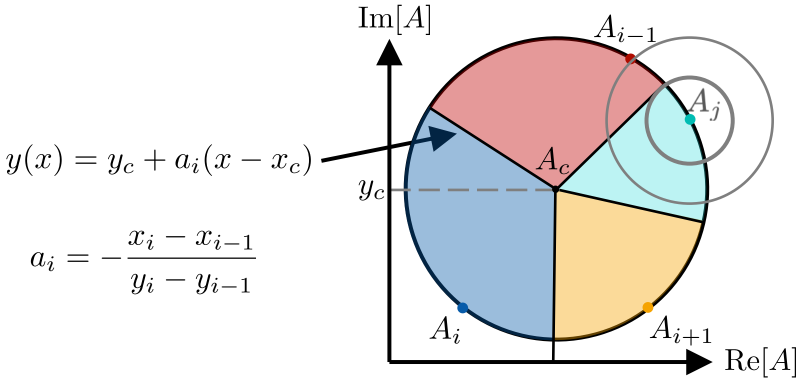

Figure 4.4: Visualization of the calculation of $M_{i,j}$ using Owen's T function. The area of integration of Eq. (4.5.7) corresponds to the dark blue region of A_i. The Gaussian probability distribution (illustrated by the gray circles) of the state $|j\rangle$ that was prepared is located at A_j.

part of A_j. The function $T(h,a,b)$ is a generalized version of Owen's T function, $T(h,a) = T(h,a,0)$ [Owen (1956), Owen (1980)] and defined as

$$T(h,a,b) = \frac{1}{2\sqrt{2\pi}} \int_h^\infty \mathrm{d}u \, \exp\left(-\frac{u^2}{2}\right) \mathrm{erf}\left(\frac{au+b}{\sqrt{2}}\right). \tag{4.5.9}$$

It can be expressed by multiple standard Owen's T functions,

$$\begin{aligned} T(h,a,b) = &\frac{1}{4}\mathrm{erf}\left(\frac{b}{\sqrt{2(1+a^2)}}\right)\left(1 - \mathrm{erf}\left(\frac{h}{\sqrt{2}}\right)\right) + T\left(\frac{b}{\sqrt{1+a^2}}, a + \frac{h(1+a^2)}{b}\right) \\ &+ T\left(h, a + \frac{b}{h}\right) - T\left(\frac{b}{\sqrt{1+a^2}}, \frac{h\sqrt{1+a^2}}{b}\right) - T\left(h, \frac{b}{h\sqrt{1+a^2}}\right). \end{aligned} \tag{4.5.10}$$

We used the standard definition of the error function, see Eq. (8.250.1) of [Gradshteyn and Ryzhik (2015)],

$$\mathrm{erf}(x) = \frac{2}{\sqrt{\pi}} \int_0^x \mathrm{d}u \, \exp(-u^2). \tag{4.5.11}$$

4.5.2 Finite Sampling

In experiments, measuring an unknown state $|\psi\rangle = \sum_j c_j |j\rangle$ in the Z basis is equivalent to estimating its populations $p_j \equiv |c_j|^2$ based on a set of N data points $\{z_j\}$, also called shots. For each shot, the total state is projected onto one of the d qudit states $|j\rangle$ with probability p_j. Therefore, the total probability distribution of measuring one shot at z given $\vec{p} = (p_j)$ is a sum of all d Gaussians defined in Eq. (4.5.1) weighted by p_j. The measurement task can be understood as learning the parameters $\vec{p}$ of this multimodal probability distribution,

$$P(z|\vec{p}) = \sum_{j=0}^{d-1} p_j G(z, A_j, \sigma_j)\,, \tag{4.5.12}$$

where A_j and σ_j are obtained from a separate calibration measurement. Using the normalization condition of $\vec{p}$,

$$p_{d-1} = 1 - \sum_{j=0}^{d-2} p_j\,, \tag{4.5.13}$$

where $p_j \in [0,1]$, the space of possible $\vec{p}$ can be mapped to a $(d-1)$-simplex. Using Bayesian inference, we define a recursion relation

$$P^{(j+1)}(\vec{p}) = \frac{P(z_j|\vec{p})}{P(z_j)} P^{(j)}(\vec{p})\,, \tag{4.5.14}$$

with

$$P(z_j) = \int \mathrm{d}^{d-1}p\, P(z_j|\vec{p}) P^{(j)}(\vec{p})\,, \tag{4.5.15}$$

between the estimated probability distribution (so-called prior) $P^{(j)}(\vec{p})$ of the Gaussian amplitudes $\vec{p}$ before and after receiving the jth data point z_j, also called shot. Each shot is drawn from the probability distribution $P(z_j|\vec{p})$ defined in Eq. (4.5.12). After obtaining N data points, the resulting probability distribution $P^{(N)}(\vec{p})$ is given by

$$P^{(N)}(\vec{p}) = \frac{\prod_{j=0}^{N-1} P(z_j|\vec{p})}{\prod_{j=0}^{N-1} P(z_j)} P^{(0)}(\vec{p})\,. \tag{4.5.16}$$

The initial prior $P^{(0)}(\vec{p})$ is chosen to be a uniform distribution.

If the width of the Gaussians is small compared to their distances, this method is equivalent to the description given in the following. For simplicity, instead of using this Bayesian ansatz of the probability distribution, each of the N shots is classified as one of the d qudit states. The classification is based on the phase-space distance (MDE) to the d qudit Fock states, whose positions have been calibrated before. The components N_j of $\vec{N}$ equal the number of shots assigned to $|j\rangle$. This procedure corresponds to neglecting the actual position z_j of this shot, i.e., its Gaussian weight G. Given N_j, the so-called posterior probability distribution $P^{(N)}(\vec{p})$ for the qudit populations p_j for a perfect measurement is equal to

$$P(\vec{p}|\vec{N}) = \mathrm{Dir}(\vec{p}, \vec{N}) = \frac{(N+d-1)!}{\prod_{k=0}^{d-1} N_k!} \prod_{k=0}^{d-1} p_k^{N_k}\,, \tag{4.5.17}$$

with

$$\sum_{j=0}^{d-1} p_j = 1, \quad \sum_{j=0}^{d-1} N_j = N, \tag{4.5.18}$$

introducing the Dirichlet distribution Dir [Kotz et al. (2000)]. It is the so-called conjugate prior of the multinomial distribution. The location of the maximum (also called mode) with respect to p_j is given by N_j/N, and its variances follow as

$$\mathrm{Var}[p_j] = \frac{(N_j+1)/(N+d)[1-(N_j+1)/(N+d)]}{N+d+1} \,. \tag{4.5.19}$$

Defining $n_j = N_j/N$, for large N the variance of p_j scales like $n_j(1-n_j)/N$.

We now consider the assignment matrix M, see Eq. (4.5.2), which describes misclassification errors. Using a Bayesian posterior ansatz, we find that the probability distribution has to be modified to

$$P(\vec{p}|\vec{N}) = \frac{1}{\mathcal{N}} \mathrm{Dir}(M\vec{p}, \vec{N}) \tag{4.5.20}$$

where

$$\mathcal{N} = \int\limits_{V_{\vec{p}}} \mathrm{d}^d p \, \mathrm{Dir}(M\vec{p}, \vec{N}) \,. \tag{4.5.21}$$

The assignment matrix M reflects the fact that some shots are classified incorrectly and maps proper states $\vec{p}$ from $V_{\vec{p}}$ (related to a $(d-1)$-simplex) to a subspace $V_{M\vec{p}} \subseteq V_{\vec{p}}$. If $\vec{N}/N \in V_{M\vec{p}}$, the location of the maximum (also called mode) can be computed analytically,

$$\vec{p}_{\mathrm{mode}} = \frac{1}{N} M^{-1} \vec{N} \,. \tag{4.5.22}$$

This result is similar to a common procedure known in Qiskit as "measurement error mitigation". Note that applying the inverse of M to $\vec{N}/N \notin V_{M\vec{p}}$ can lead to negative components of $\vec{p}_{\mathrm{mode}} \notin V_{\vec{p}}$. In Qiskit, this problem is circumvented by approximating $\vec{p}_{\mathrm{mode}}$ by the valid $\vec{p}\,'$ that is closest to $\vec{N}$, see method *least_squares* in *qiskit.utils.mitigation._filters.py* [Qiskit contributors (2023)],

$$\vec{p}\,' = \underset{\vec{p}}{\mathrm{argmin}} \left(|\vec{N}/N - M\vec{p}|^2 \right) \,. \tag{4.5.23}$$

Equation (4.5.23) is the estimate of the state populations $\vec{p}$ after measuring $\vec{N}$ shots. We will use the uncertainty of these estimates, viz., the numerically calculated standard deviations $\mathrm{SD}[p_j]$, to decide which of the proposed strategies performs best, i.e., exhibits the smallest standard deviation.

4.5.3 Comparison of Strategies

We consider two strategies that make use of either one or multiple drive frequencies. In the default readout scheme of superconducting quantum hardware, measurement pulses with a single drive frequency that maximizes the distinguishability between the qubit states $|0\rangle$ and $|1\rangle$ are applied.

The first strategy we propose replaces the default frequency by the one that optimally separates all qudit states in phase space simultaneously. Since, in general, the state $|\psi\rangle$ that we want to measure is unknown, we suggest to optimize ξ defined in Eq. (4.5.6), which is the average of the individual measurement errors ξ_j.

The second strategy uses N/d shots for each of the d different frequencies at which individual states are most isolated, i.e., ξ_j are minimal. We will show that this strategy is advantageous in cases when there is no single frequency at which all states are separated well enough. Hardware parameters and the state to be measured determine which of the two strategies outperforms the other.

To compare both strategies, we draw $N = 1000$ samples from the probability distribution given by Eq. (4.5.12) for $\sigma_j = \sigma$ and an equal-superposition state $p_j = 1/d$. The drive frequencies we use for (i) the single-drive strategy is the location of the minimum of ξ and for (ii) the multifrequency strategy are the minima of ξ_j. Each sample is classified using the MDE, see Eq. (4.5.4), i.e., by its Euclidean distance to the nearest state $|j\rangle$. The final probability distribution for the p_j of the single-frequency strategy is given in Eq. (4.5.20). The final probability distribution for the multifrequency strategy is the normalized product of the term in Eq. (4.5.20) for each measurement frequency ω_k,

$$P(\vec{p}\,|\{\vec{n}_k\}) \propto \prod_{k=0}^{d-1} \mathrm{Dir}(M(\omega_k)\vec{p}\,|\vec{n}_k)\,, \tag{4.5.24}$$

where $\{\vec{n}_k\}$ is the list of counts of classified shots for the kth measurement frequency. The standard deviation $\mathrm{SD}[p_j]$ is computed numerically from this distribution.

Figure 4.5(a) shows the dependence of the ratio of both averaged standard deviations,

$$\mathrm{SD}_{s/m} = \frac{1}{d}\sum_{j=0}^{d-1} \mathrm{SD}_{s/m}[p_j]\,, \tag{4.5.25}$$

on hardware parameters $\sigma_j = \sigma$ and κ. The blue region corresponds to setups for which the standard deviation SD_s of p_j using a single-drive frequency scheme is smaller. In contrast, the red region corresponds to hardware configurations where it is beneficial to measure at multiple frequencies, i.e., SD_m of the multidrive frequency scheme is smaller. The gray region indicates parameter values for which both standard deviations exceed $\mathrm{SD}_{s/m} \geq 0.1$. Since the expected values p_j lie in $[0, 1]$, this threshold corresponds to an uncertainty of at least 10%.

The overall trend is that for small σ, i.e., strongly located Gaussians, the single-frequency strategy performs at a similar, slightly better level than the multifrequency

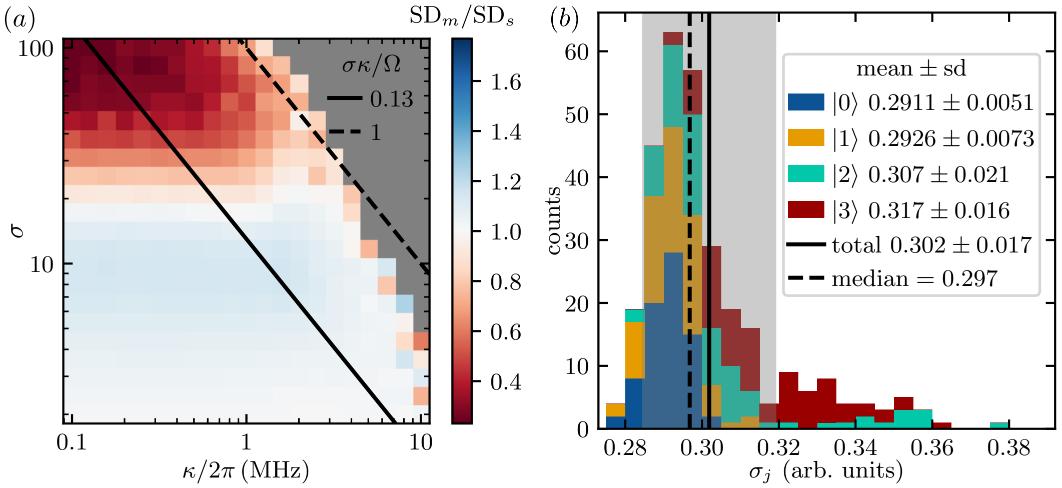

Figure 4.5: Comparison of measurement strategies. (a) Ratio of the standard deviation SD$_m$ for the multifrequency strategy and the standard deviation SD$_s$ of the single-frequency strategy applied to an equal-superposition state taking $N = 1000$ shots. The gray region indicates where both standard deviations exceed SD$_{s/m} \geq 0.1$. The straight lines denote constant values of $\sigma\kappa/\Omega$. We take the same qudit parameters as in Fig. 4.2 and choose $g/2\pi = 100\,\mathrm{MHz}$ and $\Omega/2\pi = 100\,\mathrm{MHz}$. (b) Histogram of Gaussian widths σ_j for data presented in Sec. 4.6. The distribution justifies the assumption $\sigma_j = \sigma$.

strategy. The multifrequency strategy is preferable for large σ, when the overlap of the Gaussians would be too large using a single drive frequency. Intuitively, this is expected since, for small κ and large σ, only one state is isolated from the others which group together at the origin in phase space, see discussion of regimes $\kappa \lessgtr |\chi_j - \chi_{j+1}|$ in Sec. 4.4.1. We also added lines of constant relative uncertainty $\sigma\kappa/\Omega$. Along these lines, the Gaussian widths σ are fixed in units of the diameter Ω/κ of the circle on which the states move in the rotating frame of the drive. The solid line corresponds to $\sigma = 0.13\Omega/\kappa$ chosen in Figs. 4.2(b) and 4.2(c), whereas the dashed line approximately matches the threshold of SD$_{s/m} \geq 0.1$. Following the solid black line, the standard deviation of the single-frequency strategy appears to exhibit a minimum around $\kappa/2\pi = 1 - 2\,\mathrm{MHz}$. For fixed $\sigma\kappa/\Omega$ and small resonator decay rates κ, the states move around the circle rather individually, whereas for large κ, the states move as a group, see Sec. 4.4.1 and Fig. 4.3. The histogram shown in Fig. 4.5(b) is used to justify the assumption $\sigma_j = \sigma$ for the measurement data presented in Sec. 4.6.

4.6 Measurement on IBM Quantum Hardware

In this section, we will compare the model described in Sec. 4.3 to data obtained from *ibm_lagos Q4* on July 7, 2023.

4.6.1 Preparation of Qudit States

We prepare the four lowest Fock states of an IBM Quantum transmon qudit, i.e., the a so-called ququart studied in Sec. 4.6.2, by applying sequences of calibrated qudit X

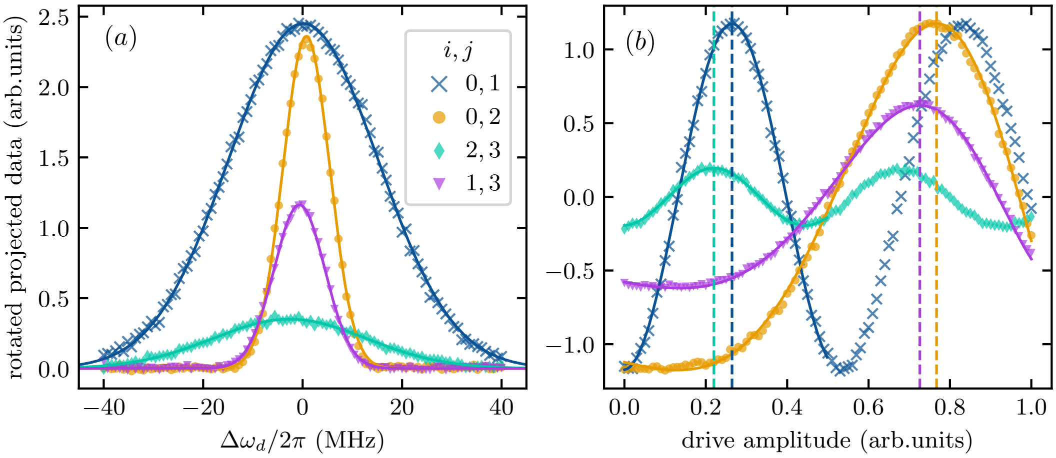

Figure 4.6: (a) Qudit resonator spectroscopy of transitions $|i\rangle \leftrightarrow |j\rangle$. Colored markers denote measured data and solid curves correspond to Gaussian fits. We plot each resonance spectrum centered around the predicted transition frequency $\tilde{\omega}_{i,j}$, see Eq. (4.3.13), using $g/2\pi = 65\,\text{MHz}$. (b) Rabi oscillations $|i\rangle \leftrightarrow |j\rangle$ depending on the drive amplitude for fixed pulse duration. We sweep the readout resonator drive amplitude while keeping all other parameters of the drive fixed. For first-order qudit state transitions, we fit a sinusoidal dependence on a linear function of the drive amplitude in the interval $[0, 0.5]$, see the lines connecting crosses and, respectively, diamonds. For second-order qudit state transitions, we fit a sinusoidal dependence on a quadratic function of the drive amplitude in the interval $[0, 1]$, see the lines connecting dots and, respectively, triangles. The vertical dashed lines indicate the locations of the first maxima obtained from the fits.

gates to the ground state $|0\rangle$. For simplicity, we implement these X gates via Gaussian pulses. For each pulse, we first calibrate its drive frequency ω_d and second, its drive amplitude Ω_q.

The optimal drive frequency is obtained from a Gaussian fit to resonance measurement data shown in Fig. 4.6(a), where we fix the pulse amplitude to an initial estimate. First, the measured $N = 2000$ complex-valued shots per qudit drive frequency, using the default readout pulse, are averaged. Second, these averages are rotated in the complex plane such that their major principal axis is oriented along the real axis. And third, the averages are projected onto the real axis which justifies the axis label “rotated projected data”. For the spectroscopy measurements, in addition, we define the origin of the ordinate of Fig. 4.6(a) to correspond to the initial state of the analyzed transition and the maximum to the final state. Our estimated frequency $\tilde{\omega}_{i,j}$ is calculated by Eq. (4.3.13) using $g/2\pi = 65\,\text{MHz}$.

To obtain the initial estimate of the qudit drive amplitude, we define the rotation angle θ of a resonant Rabi oscillation between states $|j\rangle$ and $|k\rangle$. Comparing both sides of

$$\exp(-\mathrm{i}H_{d,\text{eff}}t) = \exp\left(-\frac{\mathrm{i}}{2}\theta(|j\rangle\langle k| + |k\rangle\langle j|)\right) , \tag{4.6.1}$$

where the left-hand side is the time evolution of the effective drive Hamiltonian,

$$H_{d,\text{eff}} = \Lambda(j,k)(|j\rangle\langle k| + |k\rangle\langle j|)\,. \tag{4.6.2}$$

Therefore, the rotation angle θ depends on the effective Rabi frequency $\Lambda(j,k)$ and the pulse duration t. Starting with the Hamiltonian of a driven qudit in the rotating frame of the drive, see [Blais et al. (2021)],

$$H = H_0 + \lambda V = \sum_j (\tilde{\omega}_j - \omega_d)\,|j\rangle\langle j| + \lambda \frac{\Omega_q}{2} \sum_j \sqrt{j+1}(\mathrm{e}^{-\mathrm{i}\phi}\,|j\rangle\langle j+1| + \mathrm{e}^{\mathrm{i}\phi}\,|j+1\rangle\langle j|)\,, \tag{4.6.3}$$

for $\lambda = 1$, the rotation angle θ for Rabi oscillations between $|j\rangle$ and $|j+1\rangle$ is given by

$$\theta = t_{j,j+1}\Omega^{(j,j+1)}\sqrt{j+1}\,. \tag{4.6.4}$$

In analogy to Sec. 4.3, we now perform a Schrieffer-Wolff transformation of the Hamiltonian in Eq. (4.6.3). This method is used to predict the Rabi oscillation frequencies of second-order transitions $|j\rangle \leftrightarrow |j+2\rangle$. For previous work on multiphoton transitions, see, e.g., [Strauch et al. (2007), Danilin et al. (2018)]. An expansion in λ leads to

$$H^{(2)}_{d,\text{eff}} = -\frac{\Omega_q^2}{8} \sum_j f_j(\mathrm{e}^{-2\mathrm{i}\phi}\,|j\rangle\langle j+2| + \mathrm{e}^{2\mathrm{i}\phi}\,|j+2\rangle\langle j|)\,, \tag{4.6.5}$$

where

$$f_j = \frac{\sqrt{(j+1)(j+2)}(\tilde{\omega}_{j+2} - 2\tilde{\omega}_{j+1} + \tilde{\omega}_j)}{(\tilde{\omega}_{j+2} - \tilde{\omega}_{j+1} - \omega_d)(\tilde{\omega}_{j+1} - \tilde{\omega}_j - \omega_d)}\,. \tag{4.6.6}$$

Note that these expressions only hold for $\omega_d \neq \tilde{\omega}_{j+1} - \tilde{\omega}_j$, i.e., drive pulses that are not resonant with transitions between neighboring qudit levels $|j\rangle \leftrightarrow |j+1\rangle$. The rotation angle for Rabi oscillations between non-neighboring states $|j\rangle$ and $|j+2\rangle$ can be computed using Eq. (4.6.5),

$$\theta = t_{j,j+2}\frac{\left(\Omega^{(j,j+2)}\right)^2}{4} f_j\,. \tag{4.6.7}$$

Thus, the Rabi frequency of the $|0\rangle \leftrightarrow |2\rangle$ transition scales quadratically with $\Omega^{(0,2)}$. Using Eqs. (4.6.4) and (4.6.7), the initial estimate for the π-pulse amplitudes $\Omega_\pi^{(j,k)}$ can be related to the default X-gate amplitude $\Omega_\pi^{(0,1)}$ reported by the IBM Quantum backend,

$$\Omega_\pi^{(j,j+1)} = \frac{\Omega_\pi^{(0,1)}}{\sqrt{j+1}}\,, \tag{4.6.8}$$

$$\Omega_\pi^{(j,j+2)} = 2\sqrt{\frac{\Omega_\pi^{(0,1)} t_{0,1}}{f_j t_{j,j+2}}}\,. \tag{4.6.9}$$

Here we used that all single-qudit operations are implemented within the same duration $t_{j,j+1} = t_{0,1}$.

After evaluating the resonance measurement, we continue to calibrate the X-gate drive amplitude via Rabi oscillations, see Fig. 4.6(b). The data are rotated and projected onto the major principal axis as described before for the spectroscopy measurements. As shown in Eq. (4.6.5), the Rabi frequency for transitions $|j\rangle \leftrightarrow |j+2\rangle$ depends nonlinearly on the drive amplitude. Since these transitions are suppressed by the small factor $\Omega_q f_j$, we choose $t_{j,j+2} = 2t_{0,1}$ such that $\Omega_\pi^{(0,2)}$ does not exceed the limits of IBM Quantum software/hardware restrictions: the drive amplitude in the arbitrary units chosen in Fig. 4.6(b) has to be an element of $[-1, 1]$. The π amplitude of an X-gate pulse is identified with the location of the first maximum in Fig. 4.6(b), indicated by a dashed line. For transitions between neighboring states, we fit a sine dependence on a linear function of Ω_q and, for second-order transitions, we fit a sine dependence on a second-order polynomial of Ω_q. Using those fits, any desired rotation angle, e.g., π for an X gate or $\pi/2$ for a Hadamard gate, can be mapped back to a corresponding pulse amplitude.

The sequence of calibrating drive frequency and amplitude described above can be iterated several times to improve gate fidelity. Here, for simplicity, we consider only one round of calibrations. To increase fidelity, we chose the initial value for $\Omega_{1,3}$ based on prior test measurements.

Implementing gates in the $|j\rangle \leftrightarrow |j+2\rangle$ subspace results in two advantages. First, our implementation of an X-gate $X_{j,j+2}$ between $|j\rangle$ and $|j+2\rangle$ takes only twice the single-qudit gate duration $t_{0,1}$. In contrast, using single-qudit gates, $X_{j,j+2}$ consists of three single-qudit operations $X_{j,j+1}X_{j+1,j+2}X_{j,j+1}$ with a total duration of $3t_{0,1}$. Second, the calibration of the drive frequencies (amplitudes) for $|0\rangle \leftrightarrow |1\rangle$ and $|0\rangle \leftrightarrow |2\rangle$ are independent of each other and can therefore be combined into a single QISKIT job (set of measurements submitted to an IBM Quantum device). In contrast, the frequency calibration for the transition $|1\rangle \leftrightarrow |2\rangle$ depends on the Rabi measurement for the transition $|0\rangle \leftrightarrow |1\rangle$. In total, we can perform our calibration procedure in four QISKIT jobs:

1. drive frequency of X_{01} and X_{02},
2. drive amplitude of X_{01} and X_{02},
3. drive frequency of X_{12}, X_{23}, and X_{13},
4. drive amplitude of X_{12}, X_{23}, and X_{13}.

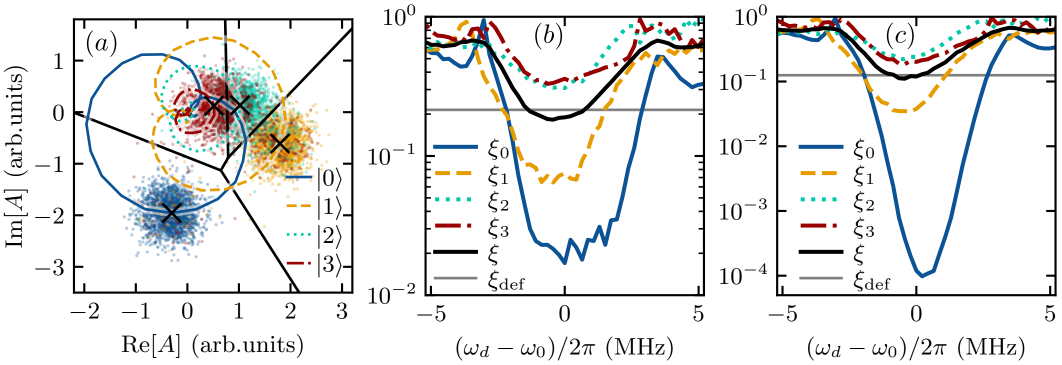

Figure 4.7: Measurement of ququart states on *ibm_lagos Q4* (July 7, 2023). (a) Drive-frequency-dependent and qudit-state-dependent resonator amplitudes, the experimental equivalent of Fig. 4.2(a). The colored dots are the measurement results of all $N = 2000$ shots for each prepared Fock state for the drive frequency $\omega_d = \omega_0 = 7.2463\,\mathrm{GHz}$. The black crosses mark the centers of their Gaussian fits and the black straight lines indicate the boundaries of regions assigned to individual Fock states. These boundaries are constructed using the minimum distance estimator, see Eq. (4.5.4). The colored curves (with white shadows) correspond to the centers of Gaussian fits to the Fock states $|j\rangle$. A video of this panel is available at [Kehrer (2025)]. (b) Measurement errors $\xi_j = 1 - M_{j,j}$ based on all measured shots of the data presented in (a). Here, the elements $M_{i,j}$ of the assignment matrix equal the relative number of shots, N_i/N, that are classified as $|i\rangle$ even if $|j\rangle$ is prepared. The horizontal gray line denotes the measurement error ξ_{def} obtained using the default measurement pulse. (c) Measurement errors ξ_j based on Gaussian fits to the data presented in (a) and the assignment matrix M defined in Eq. (4.5.2). Using the centers and average σ of Gaussian fits for each readout resonator drive frequency, see Fig. 4.5(b), we calculate M numerically. The ξ_j shown in (b) are larger than those in (c) since they do not only represent assignment errors, but also include additional errors such as qudit decay, leakage, and imperfect state preparation. In both (b) and (c), the minimum of the average assignment error ξ is smaller than ξ_{def} obtained by the default pulse.

In contrast, the standard sequential calibration of single-qudit X gates would take six jobs: two for each of the three single-qudit X gates between neighboring states.

4.6.2 Measurement of a Ququart

After calibration of the standard single-qudit gates X_{01}, X_{12}, and X_{23} as well as the higher-order (two-photon) single-qudit gates X_{02} and X_{13}, we compare the readout model described in Sec. 4.3 to measurements executed on *ibm_lagos Q4* (July 7, 2023). In Fig. 4.7(a) we show the measurements of the four lowest Fock states for various readout resonator drive frequencies. This plot is the experimental equivalent of Fig. 4.2(a). A video of this panel is available at [Kehrer (2025)][7]. For each Fock state and for each readout resonator drive frequency, we take $N = 2000$ shots while keeping the other drive parameters fixed at the default values. For $\omega_d/2\pi = \omega_0/2\pi = 7.2463\,\mathrm{GHz}$, Fig. 4.7(a) shows all shots in the color of the prepared Fock state. This value of ω_0 is $-5.5\,\mathrm{MHz}$ off the default frequency reported by the IBM Quantum device. Black crosses highlight the centers of the Gaussian fits. For other drive frequencies, we

---

[7] Direct link: https://tobias-kehrer.github.io/thesis/qudit_measurement/ [Accessed: July 30, 2025]

only plot the centers of the Gaussian fits as colored lines (with a white shadow). The straight black lines denote the boundaries of regions (defined via MDE, see Eq. (4.5.4)) that are assigned to one Fock state.

We analyze the measurement errors in two ways. First, we define the elements $M_{i,j}$ by the relative number of shots, N_i/N, classified as $|i\rangle$ even if $|j\rangle$ is prepared. In this way, M incorporates misclassification errors but also additional errors such as imperfect qudit state preparation. From this matrix, we obtain the errors ξ_j, displayed in Fig. 4.7(b). Second, we use the centers of the Gaussian fits for each qudit state and for each value of the resonator drive frequency and a fixed value of σ to compute the assignment matrix defined in Eq. (4.5.2). By examining these Gaussian fits, we find a narrow distribution of the σ values: $\sigma = (0.302 \pm 0.017)$ (same arbitrary units as in Fig. 4.7(a)), see Fig. 4.5(b). The resulting errors ξ_j are shown in Fig. 4.7(c). Here, the ξ_j only represent errors that arise from misassignment of shots drawn from the multi-Gaussian distribution, see Eqs. (4.5.1) and (4.5.2). Since real devices feature other sources of error, e.g., qubit decay, leakage, and imperfect state preparation, the values of ξ_j presented in Fig. 4.7(b) are larger than in Fig. 4.7(c).

Our model, visualized by the theory plots in Figs. 4.2(a) and 4.2(c), shows qualitative agreement with the data presented in Figs. 4.7(a) and 4.7(c). In both Figs. 4.7(b) and 4.7(c), the horizontal gray line ξ_{def} denotes the average assignment error of the four lowest Fock states using the default readout pulse and should be compared with the solid black line ξ. The corresponding data were taken from Rabi calibration measurements, similar to Fig. 4.6(b), at the drive amplitude that is closest to the fitted optimum.

We find a dependence of the measurement errors ξ_j on the readout resonator frequency as expected. The data presented in Figs. 4.7(b) and 4.7(c) suggest that the default measurement frequency is not ideal to separate all four qudit states simultaneously. However, the minima appear at only slightly different positions. Note that the difference in positions is small due to IBM Quantum software/hardware limitations: ω_m cannot be set to its ideal value $\omega_m = \omega_d$, see Sec. 4.4.2. We expect the impact of varying the readout resonator drive frequency to be much higher if it is possible to analyze all data in the rotating frame of the drive, compare Figs. 4.2(b) and 4.2(c).

In this chapter, we focused on the analysis of only four qudit states since the readout of higher excited states beyond $|3\rangle$ becomes difficult for several reasons. Higher-excited states are more sensitive to charge noise, see Fig. 4.1(a). Since χ_j depends on the qudit spectrum ω_j, charge noise leads to ambiguous steady-state amplitudes. In addition, finding a single drive frequency that properly separates all qudit states becomes more difficult with an increasing number of qudit states. For example, for the IBM Quantum device that we utilized in this chapter, we estimate $\chi_1 < \chi_4 < \chi_2$ which indicates that the steady-state amplitude corresponding to $|4\rangle$ lies between $|1\rangle$ and $|2\rangle$. We expect that the more states are involved, the better the performance of a multifrequency strategy in comparison to a single-frequency strategy given a small $\kappa \ll |\chi_i - \chi_j|$, cf. Fig. 4.5. Examples for multifrequency readout for $d = 8$ and $d = 12$ are [Wang et al. (2025), Champion et al. (2025)]. Here, E_J/E_C reaches values up to 325.

4.7 Conclusion

We have presented a model that describes phase-space measurement data of qudit states on superconducting quantum hardware. Our model qualitatively matches the data that we generated on a current IBM Quantum device. For qudit-state preparation, we employ higher-order X gates between $|j\rangle$ and $|j+2\rangle$. This scheme leads to a reduction of the execution time of qudit quantum circuits as well as of the duration of X-gate calibrations. Based on our model, we have compared the performance of two measurement strategies, a single-frequency and a multifrequency scheme, in simulations. For each strategy, we have identified the regime in hardware parameter space where it is optimal. The multifrequency strategy is superior when the qudit-state-dependent resonator states overlap significantly.

To use the full potential of both strategies, it is necessary to adjust the modulation frequency ω_m of the device. This is currently not possible on IBM Quantum hardware. Despite these software and hardware restrictions, we still find predicted differences in the frequency locations of the minima of the individual measurement errors ξ_j and an improvement over the measurement error ξ_{def} using the default measurement pulse. We expect a better performance of the strategies for setups that operate in the rotating frame of the drive $\omega_m = \omega_d$.

In the future, adaptive measurement schemes that change the drive frequency from shot to shot or between bunches of shots may be possible. This can lead to a further improvement of transmon qudit measurements.

The results and figures of this chapter have been published in parts in [Kehrer et al. (2024a)].

Chapter 5

Simulating Effective Gain by Mirroring Native Decay Using Echo Sequences

This chapter is based on preliminary and unpublished results obtained in a collaboration with T. Nadolny.

5.1 Motivation

In the current noisy-intermediate-scale quantum (NISQ) era [Preskill (2018)], available quantum computers are still far away from exceeding qubit numbers of many thousands that are of sufficient quality such that millions of logical gates can be executed. Hopefully, in the near future, we will understand what "far away" truly means. In the meantime, before achieving fault-tolerant universal quantum computing, we might focus on using quantum computing platforms as quantum simulators [Feynman (1982), Johnson et al. (2014), Altman et al. (2021)], in the spirit of classical analog computing. Taking IBM Quantum [IBM Quantum. (2025)] as an example, the former pulse-level access [Alexander et al. (2020)], which unfortunately has been removed in April 2025[8], allowed users to program custom microwave-pulse schedules to control qubits in a powerful and diverse fashion.

A quantum computer is built to perform environmentally isolated unitary time evolutions of its quantum system. On NISQ-era quantum devices, however, native qubit decay and dephasing does exist. Unsurprisingly, this noise can be used to simulate an open system that exhibits a decay and dephasing rate identical to the one of the hardware. The quantum simulation of open quantum systems is an active field [Barreiro et al. (2011), Kropf et al. (2016), Chen et al. (2018), García-Pérez et al. (2020), Del Re et al. (2020)]. In [Rost et al. (2020), Tolunay et al. (2023), Sun et al. (2024)], native decay is used to generate nontrivial mixed states. In these papers, echo sequences are used to mirror the native decay into an effective gain that leads to a fully mixed state. Echo sequences are essential in (nuclear) magnetic resonance

---

[8] https://www.ibm.com/quantum/blog/qiskit-2-0-release-summary [Accessed: July 30, 2025]

imaging [Hahn (1950), Hennig et al. (1986), Haase et al. (2011)] and are related to Ramsey interference [Ramsey (1950)].

In this chapter, we will understand the mirroring of native decay to effective gain in a detailed way. By introducing asymmetries in the echo sequence, the effective gain can be different from the resulting effective damping and lead to different mixed states than the ones that have been presented before.

The chapter is structured as follows. In Sec. 5.2, we present the spin-1/2 toy model including incoherent processes we want to simulate using the echo sequences. In Sec. 5.3, we introduce the symmetric echo sequence and in Sec. 5.4 the asymmetric echo sequence.

5.2 Model

In general, we want to simulate a nonunitary time evolution, e.g., incoherent gain and damping in addition to unitary evolution. Natively, loss is present on arguably any quantum computation platform. A special case of Lindblad master equations that we would like to simulate are related to the study of quantum synchronization (see Ch. 7), discussed in the second part of this thesis. Preferably, we want to simulate a coherent drive and detuning in combination with incoherent gain and damping.

Let us start with two-level systems, i.e., qubits. In the following, we want to model the Lindblad master equation without drive,

$$\dot{\rho} = \mathcal{L}_{\mathrm{model}}(\rho) = -\frac{\mathrm{i}}{2}\,[\Delta Z, \rho] + K_+\mathcal{D}[\sigma^+]\rho + K_-\mathcal{D}[\sigma^-]\rho + K_z\mathcal{D}[Z]\rho\,, \tag{5.2.1}$$

where K_+ and K_- are the gain and damping rates, K_z is the dephasing rate, and X, Y, and Z are the Pauli matrices. Furthermore, we use $\sigma^+ = |1\rangle\langle 0|$ and $\sigma^- = |0\rangle\langle 1|$. The corresponding evolution of $\rho^{(0)}$ for a duration $2T$ results in

$$\rho_{00}^{\mathrm{model}}(T) = \frac{K_- - \mathrm{e}^{-2(K_-+K_+)T}(K_- - (K_- + K_+)\rho_{00}^{(0)})}{K_- + K_+}\,, \tag{5.2.2}$$

$$\rho_{01}^{\mathrm{model}}(T) = \rho_{01}^{(0)}\,\mathrm{e}^{-(K_-+K_++4K_z+2\mathrm{i}\Delta)T}\,, \tag{5.2.3}$$

where $\rho_{ij} = \langle i|\,\rho\,|j\rangle$. In particular, the steady state

$$\rho_{00}^{\mathrm{model}}(T\to\infty) = \frac{K_-}{K_- + K_+}\,, \tag{5.2.4}$$

is mixed and the coherences $\rho_{01}^{\mathrm{model}}$ decay exponentially with rate $K_- + K_+ + 4K_z$.

The native Lindblad master equation of an idling qubit,

$$\dot{\rho} = \mathcal{L}_1(\rho) = -\frac{\mathrm{i}}{2}\,[\delta Z, \rho] + k_-\mathcal{D}[\sigma^-]\rho\,, \tag{5.2.5}$$

consists of a *native damping* with rate k_- and a detuning δ that is approximately constant during one time evolution [Ristè et al. (2013)]. In the quantum computing community, one such time evolution is called a “shot”. The evolution of an initial state $\rho^{(0)}$ by Eq. (5.2.5) for a duration t reads

$$\rho_{00}^{(1)}(t) = 1 - \mathrm{e}^{-k_- t}(1 - \rho_{00}^{(0)})\,, \tag{5.2.6}$$

$$\rho_{01}^{(1)}(t) = \rho_{01}^{(0)} \mathrm{e}^{-(\mathrm{i}\delta + k_-/2)t}\,. \tag{5.2.7}$$

Averaging over multiple shots, i.e., randomly drawn detunings δ that are normal distributed, leads to a Gaussian decay of coherences,

$$\bar{\rho}_{01}^{(1)}(t) = \frac{\rho_{01}^{(0)}}{\sqrt{2\pi}\sigma} \int_{-\infty}^{\infty} \mathrm{d}\delta\, \mathrm{e}^{-(\delta-\bar{\delta})^2/2\sigma^2} \mathrm{e}^{-(\mathrm{i}\delta + k_-/2)t} = \rho_{01}^{(0)} \mathrm{e}^{-(\mathrm{i}\bar{\delta} + k_-/2)t - \sigma^2 t^2/2}\,. \tag{5.2.8}$$

Here we used Eq. (2.326.3) of [Gradshteyn and Ryzhik (2015)]. The resulting coherences oscillate at the mean detuning $\bar{\delta}$ and decay both exponentially and Gaussian.

5.3 Symmetric Echo Sequence

Our echo building block consists of two X gates that are nested within three evolutions with $\mathcal{L}_1$. Using $\mathcal{L}_X(\rho) = X\rho X$, we define the evolution of one building block as the concatencation $\mathcal{L}_1 \circ \mathcal{L}_X \circ \mathcal{L}_1 \circ \mathcal{L}_X \circ \mathcal{L}_1$. The first (right) and last (left) $\mathcal{L}_1$ are applied for a duration $T/2$ and the central $\mathcal{L}_1$ is applied for a duration T. For the first and last $\mathcal{L}_1$, we set the detuning to $\delta + \Delta$, and for the central $\mathcal{L}_1$, we set the detuning to $\delta - \Delta$. In this way, the random δ part is canceled by the echo but the engineered Δ remains and can be used for quantum simulation purposes. The X gates are assumed to be implemented on timescales significantly smaller than T. For a number n_b of these echo blocks, i.e., an even number $2n_b$ of X gates, we obtain the iterative expressions

$$\rho_{00}^{(n_b)}(T) = 1 - \mathrm{e}^{-k_- T/2} + \mathrm{e}^{-3k_- T/2} - \mathrm{e}^{-2k_- T} + \mathrm{e}^{-2k_- T} \rho_{00}^{(n_b-1)}(T)\,, \tag{5.3.1}$$

$$\rho_{01}^{(n_b)}(T) = \mathrm{e}^{-(k_- + 4k_z + \mathrm{i}2\Delta)T} \rho_{01}^{(n_b-1)}(T)\,. \tag{5.3.2}$$

These recursions can be solved using the initial conditions $\rho_{00}^{(0)}(0) = \rho_{00}^{(0)}$ and $\rho_{01}^{(0)}(0) = \rho_{01}^{(0)}$,

$$\begin{aligned}\rho_{00}^{(n_b)}(T) &= 1 - \mathrm{e}^{-2n_b k_- T}(1 - \rho_{00}^{(0)}) - \mathrm{e}^{-k_- T/2} \frac{1 - \mathrm{e}^{-2n_b k_- T}}{1 + \mathrm{e}^{-k_- T}} \\ &= \left(1 - \mathrm{e}^{-2n_b k_- T}\right)\left(1 - \frac{1}{2\cosh(k_- T/2)}\right) + \mathrm{e}^{-2n_b k_- T} \rho_{00}^{(0)}\,,\end{aligned} \tag{5.3.3}$$

$$\rho_{01}^{(n_b)}(T) = \mathrm{e}^{-2n_b(k_- + 4k_z + \mathrm{i}2\Delta)T} \rho_{01}^{(0)}\,. \tag{5.3.4}$$

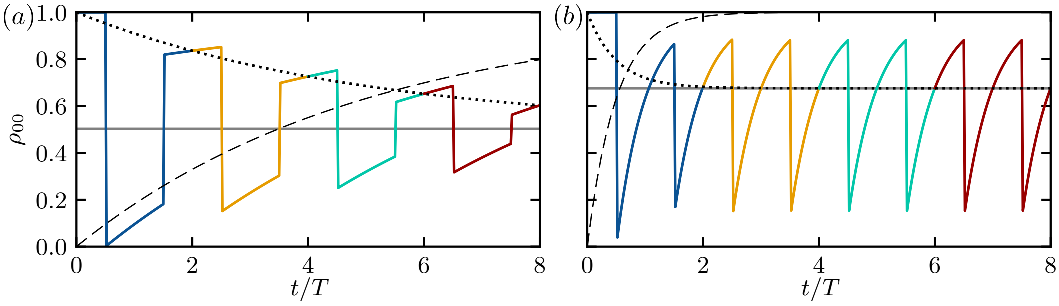

Figure 5.1: Time evolution of the symmetric echo sequence defined in Eq. (5.3.3). The colored solid zigzag curves correspond to the time evolution $\mathcal{L}_1$ between two X gates that correspond to the jumps, see Eq. (5.2.5). Each color represents one echo block. The dashed curve denotes the native decay $\rho_{00}(t) = 1 - \mathrm{e}^{-k_- t}$. The dotted curve denotes the effective time evolution of one echo block, see Eq. (5.3.7). The gray horizontal line corresponds to the steady state. (a) Small decay durations $k_-T = 0.2$. (b) Large decay durations $k_-T = 4$.

For many repetitions of these echo blocks, the resulting state is given by

$$\rho_{00}^{\infty}(T) = \rho_{00}^{(n_b\to\infty)}(T) = 1 - \frac{1}{2\cosh(k_-T/2)}\,, \tag{5.3.5}$$

$$\rho_{01}^{\infty}(T) = \rho_{01}^{(n_b\to\infty)}(T) = 0\,. \tag{5.3.6}$$

Note that $\rho_{00}^{\infty}(T) \in [0.5, 1]$. In the limit $k_-T \gg 1$ leading to $\rho_{00}^{\infty}(T) = 1$, the delay between two consecutive X gates is so long such that the state decays completely. In the limit $k_-T \ll 1$ leading to $\rho_{00}^{\infty}(T) = 0.5$, the state only decays marginally between two consecutive X gates such that eventually the maximally mixed state is reached.

Time evolutions are shown in Fig. 5.1. The colored solid curves correspond to the time evolution described by Eq. (5.2.5): one color per echo block. The jumps reflect the effects of the X gates. The dashed curve shows the native decay $\rho_{00}(t) = 1 - \mathrm{e}^{-k_- t}$. The dotted curve corresponds to the effective time evolution generated by the echo,

$$\rho_{00}^{\mathrm{block}}(t) = \left(1 - \mathrm{e}^{-k_- t}\right)\left(1 - \frac{1}{2\cosh(k_-T/2)}\right) + \mathrm{e}^{-k_- t}\rho_{00}^{(0)}\,, \tag{5.3.7}$$

matching with the actual time evolution after each echo block.

Let us compare the steady state generated by the echo defined in Eqs. (5.3.3) and (5.3.4) with the result of the Lindblad master equation in Eq. (5.2.1) that describes gain and damping given in Eqs. (5.2.2) and (5.2.3). The off-diagonal components restrict the gain and damping rates to $K_- + K_+ + 4K_z = k_- + 4k_z$, effectively fixing K_+. A Taylor expansion of the difference between $\rho^{(n_b)}(T)$ after n_b echo blocks and the model $\rho^{\mathrm{model}}(2n_bT)$ in k_-T is used to fix the values of K_z and K_-. Demanding vanishing first order,

$$0 = \left(1 - 2\frac{K_- + 4\rho_{00}^{(0)}(K_z - k_z)}{k_-}\right) n_b k_- t\,, \tag{5.3.8}$$

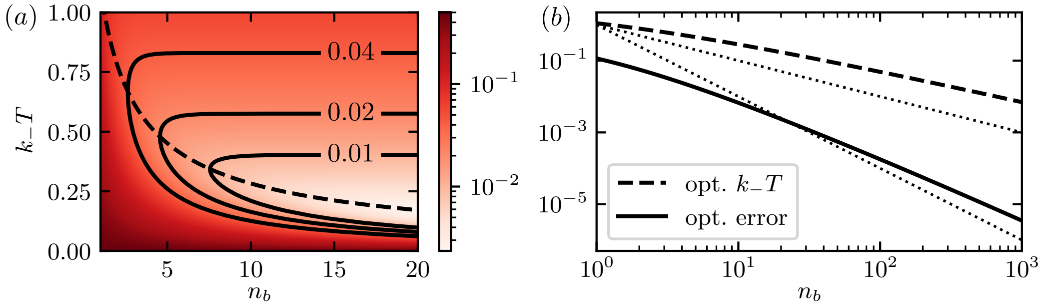

Figure 5.2: Error of symmetric echo sequence. (a) Difference between echo sequence consisting of n_b echo blocks, see Eq. (5.3.3), and $\rho_{00}^{\mathrm{model}}(t \to \infty) = 1/2$. The solid curves denote contour lines and the dashed curve indicates the local minima of the error at given k_-T. (b) The dashed curve corresponds to the one in panel (a) and the solid curve is the value of the error at this dashed curve. The two dotted lines correspond to n_b^{-1} and n_b^{-2}.

fixes K_z. Furthermore, demanding the resulting second order,

$$0 = (2\rho_{00}^{(0)} - 1)\frac{k_- - 2K_-}{2k_-\rho_{00}^{(0)}} n_b^2 (k_-T)^2 \,, \tag{5.3.9}$$

to vanish implies $K_- = k_-/2$ and $K_z = k_z$, leading to $K_+ = k_-/2$. The remaining expression reads

$$\rho_{00}^{(n_b)}(T) - \rho_{00}^{\mathrm{model}}(2n_bT) = \frac{n_b(k_-T)^3}{8} + \mathcal{O}\left((k_-T)^4\right) \,. \tag{5.3.10}$$

Thus, the error of approximating the master equation Eq. (5.2.1) by the echo sequence is linear in n_b and of third order in k_-T. Moreover, the echo sequence turns the native decay into both effective damping *and* gain.

The more relevant error measure is the difference between the echo and the steady state to be simulated. The steady state $\rho_{00}^{\mathrm{model}}(t \to \infty) = 1/2$ for equal $K_- = K_+$ differs from ρ_{00}^{∞} to second order in k_-T,

$$\rho_{00}^{\infty} = \frac{1}{2} + \frac{(k_-T)^2}{16} + \mathcal{O}\left((k_-T)^4\right) \,. \tag{5.3.11}$$

The error, i.e., difference between $\rho_{00}^{\mathrm{model}}(t \to \infty) = 1/2$ and the state at the end of an echo sequence of n_b echo blocks is shown in Fig. 5.2(a). For a given decay rate k_- of the qubit, there exists an optimal relation between T and n_b at which the error is minimal, see the dashed curve in Figs. 5.2(a) and 5.2(b). For $n_b \approx 10^3$, this minimal error scales approximately like n_b^{-2}.

5.4 Asymmetric Echo Sequence

Using the symmetric echo sequence presented in the previous section, the effective gain and loss rates are equal $K_- = K_+ = k_-/2$. We are interested in generating other steady states than $\rho_{00} = 1/2$. One way to engineer the ratio between the rates is

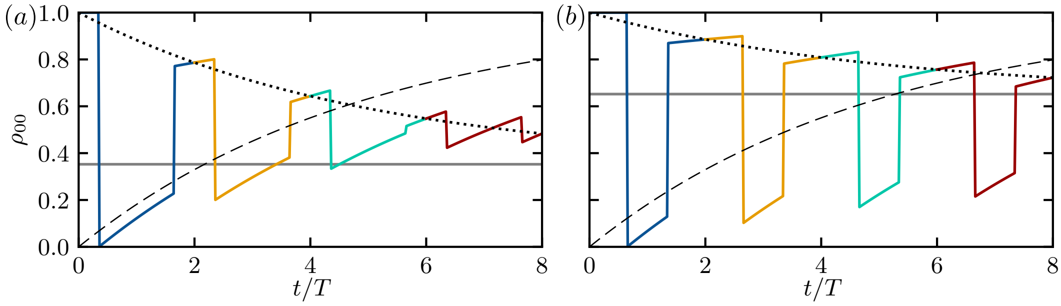

Figure 5.3: Time evolution of the asymmetric echo sequence defined in Eq. (5.4.1) for $k_-T = 0.2$. The dashed curve denotes the native decay $\rho_{00}(t) = 1 - \mathrm{e}^{-k_- t}$. The dotted curve denotes the effective time evolution of one echo block. The gray horizontal line corresponds to the steady state. (a) Negative shift $\tau = -0.3T$ leading to smaller steady-state ρ_{00}. (b) Positive shift $\tau = 0.3T$ leading to larger steady-state ρ_{00}.

to modify the individual durations of the $\mathcal{L}_1$ evolutions in our echo sequence. We introduce a shift τ that changes the durations $t/2 \to (t+\tau)/2$ of the first and last $\mathcal{L}_1$, and the duration $t \to t - \tau$ of the central $\mathcal{L}_1$. The asymmetric echo block, note the tilde, reads

$$\tilde{\rho}_{00}^{(n_b)}(T,\tau) = \mathrm{e}^{-2n_b k_- T}\rho_{00}^{(0)} + \left(1 - \frac{\sinh(k_-(T-\tau)/2)}{2\cosh(k_-T/2)\sinh(k_-T/2)}\right)(1 - \mathrm{e}^{-2n_b k_- T}), \tag{5.4.1}$$

$$\tilde{\rho}_{01}^{(n_b)}(T,\tau) = \mathrm{e}^{-2n_b(k_- + 4k_z + 2\mathrm{i}(\Delta + \delta\tau/T))T}\rho_{01}^{(0)} . \tag{5.4.2}$$

The structure of the result is quite similar to the solution for the symmetric echo in Eqs. (5.3.3) and (5.3.4). For $\tau = 0$, the sinh terms cancel. Note that due to the asymmetry, the native detuning δ is not canceled completely which results in Gaussian damping of the coherences, see Eq. (5.2.8).

In Fig. 5.3, we present time evolutions of two asymmetric echo sequences. The influence of the sign of τ on the effective gain and damping rates can be understood intuitively. The evolutions of $\mathcal{L}_1$ for a duration $(T+\tau)/2$ take place after an even number of X gates, i.e., ideally identity. If their duration is increased, the native decay is converted to an even larger effective decay. Vice versa, if the duration $T - \tau$ of the $\mathcal{L}_1$ evolutions that take place after an even number of X gates is increased, i.e., negative $\tau < 0$, the native decay is converted into a larger effective gain.

Similar to the symmetric echo, we can compute the difference between the asymmetric echo and the model solution Eq. (5.2.2). The simulated detuning equals $\Delta + \delta\tau/T$ and the off-diagonals of the state fix $K_- + K_+ + 4K_z = k_- + 4k_z$ as before. The first and second order of the Taylor expansion of the difference between the asymmetric echo and the model in k_-T and $k_-\tau$ vanish if $K_+ = k_-(1 - \tau/T)/2$ and $K_- = k_-(1 + \tau/T)/2$. The remaining term is again of third order,

$$\tilde{\rho}_{00}^{(n_b)}(T,\tau) - \rho_{00}^{\mathrm{model}}(2n_bT) = \frac{n_b}{24}(k_-T)^3\left(\frac{\tau}{T}+1\right)\left(\frac{\tau}{T}-1\right)\left(\frac{\tau}{T}-3\right) + \mathcal{O}\left((k_-T)^4\right) . \tag{5.4.3}$$

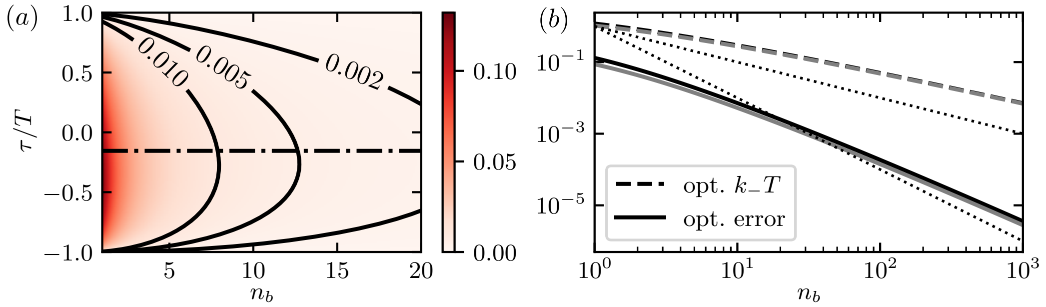

Figure 5.4: Error of asymmetric echo sequence. (a) Difference between echo sequence consisting of n_b echo blocks and $\rho_{00}^{\text{model}}(t \to \infty) = (1 + \tau/T)/2$ at the optimal k_-T for a given τ. The solid curves denote contour lines and the dash-dotted line indicates $\tau = (1 - 2/\sqrt{3})T$, i.e., the maximum deviation in Eq. (5.4.3). (b) The black (gray) dashed curve corresponds to the optimal k_-T that minimizes the difference between echo sequence and $(1 + \tau/T)/2$ for $\tau = -0.3T$ ($\tau = 0.3T$). The black (gray) solid curve represents the value of the error at the corresponding dashed curve. The two dotted lines correspond to n_b^{-1} and n_b^{-2}.

The maximum deviation for $\tau \in [-T, T]$ is achieved for $\tau/T = 1 - 2/\sqrt{3}$. Using this asymmetric echo, the effective damping *and* gain rates can be tuned to distinct values. The resulting steady state ground-state population can be tuned within the interval $[0, 1]$ and is approximately linear for small k_-T and $k_-\tau$,

$$\rho_{00}^{\infty} = \frac{1}{2}\left(1 + \frac{\tau}{T}\right) + \left(\frac{\tau}{T} + 1\right)\left(\frac{\tau}{T} - 1\right)\left(\frac{\tau}{T} - 3\right)\frac{(k_-T)^2}{48} + \mathcal{O}\left((k_-T)^4\right) . \tag{5.4.4}$$

We plot the difference between the asymmetric echo sequence consisting of n_b echo blocks and $\rho_{00}^{\text{model}}(t \to \infty) = (1 + \tau/T)/2$ in Fig. 5.4(a). For each value of τ and n_b, only the error at the optimal k_-T is shown, i.e., the minimal error for a fixed value of τ and n_b. In Fig. 5.4(b), the optimal k_-T and error are shown for $\tau/T = -0.3, 0.3$. No significant difference between both cases can be found.

5.5 Conclusion

In this chapter, we have learned how echo sequences can be used to generate mixed states of qubits, i.e., spin-1/2. These echo sequences that consist of alternating decay periods and X gates map native damping to both effective damping *and* gain of equal magnitude. This can be used to simulate simple open quantum systems on quantum hardware. However, the resulting effective gain and damping rates still depend on the actual hardware.

We have shown that by making the echo sequence asymmetric in time, the ratio of the resulting effective gain and damping rates can be changed. Thus, mixed states of arbitrary Z expectation values can be prepared. The generation of nontrivial steady states in combination with the simulation of open quantum systems is relevant for realizing quantum synchronization in experiments. For a detailed presentation of quantum synchronization see the second part of this thesis, e.g., Ch. 7.

In this regard, the simulation of spin-1 models is of special interest. It might be promising to study the echo sequences presented here for (transmon) qutrits in the future. In this case, the native loss manifests mainly as a sequential decay of higher-excited states into neighboring lower-excited states, see [Fischer et al. (2022)]. Since higher-excited states often exhibit faster decay, they could be useful for simulating effective gain and damping faster than the native rates. Echo sequences making use of standard qudit X gates $X_{j,j+1}$ operating between neighboring states as well as two-photon gates $X_{j,j+2}$, see Sec. 4.6.1, might lead to the preparation of useful steady states. Later on, one might study models consisting of multilevel qudits.

Part II

Quantum Synchronization of Oscillating Systems

Chapter 6

Classical Synchronization

Synchronization, which Christiaan Huyguens in 1665 called “la sympathie des horologes” (french for “the sympathy of clocks”), see letter no. 1335 of [Huygens (1893)], can be defined as the alignment of features of oscillators with either external signals or other oscillators. Examples for these features are the frequency of oscillation and the phase of oscillation. For modern views on Huygen’s clocks see [Oliveira and Melo (2015), Willms et al. (2017)]. In the last century, synchronization became a vivid field of research by bringing together, e.g., biology [Buck (1938), Winfree (1967)], laser physics [Stover and Steier (1966)], biochemistry/medicine [Schäfer et al. (1998), Laurent and Kellershohn (1999), Glass (2001), Enjieu Kadji et al. (2007), Feillet et al. (2014), Goldbeter and Yan (2022)], civil engineering [Strogatz et al. (2005), Rohden et al. (2012), Taher et al. (2019)], and social sciences [Hong and Strogatz (2011a), Hong and Strogatz (2011b)]. Several books on nonlinear dynamics [Pikovsky et al. (2001), Strogatz (2003), Balanov et al. (2008)] but also life sciences [Wang (2022)] feature synchronization.

About a decade ago, another avenue of synchronization emerged: *quantum synchronization* [Lee and Sadeghpour (2013)]. Here, people try to identify unique quantum features of synchronization of quantum oscillators. Starting in Ch. 7, quantum synchronization will be the main topic of this second part of the thesis. In this chapter, we will review the main aspects of classical synchronization that we will later use as a reference for studies of quantum setups.

6.1 Kuramoto Model

Thinking about a model of clocks, naively, one could start with assigning a single scalar, i.e., a phase of oscillation, to each clock. One ‘tick’ corresponds to a 2π evolution of this phase and the corresponding frequency of oscillation is defined as the inverse duration between two ticks. However, a physical clock is often realized as an oscillator with nonvanishing amplitude and therefore more than one degree of freedom. In this section, we will discuss synchronization of oscillators of *fixed* amplitude before moving on to amplitude oscillators in the subsequent sections. In [Kuramoto (1975)], Yoshiki Kuramoto proposed a model of synchronization consisting of phase oscillators, i.e.,

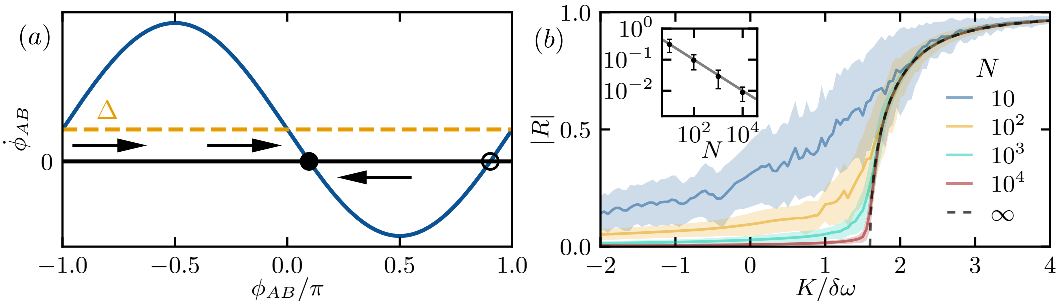

Figure 6.1: Kuramoto model for $K > 0$. (a) Schematics of a two-oscillator Kuramoto model. The blue curve depicts the right hand side of Eq. (6.1.2), the orange dashed line corresponds to the value of the frequency difference Δ. The black dot (circle) highlights the location of the stable (unstable) fixed point of $\dot{\phi}_{AB} = 0$. The arrows indicate the time evolution of the phase difference. (b) Phase diagram averaged over 50 realizations of $N = 10, 10^2, 10^3, 10^4$ oscillators after a duration $t\delta\omega = 100$. The width of each ribbon corresponds to the respective standard deviation. The black dashed curve is the formal solution in the $N \to \infty$ limit, see Eq. (6.1.9). The inset shows the $|R| = N^{-1/2}$ relation (gray line) at $K = 0$, see Eq. (6.1.12).

oscillators that are described by a phase of oscillation only. A broad review of various modifications of the Kuramoto model can be found in [Acebrón et al. (2005)]. This section is based on Ch. 13 of [Strogatz (2024)].

The Kuramoto model is described by the following set of first order nonlinear differential equations

$$\dot{\phi}_j = \omega_j + \frac{K}{N} \sum_{i=1}^{N} \sin(\phi_i - \phi_j)\,, \tag{6.1.1}$$

where $j \in [1, N]$ and N is the number of oscillators that are all-to-all coupled with strength K The jth oscillator is characterized by a phase of oscillation $\phi_j \in [-\pi, \pi]$ and a frequency ω_j. In general, the frequencies ω_j are drawn from a distribution $G(\omega)$. If $K > 0$, the coupling defined above is attractive and leads to synchronization of the phases of the oscillators. Focusing on only two oscillators A and B, we can rewrite Eq. (6.1.1) in terms of their phase difference $\phi_{AB} = \phi_A - \phi_B$,

$$\dot{\phi}_{AB} = \dot{\phi}_A - \dot{\phi}_B = \omega_A - \omega_B - K\sin(\phi_A - \phi_B) = \Delta - K\sin(\phi_{AB})\,. \tag{6.1.2}$$

In Fig. 6.1(a), this equation of motion of the two-oscillator Kuramoto model is visualized. The black dot (circle) highlights the location of the stable (unstable) fixed point of $\dot{\phi}_{AB} = 0$. The arrows indicate the time evolution of the phase difference: to the right if $\dot{\phi}_{AB} > 0$ and to the left if $\dot{\phi}_{AB} < 0$. In the presence of the frequency detuning Δ, two oscillators lock their relative phase to a single value $\phi_{AB} = \arcsin(\Delta/K)$. For $|\Delta/K| \ll 1$, this value is close to zero. If $|\Delta/K| > 1$, the oscillators do not lock their phase since no fixed point of $\dot{\phi}_{AB} = 0$ exists. They rather oscillate monotonically with varying frequency.

The dynamics of a macroscopic number of oscillators is richer. The equation of motion Eq. (6.1.1) can be rewritten in a more elegant way using the complex order parameter

$$R = |R|\mathrm{e}^{\mathrm{i}\Phi} = \frac{1}{N}\sum_{j=1}^{N} \mathrm{e}^{\mathrm{i}\phi_j}\,. \tag{6.1.3}$$

This order parameter is the average of the complex phase factors of the oscillators implying $|R| \in [0,1]$. It can be interpreted as the *mean field* of the oscillators. If the N phases ϕ_j are identical, the magnitude of R is one. If the phases are distributed equally, the magnitude of R is zero. Therefore, $|R|$ acts as a measure of phase synchronization. Interestingly, this order parameter appears natively in Eq. (6.1.1),

$$\dot{\phi}_j = \omega_j + \frac{K}{N}\sum_{i=1}^{N} \mathrm{Im}[\mathrm{e}^{\mathrm{i}\phi_i}\mathrm{e}^{-\mathrm{i}\phi_j}] = \omega_j + K|R|\,\mathrm{Im}[\mathrm{e}^{\mathrm{i}\Phi}\mathrm{e}^{-\mathrm{i}\phi_j}] = \omega_j + K|R|\sin(\Phi - \phi_j)\,. \tag{6.1.4}$$

Thus, the all-to-all coupling of oscillators can be understood as a coupling of each individual oscillator to the mean field R.

The distribution $G(\omega)$ of frequencies has to be fixed to perform simulations. Here, we choose a Gaussian distribution. Moving to a rotating frame, i.e., transforming all phases by a linear shift proportional to the average frequency $\bar{\omega}$,

$$\phi_j \to \phi_j + \bar{\omega}t\,, \tag{6.1.5}$$

$$\Phi \to \Phi + \bar{\omega}t\,, \tag{6.1.6}$$

the mean of the Gaussian distribution can effectively be chosen to be zero. Furthermore, by rescaling time with respect to the Gaussian width $\delta\omega$, we can effectively choose $G(\omega)$ to have unit variance. In Fig. 6.1(b), we present the average of the order parameter $|R|$ for $N = 10, 10^2, 10^3, 10^4$ oscillators over 50 realizations initialized with a uniform distribution of phases. The width of each ribbon corresponds to the respective standard deviation. The larger the number N of oscillators, the smaller the standard deviation and the sharper the kink at $K/\delta = 2\sqrt{2/\pi} \approx 1.596$, see the discussion below Eq. (6.1.9). The black dashed curve in Fig. 6.1(b) corresponds to the formal solution of $R(K)$ in the limit $N \to \infty$. This solution will be given in the following.

Assuming $K > 0$ and that $|R|$ is constant in time for large N, the oscillators with $|\omega_j| < K|R|$ lock to a phase value given by $\omega_j = K|R|\sin(\phi_j)$. The expectation value of the phase factor $\mathrm{e}^{\mathrm{i}\phi_j} = \cos(\phi_j) + \mathrm{i}\sin(\phi_j)$ over all frequencies can be split into a symmetric cos and antisymmetric sin part. Since for locked oscillators ω_j and $\sin(\phi_j)$ are both antisymmetric in ω_j whereas $G(\omega_j)$ is symmetric in ω_j, the sin part of the phase factor expectation value vanishes. In the rotating frame where the average frequency is zero, the average locking angle is also zero, i.e., $\Phi = 0$. Therefore, the remaining term of expectation value of the phase factor $\mathrm{e}^{\mathrm{i}\phi_j}$ is

$$|R| = \int\limits_{-K|R|}^{K|R|} \mathrm{e}^{\mathrm{i}\phi_j(\omega_j)} G(\omega_j)\mathrm{d}\omega_j = \int\limits_{-K|R|}^{K|R|} \cos(\phi_j(\omega_j))G(\omega_j)\mathrm{d}\omega_j \,, \tag{6.1.7}$$

and can be rewritten using $\omega_j = K|R|\sin(\phi_j)$,

$$|R| = K|R| \int\limits_{-\pi/2}^{\pi/2} \cos^2(\phi_j)G(K|R|\sin(\phi_j))\mathrm{d}\phi_j \,. \tag{6.1.8}$$

In [Strogatz (2024)], it is shown that the nonlocked oscillators do not contribute to this expectation value due to the symmetry of both $G(\omega_j)$ and their density function that depends on ϕ_j and ω_j. Inserting $G(\omega) = \mathrm{e}^{-\omega^2/2}/\sqrt{2\pi}$ in Eq. (6.1.8), the following implicit equation, also called self-consistency equation, for $|R(K)| \neq 0$ is obtained,

$$1 = \frac{K}{2}\mathrm{e}^{-K^2|R|^2/4}\sqrt{\frac{\pi}{2}}\left(I_0\left(\frac{K^2|R|^2}{4}\right) + I_1\left(\frac{K^2|R|^2}{4}\right)\right) \,, \tag{6.1.9}$$

where I_ν is the modified Bessel function of the first kind. This function, see Eq. (8.406.1) of [Gradshteyn and Ryzhik (2015)],

$$I_\nu(z) = \mathrm{e}^{-\mathrm{i}\pi\nu/2} J_\nu(\mathrm{e}^{\mathrm{i}\pi/2}z) \tag{6.1.10}$$

can be expressed by the Bessel function of the first kind, see Eq. (8.402) of [Gradshteyn and Ryzhik (2015)],

$$J_\nu(z) = \frac{z^\nu}{2^\nu}\sum_{k=0}^{\infty}(-1)^k \frac{z^{2k}}{2^{2k}k!\Gamma(\nu+k+1)} \,. \tag{6.1.11}$$

Using $I_0(0) = 1$ and $I_1(0) = 0$, the critical value $K_c = 2\sqrt{2/\pi} \approx 1.596$ at which the transition from $|R| = 0$ to $|R| \neq 0$ occurs can be extracted from Eq. (6.1.8) analytically.

At $K = 0$, the system exhibits trivial dynamics: each oscillator oscillates with its frequency ω_j. For a uniform distribution of initial phases, the square of the magnitude $|R|^2 = R^*R$ of the order parameter R has the following expectation value,

$$\frac{1}{N^2(2\pi)^N}\int \mathrm{d}\phi_1 \cdots \int \mathrm{d}\phi_N \sum_{i,j=1}^{N} \mathrm{e}^{\mathrm{i}(\phi_j - \phi_i)} = \frac{1}{N} \,. \tag{6.1.12}$$

Only the N terms $\mathrm{e}^{\mathrm{i}(\phi_j-\phi_i)} = 1$ where $\phi_i = \phi_j$ survive the integrals over each ϕ_j. The result of each of these terms after integration over all ϕ_j yields $(2\pi)^N$. In the inset of Fig. 6.1(b), this prediction $|R| = N^{-1/2}$ is compared to the results of the simulation.

This study sets the basics of synchronization at the level of phase oscillators. What happens if we add a second degree of freedom, i.e., an amplitude, and what is the connection between phase oscillators and amplitude oscillators? An answer to the second question is already hidden in this section: interpret the order parameter $R = |R|\mathrm{e}^{\mathrm{i}\Phi}$ defined in Eq. (6.1.3), which is based on many *phase* oscillators, as an oscillator that exhibits an *amplitude* $|R| \in [0, 1]$, a phase Φ, and oscillates with the mean frequency of $G(\omega)$. The connection between the order parameter and an actual amplitude oscillator has been presented in [Ott and Antonsen (2008), Pikovsky and Rosenblum (2015)].

6.2 Limit Cycles

This section on *limit cycles*, the fundamental building blocks of describing synchronization of amplitude oscillators, is based on Chs. 7 and 8 of [Strogatz (2024)] and Ch. 7 of [Pikovsky et al. (2001)]. A *limit-cycle oscillator* is an oscillator whose phase space hosts a limit cycle. In some sense, the Kuramoto model implicitly consists of limit-cycle oscillators that all exhibit a time-independent (and maybe even equal) radius. But what is a limit cycle? A limit cycle is an isolated, closed, and one-dimensional trajectory in the phase space of an oscillator. The adjective *isolated* refers to the non-existence of other closed trajectories in its neighborhood. *Closed*, on the other hand, can be rephrased as: we can find an angle-like S^1 (1-sphere) parametrization of the limit cycle, which will be called the *phase (of oscillation)*. For example, this definition of a limit cycle excludes: (i) orbits of a harmonic oscillator, since they are dense in phase space, or (ii) the strange Lorenz attractor since even if it lives in a bounded subset of its phase space, it is not closed. Often in this thesis, the term 'limit cycle' will be used as a synonym for 'limit-cycle oscillator'.

Intuitively, the closedness can be achieved by making a single orbit either stable/attracting, unstable/repulsive, or both. A class of systems that feature a unique stable limit cycle is the *Liénard system* [Liénard (1928), Perko (2001), Leonov and Kuznetsov (2013)] defined by the second-order differential equation

$$\frac{\mathrm{d}^2 x}{\mathrm{d}t} + f(x)\frac{\mathrm{d}x}{\mathrm{d}t} + g(x) = 0\,. \tag{6.2.1}$$

This equation can be reduced to the following set of first-order differential equations,

$$\frac{\mathrm{d}x}{\mathrm{d}t} = \dot{x} = y\,, \tag{6.2.2}$$

$$\frac{\mathrm{d}y}{\mathrm{d}t} = \dot{y} = -f(x)y - g(x)\,. \tag{6.2.3}$$

This Liénard system hosts a stable limit cycle if the continuously differentiable functions $f(x) = f(-x)$ and $g(x) = -g(-x)$ satisfy:

(1) $g(x) > 0$ for $x > 0$,

(2) $F(x) = \int\limits_0^x f(y)\mathrm{d}y$ has exactly one zero at $x = x_0 > 0$,

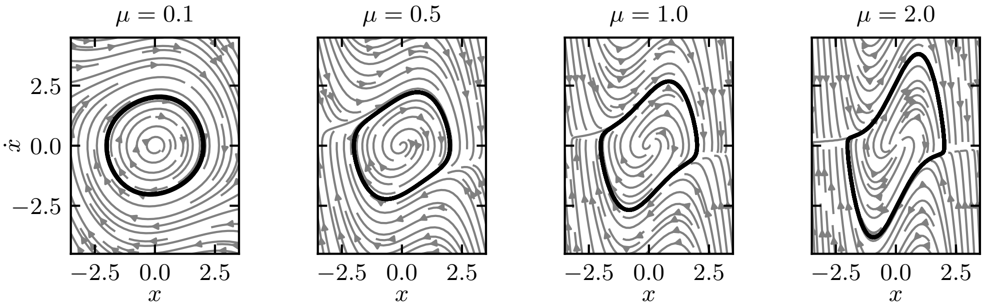

Figure 6.2: Phase portraits of the van der Pol oscillator for various values of μ. The gray arrows correspond to the vector field of the equations of motion, see Eqs. (6.2.2) and (6.2.3). The black curve marks the limit cycle to which every trajectory converges.

(3) $F(x) < 0$ for $0 < x < x_0$,

(4) $\frac{\mathrm{d}F}{\mathrm{d}x}(x) = f(x) \geq 0$ for $x \geq x_0$,

(5) $F(x) \to \infty$ for $x \to \infty$,

see [Perko (2001)] for a proof.

Bifurcations are, e.g., changes in the number or stability properties of fixed points or stabilized closed orbits in phase space depending on the value of a particular tuning parameter. Examples in 2D are the saddle-node bifurcation, pitchfork bifurcations, and the Hopf bifurcation. The saddle-node bifurcation describes the existence of a saddle and fixed point above a critical value of the parameter and the coalescence of both at the critical value. Below this critical value, no fixed point occurs. The supercritical (subcritical) pitchfork bifurcation describes the existence of a single stable (unstable) fixed point below (above) a critical value of the parameter. Above (below) this critical value this fixed point becomes unstable (stable) and is accompanied by two symmetrically distributed stable (unstable) fixed points. All three fixed points coalesce at the critical value. The supercritical Hopf bifurcation is the change of a stable spiral into an unstable spiral that is enclosed by a limit cycle. The subcritical Hopf bifurcation describes the transition of a stable fixed point surrounded by an unstable limit cycle that itself is surrounded by a stable limit cycle below a critical value of the tuning parameter to an unstable fixed point that is surrounded by a stable limit cycle. The unstable limit cycle and the stable fixed point coalesce at the critical value. In this latter case, hysteresis occurs. An overview of different types of bifurcation is given in [Chia et al. (2025)].

6.2.1 Van der Pol Oscillator

A famous example that exhibits a limit cycle is the *van der Pol (vdP) oscillator* [Pol (1920), Pol (1927)]. It is a special case of a Liénard system where $f(x) = \mu(x^2 - 1)$ and $g(x) = x$. Note that originally in [Pol (1927)], rather $f(x) = 3\mu_1 x^2 - \mu_2$ has been considered. Since $F(x) = \mu x(x^2 - 3)/3$ has a single positive zero at $x_0 = \sqrt{3}$, the vdP oscillator exhibits a stable limit cycle. Limit cycles of the vdP oscillator for various values of μ are shown in Fig. 6.2. For small μ, the limit cycle looks like a stabilized orbit of the harmonic oscillator, whereas for large μ the limit cycle appears to be quite distorted. In the chapter on quantum synchronization, see Ch. 7, we will often talk about the “quantum van der Pol” oscillator. As discussed in [Chia et al. (2020), Ben Arosh et al. (2021)], that model is rather the quantum analogue of the *Stuart-Landau oscillator* [Stuart (1960), Landau (1965)], described in the next section. By adding a drive term with strength Ω and performing a rotating-wave approximation in the rotating frame of the drive, the equation of motion of the van der Pol oscillator exhibits the same form as the one of the Stuart-Landau oscillator. Using the complex variable $z = x + \mathrm{i}y$, we obtain an approximate equation of motion for the van der Pol oscillator in the rotating frame of its drive,

$$\dot{z} \approx -\mathrm{i}\Omega - \mathrm{i}\Delta z + \frac{\mu}{2} z - \frac{\mu}{8} |z|^2 z \,. \tag{6.2.4}$$

Here, Δ is the detuning between the oscillator and the drive.

6.2.2 Stuart-Landau Oscillator

As mentioned in the previous section, the Stuart-Landau oscillator can be interpreted as an approximation of the van der Pol oscillator. In the rotating frame of an external drive of strength $\Omega > 0$, the Stuart-Landau oscillator is defined by the first-order differential equation

$$\frac{\mathrm{d}z}{\mathrm{d}t} = \dot{z} = -\mathrm{i}\Omega - \mathrm{i}\Delta z + \frac{\gamma_1}{2} z - \gamma_2 |z|^2 z \,, \tag{6.2.5}$$

for the complex amplitude $z = r\mathrm{e}^{\mathrm{i}\phi}$. The detuning between the eigenfrequency of the oscillator and the frequency drive is $\Delta = \omega_0 - \omega_d$, the gain rate is denoted by γ_1, and the damping rate is denoted by γ_2. Note that we recover the approximation of the van der Pol oscillator for $\gamma_1 = \mu$ and $\gamma_2 = \mu/8$. For $\Omega = 0$, the Stuart-Landau oscillator exhibits a U(1) symmetry: invariance of Eq. (6.2.5) under the time-independent transformation $z \to z\mathrm{e}^{\mathrm{i}\theta}$. Therefore, it is often convenient to study the equation of motion of the radius and phase separately. Both equations are obtained in an elegant way by extracting the amplitude and phase part of $\dot{z} = \dot{r}\mathrm{e}^{\mathrm{i}\phi} + \mathrm{i}r\mathrm{e}^{\mathrm{i}\phi}\dot{\phi}$ Eq. (6.2.5),

$$\dot{r} = \mathrm{Re}[\dot{z}\mathrm{e}^{-\mathrm{i}\phi}] = r\left(\frac{\gamma_1}{2} - \gamma_2 r^2\right) - \Omega \sin(\phi) \,, \tag{6.2.6}$$

$$\dot{\phi} = \mathrm{Im}[\dot{z}/z] = -\Delta - \frac{\Omega}{r}\cos(\phi) \,. \tag{6.2.7}$$

If $\Omega = 0$, the steady-state value of the radius can be read off Eq. (6.2.6): the ratio of the gain and damping rates γ_1 and γ_2 determine $r_0 = \sqrt{\gamma_1/2\gamma_2}$. Intuitively, the linear gain leads to an exponential increase of the radius. However, the nonlinear damping that vanishes for small radii will eventually cancel the gain at a certain value of the radius. Since there is only a single positive value at which both effects cancel, a stable limit cycle is formed. For trajectories starting below r_0, the gain wins such that they

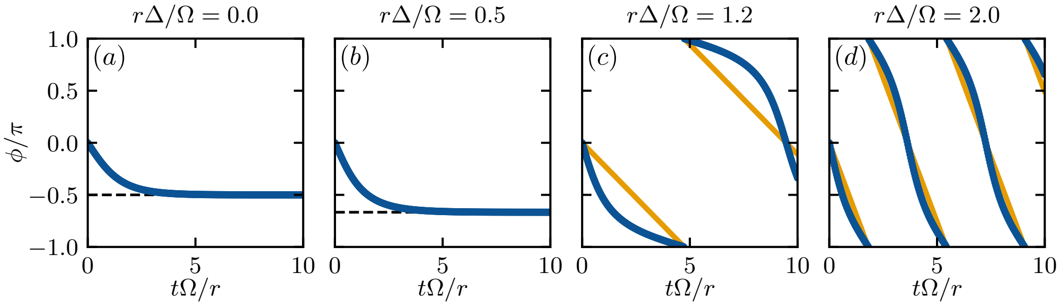

Figure 6.3: Time evolutions of Adler's equation Eq. (6.2.7) for constant radius r. (a), (b) For $r|\Delta| < \Omega$, the phase (blue curve) converges to a fixed point $\phi = -\arccos(-r\Delta/\Omega)$ that is indicated by the dashed black line. (c), (d) For $r|\Delta| > \Omega$, the phase (blue curve) oscillates continuously with a mean frequency ν_A (orange line) defined in Eq. (6.2.9).

are pushed toward to the limit cycle. For trajectories starting above r_0, the damping wins such that they are pulled toward to the limit cycle.

If $\Omega \neq 0$, the equation of motion of the phase, Eq. (6.2.7), can be viewed as a modified version of Adler's equation [Adler (1946)] that is basically the equation of motion of the two-oscillator Kuramoto model, see Eq. (6.1.2). Here, *modified* refers to $\sin \leftrightarrow \cos$.

Let us consider the case of a constant radius. Here, an analytical solution of the time evolution of the phase can be found. For $\phi(0) = 0$,

$$\phi(t) = -2\arctan\left(\frac{\Delta + \Omega/r}{\nu_A}\tan(t\nu_A/2)\right), \tag{6.2.8}$$

where

$$\nu_A = \sqrt{r^2\Delta^2 - \Omega^2}/r\,. \tag{6.2.9}$$

In Fig. 6.3, time evolutions are shown. Note that for ν_A to be real, $r|\Delta| > \Omega$ must hold which leads to oscillating solutions. For $r|\Delta| < \Omega$, the identity $\tan \mathrm{i}z = \mathrm{i}\tanh z$ can be used to realize that solutions decay to a fixed point $\phi = -\arccos(-r\Delta/\Omega)$. Since tan is π-periodic, the mean frequency of Eq. (6.2.8) is ν_A. The fact that the equations of motion of the oscillator are defined in the rotating frame of the drive, the observed frequency of the oscillator is the difference between the actual frequency of the oscillator and the drive frequency ω_d. Thus, if the phase of the oscillator is constant in time, the oscillator aligns its frequency to the one of the drive. This effect is also called *frequency synchronization*. Furthermore, if the phase of the oscillator is fixed to a particular value, *phase synchronization* occurs. Both terms will be discussed in the following.

6.3 Frequency Synchronization

In the previous section, the analytical solution of the phase of a Stuart-Landau oscillator for a constant radius r was presented showing frequency synchronization

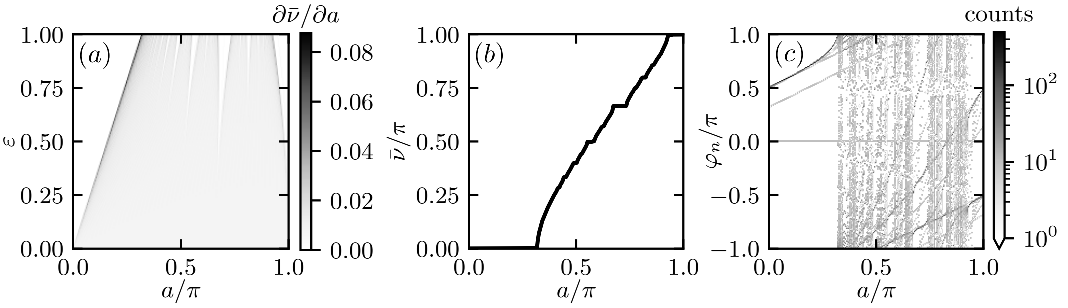

Figure 6.4: Mode locking of the circle map defined in Eq. (6.3.1). A total number of 500 iteration steps were computed. (a) Arnold tongues of the mode locking measure $\partial\bar{\nu}/\partial a$. For various intervals of a in which this derivative is zero, the circle map exhibits mode locking. White regions correspond to the plateaus in (b). (b) Mode locking measure $\partial\bar{\nu}/\partial a$ for $\varepsilon = 1$. The plateaus correspond to the white regions in (a). (c) Bifurcation diagram of the circle map for $\varepsilon = 1$ as a histogram with 200 bins in φ_n. For the values of a for which the circle maps exhibits mode locking, the bifurcation diagram shows $2\pi/\bar{\nu}$ accumulation points between the sequence φ_n jumps.

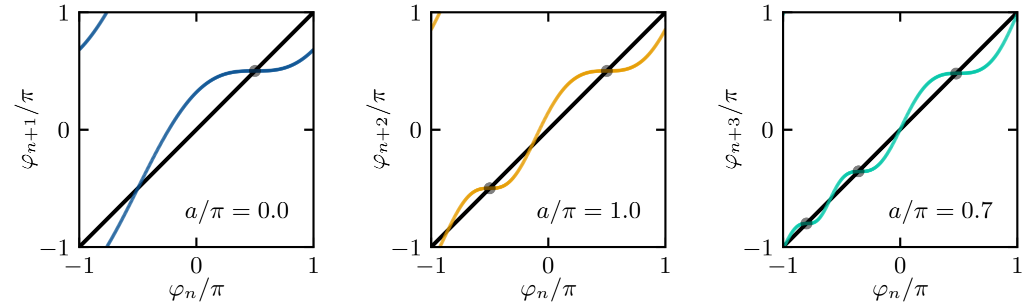

Figure 6.5: Visualization of m-cycles for $\varepsilon = 1$ of the circle map defined in Eq. (6.3.1). The colored curves correspond to an m-fold application of the circle map $\varphi_{n+m}(\varphi_n)$ at different values of a. The black line corresponds to $\varphi_{n+0} = \varphi_n$. The dots indicate where $\varphi_{n+m}(\varphi_n) = \varphi_n$ and $|\partial\varphi_{n+m}/\partial\varphi_n| < 1$, i.e., the values of some accumulation points shown in Fig. 6.4(c).

for $r|\Delta| < \Omega$, where Δ is the detuning between the oscillator and an external drive of strength Ω. Here, we will simulate both the equations of motion for the radius and the phase to study frequency synchronization of the Stuart-Landau oscillator. So-called *Arnold tongues* named after Vladimir Igorevich Arnol'd will appear. In the original work [Arnol'd (1961)], the circle map

$$\varphi_{n+1} = \varphi_n + a + \varepsilon\cos(\varphi_n) \tag{6.3.1}$$

has been studied. This map can be seen as the discretized version of Eq. (6.2.7), where the parameters a and ε are related to Δ and Ω/r. Depending on a and ε, regions of *mode locking* are identified in which the effective mean frequency

$$\bar{\nu} = \lim_{n\to\infty}\frac{\varphi_n}{n} \tag{6.3.2}$$

is constant in a, see Figs. 6.4(a) and 6.4(b). Here, when $\partial\bar{\nu}/\partial a = 0$, the sequence of phases φ_n exhibits $m = 2\pi/\bar{\nu}$ accumulation points that in general are not equally

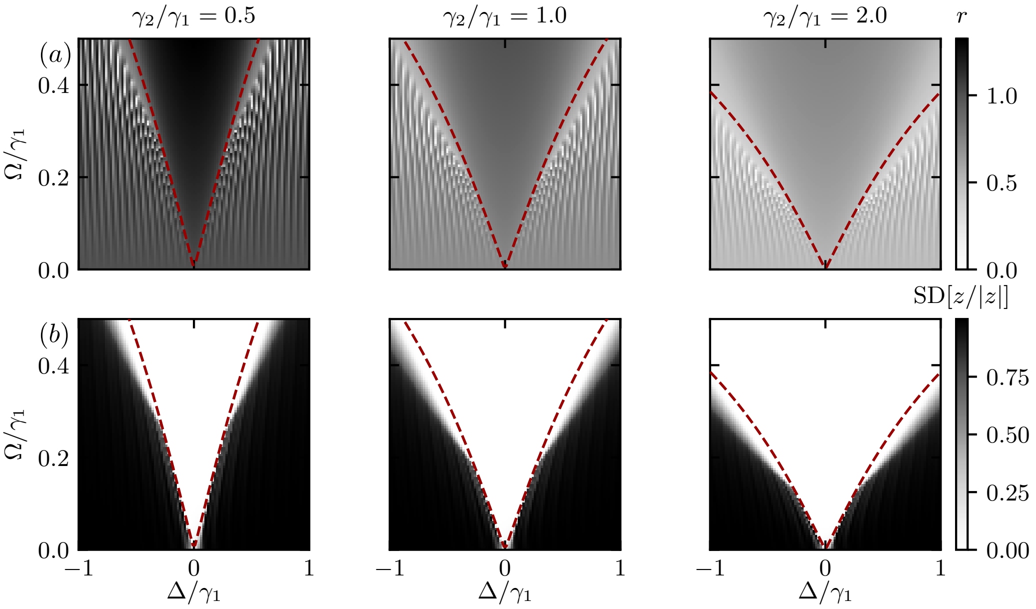

Figure 6.6: Arnold tongues of the Stuart-Landau oscillator. (a) Final value of the radius r at $t\gamma_1 = 100$. Striped regions indicate time dependence of the radius. (b) Standard deviation of the normalized complex amplitudes $z/|z|$. Small values indicate static phases and high values indicate oscillating solutions. In both panels, the dashed red curves correspond to Eq. (6.3.6), which is linear for small Δ: $\Omega = \Delta\sqrt{\gamma_1/2\gamma_2}$.

spaced, see Figs. 6.4(c) and 6.5. These are so-called m-cycles. If $\bar{\nu} = 0$, a single accumulation point exists: a 1-cycle with $\varphi_n = \arccos(-a/\varepsilon)$. For another map example, see the discussion of the logistic map in [Strogatz (2024)]. In Fig. 6.5, the m-fold application of the circle map $\varphi_{n+m}(\varphi_n)$ is shown as colorful curves. Dots indicate phases for which $\varphi_{n+m}(\varphi_n) = \varphi_n$ and $|\partial\varphi_{n+m}/\partial\varphi_n| < 1$ holds. These are stable fixed points of the m-fold application of the circle map. Their values correspond to the accumulation points that can be identified in Fig. 6.4(c).

In the field of (quantum) synchronization, similar looking triangular-like shapes that indicate locking regimes are also called Arnold tongues, e.g., see Chs. 7 and 10. In Fig. 6.6(a) the final value of the radius r is shown depending on Δ and Ω. The regions above the dashed red curves correspond to time-independent radii while the striped region below the dashed red curves indicate solution with oscillating radius. A better quantity to identify oscillations is the standard deviation of $z/|z|$ shown in Fig. 6.6(b). Here, modulations of the radius are excluded. For both small Δ and Ω, the separatrix between static and oscillating solutions follows $\Omega = \Delta\sqrt{\gamma_1/2\gamma_2}$. For larger values of the drive strength, the amplitude of the oscillator deviates significantly from $r_0 = \sqrt{\gamma_1/2\gamma_2}$ leading to a change in the ratio Ω/Δ. To obtain an approximate expression for the separatrix between static and oscillating solutions, we perform a perturbation expansion of Eqs. (6.2.6) and (6.2.7) about $r = r_0$, cf. Ch. 8 of [Pikovsky and Rosenblum (2015)]. Let $r = r_0 + \epsilon r^{(1)}$ with $\epsilon = \Omega/\gamma_1 \ll 1$. Solving Eq. (6.2.6) to first order in ϵ yields $r^{(1)} = -\sin(\phi)$. Using this result, Eq. (6.2.7) can be approximated

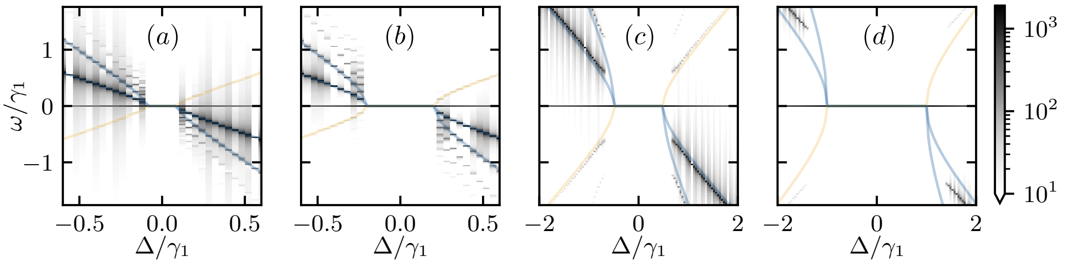

Figure 6.7: Spectra $|\mathcal{S}(\omega)|$ of Stuart-Landau oscillator, see Eq. (6.3.7). (a) $\Omega = 0.1\gamma_1$, $\gamma_2 = 0.5\gamma_1$. (b) $\Omega = 0.1\gamma_1$, $\gamma_2 = 2\gamma_1$. (c) $\Omega = 0.5\gamma_1$, $\gamma_2 = 0.5\gamma_1$. (d) $\Omega = 0.5\gamma_1$, $\gamma_2 = 2\gamma_1$. The orange (blue) curves in all panels correspond to integer multiples of $(-)\text{sign}(\Delta)\nu_A$.

to first order in ϵ as

$$\dot{\phi} = -\Delta - \Omega\sqrt{\frac{2\gamma_2}{\gamma_1}}\cos(\phi) - \Omega^2\frac{\gamma_2}{\gamma_1^2}\sin(2\phi)\,. \tag{6.3.3}$$

The last term shifts the location of the minimum of $\dot{\phi}$ to

$$\phi \approx \frac{\sqrt{(\gamma_1^3 + 16\gamma_2\Omega^2)} - \sqrt{\gamma_1^3}}{4\sqrt{2\gamma_2}\Omega} \approx \frac{\Omega}{r_0\gamma_1}\,. \tag{6.3.4}$$

At this value of the phase ϕ, its equation of motion

$$\dot{\phi} \approx -\Delta - \frac{\Omega}{r_0} - \sqrt{\frac{2\gamma_2^3}{\gamma_1^7}}\Omega^3\,, \tag{6.3.5}$$

vanishes for

$$\Omega \approx \gamma_1^{7/6}\frac{2(3\gamma_1^2)^{1/3} - (9\Delta + \sqrt{24\gamma_1^2 + 81\Delta^2})^{2/3}}{\sqrt{2\gamma_2}3^{2/3}(9\Delta + \sqrt{24\gamma_1^2 + 81\Delta^2})^{1/3}}\,. \tag{6.3.6}$$

This expression is visualized by the dashed red curves in Fig. 6.6.

Another way of identifying oscillating solutions is to compute the spectrum

$$\mathcal{S}(\omega) = \frac{1}{\sqrt{2\pi}}\int\limits_{\mathbb{R}} z(t)\mathrm{e}^{-\mathrm{i}\omega t}\mathrm{d}t \tag{6.3.7}$$

of z. If $z(t) = r\mathrm{e}^{\mathrm{i}\omega_0 t}$, the spectrum exhibits a single peak at $\omega = \omega_0$. In Fig. 6.7, spectra of the Stuart-Landau oscillator are presented together with the approximation ν_A defined in Eq. (6.2.9) evaluated for a fixed radius $r = 0$. The most dominant maxima of the spectra lie at $-\text{sign}(\Delta)\nu_A$ (blue curves) and correspond to the mean frequency of the solution of Adler's equation, see Eq. (6.2.8) and Figs. 6.3(c) and 6.3(d). Higher-frequency contributions of this solution are visible as less dominant maxima of the spectra at positive integer multiples of $-\text{sign}(\Delta)\nu_A$ (blue curves). The maxima at $\text{sign}(\Delta)\nu_A$ (orange curves) originate from the oscillation of the radii. The simplistic example $r = r_0 + \delta r \cos(\nu_A t)$ has two frequency contributions at $\pm\nu_A$. For small drive strengths, see Figs. 6.7(a) and 6.7(b), the approximation ν_A seems to be valid. For small drive strengths, however, see Figs. 6.7(c) and 6.7(d), the observed frequencies deviate from ν_A. For small detunings, a jump from zero to nonzero frequencies occur. The region of frequency locking is larger for oscillators with smaller radius (larger γ_2).

6.4 Phase Synchronization

In the last section, we saw that the Stuart-Landau oscillator exhibits regimes in which the observed frequency of oscillation in the rotating frame of an external drive is zero, i.e., the oscillator locks its frequency to the one of the drive. Outside this region, both radius and phase start to oscillate, see Figs. 6.6 and 6.7. To lowest order, the frequency of oscillation can be approximated by ν_A defined in Eq. (6.2.9). In this section, we will focus on the region in which frequency locking occurs. In particular, we want to answer the question: to which values does the phase of the oscillator lock? The locking of the phase of an oscillator to a particular value is called *phase synchronization*. We directly start with the equation of motion after a first perturbation expansion step, i.e., Eq. (6.3.3). For small drive strengths, the steady state of the phase to leading order in the drive strength is given by $\phi = -\arccos(-r\Delta/\Omega)$. For vanishing detuning $\Delta = 0$, the Stuart-Landau oscillator locks to $\phi = -\pi/2$. Note, that this value depends on the phase of the complex drive amplitude Ω: in general, the oscillator locks to $\phi = \arg(\Omega) - \pi/2$. Furthermore, at $\Delta = 0$, the slope $\partial\phi/\partial\Delta = -r/\Omega$ increases for oscillators with a larger radius. For larger drive strengths $\Omega > r_0\gamma_1$, Eq. (6.3.3) exhibits two new stable fixed points close to the now unstable fixed point $\phi = -\pi/2$. However, this perturbation expansion is invalid for values as large as $\Omega > r_0\gamma_1$. Studying the next order of correction, $r = r_0 + \epsilon r^{(1)} + \epsilon^2 r^{(2)}$ with

$$r^{(2)} = \frac{3}{2r_0}\sin^2(\phi)\,, \tag{6.4.1}$$

that leads to

$$\dot{\phi} = -\Delta - \Omega\sqrt{\frac{2\gamma_2}{\gamma_1}}\cos(\phi) - \Omega^2\frac{\gamma_2}{\gamma_1^2}\sin(2\phi) - \Omega^3\frac{5\gamma_2^2}{2r_0\gamma_1^3}\sin(2\phi)\sin(\phi)\,, \tag{6.4.2}$$

these new fixed points disappear again. Numerical simulations presented in Fig. 6.8 show only one stable fixed point of the phase. In Figs. 6.8(b) and 6.8(c), the thin red curves correspond to the steady-state solution $\phi = -\arccos(-r_0\Delta/\Omega)$ of Eq. (6.2.7) and the thick blue curves correspond to the steady-state solution of Eq. (6.4.2). For small drive strengths, see Fig. 6.8(b), and for large drive strengths, see Fig. 6.8(c), both approximations are good predictions of the numerically achieved values of the phase. Here, for small detuning, the red curve seems to be a better approximation than the blue one and for large detuning vice versa. Especially, for large detuning, their domains (regions of phase locking) and slopes at $\Delta = 0$ are different. Note that phase locking implies frequency locking. In general, the opposite is not true.

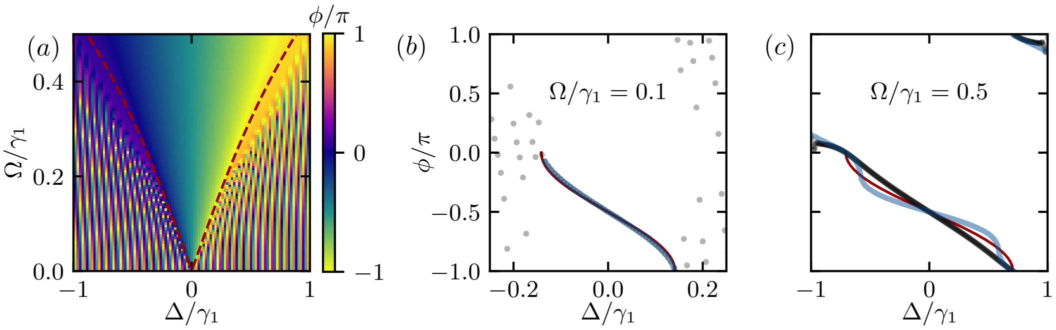

Figure 6.8: Phase locking of the driven Stuart-Landau oscillator. (a) Final value of the phase ϕ/π at $t\gamma_1 = 100$. Similar to Fig. 6.6(a), striped regions indicate time dependence of the phase. The dashed red curves correspond to Eq. (6.3.6), which is linear for small Δ: $\Omega = \Delta\sqrt{\gamma_1/2\gamma_2}$. (b), (c) Final values of the phase for particular values of the drive strength Ω (gray dots). The thin red curves correspond to the steady state of Eq. (6.2.7). The thick blue curves correspond to the steady state of Eq. (6.4.2).

6.5 Multiple Limit-Cycle Oscillators

So far, we have discussed the synchronization of individual limit cycle oscillators in the presence of an external drive. Now, we want to replace the drive, that can be interpreted as a perfectly stabilized oscillator, by other interacting oscillators. Let us start with two Stuart-Landau oscillators that are coupled

$$\dot{z}_A = -\mathrm{i}\omega_A z_A + \frac{\gamma_1^A}{2} z_A - \gamma_2^A |z_A|^2 z_A - \mathrm{i} g_{AB} z_B \,, \tag{6.5.1}$$

$$\dot{z}_B = -\mathrm{i}\omega_B z_B + \frac{\gamma_1^B}{2} z_B - \gamma_2^B |z_B|^2 z_B - \mathrm{i} g_{AB} z_A \,. \tag{6.5.2}$$

Here, ω_j are the eigenfrequencies of the oscillators with complex amplitude z_j and g_{AB} is the coupling strength. This coupling is reciprocal, meaning that the coupling of A to B is as strong as the coupling from B to A. We will break this symmetry in Ch. 9, where we discuss the publication [Kehrer and Bruder (2025)]. There, the nonreciprocal interactions result in various active states in the classical model. As exemplary references, see [Lotka (1925), Volterra (1926), Fruchart et al. (2021)].

Similar to Sec. 6.2.2, the equations of motion of both oscillators are split into amplitude and phase parts, $z_j = r_j \mathrm{e}^{\mathrm{i}\phi_j}$,

$$\dot{r}_j = \mathrm{Re}[\dot{z}_j \mathrm{e}^{-\mathrm{i}\phi_j}] = r_j \left(\frac{\gamma_1^j}{2} - \gamma_2^j r_j^2 \right) - g_{AB} r_i \sin(\phi_j - \phi_i) \,, \tag{6.5.3}$$

$$\dot{\phi} = \mathrm{Im}[\dot{z}_j / z_j] = -\omega_j - g_{AB} \frac{r_i}{r_j} \cos(\phi_j - \phi_i) \,, \tag{6.5.4}$$

with $i, j = A, B$ and $i \neq j$. Due to the U(1) symmetry of Eqs. (6.5.1) and (6.5.2), i.e., invariance under the time-independent transformation $z_j \to z_j \mathrm{e}^{\mathrm{i}\theta}$, the equations of motion depend on the phase difference $\phi_{AB} = \phi_A - \phi_B$ and not on the individual phases. Thus, let us define the equation of motion of ϕ_{AB}, also called *relative phase*,

$$\dot{\phi}_{AB} = -\Delta - g_{AB}\left(\frac{r_B}{r_A} - \frac{r_A}{r_B}\right)\cos(\phi_{AB})\,, \tag{6.5.5}$$

where $\Delta = \omega_A - \omega_B$. This equation looks similar to the equation of motion of a driven Stuart-Landau oscillator, Eq. (6.2.7), where the coupling g_{AB} together with the radii takes the role of the drive strength Ω. In general, the gain and damping rates of the oscillators are different and lead to steady-state amplitudes $\sqrt{\gamma_1^j/2\gamma_2^j}$. Furthermore, the relative phase locks to a single value. However, if the rates are chosen to be equal, the coupling term in Eq. (6.5.5) vanishes resulting in the absence of phase locking to a single value. This so-called *synchronization blockade* that is observed in quantum systems [Lee and Sadeghpour (2013), Roulet and Bruder (2018b)] and will be discussed later in Secs. 7.1.4 and 7.2.2 as well as Chs. 8 to 10, already shows up here for classical oscillators. In contrast to the suppression of phase locking to a single value, a second-order coupling survives that induces bistable locking, as we will see below. We have to take a closer look at the equations of motion and perform a perturbation expansion about the steady-state amplitudes $r_j = \sqrt{\gamma_1^j/2\gamma_2^j} + \epsilon r_j^{(1)}$, where $\epsilon = g_{AB}/\gamma_1^A$ and

$$r_A^{(1)} = -\sqrt{\frac{\gamma_1^B}{2\gamma_2^B}}\sin(\phi_{AB}) = -\sqrt{\frac{\gamma_2^A}{\gamma_2^B}}\left(\frac{\gamma_1^B}{\gamma_1^A}\right)^{3/2} r_B^{(1)}\,. \tag{6.5.6}$$

Inserting this correction in Eq. (6.5.5), the equation of motion of the relative phase becomes

$$\begin{aligned}\dot{\phi}_{AB} =& -\Delta - g_{AB}\sqrt{\frac{\gamma_1^A\gamma_1^B}{\gamma_2^A\gamma_2^B}}\left(\frac{\gamma_2^A}{\gamma_1^A} - \frac{\gamma_2^B}{\gamma_1^B}\right)\cos(\phi_{AB})\\ &- \frac{g_{AB}^2}{2}\left(\frac{1}{\gamma_1^A} + \frac{1}{\gamma_1^B} + \frac{\gamma_1^A\gamma_2^B}{\gamma_2^A(\gamma_1^B)^2} + \frac{\gamma_2^A\gamma_1^B}{(\gamma_1^A)^2\gamma_2^B}\right)\sin(2\phi_{AB})\,.\end{aligned} \tag{6.5.7}$$

If the cos term vanishes and the sin term remains, the steady state exhibits two possible values of ϕ_{AB}. In contrast to phase locking, this feature is called *bistable locking*, meaning that ϕ_{AB} can lock to two values with equal probability. To gain insights about the blockades, the number of free parameters has to be reduced. This can be done in different ways.

6.5.1 Equal Rate Ratios

The first simplification one can choose is to fix the ratio between gain and damping rate of both oscillators $\gamma_1^A/\gamma_2^A = \gamma_1^B/\gamma_2^B = \lambda$. This choice of rates leads to the vanishing of the cos term in Eq. (6.5.7), naively speaking, since the lowest-order steady-state radii

$r_j = \sqrt{\lambda/2}$ are equal. The remaining equation is

$$\dot{\phi}_{AB} = -\,\Delta - g_{AB}^2 \frac{\gamma_1^A + \gamma_1^B}{\gamma_1^A \gamma_1^B} \sin(2\phi_{AB})\,, \tag{6.5.8}$$

and exhibits two stable solutions $\phi_{AB}, \pi + \phi_{AB} = -\arcsin\bigl(\gamma_1^A\gamma_1^B\Delta/(\gamma_1^A+\gamma_1^B)g_{AB}^2\bigr)/2$ for $|\Delta| < g_{AB}^2(\gamma_1^A+\gamma_1^B)/\gamma_1^A\gamma_1^B$. Note that the value of the steady-state phase does not depend on λ.

6.5.2 Identical Oscillators

The next choice we often call the case of 'identical oscillators'. Here, we choose the same gain rate and the same damping rate for every oscillator: $\gamma_1^A = \gamma_1^B$ and $\gamma_2^A = \gamma_2^B$. Similar to the previous section about equal rate *ratios*, the remaining terms of Eq. (6.5.7) are

$$\dot{\phi}_{AB} = -\,\Delta - g_{AB}^2 \frac{2}{\gamma_1^A} \sin(2\phi_{AB})\,. \tag{6.5.9}$$

This equation can be obtained by setting $\gamma_1^A = \gamma_1^B$ in Eq. (6.5.8) and also exhibits two stable solutions $\phi_{AB}, \pi + \phi_{AB} = -\arcsin\bigl(\gamma_1^A\Delta/2g_{AB}^2\bigr)/2$ for $|\Delta| < 2g_{AB}^2/\gamma_1^A$.

6.5.3 Almost Identical Oscillators

In Eq. (6.5.5), we saw that if the oscillators have different gain and damping rates, the relative phase locks to a single value. In contrast, if the oscillators have identical rates or the ratio of gain versus damping is identical, the synchronization blockade and bistable locking occurs, see Eqs. (6.5.8) and (6.5.9). A remaining question is: when does the transition from locking to bistable locking occur? In Ch. 9, we will answer this question for quantum van der Pol oscillators.

To identify the transition in the classical case, let us choose different oscillators with rates $\gamma_1^A = \gamma_1^B$ and $\gamma_2^A \neq \gamma_2^B$. There is one free parameter γ_2^B/γ_2^A left that can be used to tune between phase locking and bistable locking. For $\Delta = 0$, $\phi_{AB} = \pm\pi/2$ are fixed points. If $g_{AB} < \gamma_1^A\sqrt{\gamma_2^A\gamma_2^B}|\gamma_2^A - \gamma_2^B|/(\gamma_2^A+\gamma_2^B)^2$, these two are the only fixed points of which $\phi_{AB} = (-)\pi/2$ is stable for $\gamma_2^B > \gamma_2^A$ ($\gamma_2^B < \gamma_2^A$). If $g_{AB} > \gamma_1^A\sqrt{\gamma_2^A\gamma_2^B}|\gamma_2^A - \gamma_2^B|/(\gamma_2^A+\gamma_2^B)^2$ two new fixed points $\phi_{AB}, \pi - \phi_{AB} = -\arcsin\left(\gamma_1^A\sqrt{\gamma_2^A\gamma_2^B}(\gamma_2^A - \gamma_2^B)/(\gamma_2^A+\gamma_2^B)^2\right)$ emerge in the vicinity of the stable one of $\phi_{AB} = \pm\pi/2$. In Fig. 6.9(a), the approximation Eq. (6.5.7) is shown. The histogram of final values of the relative phase after a duration of $t\gamma_1^A = 500$ of numerical simulations of 20 random initializations per g_{AB} leads to a similar bifurcation around the predicted value of g_{AB}, see Fig. 6.9(b). A special Arnold tongue is presented in Fig. 6.9(c). Here three regions can be distinguished. For large detuning Δ (checkered colorful region), the oscillators do not synchronize such that their relative phase takes every possible value. For small detuning Δ and large coupling (checkered two-colored

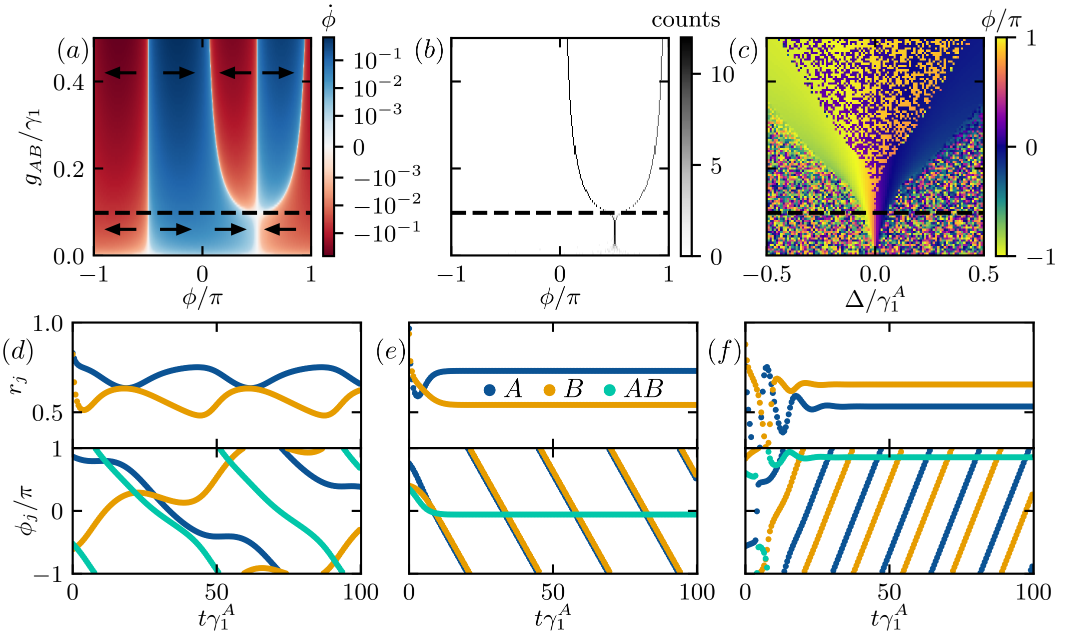

Figure 6.9: Phase locking of two Stuart-Landau oscillators with $\gamma_1^A = \gamma_1^B$ and $\gamma_2^B/\gamma_2^A = 1.5$. (a) Plot of $\dot{\phi}_{AB}$ based on Eq. (6.5.7), i.e., pitchfork bifurcation mentioned in Sec. 6.2. The arrows indicate the flow direction of time evolutions of the relative phase, i.e., they point toward stable fixed points. The color is scaled linear in the interval $[-10^{-3}, 10^{-3}]$ and logarithmic elsewhere. (b) Histogram for each value of g_{AB} of final values of the relative phase after a duration of $t\gamma_1^A = 500$ of numerical simulations of 20 random initializations with 200 bins in ϕ. (c) Arnold tongue based on the final values of the relative phase after a duration of $t\gamma_1^A = 500$. Each pixel corresponds to a random initialization. The dashed black line in panels (a), (b), and (c) corresponds to the approximation of the onset of bistable locking $g_{AB} = \gamma_1^A \sqrt{\gamma_2^A \gamma_2^B} |\gamma_2^A - \gamma_2^B| / (\gamma_2^A + \gamma_2^B)^2$. (d), (e), (f) Time evolutions for $\Delta = 0.15\gamma_1^A$ and $g_{AB}/\gamma_1^A = 0.1, 0.2, 0.4$ (from left to right), i.e., examples of each of the three regions in panel (c). All examples are time dependent, whereas in panel (e) and (f), the relative phase ϕ_{AB} is time independent: (bistable) locking of the relative phase.

region), the oscillators do synchronize and their relative phase takes two possible values, i.e., see the discussion about bistable locking in the previous paragraphs. Since $\gamma_2^B/\gamma_1^B = 1.5 \neq 1$, there exists a third region (smooth strips) in which only one value of the relative phase is attained.

Time evolutions for $\Delta = 0.2\gamma_1^A$ and $g_{AB}/\gamma_1^A = 0.1, 0.2, 0.4$ (from left to right), i.e., for each of the three regions, are presented in Figs. 6.9(d) to 6.9(f). All examples are time-dependent solutions. The solutions in Figs. 6.9(e) and 6.9(f) exhibit time-independent radii and relative phases but time-dependent individual phases ϕ_A and ϕ_B. Such states are called *traveling-wave states*. Note that in general, the two steady-state values of the relative phase depend on the complex phase of the coupling g_{AB}: $\phi_{AB} = \arg(g_{AB}), \arg(g_{AB}) + \pi$. Here, we chose $\arg(g_{AB}) = 0$. A different choice $\arg(g_{AB}) = -\pi/2$ is discussed in Ch. 9.

Since the solutions are time-dependent, we want to know more about the oscillation frequencies. Using Eq. (6.3.7), we obtain the spectra $\mathcal{S}_j(\omega_j)$ of the oscillators and show them in Figs. 6.10(a) and 6.10(b). The spectrum of the relative phase shown in

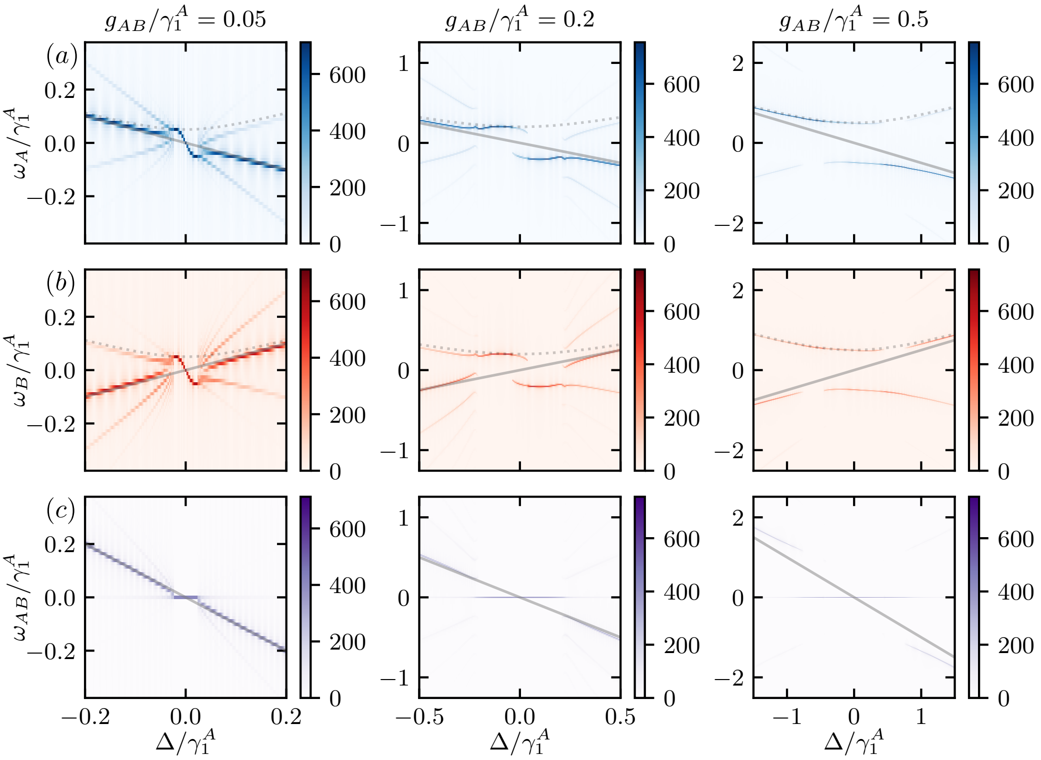

Figure 6.10: Spectra of two Stuart-Landau oscillators with $\gamma_1^A = \gamma_1^B$ and $\gamma_2^B/\gamma_2^A = 1.5$ averaged over 20 random realizations within $t\gamma_1^A \in [500, 1000]$. The three columns of this figure correspond to horizontal line cuts of Fig. 6.9(c). (a) Spectra $|\mathcal{S}_A(\omega_A)|$ of oscillator A. The gray line indicates $\omega_A = -\Delta/2$. (a) Spectra $|\mathcal{S}_B(\omega_B)|$ of oscillator B. The gray line indicates $\omega_B = \Delta/2$. The dotted curve in both panels (a) and (b) corresponds to $\omega_j = \sqrt{g_{AB}^2 + (\Delta/2)^2}$. For the definition of the spectrum for a single oscillator see Eq. (6.3.7). (c) Spectra $|\mathcal{S}_{AB}(\omega_{AB})|$ of the relative phase ϕ_{AB}, see Eq. (6.5.10). The gray line corresponds to $\omega_{AB} = -\Delta$.

Fig. 6.10(c) is defined by

$$\mathcal{S}_{AB}(\omega_{AB}) = \frac{1}{\sqrt{2\pi}} \int_{\mathbb{R}} z_A(t) z_B^*(t) \mathrm{e}^{-\mathrm{i}\omega_{AB}t} \mathrm{d}t \,. \tag{6.5.10}$$

The three columns of Fig. 6.10 correspond to horizontal line cuts of Fig. 6.9(c). The first column of Fig. 6.10 shows two regions. For small $|\Delta|$, both oscillators exhibit the same frequency, i.e., $\omega_{AB} = 0$. For large $|\Delta|$, the observed frequency of oscillator A (B) is $\omega_A = -\Delta/2$ ($\omega_B = \Delta/2$), i.e., $\omega_{AB} = \Delta$. In the remaining two columns of Fig. 6.10 three regions can be identified. For small $|\Delta|$, two oscillation frequencies for both oscillators are visible, i.e., bistable locking of frequency and phase. However, since $\omega_{AB} = 0$, the oscillators always choose identical frequencies $\omega_j \approx \sqrt{g_{AB}^2 + (\Delta/2)^2}$. Moreover, the value of the relative phase is correlated with the sign of the observed frequency: $\phi_{AB} = 0 \leftrightarrow \omega_{AB} < 0$ and $\phi_{AB} = \pi \leftrightarrow \omega_{AB} > 0$. This is the reason, why we often consider bistable phase locking as an indicator for traveling-wave states. For a bit larger $|\Delta|$, only one frequency to which both oscillators lock is visible. This region corresponds to the smooth stripes in Fig. 6.9(c). For a large $|\Delta|$, the observed frequency of oscillator A (B) is $\omega_A = -\Delta/2$ ($\omega_B = \Delta/2$), i.e., $\omega_{AB} = \Delta$. Even if this seems to be a simple model of two amplitude oscillators, interesting active states with locking of frequency and relative phase emerge. Similar results are obtained for two groups of active quantum spins in [Nadolny et al. (2025a)].

In Ch. 9, we will study similar classical oscillators and their quantum analogues. There, the interactions are nonreciprocal and can be tuned to be unidirectional. Besides traveling waves, other active states will occur. For a thorough study of nonreciprocal phase transitions see [Fruchart et al. (2021)] and its supplemental material.

In Ch. 10, we will discuss oscillators whose phase space hosts *multiple* limit cycles and study their quantum analogues. These can be imagined intuitively by realizing multiple fixed points in Liénard systems defined in Eq. (6.2.1), where $f(x)$ is a highly-nonlinear function or by replacing the quadratic dependence on r in Eq. (6.2.6) by a suitable higher-order polynomial.

Bistable locking, e.g., two possible steady-state values of the relative phase of two oscillators, as presented on the previous pages, can also be generated by higher-order coupling terms. For $\dot{z}_A = -\mathrm{i}g_2 z_A^* z_B^2$, the resulting term for the equation of motion of the phase is $\dot{\phi}_A = -g_2 r_B^2 \cos(2\phi_{AB})$. An example for bistable locking of a single driven oscillator is a so-called squeezing drive $\dot{z} = -\mathrm{i}\Omega_2 z^*$ that leads to $\dot{\phi} = -\Omega_2 \cos(2\phi)$. In these cases, bistable locking occurs *natively* and not in a perturbative sense. Most often in (quantum) synchornization, linear interactions are considered as native. Therefore, bistable locking will occur in perturbation expansions and thus as an indicator for synchronization blockades.

In this section, we discussed the interplay of only two oscillators. For examples of studies on networks of oscillators see [Choe et al. (2010), Heinrich et al. (2011), Luccioli et al. (2012), Tumash et al. (2017)].

6.6 Swarmalators

When we discussed multiple coupled oscillators in the previous sections, we did not think about the physical implementation of the coupling: the oscillators only had internal degrees of freedom that were interacting with the ones of other oscillators. In reality, the coupling might be mediated by, e.g., springs or the Coulomb interaction. Remembering Huygens' clocks, the interaction might also be induced by friction. Most of these interactions can be interpreted as position-dependent forces or stemming from some position-dependent potential. So why not considering oscillators that move in space? This section serves as an outlook and inspiration for future work but is not relevant for the core of the following chapters.

By the work "Oscillators that synch and swarm" [O'Keeffe et al. (2017)], a new avenue in the field of synchronization and active matter was established: *swarmalators*. This section is based on [O'Keeffe et al. (2017)] and [Hughes (2024)].

The basic idea is to combine swarming [Couzin (2007), Sumpter (2010)] and phase synchronization. This is done by assigning a internal degree of freedom, i.e., a phase of oscillation ϕ, to agents that move in a two-dimensional space $\vec{x} \in \mathbb{R}^2$. These swarmalators obey the following equations of motion [O'Keeffe et al. (2017)],

$$\dot{\vec{x}}_j = \vec{v}_j + \frac{1}{N}\sum_{i\neq j}^{N}\left(\frac{\vec{x}_i - \vec{x}_j}{|\vec{x}_i - \vec{x}_j|}(A + J\cos(\phi_i - \phi_j)) - B\frac{\vec{x}_i - \vec{x}_j}{|\vec{x}_i - \vec{x}_j|^2}\right), \tag{6.6.1}$$

$$\dot{\phi}_j = \omega_j + \frac{K}{N}\sum_{i\neq j}^{N}\frac{\sin(\phi_i - \phi_j)}{|\vec{x}_i - \vec{x}_j|}. \tag{6.6.2}$$

The vector $\vec{x}_j$ denotes the 2D position and $\vec{v}_j$ the self-propulsion velocities of the jth swarmalator. The phase ϕ_j is the phase of the jth swarmalator that couples to the other swarmalators in a Kuramoto-like fashion with a distance-dependent strength $K/|\vec{x}_i - \vec{x}_j|$. Similar to the Kuramoto model, ω_j are the eigenfrequencies of the swarmalators. The first coupling term of Eq. (6.6.1) is always attractive for $A > J > 0$ and distance independent, whereas the second coupling term is always repulsive for $B > 0$ and decreases with distance. The larger J, the larger is the feedback of phase (anti)alignment on the attraction between swarmalators.

By setting $\vec{v}_j = \vec{v}$, we can go to the center of mass frame and subtract $\sum_j \dot{\vec{x}}_j/N = \vec{v}$ for the equations of motion: equivalent to $\vec{v}_j \to 0$. Similarly, we go to a rotating frame that is rotating at the mean frequency. If identical oscillators $\omega_j = \omega$ are considered, it is equivalent to set $\omega_j \to 0$. Rescaling space and time to unitless quantities, i.e., $\vec{x} \to \xi\vec{x}$ and $t \to \tau t$, leads to $\dot{\vec{x}} \to \dot{\vec{x}}\xi/\tau$. Therefore, we can replace $K\tau/\xi$ and $J\tau/\xi$ by new unitless quantities K and J too. Furthermore, for simplicity, we set $A\tau/\xi = B\tau/\xi^2 = 1$.

In the remaining parameter space (K, J), a phase diagram with beautiful steady states emerges, see Fig. 1 of [O'Keeffe et al. (2017)]. Representatives of each class of steady states are shown in Fig. 6.11, where each column corresponds to one state. Here, $N = 100$ are simulated for a duration of $t = 1000$. A video of this figure is available at [Kehrer (2025)][9]. To characterize the different classes of steady states, the Kuramoto order parameter R defined in Eq. (6.1.3) is used as well as another order parameter W,

$$W = |W|e^{i\Psi} = \begin{cases} W_+ & \text{for } |W_+| > |W_-|, \\ W_- & \text{for } |W_+| < |W_-|, \end{cases} \tag{6.6.3}$$

where

$$W_\pm = \frac{1}{N}\sum_{j=1}^{N} e^{i(\varphi_j \pm \phi_j)}. \tag{6.6.4}$$

The value of $|R| \in [0, 1]$ quantifies the level of phase synchronization among the swarmalators. The value of $|W_\pm| \in [0, 1]$ indicates the (anti)correlation between the phase ϕ_j and the azimuthal angle φ_j of a swarmalator, i.e., the (anti)correlation

---

[9] Direct link: https://tobias-kehrer.github.io/thesis/swarmalators/ [Accessed: July 26, 2025]

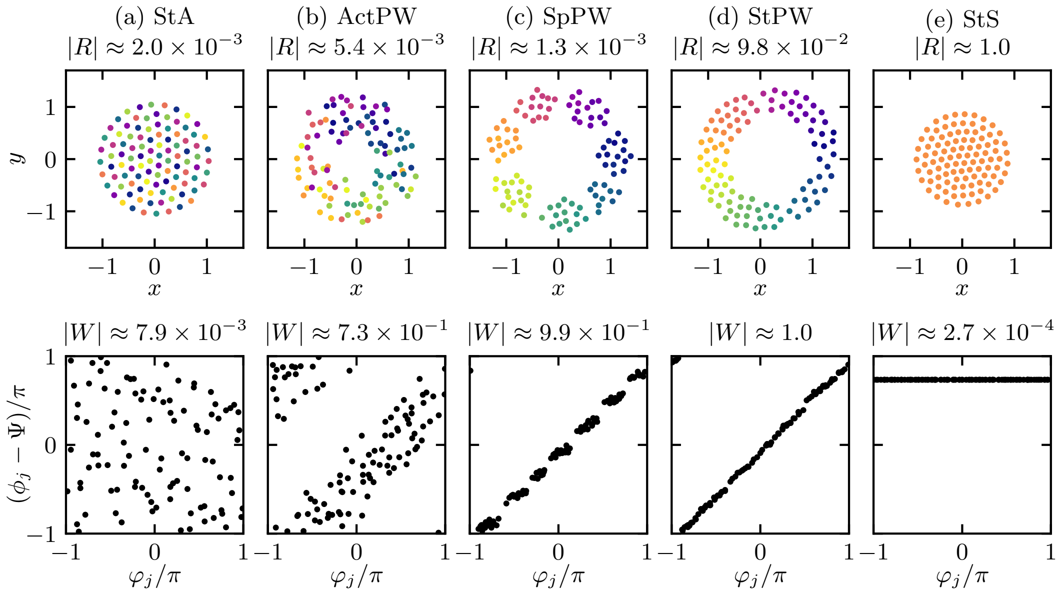

Figure 6.11: Classes of steady states of $N = 100$ swarmalators after a duration of $t = 1000$. The top row shows the steady states in 2D position space where the color corresponds to $\phi_j - \Psi$, i.e., the phase of each swarmalator subtracted by the complex phase of the order parameter W defined in Eq. (6.6.3). The order parameter R is the Kuramoto model order parameter defined in Eq. (6.1.3). The second row shows the correlation between the phase $\phi_j - \Psi$ of the swarmalators and their azimuthal angle φ_j. (a) Static Asynch (StA) for $(K, J) = (-0.8, 0.2)$. (b) Active Phase Wave (ActPW) for $(K, J) = (-0.8, 1)$. (c) Splintered Phase Wave (SpPW) for $(K, J) = (-0.1, 1)$. (d) Static Phase Wave (StPW) for $(K, J) = (0, 1)$. (e) Static Synch (StS) for $(K, J) = (0.1, 0.2)$. A video of this figure is available at [Kehrer (2025)].

between the internal degree of freedom and the position in space. For $K < 0$ the swarmalators want to antialign their phases ϕ_j. If additionally $K \lesssim -1.2J$, the resulting steady state exhibits both small $|R|$ and $|W|$, i.e., antialignment of phases and no correlation between ϕ_j and φ_j: *Static Aysnch* (StA) for $(K, J) = (-0.8, 0.2)$ in Fig. 6.11(a). If $-1.2J \lesssim K \lesssim -0.35J$, the swarmalators are actively moving and align on a ring where the phase shows (anti)correlation with the azimuthal angle: *Active Phase Wave* (ActPW) for $(K, J) = (-0.8, 1)$ in Fig. 6.11(b). If $-0.35J \lesssim K < 0$, the swarmalators arrange themselves into groups of approximately equal phase. In the groups that are aligned on a ring, the swarmalators are actively moving and exhibit (anti)correlation between ϕ_j and φ_j: *Splintered Phase Wave* (SpPW) for $(K, J) = (-0.1, 1)$ in Fig. 6.11(c). If $K = 0$, no phase dynamics take place and the swarmalators arrange themselves in a ring that shows high (anti)correlation between ϕ_j and φ_j: *Static Phase Wave* (StPW) for $(K, J) = (0, 1)$ in Fig. 6.11(d). If $K > 0$, the swarmalators want to align their phases ϕ_j resulting in a large value of $|R|$: *Static Synch* (StS) for $(K, J) = (0.1, 0.2)$ in Fig. 6.11(d). Since they arrange themselves in one group centered at the origin, $|W|$ is very small.

Several extensions of this model exist, e.g., swarmalators in 1D [O'Keeffe and Hong (2022)] and 3D [O'Keeffe et al. (2017)], more internal degrees of freedom [Yadav

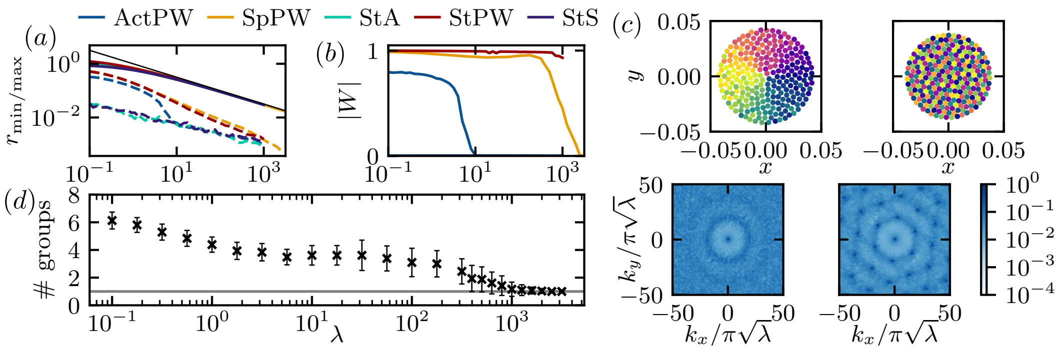

Figure 6.12: Overview of effects due to the pseudo force λ (preliminary data). (a) Minimum (dashed) and maximum (solid) distance of swarmalators from the center for several steady states. The black line corresponds to $1/\sqrt{\lambda}$. (b) Order parameter $|W|$ defined in Eq. (6.6.3). (c) Top row: steady states for $(K, J) = (-0.1, 1)$ and $\lambda = 10^{2.7}, 10^{2.8}$ (left to right). Bottom row: corresponding spatial Fourier transformations defined in Eq. (6.6.5). (d) Number of groups in SpPW steady states. The gray line indicates the minimum of one group. The data shown in (a), (b), and (d) are averaged over 31 random initializations.

et al. (2024)], and delayed interactions [Blum et al. (2024)]. In [Lizarraga and Aguiar (2020)], a term $F\cos(\omega_s t - \phi_j)/|\vec{x}_0 - \vec{x}_j|$ is added to $\dot{\phi}_j$ and acts as an external seed for frequency and phase synchronization. This force natively only modifies the phase dynamics, however, due to the backaction of phase synchronization on the spatial attraction in Eq. (6.6.1), swarmalators that synchronize with the seed move closer to $\vec{x}_0$. In the yet-unpublished work presented in [Hughes (2024)], we add a pseudo-force term $\lambda(\vec{x}_0 - \vec{x}_j)$ to $\dot{\vec{x}}_j$. In [Fetecau et al. (2011)], a linear attraction $\propto \vec{x}_i - \vec{x}_j$ between members of a swarm is considered, which leads to a $\propto 1/\sqrt{1+J}$ scaling of the disk radius of the StS state. As demonstrated in [O'Keeffe et al. (2017)], in this case, the inner and outer radii of StPW increase for larger J. In our pseudo-force extension model, a preliminary analysis shows: the radii of StS and StA, the inner and outer radii of StPW, SpPW, and ActPW as well as the number of groups in SpPW *decrease* for increasing λ, see Figs. 6.12(a) and 6.12(d). Furthermore, for $K < 0$, the states ActPW, SpPW, and StPW transition to StA for large enough values of λ, see Figs. 6.12(b) and 6.12(c). Inspired by the usage of the term "crystal" for StS and StA in [O'Keeffe et al. (2017)], we defined another indicator $\mathcal{F}$ that is based on the spatial Fourier transform,

$$\mathcal{F}(\vec{k}) = \frac{1}{N}\sum_{j=1}^{N} \mathrm{e}^{-\mathrm{i}\vec{k}\vec{x}_j} \,. \tag{6.6.5}$$

If the swarmalators align themselves in a highly symmetric pattern, only few spatial frequencies appear in the spectrum. The more order, the fewer spatial frequencies with larger local maxima in the spectrum, see Fig. 6.12(c).

With the combination of spatial swarming and phase synchronization, i.e., swarmalators, I would like to conclude this chapter on synchronization of classical oscillators. In the next chapter, the quantum analogue of synchronization will be introduced.

Chapter 7

Quantum Synchronization

Succeeding the previous chapter on classical synchronization – from the Kuramoto model over the Stuart-Landau oscillator to swarmalators – we now focus on the main topic of this second part of the thesis: *quantum synchronization*. This relatively young field took off by considering quantized self-sustained oscillators in [Lee and Sadeghpour (2013)] even if the term "quantum synchronization" has been introduced earlier in [Zhirov and Shepelyansky (2006)]. The model that is also one of the protagonists of this thesis, called the *quantum van der Pol* oscillator, became the standard example of quantum synchronization. As mentioned at the end of Sec. 6.2.1, the quantum van der Pol oscillator is rather the quantum analogue of the classical Stuart-Landau oscillator. However, in this thesis, we will stick to the widely used terminology "quantum van der Pol" while keeping in mind the maybe more adequate term "quantum Stuart-Landau". The quantum van der Pol oscillator will be discussed in Sec. 7.1.2. The following paragraph is based on the introductions of the publications [Kehrer et al. (2024b), Kehrer and Bruder (2025), Kehrer et al. (2025)].

Over the years, many different types of quantum oscillators have been studied. Examples are harmonic-oscillator-like (infinite-level) oscillators [Ludwig and Marquardt (2013), Lee and Sadeghpour (2013), Lörch et al. (2014), Walter et al. (2015), Davis-Tilley and Armour (2016), Weiss et al. (2017), Amitai et al. (2017), Es'haqi-Sani et al. (2020), Chia et al. (2020), Ben Arosh et al. (2021), Wächtler and Platero (2023)] and spin-like (few-level) models [Roulet and Bruder (2018a), Cabot et al. (2019), Parra-López and Bergli (2020), Cabot et al. (2021)]. Also many-body scenarios have been considered [Manzano et al. (2013), Xu et al. (2014), Zhu et al. (2015), Roth and Hammerer (2016), Nadolny et al. (2025a)]. These scenarios have in common that incoherent gain and damping stabilize a particular steady state. In addition to stabilization, these states have to feature a free phase which is ideally uniformly distributed, i.e., the oscillator does not exhibit phase preference. To realize synchronization, this symmetry is broken and a particular value or multiple discrete values of the phase are preferred. In contrast to classical synchronization, where phase locking is often equal to Dirac-δ-like probability distributions, the term "phase locking" in quantum synchronization is used when the probability distribution of the phase exhibits a global maximum. We say "the quantum oscillator locks to ϕ_0" when the synchronization measure of the phase exhibits a global maximum at ϕ_0. In a similar way, multi-stable locking occurs when the global maximum is degenerate, i.e., multiple local maxima of identical value coincide with the global maximum.

One starting point in a top-down approach to quantum synchronization is to canonically quantize classical limit cycle systems [Chia et al. (2020), Ben Arosh et al. (2021), Chia et al. (2025)] and study the resulting system in the quantum limit of few excitations. Some unique quantum features are related to entanglement [Giorgi et al. (2012), Mari et al. (2013), Lee et al. (2014), Ameri et al. (2015), Yin et al. (2017), Roulet and Bruder (2018b), He et al. (2024)] or interference [Roulet and Bruder (2018a), Roulet and Bruder (2018b)] and manifest in the unexpected occurrence or suppression of frequency locking [Walter et al. (2014), Lörch et al. (2016)] and phase locking [Lörch et al. (2017), Roulet and Bruder (2018a)]. In particular, the suppression of classical synchronization is called a synchronization blockade, see Ch. 6. In quantum analogues of limit-cycle oscillators, blockades [Solanki et al. (2023)] are observed in similar but also different cases. Examples of unique quantum blockades are the quantum interference blockade of a driven spin-1 [Roulet and Bruder (2018a)] and the energy quantization blockade [Lörch et al. (2017)].

Quantum synchronization is also studied in more exotic scenarios like chimera states [Bastidas et al. (2015), Viennot and Aubourg (2016)], nonlinear interactions [Thomas and Senthilvelan (2022)], and nonlinear driving [Sonar et al. (2018)]. Furthermore, quantum synchronization is in some aspects related to quantum sensing [Vaidya et al. (2025)], quantum thermodynamics [Jaseem et al. (2020b), Solanki et al. (2022), Aifer et al. (2024)], and time-crystals [Hajdušek et al. (2022), Buča et al. (2022), Solanki et al. (2024)].

First steps toward experimental realization have been taken on several platforms including cold atoms [Laskar et al. (2020)], nuclear spins [Krithika et al. (2022)], trapped-ions [Behrle et al. (2023), Zhang et al. (2023)], and superconducting circuits [Koppenhöfer et al. (2020), Tao et al. (2025)].

In the following sections, the fundamental aspects of quantum synchronization of infinite-level and few-level oscillators will be presented. This serves as a preparation for Chs. 8 to 10 where the publications [Kehrer et al. (2024b), Kehrer and Bruder (2025), Kehrer et al. (2025)] will be presented.

7.1 Infinite-Level Quantum Oscillators

The standard example of a quantum limit-cycle oscillator is based on the quantum harmonic oscillator. A key property of the classical harmonic oscillator is that its phase space exhibits an infinite number of closed orbits. To obtain a stabilized quantum limit cycle, gain and damping terms, e.g., incoherent Lindbladian jump processes, have to be introduced. Once such a limit cycle is prepared, it can be synchronized to external quantum signals or other quantum limit cycles.

7.1.1 Synchronization Measures

A crucial aspect of quantum synchronization is the definition of suitable synchronization measures. Various types of measures have been considered in the literature. Some of them are constructed by projections onto particular states [Barak and Ben-Aryeh (2005), Hush et al. (2015), Weiss et al. (2016), Roulet and Bruder (2018a)], others are based on entanglement [Ameri et al. (2015)] or distances in phase space [Mari et al. (2013)]. In the following, a selection of common measures that quantify synchronization is presented. These are in some sense measures of localization in phase space. To get an intuition for the features of the different measures of synchronization, let us evaluate them for coherent states $\left|\alpha = r\mathrm{e}^{\mathrm{i}\phi}\right\rangle$ defined in Eq. (2.4.4). Using $(\Delta a)^2 = \langle a^2\rangle - \langle a\rangle^2 = 0$, the variance of position $X = (a^\dagger + a)/2$ and momentum $P = \mathrm{i}(a^\dagger - a)/2$ operators

$$(\Delta X)^2 = \langle X^2\rangle - \langle X\rangle^2 = \frac{1}{4}(\alpha^{*2} + \alpha^2 + \langle a^\dagger a + aa^\dagger\rangle - \alpha^{*2} - \alpha^2 - 2\alpha\alpha^*) = \frac{1}{4}\,, \tag{7.1.1}$$

$$(\Delta P)^2 = \langle P^2\rangle - \langle P\rangle^2 = \frac{1}{4}(-\alpha^{*2} - \alpha^2 + \langle a^\dagger a + aa^\dagger\rangle + \alpha^{*2} + \alpha^2 - 2\alpha\alpha^*) = \frac{1}{4}\,, \tag{7.1.2}$$

reduces to the simple equation $\Delta X = \Delta P = 1/2$. The Gaussian width of a coherent state $|\alpha\rangle$ in phase space is constant. Therefore, the variance $(\Delta\phi)^2$ of the phase

$$\phi = \arg(\alpha) = \arctan(\langle P\rangle/\langle X\rangle)\,, \tag{7.1.3}$$

that is approximated by

$$(\Delta\phi)^2 = \left(\frac{\partial\phi}{\partial\langle X\rangle}\Delta X\right)^2 + \left(\frac{\partial\phi}{\partial\langle P\rangle}\Delta P\right)^2 = \frac{1}{2|\alpha|^2}\,, \tag{7.1.4}$$

is decreasing for increasing $|\alpha|$. This means that a coherent state $|\alpha\rangle$ is more phase localized than $|\beta\rangle$ if $|\alpha| > |\beta|$. Intuitively, one can rephrase it as: since the noise in position and momentum is constant, for larger $|\alpha|$, a smaller fraction of the circumference at $r = |\alpha|$ is covered by the Gaussian blob of the coherent state.

The computationally simple measure

$$S' = \frac{\langle a\rangle}{\sqrt{\langle a^\dagger a\rangle}}\,, \tag{7.1.5}$$

presented in [Weiss et al. (2016)], effectively measures the ‘coherent-stateness’ of a state. Evaluated for coherent states, it reduces to the complex phase factor $S' = \alpha/|\alpha| = \mathrm{e}^{\mathrm{i}\phi}$. The fact that it is not depending on $|\alpha|$ results in the issue that a coherent state infinitesimally close to the origin ($|\alpha| \ll 1$) is assigned to the same level of phase localization as a coherent state far away from the origin ($|\alpha| \gg 1$). This, however, contradicts the intuition gained by Eq. (7.1.4).

Another measure P_1, which will be used in Chs. 9 and 10 that are based on [Kehrer and Bruder (2025), Kehrer et al. (2025)], is defined as the projection of the density matrix ρ onto phase states [Barak and Ben-Aryeh (2005), Hush et al. (2015)],

$$|\phi\rangle = \frac{1}{\sqrt{2\pi}} \sum_{n=0}^{\infty} \mathrm{e}^{in\phi} |n\rangle \ , \tag{7.1.6}$$

where $|n\rangle$ are Fock basis states. This measure,

$$P_1(\phi) = \langle\phi| \rho |\phi\rangle - \frac{1}{2\pi} = \frac{1}{2\pi} \sum_{n,m=0}^{\infty} \mathrm{e}^{\mathrm{i}(m-n)\phi} \langle n| \rho |m\rangle - \frac{1}{2\pi} \, , \tag{7.1.7}$$

can be interpreted as the deviation of the probability distribution $\langle\phi| \rho |\phi\rangle$ of the phase ϕ from a uniform distribution. It can be rewritten in terms of constant $k = m - n$,

$$P_1(\phi) = \frac{1}{2\pi} \sum_{k=1}^{\infty} \sum_{n=0}^{\infty} (\mathrm{e}^{\mathrm{i}k\phi} \langle n| \rho |n+k\rangle + \mathrm{e}^{-\mathrm{i}k\phi} \langle n+k| \rho |n\rangle) \, . \tag{7.1.8}$$

The sum over n covers all matrix elements that lie on the kth off-diagonal. The contribution for $m - n = 0$ reduces to $\mathrm{Tr}[\rho]/2\pi = 1/2\pi$ and cancels the second term in Eq. (7.1.7). In [Kehrer and Bruder (2025)] presented in Ch. 9, the remaining expectation values in Eq. (7.1.8) are identified as expectation values of an operator. For coherent states $\left|\alpha = r\mathrm{e}^{\mathrm{i}\phi_0}\right\rangle$, the synchronization measure P_1 can be approximated in the following two limits

$$P_1(\phi) \overset{|\alpha|\ll 1}{\approx} \frac{|\alpha|}{\pi} \cos(\phi_0 - \phi) \, , \tag{7.1.9}$$

$$P_1(\phi) \overset{|\alpha|\gg 1}{\approx} \frac{1}{2\pi} \sum_{k=-\infty}^{\infty} \mathrm{e}^{\mathrm{i}k(\phi_0-\phi)} - \frac{1}{2\pi} = \delta(\phi_0 - \phi) - \frac{1}{2\pi} \, . \tag{7.1.10}$$

States are expected to show no synchronization if their phase noise covers a majority of 2π, e.g., coherent states that are close to the origin. Thus, it is not surprising that for coherent states close to the origin the first moment of P_1 dominates. In contrast, for $|\alpha| \gg 1$, the phase distribution P_1 diverges at ϕ_0 in the sense of a Dirac δ. To understand the scaling of the maximum of P_1 for large $|\alpha|$, we compute its derivative with respect to r at $\phi = \phi_0$. We use

$$\partial_r \left(\mathrm{e}^{-r^2} r^{k+2n}\right) = \mathrm{e}^{-r^2} r^{k+2n-1} (k + 2n - 2r^2) \, , \tag{7.1.11}$$

to obtain

$$\partial_r P_1(\phi_0) = \frac{\mathrm{e}^{-r^2}}{2\pi r} \sum_{k=1}^{\infty} \sum_{n=0}^{\infty} \frac{r^{k+2n}(k + 2n - 2r^2)}{n!\sqrt{(n+1)\dots(n+k)}} + \text{H.c.} \, . \tag{7.1.12}$$

We find numerical indications supporting $\partial_r P_1(\phi_0) \overset{r\gg 1}{\approx} \sqrt{2/\pi}$. The measure P_1 and

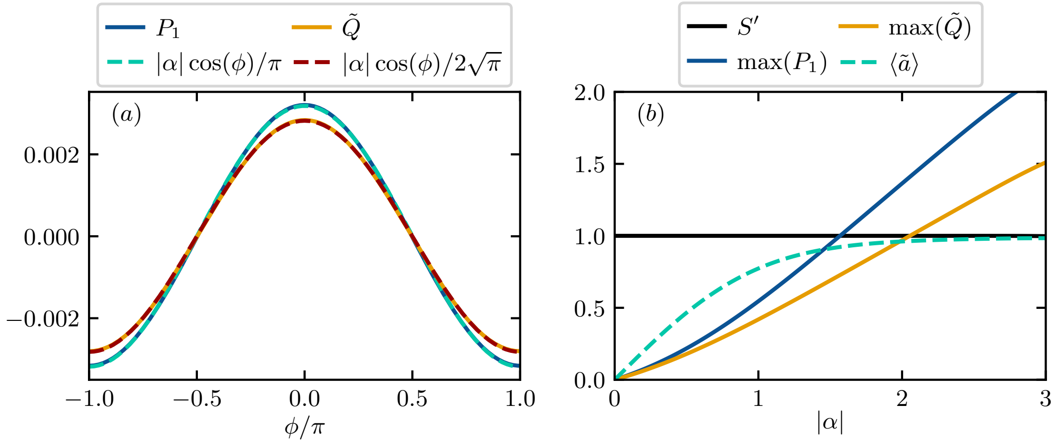

Figure 7.1: Comparison of synchronization measures for coherent states $|\alpha\rangle$. (a) Measures of states close to the origin, $\alpha = 0.01$, are dominated by their first momentum (dashed lines). (b) Large-$|\alpha|$ scaling of quantum synchronization measures.

its approximation given in Eq. (7.1.9) are shown in Fig. 7.1(a). The dependence of S', the maximum of P_1, and $\langle\alpha|\,\tilde{a}\,|\alpha\rangle$ on $|\alpha|$ is presented in Fig. 7.1(b).

Another widely used measure is the Husimi Q function defined in Eq. (2.4.13) as a projection of a state ρ onto coherent states. A phase synchronization measure can be obtained by integrating out the radial part of the coherent states

$$\left|\alpha = r\mathrm{e}^{\mathrm{i}\phi}\right\rangle = \mathrm{e}^{-r^2/2}\sum_{n=0}^{\infty}\frac{r^n}{\sqrt{n!}}\mathrm{e}^{\mathrm{i}n\phi}\,|n\rangle\ , \tag{7.1.13}$$

note the differences to Eq. (7.1.6). The phase synchronization measure $\tilde{Q}(\phi)$ is given by

$$\begin{aligned}\tilde{Q}(\phi) &= \frac{1}{\pi}\int_0^\infty \mathrm{d}r\, r \left\langle \alpha = r\mathrm{e}^{\mathrm{i}\phi}\right|\rho\left|\alpha = r\mathrm{e}^{\mathrm{i}\phi}\right\rangle - \frac{1}{2\pi}\\ &= \frac{1}{\pi}\int_0^\infty \mathrm{d}r\,\mathrm{e}^{-r^2}\sum_{n,m=0}^{\infty}\frac{r^{n+m+1}}{\sqrt{n!m!}}\mathrm{e}^{\mathrm{i}(m-n)\phi}\,\langle n|\,\rho\,|m\rangle - \frac{1}{2\pi}\\ &= \frac{1}{2\pi}\sum_{n,m=0}^{\infty}\frac{\Gamma\left(\frac{n+m}{2}+1\right)}{\sqrt{n!m!}}\mathrm{e}^{\mathrm{i}(m-n)\phi}\,\langle n|\,\rho\,|m\rangle - \frac{1}{2\pi}\,.\end{aligned} \tag{7.1.14}$$

In the last step we used Eq. (3.326.2) of [Gradshteyn and Ryzhik (2015)]. Similar to Eq. (7.1.8), $\tilde{Q}$ can be expressed in terms of equal $m - n = k$,

$$\tilde{Q}(\phi) = \frac{1}{2\pi}\sum_{k=1}^{\infty}\sum_{n=0}^{\infty}\frac{\Gamma\left(n+\frac{k}{2}+1\right)}{\sqrt{\Gamma(n+1)\Gamma(n+k+1)}}\mathrm{e}^{\mathrm{i}k\phi}\,\langle n|\,\rho\,|n+k\rangle + \text{H.c.}\,. \tag{7.1.15}$$

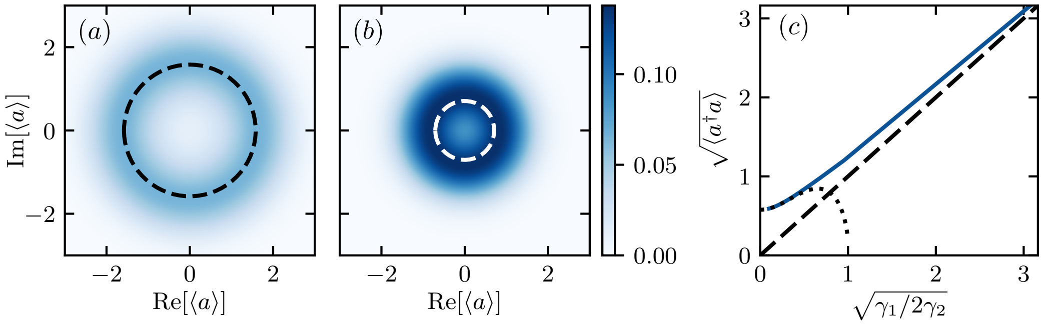

Figure 7.2: Quantum van der Pol steady states for $\Omega = 0$, see Eq. (7.1.17). (a), (b) Wigner functions for $\gamma_2/\gamma_1 = 0.2, 1$ (from left to right). The dashed rings correspond to the mean-field prediction of the radius $\sqrt{\gamma_1/2\gamma_2}$. (c) Expectation value $\sqrt{\langle a^\dagger a\rangle}$ evaluated for the steady state (blue curve) and the quantum limit ρ_q (dotted curve) defined in Eq. (7.1.23), compared to the mean-field prediction (dashed line).

For coherent states close to the origin, $\tilde{Q}$ reduces to

$$\tilde{Q}(\phi) \overset{|\alpha|\ll 1}{\approx} \frac{|\alpha|}{2\sqrt{\pi}} \cos(\phi_0 - \phi)\,. \tag{7.1.16}$$

We compare $\tilde{Q}$ with P_1 in Fig. 7.1.

7.1.2 Standard Quantum van der Pol Oscillator

The standard example of quantum synchronization, the quantum van der Pol oscillator was introduced in [Lee and Sadeghpour (2013)]. In the case of the classical Stuart-Landau oscillator, the infinite number of closed orbits in phase space of the harmonic oscillator is reduced to one by nonlinearities in the equation of motion, i.e., gain and damping. In the quantum case, these gain and damping terms are defined as Lindblad jump operators. This and the following two sections is based on [Lee and Sadeghpour (2013)].

The gain corresponds to incoherent single-phonon gain $L = a^\dagger$ and the damping originates from two-phonon loss $L = a^2$. The total Lindblad master equation reads

$$\frac{\mathrm{d}}{\mathrm{d}t}\rho = \dot{\rho} = -\mathrm{i}[H, \rho] + \gamma_1 \mathcal{D}[a^\dagger](\rho) + \gamma_2 \mathcal{D}[a^2](\rho)\,, \tag{7.1.17}$$

where a common Hamiltonian

$$H = \Delta a^\dagger a + K a^{\dagger 2} a^2 + \Omega a^\dagger + \Omega^* a \tag{7.1.18}$$

contains a coherent drive term of strength Ω, a detuning Δ, or a Kerr nonlinearity K. In Fig. 7.2, Wigner functions of two choices of γ_2/γ_1 are shown.

The corresponding mean-field equation is obtained from the Heisenberg equation of motion

$$\frac{\mathrm{d}}{\mathrm{d}t}a = -\mathrm{i}\Delta a - 2\mathrm{i}K a^\dagger a^2 - \mathrm{i}\Omega + \frac{\gamma_1}{2}a - \gamma_2 a^\dagger a^2 \,, \tag{7.1.19}$$

by performing a cumulant expansion of the expectation value to lowest order,

$$\frac{\mathrm{d}}{\mathrm{d}t}\langle a\rangle \approx -\mathrm{i}\Delta\langle a\rangle - 2\mathrm{i}K|\langle a\rangle|^2\langle a\rangle - \mathrm{i}\Omega + \frac{\gamma_1}{2}\langle a\rangle - \gamma_2|\langle a\rangle|^2\langle a\rangle \,. \tag{7.1.20}$$

To gain intuition of this equation of motion, it is useful to set $\langle a\rangle = r\mathrm{e}^{\mathrm{i}\phi}$ in order to split the amplitude part,

$$\dot{r} = \mathrm{Re}\left[\mathrm{e}^{-\mathrm{i}\phi}\frac{\mathrm{d}}{\mathrm{d}t}\langle a\rangle\right] = r\left(\frac{\gamma_1}{2} - \gamma_2 r^2\right) - |\Omega|\sin(\phi - \arg(\Omega))\,, \tag{7.1.21}$$

from the phase part,

$$\dot{\phi} = \mathrm{Im}\left[\frac{1}{\langle a\rangle}\frac{\mathrm{d}}{\mathrm{d}t}\langle a\rangle\right] = -\Delta - 2Kr^2 - \frac{|\Omega|}{r}\cos(\phi - \arg(\Omega))\,. \tag{7.1.22}$$

For vanishing drive strength $\Omega = 0$, the radial equation of motion is solved by $r_0 = \sqrt{\gamma_1/2\gamma_2}$. The larger the gain or the smaller the damping, the larger the amplitude of the resulting limit cycle, see Fig. 7.2(c). In the quantum limit $\lambda = \gamma_1/\gamma_2 \ll 1$, the Taylor expansion of the steady state for $\Omega = 0$ reads

$$\begin{aligned}\rho_q \approx &\left(\frac{3}{2} - \frac{5}{9}\lambda + \frac{31}{52}\lambda^2\right)|0\rangle\langle 0| + \left(\frac{1}{3} + \frac{2}{9}\lambda - \frac{25}{52}\lambda^2\right)|1\rangle\langle 1| \\ &+ \left(\frac{\lambda}{3} - \frac{5}{18}\lambda^2\right)|2\rangle\langle 2| + \frac{\lambda^2}{6}|3\rangle\langle 3| \,.\end{aligned} \tag{7.1.23}$$

The dotted curve in Fig. 7.2(c) corresponds to the radius $\sqrt{\mathrm{Tr}[a^\dagger a\rho_q]} \approx (3 + 4\lambda - 5\lambda^2)/3\sqrt{3}$ of the ring-like state evaluated in the quantum limit.

7.1.3 Quantum Synchronization of the Standard Quantum van der Pol Oscillator

In this section, we will present the synchronization of a single driven quantum van der Pol oscillator to an external coherent drive. In Fig. 7.3, we show the steady-state Wigner functions of a driven oscillator for $\Delta = K = 0$. From left to right we increase the order n of the drive term $\Omega(a^{\dagger n} + a^n)$ from $n = 1$ to $n = 4$. A squeezing drive $n = 2$ has been studied as an improvement of quantum synchronization [Sonar et al. (2018)] and also in the context of time crystals [Cabot et al. (2024)]. The number of local maxima in the Wigner function corresponds to n. Their locations are $\phi_k = n\arg(\Omega) - \pi/2n + k2\pi/n$ with $k \in \mathbb{Z}$.

Considering a standard coherent drive as studied in [Lee and Sadeghpour (2013)], the quantum analogue of an Arnold tongue presented in Fig. 6.6 is shown in Fig. 7.4. The first row corresponds to varying detuning Δ at $K = 0$ and the second row corresponds

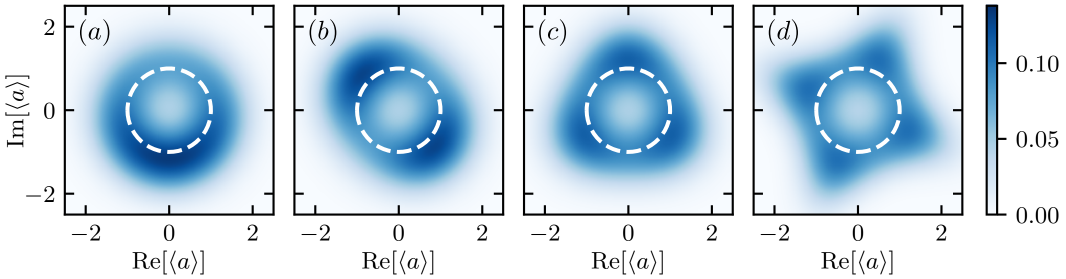

Figure 7.3: Wigner functions of a quantum van der Pol oscillator locking to a coherent drive $\Omega(a^{\dagger n} + a^n)$ with $n = 1, 2, 3, 4$ (from left to right for $\Delta = K = 0$ and $\gamma_2 = 0.5\gamma_1$). (a), (b) $\Omega = 0.1$. (c), (d) $\Omega = 0.05$. The dashed rings correspond to the mean-field prediction of the radius $\sqrt{\gamma_1/2\gamma_2}$. The number of local maxima corresponds to the order n of the drive.

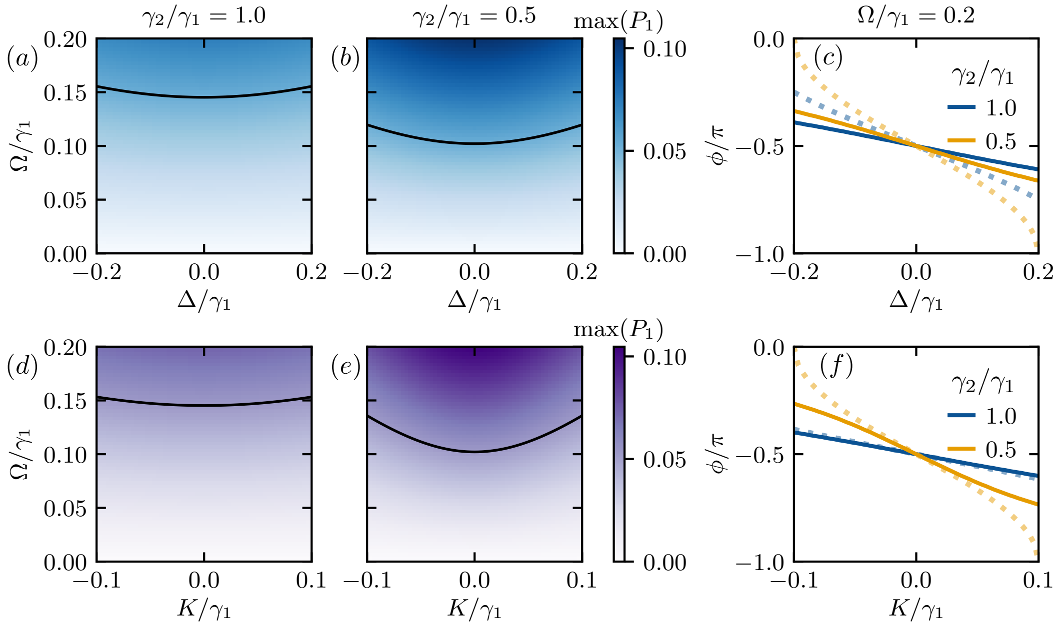

Figure 7.4: Phase locking of a coherently driven standard quantum van der Pol oscillator. In the top row we set $K = 0$ and in the bottom row we set $\Delta = 0$. (a), (b), (d), (e) Maximum of P_1 showing Arnold tongues, see Fig. 6.6. (c), (f) The solid curves correspond to the argmax of P_1 and the dotted curves to the mean-field prediction, see Eq. (7.1.22). The black curves denote contour lines at half the maximum value of the color scale.

to varying Kerr nonlinearity K at $\Delta = 0$. The mean-field steady-state solution of the phase is based on Eq. (7.1.22). For real-valued drive strengths Ω,

$$\phi_{\mathrm{MF}} = -\arccos\left(-\frac{r\Delta + 2r^3 K}{\Omega}\right), \tag{7.1.24}$$

solves $\dot{\phi} = 0$. This solution corresponds to the dotted lines in Figs. 7.4(c) and 7.4(f).

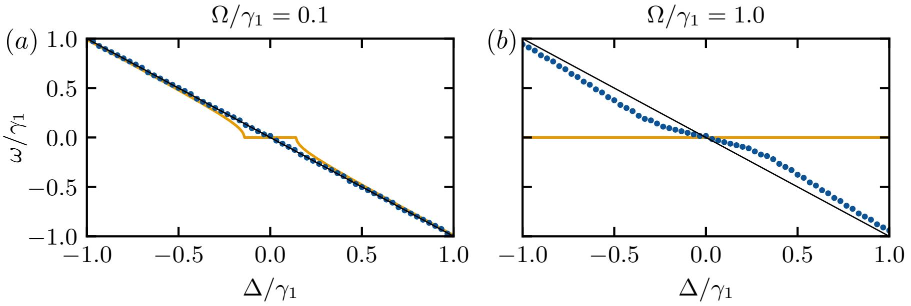

Figure 7.5: Frequency pulling of a coherently driven standard quantum van der Pol oscillator for $\gamma_2 = \gamma_1$. The blue dots correspond to the location of the frequency maxima of $\mathcal{S}$, see Eq. (7.1.27). (a) No influence of the drive on the oscillator frequency ω. (b) Frequency of the oscillator pulled toward $\omega = 0$ for small Δ. The solid curve corresponds to the classical case $\omega = -\nu_A$, see Eq. (6.2.9). The black line indicates $\omega = -\Delta$.

At $\Delta = K = 0$, the slope of ϕ_{MF} depending on both Δ and K increases with r,

$$\frac{\partial \phi_{\mathrm{MF}}}{\partial \Delta} = -\frac{r}{\Omega}\,, \tag{7.1.25}$$

$$\frac{\partial \phi_{\mathrm{MF}}}{\partial K} = -\frac{2r^3}{\Omega}\,. \tag{7.1.26}$$

This same qualitative behavior is found in the full quantum case (solid curves in Figs. 7.4(c) and 7.4(f)): the phase of the driven oscillator reacts stronger to detuning Δ and Kerr nonlinearity K for a *larger* radius of the limit cycle. Furthermore, for limit cycles with larger radii, the same value of $\max(P_1)$, see black curves in Fig. 7.4, is achieved for a smaller drive strength: larger limit cycles show *stronger* synchronization due to smaller relevance of noise.

In [Walter et al. (2014)], the spectra

$$\mathcal{S}(\omega) = \lim_{t\to\infty} \int_{-\infty}^{\infty} \mathrm{d}\tau\, \langle a^\dagger(t+\tau) a(\tau)\rangle \mathrm{e}^{\mathrm{i}\omega\tau}\,, \tag{7.1.27}$$

based on two-time correlations of driven quantum van der Pol oscillators have been studied. The frequency locking in the quantum case is much weaker than in the classical case shown in Fig. 6.7. Two examples for $\Omega/\gamma_1 = 0.1, 1$ for the choice $\gamma_2 = \gamma_1$ are presented in Fig. 7.5. In Fig. 7.5(a), no frequency locking plateau is visible compared to the one of the classical solution (solid curve). Only for larger drive strength considered in Fig. 7.5(b), the frequency of the quantum van der Pol is pulled toward $\omega = 0$ for small detunings. Remarkably, even if the frequency of the quantum oscillator is not altered drastically, phase synchronization is visible.

Intuitively speaking, in several aspects, the quantum van der Pol oscillator behaves similar to a classical Stuart-Landau oscillator with noise, e.g., sharp edges in Arnold tongues or spectra are smoothed out in the quantum case. True quantum features of synchronization are hard to find.

7.1.4 Quantum Synchronization of Two Standard Quantum van der Pol Oscillators

In the previous section, the reaction of a quantum van der Pol oscillator to an external drive has been presented. Such an external drive can be interpreted as another oscillator with fixed dynamics: there is no backaction from the oscillator to the drive. In this section, we consider two coherently coupled oscillators A and B with backaction, see [Lee and Sadeghpour (2013)]. Their Lindblad master equation

$$\dot{\rho} = -\mathrm{i}[H,\rho] + \sum_{j=A,B} (\gamma_1^j \mathcal{D}[a^\dagger](\rho) + \gamma_2^j \mathcal{D}[a^2](\rho)) \tag{7.1.28}$$

features the Hamiltonian

$$H = \sum_{j=A,B} \Delta_j a_j^\dagger a_j + g_{AB}(\mathrm{e}^{\mathrm{i}\phi} a_A^\dagger a_B + \mathrm{e}^{-\mathrm{i}\phi} a_A a_B^\dagger)\,. \tag{7.1.29}$$

As before, the corresponding mean-field equations are obtained from the Heisenberg equations of motion of $a = a_A$ and $b = a_B$,

$$\frac{\mathrm{d}}{\mathrm{d}t} a = -\mathrm{i}\Delta_A a - \mathrm{i} g_{AB} \mathrm{e}^{\mathrm{i}\phi} b + \frac{\gamma_1^A}{2} a - \gamma_2^A a^\dagger a^2\,, \tag{7.1.30}$$

$$\frac{\mathrm{d}}{\mathrm{d}t} b = -\mathrm{i}\Delta_B b - \mathrm{i} g_{AB} \mathrm{e}^{-\mathrm{i}\phi} a + \frac{\gamma_1^B}{2} b - \gamma_2^B b^\dagger b^2\,, \tag{7.1.31}$$

by performing a cumulant expansion of the expectation value to lowest order,

$$\frac{\mathrm{d}}{\mathrm{d}t} \langle a\rangle \approx -\mathrm{i}\Delta_A \langle a\rangle - \mathrm{i} g_{AB} \mathrm{e}^{\mathrm{i}\phi} \langle b\rangle + \frac{\gamma_1^A}{2} \langle a\rangle - \gamma_2^A |\langle a\rangle|^2 \langle a\rangle\,, \tag{7.1.32}$$

$$\frac{\mathrm{d}}{\mathrm{d}t} \langle b\rangle \approx -\mathrm{i}\Delta_B \langle b\rangle - \mathrm{i} g_{AB} \mathrm{e}^{-\mathrm{i}\phi} \langle a\rangle + \frac{\gamma_1^B}{2} \langle b\rangle - \gamma_2^B |\langle b\rangle|^2 \langle b\rangle\,. \tag{7.1.33}$$

For $\phi = 0$, by setting $\langle a_j\rangle = r_j \mathrm{e}^{\mathrm{i}\phi_j}$, we split the amplitude part,

$$\dot{r}_j = \mathrm{Re}\left[\mathrm{e}^{-\mathrm{i}\phi_j} \frac{\mathrm{d}}{\mathrm{d}t} \langle a_j\rangle\right] = r_j \left(\frac{\gamma_1^j}{2} - \gamma_2^j r_j^2\right) + g_{AB} r_i \sin(\phi_i - \phi_j)\,, \tag{7.1.34}$$

from the phase part,

$$\dot{\phi} = \mathrm{Im}\left[\frac{1}{\langle a_j\rangle} \frac{\mathrm{d}}{\mathrm{d}t} \langle a_j\rangle\right] = -\Delta_j - g_{AB} \frac{r_i}{r_j} \cos(\phi_i - \phi_j)\,. \tag{7.1.35}$$

Here, $i, j \in \{A, B\}$ and $i \neq j$. This model exhibits a U(1) symmetry, i.e., invariance under the transformation $a_j \to a_j \mathrm{e}^{\mathrm{i}\theta}$. Therefore, an interesting quantity is the relative phase $\phi_{AB} = \phi_A - \phi_B$ between the oscillators. Its dynamics are given by

$$\dot{\phi}_{AB} = -\delta + g_{AB} \frac{r_A^2 - r_B^2}{r_A r_B} \cos(\phi_{AB})\,, \tag{7.1.36}$$

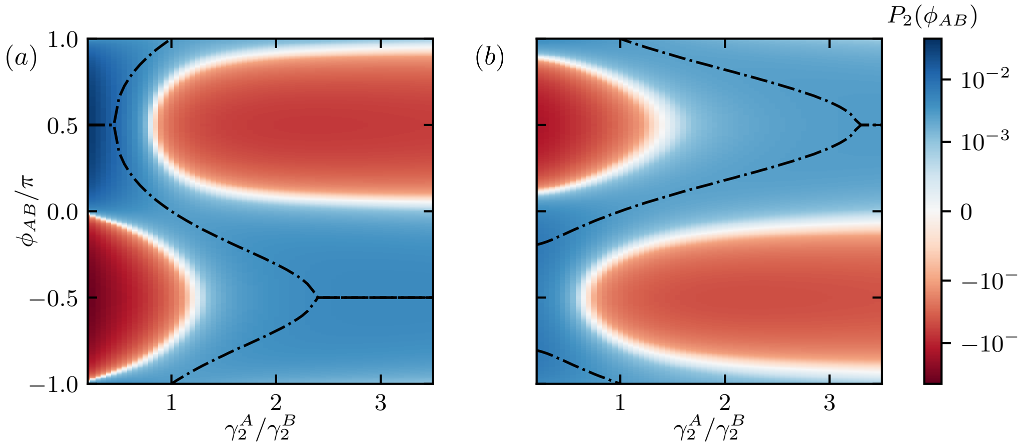

Figure 7.6: Regions of the quantum synchronization blockade for $g = \gamma_1^B$, and $\gamma_2^B = 2.5\gamma_1^B$. In all panels, P_2 is shown and maxima in ϕ_{AB} are indicated by dash-dotted lines. (a) Two standard limit cycles with fixed $\gamma_1^A = \gamma_1^B$, i.e., different mean-field radii. (b) Two standard limit cycles with fixed $\gamma_2^A = 2.5\gamma_1^A$, i.e., identical mean-field radii. The color scale is linear in the interval $[-10^{-3}, 10^{-3}]$ and logarithmic elsewhere.

where $\delta = \Delta_A - \Delta_B$. The equation of motion of the relative phase Eq. (7.1.36) is identical to the one of two classical Stuart-Landau oscillators defined in Eq. (6.5.5). Therefore, the synchronization blockade and bistable phase locking that we saw in Sec. 6.5.3 also shows up here.

The phase distribution measure $P_2(\phi_{AB})$ of the relative phase of two oscillators, see [Hush et al. (2015)], reads

$$P_2(\phi_{AB}) = \int_0^{2\pi} \mathrm{d}\phi_B \, \langle \phi_{AB} + \phi_B, \phi_B | \, \rho \, | \phi_{AB} + \phi_B, \phi_B \rangle - \frac{1}{2\pi} \, . \tag{7.1.37}$$

This measure is based on the projection of a state ρ onto tensor products of phase states. Similar to P_1 defined in Eq. (7.1.7), a uniform distribution of the relative phases is subtracted by the second term in Eq. (7.1.37). Bistable phase locking in the quantum case is defined in analogy to phase locking: if two local maxima of P_2 of equal height coincide with the global maximum, bistable locking to these two values occurs. In Fig. 7.6(a), we fix both $\gamma_1^A = \gamma_1^B$ and $\gamma_2^B = 2.5\gamma_1^A$. Depending on the ratio γ_2^A/γ_2^B of the damping rates, the mean-field radii of the limit cycles differ and the synchronization measure $P_2(\phi_{AB})$ of the relative phase exhibits one or two maxima. If there are two maxima at a given value of the ratio γ_2^A/γ_2^B, the quantum synchronization blockade (bistable locking) occurs.

Another scenario is presented in Fig. 7.6(b). Here, both ratios $\gamma_2^A/\gamma_1^A = \gamma_2^B/\gamma_1^B = 2.5$ are fixed and lead to identical mean-field radii independent of the value of ratio γ_2^A/γ_2^B. Therefore, in the classical model presented in Sec. 6.5.1, bistable locking to $\phi_{AB} = 0, \pi$ is independent of γ_2^A/γ_2^B, i.e., both oscillators are permanently in the blockade regime. However, in the quantum model, the values of ϕ_{AB} vary and the blockade disappears above a particular value of γ_2^A/γ_2^B. This preliminary result is a good candidate for

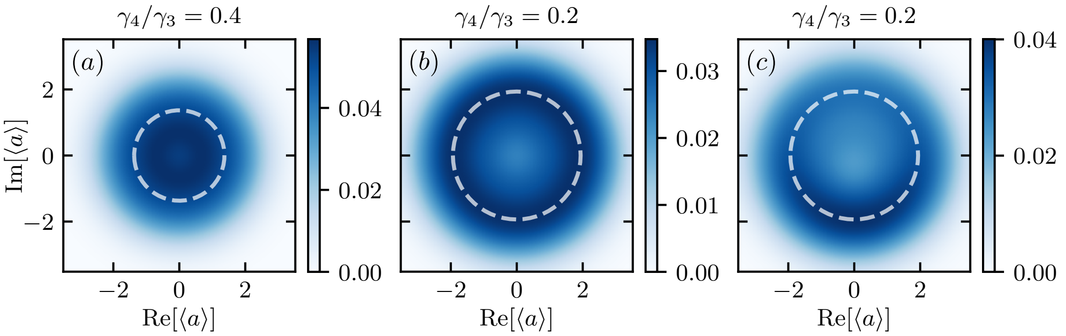

Figure 7.7: Wigner functions of the quantum limit-cycle oscillator stabilized by Lindblad jump operators $L = a^{\dagger 3}$ and $L = a^4$, see Eq. (7.1.38). (a), (b) No drive $\Omega = 0$. (c) Phase locking to a coherent drive $\Omega = 5\gamma_3$. The dashed white circles correspond to the mean-field predictions $\sqrt{3\gamma_3/4\gamma_4}$.

another quantum feature of synchronization. Future studies might describe potential interferences of coherences that lead to the blockade, similar to Sec. 7.2.2.

A unique quantum feature of synchronization has been described in [Lörch et al. (2017)]: the energy quantization blockade. In the case of two coherently coupled anharmonic oscillators, interaction and therefore synchronization can be enhanced by a certain amount of detuning between the oscillators. Due to the quantized energy that can be transferred between the oscillators and the anharmonic level structure, the detuned case has larger overlap between energy transitions than the nondetuned case. This contradicts the classical intuition that synchronization is maximized on resonance.

7.1.5 Quantum van der Pol Oscillator with Higher-Order Gain and Damping

In Ch. 10, the work published in [Kehrer et al. (2025)] will be presented. In that work, higher-order gain and damping channels are considered. In this section, let us take a brief look at a limit cycle that is stabilized by the Lindblad jump operators $L = a^{\dagger 3}$ and $L = a^4$,

$$\dot{\rho} = -\mathrm{i}[\Delta a^\dagger a + K a^{\dagger 2} a^2 + \Omega(a^\dagger + a), \rho] + \gamma_3 \mathcal{D}[a^{\dagger 3}](\rho) + \gamma_4 \mathcal{D}[a^4](\rho)\,. \tag{7.1.38}$$

The corresponding mean-field equations of the amplitude and phase are

$$\dot{r} = r^5 \left(\frac{3\gamma_3}{2} - 2\gamma_4 r^2 \right) - \Omega \sin(\phi)\,, \tag{7.1.39}$$

$$\dot{\phi} = -\Delta - 2Kr^2 - \frac{\Omega}{r} \cos(\phi)\,. \tag{7.1.40}$$

The mean-filed prediction of the steady-state radius of the limit cycle is $\sqrt{3\gamma_3/4\gamma_4}$, corresponding to the dashed white circles in Fig. 7.7. The steady state in the quantum

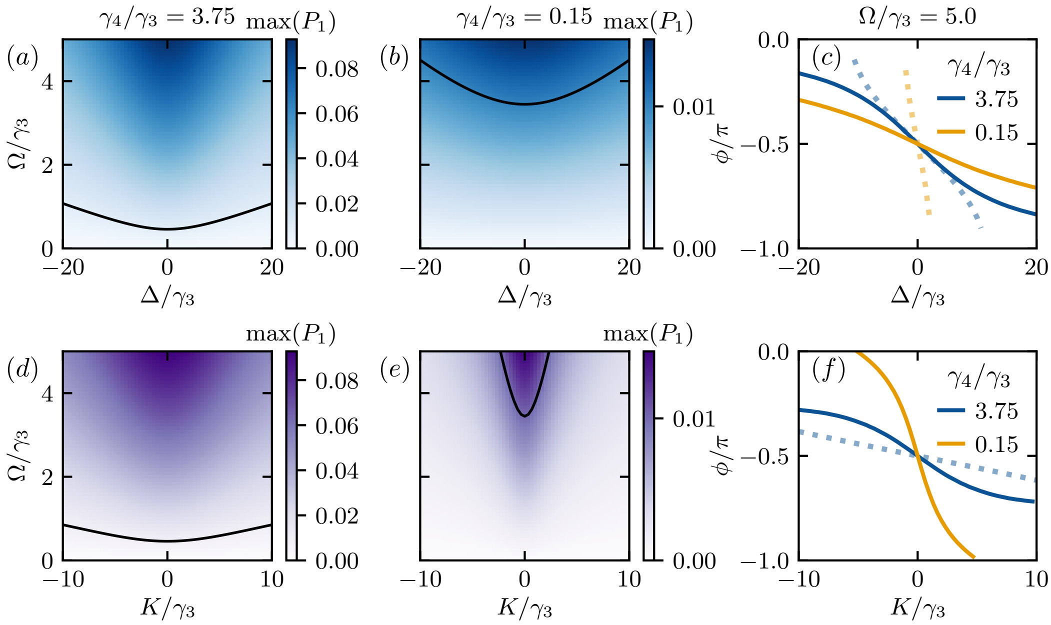

Figure 7.8: Phase locking of a coherently driven modified quantum van der Pol oscillator, see Eq. (7.1.38). In the top row we set $K = 0$ and in the bottom row we set $\Delta = 0$. (a), (b), (d), (e) Maximum of P_1 showing Arnold tongues, see Fig. 6.6. (c), (f) The solid curves correspond to the argmax of P_1 and the dotted curves to the mean-field prediction, see Eq. (7.1.40). The black curves denote contour lines at 0.01.

limit $\lambda = \gamma_3/\gamma_4 \ll 1$ has several contributions,

$$\rho_q \approx \left(\frac{5}{7} - \frac{1145}{588}\lambda\right)|0\rangle\langle 0| + \left(\frac{5}{28} + \frac{1265}{1176}\lambda\right)|1\rangle\langle 1| + \left(\frac{1}{14} + \frac{253}{588}\lambda\right)|2\rangle\langle 2| \\ + \left(\frac{1}{28} + \frac{253}{1176}\lambda\right)|3\rangle\langle 3| + \frac{5\lambda}{28}|4\rangle\langle 4| + \frac{\lambda}{28}|5\rangle\langle 5| + \frac{\lambda}{84}|6\rangle\langle 6| \,. \qquad (7.1.41)$$

Its limit-cycle radius $\sqrt{\mathrm{Tr}[a^\dagger a \rho_q]} \approx \sqrt{3/7 + 695\lambda/56\sqrt{21}}$ is slightly larger than the one of the standard quantum van der Pol oscillator.

This oscillator exhibits different phase locking behavior, presented in Fig. 7.8, in comparison to the standard quantum van der Pol oscillator, shown in Fig. 7.4. The *smaller* limit cycle reacts stronger to detuning Δ than the larger limit cycle, see Fig. 7.8(c). Moreover, the larger limit cycle needs to be driven with a larger Ω to achieve the same value of synchronization P_1: the smaller limit cycle synchronizes stronger. These findings will become relevant in Ch. 10 but need to be studied in more detail separately.

7.2 Spin Oscillators

In the previous sections, quantum synchronization was studied in some sort of a top-down approach: the classical Stuart-Landau oscillator has been quantized in a canonical way. The resulting quantum van der Pol oscillator is then taken to the quantum limit. In this limit, the quantum van der Pol oscillator and its modification incorporating third-order gain and fourth-order damping consists of only two and four levels, respectively. Outside this quantum limit, the number of significantly populated levels grows rather rapidly and the quantum model does not show a substantial distinction from a noisy classical model. The energy quantization blockade [Lörch et al. (2017)], a unique quantum feature of synchronization, has been found in a case where only few levels are populated.

Another approach to quantum synchronization is to go bottom-up: consider native few-level systems, i.e., spins. Spin oscillators are few-level quantum oscillators that are expected to show more genuine quantum effects of synchronization than infinite-level oscillators discussed in Sec. 7.1. Similar to the quantum van der Pol oscillator, one can interpret a large-spin-s system as an 'almost-infinite-level oscillator' with truncated Fock space where $2s+1$ is the maximum Fock number [Kato and Nakao (2024)]. The creation and annihilation operators $a^\dagger$ and a are replaced by spin ladder operators S^+ and S^- using a Holstein-Primakoff transformation [Holstein and Primakoff (1940)].

Other scenarios involving different gain and damping terms have been considered [Roulet and Bruder (2018a), Koppenhöfer and Roulet (2019), Parra-López and Bergli (2020), Tan et al. (2022)]. In general, as in the previous section, incoherent gain and damping stabilize particular states. These stabilized states are limit-cycle states if they exhibit a free phase of oscillation that can be locked to an external drive or other spin oscillators.

7.2.1 Synchronization Measure

The free phase of oscillation of a limit-cycle state for spin oscillators is defined by projection onto the so-called *spin coherent states* $|\theta,\phi\rangle$. These states are generated by spin rotations of the extremal spin state $|s,m_s=s\rangle$. Since SU(2) is three-dimensional, i.e., it has three group elements, we can interpret these rotations as an analogy to SO(3) rotations of the spin vector (S^x,S^y,S^z). This way of defining angles is identical to the definition of the polar angles θ and azimuthal angles ϕ in spherical coordinates. Spin coherent states can be expressed by the (small) Wigner D matrix [Wigner (1959)],

$$|\theta,\phi\rangle = \mathrm{e}^{-\mathrm{i}\phi S^z}\mathrm{e}^{-\mathrm{i}\theta S^y}|s,s\rangle = \sum_n \mathrm{e}^{-\mathrm{i}n\phi} d^s_{n,s}(\theta)\,|s,n\rangle\ , \tag{7.2.1}$$

$$|\theta,\phi\rangle\langle\theta,\phi| = \sum_{n,m} \mathrm{e}^{\mathrm{i}(m-n)\phi} d^s_{n,s}(\theta) d^s_{m,s}(\theta)\,|s,n\rangle\langle s,m|\ , \tag{7.2.2}$$

where $d^s_{n,m}$

$$\begin{aligned} d^s_{n,m}(\theta) =& \sqrt{(s+n)!(s-n)!(s+m)!(s-m)!} \\ &\times \sum_{r=s_{\min}}^{s_{\max}} \frac{(-1)^{n-m+r}\cos\left(\frac{\theta}{2}\right)^{2s+m-n-2r}\sin\left(\frac{\theta}{2}\right)^{n-m+2r}}{(s+m-r)!r!(n-m+r)!(s-n-r)!}\ , \end{aligned} \tag{7.2.3}$$

$s_{\min} = \max(0, m-n)$, and $s_{\max} = \min(s+m, s-n)$. The relevant entries are the ones for $m = s$ leading to $s_{\min} = s_{\max} = s - n$ and

$$d^s_{n,s}(\theta) = \sqrt{\frac{(2s)!}{(s+n)!(s-n)!}} \cos\left(\frac{\theta}{2}\right)^{s+n} \sin\left(\frac{\theta}{2}\right)^{s-n} . \tag{7.2.4}$$

In this thesis, we use the measure of quantum synchronization for single spin-s oscillators introduced in [Roulet and Bruder (2018a)],

$$S_1(\phi) = \int_0^\pi \mathrm{d}\theta \, \sin(\theta) Q(\theta, \phi, \rho) - \frac{1}{2\pi} , \tag{7.2.5}$$

where

$$Q(\theta, \phi, \rho) = \frac{2s+1}{4\pi} \langle \theta, \phi | \, \rho \, | \theta, \phi \rangle \tag{7.2.6}$$

is the Husimi Q function of ρ with respect to spin coherent states. One can interpret S_1 as the difference between a proper probability distribution and a uniform distribution, see the $-1/2\pi$ term in Eq. (7.2.5). The proper probability distribution only depends on the azimuthal angle ϕ since the polar angle θ has been integrated out. Using Eq. (7.2.1), we can express Eq. (7.2.6) as

$$Q(\theta, \phi, \rho) = \frac{2s+1}{4\pi} \sum_{n,m} \mathrm{e}^{\mathrm{i}(n-m)\phi} d^s_{n,s}(\theta) d^s_{m,s}(\theta) \rho_{n,m} . \tag{7.2.7}$$

The integration over θ in Eq. (7.2.5) can be mapped to Eq. (3.621.5) of [Gradshteyn and Ryzhik (2015)],

$$\int_0^\pi \mathrm{d}\theta \, \sin(\theta) \cos\left(\frac{\theta}{2}\right)^n \sin\left(\frac{\theta}{2}\right)^m = 2 \frac{\Gamma\left(1 + \frac{n}{2}\right) \Gamma\left(1 + \frac{m}{2}\right)}{\Gamma\left(2 + \frac{n+m}{2}\right)} , \tag{7.2.8}$$

where $\Gamma(z)$ is the Gamma function

$$\Gamma(z) = \int_0^\infty \mathrm{d}t \, \mathrm{e}^{-t} t^{z-1} , \tag{7.2.9}$$

see Eq. (8.310.1) of [Gradshteyn and Ryzhik (2015)]. Using this expression, we simplify S_1 to [Tan et al. (2022)],

$$S_1(\phi) = \sum_{n,m} c^s_{n,m}(\phi) \rho_{n,m} , \tag{7.2.10}$$

where

$$\begin{aligned} c^s_{n,m}(\phi) =& \mathrm{e}^{\mathrm{i}(n-m)\phi}\frac{2s+1}{4\pi}\int_0^\pi \mathrm{d}\theta\ \sin(\theta) d^s_{n,s}(\theta) d^s_{m,s}(\theta) \\ =& \frac{\mathrm{e}^{\mathrm{i}(n-m)\phi}}{2\pi}\frac{\Gamma\left(1+s+\frac{n+m}{2}\right)\Gamma\left(1+s-\frac{n+m}{2}\right)}{\sqrt{(s+n)!(s-n)!(s+m)!(s-m)!}} \,. \end{aligned} \tag{7.2.11}$$

In [Kehrer et al. (2024b)] presented in Ch. 8, an operator $c^s(\phi)$ is defined such that S_1 can be rewritten as an expectation value of this operator. With this trick, the synchronization measure becomes more interpretable and faster to compute.

The definition of the synchronization measure in Eq. (7.2.5) can be generalized to systems consisting of N spin-s oscillators by considering tensor products of spin coherent states, see [Roulet and Bruder (2018b)],

$$S_N(\vec{\phi}) = \int_0^\pi \mathrm{d}\theta_1 \sin(\theta_1)\cdots\int_0^\pi \mathrm{d}\theta_N \sin(\theta_N) Q(\vec{\theta},\vec{\phi},\rho) - \frac{1}{(2\pi)^N} \,, \tag{7.2.12}$$

where

$$Q(\vec{\theta},\vec{\phi},\rho) = \left(\frac{2s+1}{4\pi}\right)^N \left\langle \vec{\theta},\vec{\phi}\right| \rho \left|\vec{\theta},\vec{\phi}\right\rangle \,, \tag{7.2.13}$$

and

$$\left|\vec{\theta},\vec{\phi}\right\rangle = \bigotimes_{j=1}^N \exp(-\mathrm{i}\phi_j S^z)\exp(-\mathrm{i}\theta_j S^y)\left|s,s\right\rangle \,. \tag{7.2.14}$$

In the synchronization measure S_N, each polar angle θ_j is integrated out such that only the azimuthal angle information remains. Due to particular symmetries in a model, synchronization will be found in the distribution of a subset of coordinates ϕ_j, e.g., relative phases $\phi_i - \phi_j$. In these cases, a synchronization measure can be defined by integrating out the irrelevant combinations of ϕ_j.

7.2.2 Spin-1

There has been work published on quantum synchronization of spin-1/2 oscillators, e.g., [Zhirov and Shepelyansky (2008), Cabot et al. (2019), Parra-López and Bergli (2020)]. However, here, we will focus on models consisting of spins 1. This section is based on [Roulet and Bruder (2018a), Roulet and Bruder (2018b)]. The first scenario that is considered when studying quantum synchronization of a particular model is the coupling to an external coherent drive. This drive can be interpreted as an oscillator whose dynamics are fixed, i.e., there is no backaction from the free oscillator to the drive. In a spin model, a coherent drive is described by $H_d = \Omega(S^+ + S^-)/2$, where $S^\pm = \sqrt{2}(|\pm 1\rangle\langle 0| + |0\rangle\langle \mp 1|)$ are the ladder operators and Ω is the real-valued

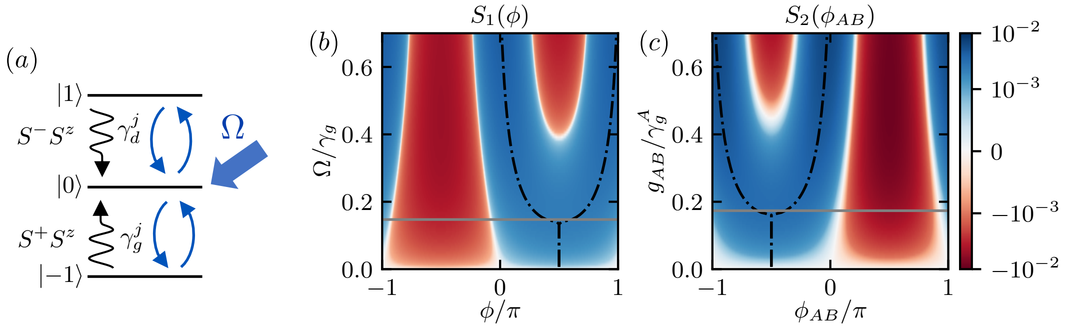

Figure 7.9: Quantum synchronization of spins 1. (a) Schematics of gain, damping, and drive of a spin-1 oscillator, see Eq. (7.2.15). (b) Synchronization measure $S_1(\phi)$ for $\gamma_d = 1.5\gamma_g$. The gray line denotes the switch from a single maximum to two maxima at approximately $\Omega = 3\pi|\gamma_d - \gamma_g|/32$. (c) Synchronization measure $S_2(\phi_{AB})$ for $\gamma_d^A = 1.5\gamma_g^A$, $\gamma_d^B = 2\gamma_g^A$, and $\gamma_g^B = \gamma_g^A$. The gray line denotes the switch from a single maximum to two maxima at approximately $g_{AB} = 9\pi^2|\gamma_d^A + \gamma_g^B - \gamma_g^A - \gamma_d^B|/256$. In panels (b) and (c), the color is scaled linear in the interval $[-10^{-3}, 10^{-3}]$ and logarithmic elsewhere.

drive strength. Since in this section only $s = 1$ is considered, we will abbreviate $|s = 1, m_s\rangle = |m_s\rangle$.

In the setup considered in [Roulet and Bruder (2018a), Roulet and Bruder (2018b)], the stabilized limit-cycle state is the central spin state $|0\rangle$. The gain (damping) process is described by the Lindblad jump operator $L = S^+S^z$ ($L = S^-S^z$). The S^z operator ensures that there is no excitation from $|0\rangle \to |1\rangle$ and no deexcitation from $|0\rangle \to |-1\rangle$, see Fig. 7.9(a). The total Lindblad master equation in the rotating frame of the drive reads

$$\frac{\mathrm{d}}{\mathrm{d}t}\rho = \dot{\rho} = -\mathrm{i}[\Delta S^z + H_d, \rho] + \frac{\gamma_g}{2}\mathcal{D}[S^+S^z](\rho) + \frac{\gamma_d}{2}\mathcal{D}[S^-S^z](\rho)\,. \tag{7.2.15}$$

An analytical expression for the steady state $\dot{\rho} = 0$ exists but is quite lengthy. Using the definition

$$\begin{aligned}\mathcal{N}_1 =&\gamma_d\gamma_g(\gamma_d^2 + 4\Delta^2)(\gamma_g^2 + 4\Delta^2)((\gamma_d + \gamma_g)^2 + 16\Delta^2) + 32(\gamma_d + \gamma_g)^2\Omega^6\\ &+ 4(\gamma_d + \gamma_g)^2((2\gamma_d + \gamma_g)(\gamma_d + 2\gamma_g) + 20\Delta^2)\Omega^4\\ &+ 4\gamma_d\gamma_g(\gamma_d^2 + \gamma_d\gamma_g + \gamma_g^2 + 4\Delta^2)((\gamma_d + \gamma_g)^2 + 16\Delta^2)\Omega^2\,,\end{aligned} \tag{7.2.16}$$

the expectation values of S^z, S^+, and S^{+2} can be reduced to

$$\langle S^z\rangle\mathcal{N}_1 = 2(\gamma_g^2 - \gamma_d^2)((\gamma_d + \gamma_g)^2 + 16\Delta^2)(\gamma_d\gamma_g + 2\Omega^2)\Omega^2\,, \tag{7.2.17}$$

$$\begin{aligned}\langle S^+\rangle\mathcal{N}_1 =&2(\gamma_d - \gamma_g)\Omega\Big(\gamma_d\gamma_g((\gamma_d + \gamma_g)^2 + 16\Delta^2)(2\mathrm{i}\Delta + \gamma_g)(2\Delta - \mathrm{i}\gamma_d)\\ &+ 4\mathrm{i}(\gamma_d + \gamma_g)(\gamma_d + \gamma_g + 8\mathrm{i}\Delta)\Omega^4\Big)\,,\end{aligned} \tag{7.2.18}$$

$$\begin{aligned}\langle S^{+2}\rangle\mathcal{N}_1 =&4\Omega^2\Big(\gamma_d\gamma_g((\gamma_d + \gamma_g)^2 + 16\Delta^2)(2\mathrm{i}\Delta + \gamma_g)(2\mathrm{i}\Delta + \gamma_d) + 4(\gamma_d + \gamma_g)^2\Omega^4\\ &+ 4\gamma_d\gamma_g(\gamma_d + \gamma_g)(\gamma_d + \gamma_g + 4\mathrm{i}\Delta)\Omega^2\Big)\,.\end{aligned} \tag{7.2.19}$$

Note that both $\langle S^z \rangle$ and $\langle S^+ \rangle$ vanish for equal rates $\gamma_g = \gamma_d$. In the quantum synchronization regime of small drive strengths and detunings $\Omega, \Delta \ll \gamma_d, \gamma_g$, the density matrix reads

$$\rho \approx \begin{pmatrix} \frac{2\Omega^2}{\gamma_d^2} & -\frac{\sqrt{2}(\mathrm{i}\gamma_d+2\Delta)\Omega}{\gamma_d^2} & \frac{2\Omega^2}{\gamma_d\gamma_g} \\ \frac{\sqrt{2}(\mathrm{i}\gamma_d-2\Delta)\Omega}{\gamma_d^2} & 1-\frac{2\Omega^2}{\gamma_d^2}-\frac{2\Omega^2}{\gamma_g^2} & \frac{\sqrt{2}(\mathrm{i}\gamma_g+2\Delta)\Omega}{\gamma_g^2} \\ \frac{2\Omega^2}{\gamma_d\gamma_g} & \frac{\sqrt{2}(-\mathrm{i}\gamma_g+2\Delta)\Omega}{\gamma_g^2} & \frac{2\Omega^2}{\gamma_g^2} \end{pmatrix}, \tag{7.2.20}$$

and the expectation values of S^z, S^+, and S^{+2} are

$$\langle S^z \rangle \approx 2\frac{\gamma_g^2-\gamma_d^2}{\gamma_d^2\gamma_g^2}\Omega^2\,, \tag{7.2.21}$$

$$\langle S^+ \rangle \approx 2\frac{(\gamma_d-\gamma_g)(2(\gamma_d+\gamma_g)\Delta-\mathrm{i}\gamma_d\gamma_g)}{\gamma_d^2\gamma_g^2}\Omega\,, \tag{7.2.22}$$

$$\langle S^{+2} \rangle \approx \frac{4\Omega^2}{\gamma_d\gamma_g}\,. \tag{7.2.23}$$

The synchronization measure for this approximation yields

$$S_1(\phi) \approx 3(\gamma_d-\gamma_g)\frac{\gamma_d\gamma_g\sin(\phi)+2(\gamma_d+\gamma_g)\Delta\cos(\phi)}{8\gamma_d^2\gamma_g^2}\Omega+\frac{\Omega^2\cos(2\phi)}{\pi\gamma_d\gamma_g}\,. \tag{7.2.24}$$

This equation shows that the terms proportional to Ω lead to *phase locking* to (i)

$$\phi = \arctan(\gamma_d\gamma_g/2(\gamma_d+\gamma_g)\Delta)\,, \tag{7.2.25}$$

for $\Delta > 0$ and $\gamma_g < \gamma_d$ or $\Delta < 0$ and $\gamma_g > \gamma_d$ and to phase locking to (ii)

$$\phi = \pi + \arctan(\gamma_d\gamma_g/2(\gamma_d+\gamma_g)\Delta)\,, \tag{7.2.26}$$

for $\Delta > 0$ and $\gamma_g > \gamma_d$ or $\Delta < 0$ and $\gamma_g < \gamma_d$.

In contrast, the term proportional to Ω^2 in Eq. (7.2.24) leads to *bistable locking* of the oscillator to $\phi = 0, \pi$. Therefore, for small Ω, the phase of the oscillator locks to a single value and if Ω is larger than a critical value, bistable phase locking occurs. For $\Delta = 0$ the critical value is $\Omega = 3\pi|\gamma_d - \gamma_g|/32$, see the gray line in Fig. 7.9(b). Similarly, if $\gamma_d = \gamma_g$, any value of Ω will lead to bistable locking to $\phi = 0, \pi$. This bistable locking is called the *quantum synchronization blockade* or to be more precise the *quantum interference blockade* and will be relevant in Ch. 8. The terms in S_1 proportional to Ω originate form different coherences $|\pm1\rangle\langle 0|$ and $|0\rangle\langle \pm1|$. If $\gamma_d = \gamma_g$, these coherences interfere destructively, i.e., the pairs $|1\rangle\langle 0|$ and $|0\rangle\langle -1|$ as well as $|-1\rangle\langle 0|$ and $|0\rangle\langle 1|$ have the same absolute value but opposite sign. Similar to the energy quantization blockade [Lörch et al. (2017)], this is a genuine quantum effect of synchronization: a single driven spin-1 oscillator exhibits a synchronization blockade (bistable locking) due to quantum interference. Note that neither classical cases nor quantum van der Pol oscillators exhibit this type of blockade. For other examples of blockades see Secs. 6.2.1 and 7.1.4.

The original definition of phase synchronization in Ch. 6 requires a small drive strength such that the driven oscillator exhibits a phase preference without a significant distortion of its limit-cycle state. Significant in this case means that the population changes, e.g., $\langle S^z \rangle$, are proportional to Ω^2 and therefore subleading order. Whether bistable locking should be considered a (quantum) synchronization effect or not is debatable, since it is of the same order as the population changes. In this thesis, such higher-order effects are considered a part of (quantum) synchronization while keeping in mind the original definition.

In a system consisting of two coherently coupled spins 1 A and B [Roulet and Bruder (2018b)], the measure

$$S_2(\phi_{AB}) = \int_0^{2\pi} \mathrm{d}\phi_B \, S_2(\phi_{AB} + \phi_B, \phi_B) \,, \tag{7.2.27}$$

is employed to determine the distribution of the relative phase $\phi_{AB} = \phi_A - \phi_B$ between the two oscillators. Here, the Lindblad master equation in the rotating frame of the drive reads

$$\dot{\rho} = -\frac{\mathrm{i}}{2}[g_{AB} S_A^+ S_B^- + \mathrm{H.c.}, \rho] + \sum_{j=A,B} \left(\frac{\gamma_g^j}{2} \mathcal{D}[S_j^+ S_j^z](\rho) + \frac{\gamma_d^j}{2} \mathcal{D}[S_j^- S_j^z](\rho) \right) \,, \tag{7.2.28}$$

where g_{AB} is the coherent coupling strength, $S_j^{\pm}$ and S_j^z are spin operators that act on the jth oscillator, and γ_g^j and γ_d^j are the gain and damping rates of oscillator j. The steady state for $g_{AB} = 0$ is $\rho^{(0)} = |0,0\rangle\langle 0,0|$. Due to the U(1) symmetry of the model, i.e., invariance under the transformation $S_j^+ \to S_j^+ \mathrm{e}^{\mathrm{i}\theta}$, only the relative phase between the oscillators is relevant.

Similar to the single driven spin, an analytical expression of the steady state exists but is too lengthy to be shown here. In the quantum synchronization regime of small coupling $g_{AB} \ll \gamma_g^j, \gamma_d^j$, the synchronization measure evaluated for the perturbation expansion of the steady state reads

$$S_2(\phi_{AB}) = g_{AB} \frac{9\pi}{64} \frac{\gamma_d^A + \gamma_g^B - \gamma_g^A - \gamma_d^B}{(\gamma_d^A + \gamma_g^B)(\gamma_g^A + \gamma_d^B)} \sin(\phi_{AB}) + g_{AB}^2 \frac{\cos(2\phi_{AB})}{\pi(\gamma_d^A + \gamma_g^B)(\gamma_g^A + \gamma_d^B)} \,. \tag{7.2.29}$$

Similar to Eq. (7.2.24), the term linear in g_{AB} leads to phase locking to $\phi_{AB} = \pi/2$ ($\phi_{AB} = -\pi/2$) if $\gamma_d^A + \gamma_g^B > \gamma_g^A + \gamma_d^B$ ($\gamma_d^A + \gamma_g^B < \gamma_g^A + \gamma_d^B$) and the term proportional to g_{AB}^2 leads to bistable locking to $\phi_{AB} = 0, \pi$. Two maxima of S_2 in Eq. (7.2.29) exist if $g_{AB} > 9\pi^2 |\gamma_d^A + \gamma_g^B - \gamma_g^A - \gamma_d^B|/256$, see the gray line in Fig. 7.9(c). If $\gamma_d^A + \gamma_g^B = \gamma_g^A + \gamma_d^B$, the pairs of coherences $|1,-1\rangle\langle 0,0|$ and $|0,0\rangle\langle -1,1|$ as well as $|-1,1\rangle\langle 0,0|$ and $|0,0\rangle\langle 1,-1|$ that form the term linear in g_{AB} exhibit the identical absolute value but opposite sign and therefore cancel. In this case, the two spin oscillators are in the synchronization blockade, similar to quantum vdP oscillators Sec. 7.1.2. Here, for spins 1, we can understand the blockade in more detail, i.e., as the destructive interference of coherences.

There are different choices of rates that lead to the vanishing of the term linear in g_{AB}, i.e., vanishing locking to a single value of the phase. The first, second, and third choice that we know from classical vdP oscillators are: (i) $\gamma_g^A = \gamma_g^B$ and $\gamma_d^A = \gamma_d^B$, called *identical oscillators*, (ii) $\gamma_g^A/\gamma_d^A = \gamma_g^B/\gamma_d^B = \lambda$, called *equal rate ratios*, and (iii) $\gamma_d^A = \gamma_d^B = \gamma_d^B = \gamma$, called *equal rates.* Another choice that is available in this spin setup are so-called *inverted rates* $\gamma_g^A = \gamma_d^B$ and $\gamma_d^A = \gamma_g^B$ [Roulet and Bruder (2018b)].

In Ch. 8, we will study cases in which two blockades occur. First, for two coherently coupled spins 1, we consider the blockade between the drive and one of the oscillators and the blockade between both oscillators. Second, for a chain of three coherently coupled spins 1, we consider the two blockades between neighboring spins. We will find that in some parameter regime quantum synchronization *through* the blockades of indirectly coupled oscillators exists, i.e., without lifting the blockades.

7.3 Many Quantum Oscillators

An interesting research direction is to go beyond two-oscillator models, i.e., the study of networks of quantum oscillators in contrast to classical oscillators [Kuramoto (1984), Acebrón et al. (2005), Ott and Antonsen (2008)]. Already in [Lee and Sadeghpour (2013)], the mean-field equations of the model have been analyzed in the limit of an infinite number of identical all-to-all connected oscillators. A transition between synchronized and unsynchronized states is found. In [Nadolny and Bruder (2023)], the question whether quantum effects of synchronization survive in large groups of limit-cycle oscillators is answered affirmatively. In the setups of (i) a single driven and (ii) two reactively coupled large groups of anharmonic spin-1 oscillators, macroscopic manifestations of the quantum interference blockade [Roulet and Bruder (2018a)] and the energy quantization blockade [Lörch et al. (2017)] are found. Considering a specific connectivity, e.g., topological networks [Wanjura et al. (2020), Wächtler et al. (2020), Sone et al. (2022)], the enhancement of robustness of synchronization is studied [Wächtler and Platero (2023), Wächtler and Moore (2024)]. In macroscopic networks, the relation between frustration and quantum synchronization has been touched [Ha and Kim (2019), Karpat et al. (2020)].

Another direction is the one of active quantum matter. First steps toward describing self-propelled quantum objects powered by environmental energy have been taken [Yamagishi et al. (2024), Antonov et al. (2025), Penner et al. (2025)]. A precursor of spatially active quantum matter are active oscillatory states, e.g., quantum analogues of traveling-wave states [Fruchart et al. (2021)] found in coupled groups of spins [Nadolny et al. (2025a), Nadolny et al. (2025b)] and coupled quantum van der Pol oscillators [Kehrer and Bruder (2025)]. The latter example will be presented in detail in Ch. 9.

Chapter 8

Quantum Synchronization of Spin-1 Oscillators in the Presence of Interference Blockades

This chapter is based on the results published in:

T. Kehrer, T. Nadolny, and C. Bruder,
Quantum synchronization through the interference blockade,
Physical Review A **110**, 042203 (2024)

8.1 Motivation

As described in the previous chapter, in the last decade, there has been a lot of activity in the study of synchronization in quantum systems. A three-level quantum system in which one of the three states is stabilized by incoherent gain and damping processes has been established as a minimal quantum limit-cycle oscillator [Roulet and Bruder (2018a)]. Subject to an external drive, this spin-1 oscillator aligns its phase of oscillation with the one of the drive. The magnitude of this so-called 1:1 phase locking is proportional to the drive strength. In this chapter, we will use the term n:1 phase locking if the probability distribution of the phase of an oscillator exhibits n maxima that corresponds to *multistable* locking. If the gain and damping rates are equal, an *interference blockade* emerges leading to a complete suppression of 1:1 phase locking. In this case, the oscillator tends to align its phase in one of two positions: in phase or opposite the phase of the drive. This corresponds to 2:1 phase locking which could be called *passing by* the blockades. A similar effect is observed for the synchronization of two identical coupled spins 1, i.e., the absence of 1:1 phase locking and the presence of 2:1 phase locking [Roulet and Bruder (2018b), Koppenhöfer and Roulet (2019)]. Interference blockades [Solanki et al. (2023)] are not the only type of blockades that have been studied in systems of quantum oscillators, for another example see [Lörch et al. (2017)].

In this chapter, we first consider a drive applied to one of two coherently coupled

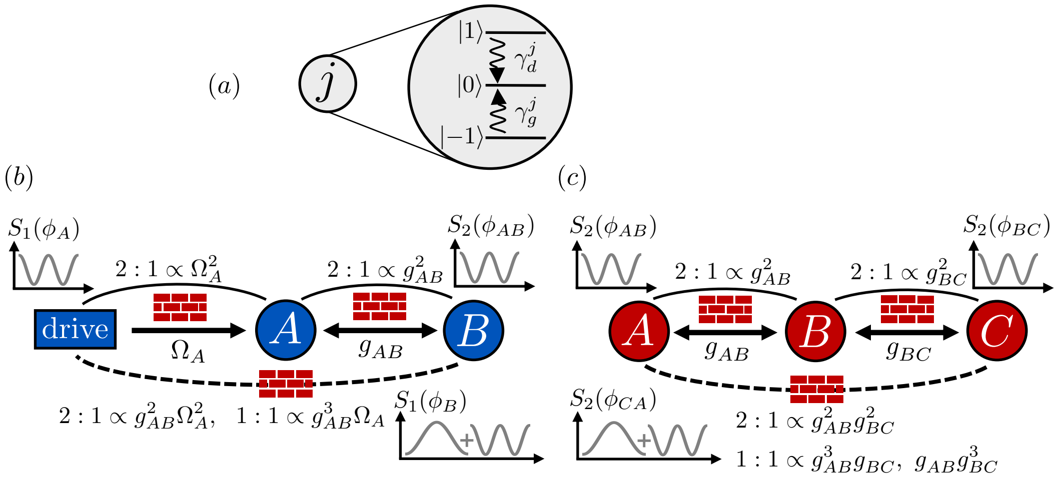

Figure 8.1: Schematics of the models. (a) Each minimal quantum limit-cycle oscillator labeled A, B, and C consists of three spin-1 states $|-1\rangle$, $|0\rangle$, and $|1\rangle$. It is subject to two independent gain and damping processes with rates γ_g^j and γ_d^j that incoherently drive the population toward the state $|0\rangle$. (b) Two spins A and B are coherently coupled with strength g_{AB}, see Sec. 8.3. Spin A is furthermore driven by an external drive with strength Ω_A. (c) Chain of three coupled spins without external drive, see Sec. 8.4. The insets in (b) and (c) qualitatively show the resulting (bistable) phase locking of the spins. Due to blockades (red brick walls), 1:1 phase locking vanishes. Solid arcs denote second-order effects leading to 2:1 phase locking *passing by* blockades. Dashed arcs denote fourth-order effects leading to 1:1 and 2:1 phase locking between not directly coupled elements *through* the blockades.

spin-1 oscillators. In the parameter regime of equal gain and damping rates, see Fig. 8.1(b), both spins are blockaded: there is no 1:1 phase locking of the driven spin to the drive as well as no 1:1 phase locking between both spins. They both align in and out of phase corresponding to 2:1 phase locking. Remarkably, the undriven spin *does* exhibit 1:1 phase locking to the external drive. In other words, the undriven oscillator synchronizes to the external drive *through* both (drive-spin and spin-spin) interference blockades *without* lifting them. The locking strength is linear in the drive strength and of third order in the coupling strength. The second system that we study is a chain of three coupled spin-1 oscillators. An unexpected 1:1 phase locking, in analogy to the two-spin case, is found between the first and last spin, see Fig. 8.1(c). However, the central spin mediating this locking is itself not 1:1 phase locked to any of the two other spins.

This chapter is structured as follows. In Sec. 8.2, we define the Lindblad master equation of our systems and the measure of quantum synchronization we will use. In Sec. 8.3, we study the behavior of two spin-1 oscillators in and outside the interference blockades. In Sec. 8.4, we analyze a system of three coupled spins 1. We discuss entanglement measures in Sec. 8.5.

8.2 Model and Quantum Synchronization Measure

We consider models of coupled spin-1 oscillators subject to gain and damping processes, visualized in Fig. 8.1. The systems are described by the following Lindblad master equation

$$\frac{\mathrm{d}}{\mathrm{d}t}\rho = \dot{\rho} = \mathcal{L}(\rho) = -\mathrm{i}[H,\rho] + \sum_j \mathcal{L}_j(\rho)\,, \tag{8.2.1}$$

$$\mathcal{L}_j(\rho) = \frac{\gamma_g^j}{2}\mathcal{D}[S_j^+ S_j^z](\rho) + \frac{\gamma_d^j}{2}\mathcal{D}[S_j^- S_j^z](\rho)\,, \tag{8.2.2}$$

where the Hamiltonian H that encodes a coherent drive and spin-spin interactions will be specified later in Eqs. (8.3.1) and (8.4.1). Both incoherent gain and damping processes are combined in the Liouvillian $\mathcal{L}_j$ and provide limit-cycle stabilization of the jth spin, see the black wavy arrows in Fig. 8.1(a). The gain and damping rates of the jth spin are denoted by γ_g^j and γ_d^j and we choose $S^z = |1\rangle\langle 1| - |-1\rangle\langle -1|$ and $S^{\pm} = \sqrt{2}(|\pm 1\rangle\langle 0| + |0\rangle\langle \mp 1|)$ as defined in Sec. 2.2. We use the standard notation $\mathcal{D}[L](\rho) = L\rho L^\dagger - (L^\dagger L\rho + \rho L^\dagger L)/2$. The steady state for $H = 0$ is the product state $\rho^{(0)} = |0,0\rangle\langle 0,0|$.

A previous work shows that quantum synchronization of a single spin-1 oscillator to an external resonant drive is observed if $\gamma_g^j \neq \gamma_d^j$ [Roulet and Bruder (2018a)]. For two resonant spin-1 oscillators, quantum synchronization occurs if $\gamma_d^i + \gamma_g^j \neq \gamma_g^i + \gamma_d^j$ [Roulet and Bruder (2018b)]. In those works, quantum synchronization is defined as an effect that is linear in the drive strength or the interaction strength, respectively. If the rate conditions mentioned above are violated, only higher-order synchronization can be observed, i.e., the system is in the quantum interference synchronization blockade, see also Sec. 7.2.2.

A variety of measures to quantify the degree of quantum synchronization has been proposed in the literature [Ludwig and Marquardt (2013), Hush et al. (2015), Weiss et al. (2016), Roulet and Bruder (2018a)]. For N spin-1 oscillators, we choose the synchronization measure $S_N(\vec{\phi})$ defined in [Roulet and Bruder (2018b)] and Eq. (7.2.12),

$$S_N(\vec{\phi}) = \left(\frac{3}{4\pi}\right)^N \int_0^\pi \mathrm{d}\theta_1 \sin(\theta_1) \cdots \times \int_0^\pi \mathrm{d}\theta_N \sin(\theta_N) \left\langle \vec{\theta},\vec{\phi}\right| \rho \left|\vec{\theta},\vec{\phi}\right\rangle - \frac{1}{(2\pi)^N}\,, \tag{8.2.3}$$

where

$$\left|\vec{\theta},\vec{\phi}\right\rangle = \bigotimes_{j=1}^{N} \exp(-\mathrm{i}\phi_j S^z)\exp(-\mathrm{i}\theta_j S^y)\left|1,1\right\rangle\,. \tag{8.2.4}$$

This measure is a probability distribution of phases ϕ_j of each oscillator j that are defined by projections of the density matrix to spin coherent states $\left|\vec{\theta},\vec{\phi}\right\rangle$, where $|s,m_s\rangle = |1,1\rangle$ is the extremal spin-1 state. Using S_N, we will calculate probability distributions of relative phase angles as marginals by integrating over global phases, see, e.g., Eq. (8.2.14). If the synchronization measure is flat, there is no phase preference, i.e., no synchronization in the system. Maxima of S_N are related to locking of the oscillator phases. In Eq. (7.2.10), we saw that the synchronization measure of one spin-s oscillator can be written as

$$S_1(\phi) = \sum_{n,m} c^s_{n,m}(\phi)\rho_{n,m}\,, \tag{8.2.5}$$

where [Tan et al. (2022)]

$$c^s_{n,m}(\phi) = \frac{\mathrm{e}^{\mathrm{i}(n-m)\phi}}{2\pi}\,\frac{\Gamma\left(1+s+\frac{n+m}{2}\right)\Gamma\left(1+s-\frac{n+m}{2}\right)}{\sqrt{(s+n)!(s-n)!(s+m)!(s-m)!}}\,. \tag{8.2.6}$$

Here, we interpret $c^s_{n,m}(\phi)$ as the components of an operator $c^s(\phi)$. For spin-1/2 and spin-1 oscillators, we find explicit expressions for $c^s(\phi)$,

$$c^{1/2}(\phi) = \frac{\mathbb{1}}{2\pi} + \frac{1}{8}\left(\mathrm{e}^{\mathrm{i}\phi}S^+ + \mathrm{e}^{-\mathrm{i}\phi}S^-\right)\,, \tag{8.2.7}$$

$$c^{1}(\phi) = \frac{\mathbb{1}}{2\pi} + \left(\frac{3\mathrm{e}^{\mathrm{i}\phi}}{32}S^+ + \frac{\mathrm{e}^{\mathrm{i}2\phi}}{8\pi}(S^+)^2 + \text{H.c.}\right)\,. \tag{8.2.8}$$

For larger spins, the expression of c^s becomes more complex, e.g., $c^{3/2}(\phi)$ features terms of the form $(S^+)^2S^-$ and $S^-(S^+)^2$. Due to the tensor-product structure of S_N, we can express Eq. (7.2.12) in a compact way,

$$S_N(\vec{\phi}\,) = \mathrm{Tr}\left[\rho\bigotimes_{j=1}^{N} c^s(\phi_j)\right] - \frac{1}{(2\pi)^N} = \left\langle\bigotimes_{j=1}^{N} c^s(\phi_j)\right\rangle - \frac{1}{(2\pi)^N}\,. \tag{8.2.9}$$

In this chapter, we are interested in up to three spin-1 oscillators. Combining Eqs. (8.2.8) and (8.2.9), for a single spin 1, we obtain

$$S_1(\phi) = \left\langle\frac{3}{32}\mathrm{e}^{\mathrm{i}\phi}S^+ + \frac{\mathrm{e}^{\mathrm{i}2\phi}}{8\pi}S^{+2} + \text{H.c.}\right\rangle\,, \tag{8.2.10}$$

and for a system consisting of two spins 1,

$$\begin{aligned} S_2(\phi_{AB}) &= \int_0^{2\pi} \mathrm{d}\phi_B\, S_2(\phi_{AB}+\phi_B,\phi_B) \\ &= \left\langle\frac{9\pi}{512}\mathrm{e}^{\mathrm{i}\phi_{AB}}S_A^+S_B^- + \frac{\mathrm{e}^{\mathrm{i}2\phi_{AB}}}{32\pi}(S_A^+S_B^-)^2 + \text{H.c.}\right\rangle\,, \end{aligned} \tag{8.2.11}$$

where $\phi_{AB} = \phi_A - \phi_B$ is the relative phase between oscillator A and B. Note that the coefficients of Eq. (8.2.11), $9\pi/512 = 2\pi(3/32)^2$ and $1/32\pi = 2\pi/(8\pi)^2$, are related to squares of the coefficients of Eq. (8.2.10), where the additional factor of 2π arises from the integration over ϕ_B. Similarly, for three spins, we define

$$S_3(\phi_{AB},\phi_{BC}) = \int_0^{2\pi} \mathrm{d}\phi_B\, S_3(\phi_{AB}+\phi_B,\phi_B,\phi_B-\phi_{BC})\,, \tag{8.2.12}$$

$$S_3(\phi_{AB},\phi_{CA}) = \int_0^{2\pi} \mathrm{d}\phi_A\, S_3(\phi_A,\phi_A-\phi_{AB},\phi_{CA}+\phi_A)\,. \tag{8.2.13}$$

The structure of Eq. (8.2.10), i.e., S_1 consists of terms $\propto \mathrm{e}^{\mathrm{i}k\phi}S^{+k}$, allows us to express the Fourier transform of S_N as expectation values of powers of the spin-1 ladder operators S_j^+. In particular, we find that the phase distributions can be written as

$$\begin{aligned} S_1(\phi_j) &= 2(m_j^{(1)}\cos(\phi_j) + m_j^{(2)}\cos(2\phi_j))\,, \\ S_2(\phi_{ij}) &= \int_0^{2\pi} \mathrm{d}\phi\, S_2(\phi_{ij}+\phi,\phi) = 2(m_{ij}^{(1)}\cos(\phi_{ij}) + m_{ij}^{(2)}\cos(2\phi_{ij}))\,, \end{aligned} \tag{8.2.14}$$

where $\phi_{ij}=\phi_i-\phi_j$ is the relative phase of two oscillators i and j. Here, we define the moments

$$m_j^{(n)} = \langle S_j^{+n}\rangle \times \begin{cases} \frac{3}{32} & n=1\,, \\ \frac{1}{8\pi} & n=2\,, \end{cases} \tag{8.2.15}$$

$$m_{ij}^{(n)} = \langle (S_i^+S_j^-)^n\rangle \times \begin{cases} \frac{9\pi}{512} & n=1\,, \\ \frac{1}{32\pi} & n=2\,, \end{cases} \tag{8.2.16}$$

where the label n corresponds to n:1 phase locking and equals the number of maxima in the synchronization measure. Thus, these moments are linked to the Fourier coefficients of the phase distributions and we will use them to quantify synchronization.

8.3 Two Spins and an External Drive

In this section, we consider two coherently coupled spins 1 labeled A and B. A resonant coherent drive with strength Ω_A acts on spin A, see Fig. 8.1(b). The system is described by Eq. (8.2.1) with the Hamiltonian in the rotating frame of the drive

$$H = \frac{\Omega_A}{2}S_A^+ + \frac{g_{AB}}{2}S_A^+S_B^- + \text{H.c.}\,, \tag{8.3.1}$$

where g_{AB} denotes the strength of the coherent coupling. We choose both Ω_A and g_{AB} to be positive. Note that both spins are assumed to be in resonance with the coherent drive, i.e., the frequency of the external drive is chosen to match exactly the level spacing of the spins.

8.3.1 In the Interference Blockade

To study two spins 1 in the quantum interference synchronization blockade, we set the gain and damping rates $\gamma_g^A = \gamma_d^A = \gamma_g^B = \gamma_d^B = \gamma$ to be equal. In the case of $\Omega_A = 0$, we obtain

$$\rho^{\mathrm{ss}} = \left(1 - \frac{8g_{AB}^2}{8g_{AB}^2 + \gamma^2}\right)\rho^{(0)} + \frac{32g_{AB}^2}{32g_{AB}^2 + 4\gamma^2}\rho^{(\infty)} - \mathrm{i}\frac{g_{AB}\gamma}{16g_{AB}^2 + 2\gamma^2}[S_A^+ S_B^- + \mathrm{H.c.}, \rho^{(0)}]\,, \tag{8.3.2}$$

where

$$\rho^{(\infty)} = \frac{1}{8}\sum_{J=1,2}\sum_{M=-1,1} |J,M\rangle_c \langle J,M|_c + \frac{1}{4}\sum_{J=0,2} |J,0\rangle_c \langle J,0|_c = \frac{1}{32}(S_A^+ S_B^- + S_A^- S_B^+)^2 \tag{8.3.3}$$

is the state in the limit $g_{AB} \gg \gamma$. It is diagonal in the combined spin basis $|J,M\rangle_c$ of two spins 1. We now consider a drive that acts on spin A as a small perturbation. This results in the following leading-order contributions in Ω_A/γ to the first moment of the synchronization measure of the undriven spin B

$$\begin{aligned} m_B^{(1)} &\approx \frac{3}{4}\frac{g_{AB}^3\Omega_A(64g_{AB}^4 + 348g_{AB}^2\gamma^2 + 135\gamma^4)}{(8g_{AB}^2 + \gamma^2)(4g_{AB}^2 + 9\gamma^2)(16g_{AB}^4 + 72g_{AB}^2\gamma^2 + 9\gamma^4)} \\ &\overset{g_{AB}\gg\gamma}{\approx} \frac{3\Omega_A}{32g_{AB}} \\ &\overset{g_{AB}\ll\gamma}{\approx} \frac{5g_{AB}^3\Omega_A}{4\gamma^4}\,, \end{aligned} \tag{8.3.4}$$

as well as to the second moment

$$\begin{aligned} m_B^{(2)} &\approx \frac{3}{2\pi}\frac{g_{AB}^2\Omega_A^2}{(g_{AB}^2 + \gamma^2)(4g_{AB}^2 + \gamma^2)} \\ &\quad\times \frac{96g_{AB}^8 + 656g_{AB}^6\gamma^2 + 518g_{AB}^4\gamma^4 + 108g_{AB}^2\gamma^6 + 81\gamma^8}{(8g_{AB}^2 + \gamma^2)(4g_{AB}^2 + 9\gamma^2)(16g_{AB}^4 + 72g_{AB}^2\gamma^2 + 9\gamma^4)} \\ &\overset{g_{AB}\gg\gamma}{\approx} \frac{9\Omega_A^2}{128\pi g_{AB}^2} \\ &\overset{g_{AB}\ll\gamma}{\approx} \frac{3g_{AB}^2\Omega_A^2}{2\pi\gamma^4}\,. \end{aligned} \tag{8.3.5}$$

The undriven spin B exhibits a 1:1 phase locking to the drive with a magnitude that to leading order is linear in Ω_A/γ, for both large and small g_{AB}/γ. The second moment of the combined synchronization measure for both spins up to second order in Ω_A/γ

is proportional to

$$\begin{aligned} m_{AB}^{(2)} &\approx \frac{1}{8\pi}\frac{g_{AB}^2}{8g_{AB}^2+\gamma^2}\left(1-\frac{\Omega_A^2(848g_{AB}^6+4600g_{AB}^4\gamma^2+1905g_{AB}^2\gamma^4+702\gamma^6)}{(8g_{AB}^2+\gamma^2)(4g_{AB}^2+9\gamma^2)(16g_{AB}^4+72g_{AB}^2\gamma^2+9\gamma^4)}\right) \\ &\overset{g_{AB}\gg\gamma}{\approx} \frac{1}{64\pi}-\frac{53\Omega_A^2+4\gamma^2}{2048\pi g_{AB}^2} \\ &\overset{g_{AB}\ll\gamma}{\approx} \frac{g_{AB}^2}{8\pi\gamma^2}\left(1-\frac{26\Omega_A^2+24g_{AB}^2}{3\gamma^4}\right). \end{aligned} \tag{8.3.6}$$

Analogously, for a vanishing spin-spin interaction strength $g_{AB}=0$, we obtain

$$\rho^{\mathrm{ss}}=\left(1-\frac{8\Omega_A^2}{8\Omega_A^2+\gamma^2}\right)\rho^{(0)}-\frac{\Omega_A^2}{8\Omega_A^2+\gamma^2}[S_A^++S_A^-,\rho^{(0)}]^2-\mathrm{i}\frac{\Omega_A\gamma}{8\Omega_A^2+\gamma^2}[S_A^++S_A^-,\rho^{(0)}], \tag{8.3.7}$$

leading to the following contribution to the second moment of the synchronization measure of the driven spin A up to second order in g_{AB}/γ,

$$\begin{aligned} m_A^{(2)} &\approx \frac{1}{2\pi}\frac{\Omega_A^2}{8\Omega_A^2+\gamma^2}\left(1-\frac{g_{AB}^2(448\Omega_A^4+456\Omega_A^2\gamma^2+189\gamma^2)}{(8\Omega_A^2+\gamma^2)(16\Omega_A^4+30\Omega_A^2\gamma^2+9\gamma^4)}\right) \\ &\overset{\Omega_A\gg\gamma}{\approx} \frac{1}{16\pi}-\frac{28g_{AB}^2+\gamma^2}{128\pi\Omega_A^2} \\ &\overset{\Omega_A\ll\gamma}{\approx} \frac{\Omega_A^2}{2\pi\gamma^2}\left(1-\frac{21g_{AB}^2+8\Omega_A^2}{\gamma^4}\right). \end{aligned} \tag{8.3.8}$$

Note that for equal gain and damping rates, the first moment $m_A^{(1)}$ of the synchronization measure of the single spin A and $m_{AB}^{(1)}$ of the combined synchronization measure vanish, i.e., the system exhibits two quantum interference blockades.

In conclusion, we expand the steady state $\rho_{\mathrm{ss}}=\sum_{n=0}^{\infty}\epsilon^n\rho^{(n)}$ of Eq. (8.2.1) in powers of ϵ for the small Hamiltonian ϵH of Eq. (8.3.1). The terms $\rho^{(n)}$ obey

$$\sum_j \mathcal{L}_j(\rho^{(n+1)})=\mathrm{i}[H,\rho^{(n)}]. \tag{8.3.9}$$

The synchronization measures up to a combined fourth order in Ω_A/γ and g_{AB}/γ are

$$S_2(\phi_{AB})\approx\frac{g_{AB}^2}{\pi\gamma^2}\cos(2\phi_{AB})\left(\frac{1}{4}-2\frac{g_{AB}^2}{\gamma^2}-\frac{13}{6}\frac{\Omega_A^2}{\gamma^2}\right), \tag{8.3.10}$$

$$S_1(\phi_A)\approx\frac{\Omega_A^2}{\pi\gamma^2}\cos(2\phi_A)\left(1-21\frac{g_{AB}^2}{\gamma^2}-8\frac{\Omega_A^2}{\gamma^2}\right), \tag{8.3.11}$$

$$S_1(\phi_B)\approx\frac{5g_{AB}^3\Omega_A}{2\gamma^4}\cos(\phi_B)+\frac{3g_{AB}^2\Omega_A^2}{\pi\gamma^4}\cos(2\phi_B). \tag{8.3.12}$$

In this regime of equal gain and damping rates there is no $\cos(\phi_A)$ and $\cos(\phi_{AB})$ contribution since both $m_A^{(1)}$ and $m_{AB}^{(1)}$ vanish. This is a consequence of the (drive-spin and spin-spin) interference blockades that persist for arbitrary drive and coupling strengths: no 1:1 phase locking of spin A to the drive and no 1:1 phase locking between spins A and B. However, the synchronization measure $S_1(\phi_B)$ in Eq. (8.3.12) features $\cos(\phi_B)$. Hence, there is an effective first-order $\propto \Omega_A$ 1:1 phase locking of the undriven spin-1 oscillator to the drive. This 1:1 phase locking is surprising, since spin A does not distinguish between the phase of the drive and its polar opposite as well as spin B does not distinguish between in and out of phase locking to spin A. We refer to this as synchronization *through* the interference blockade. It is mediated by a third-order $\propto g_{AB}^3$ spin-spin interaction as we will explain in more detail below. The second term in Eq. (8.3.12) denotes 2:1 phase locking of spin B.

In the synchronization regime where both Ω_A and g_{AB} are small compared to γ, the single-maximum 1:1 phase locking of the undriven spin B to the drive is a small fourth-order effect. However, there is neither 1:1 phase locking of oscillator A to the drive nor between oscillators A and B at any order in Ω_A and g_{AB}. Both the phase distribution of oscillator A and the distribution of the relative phase of oscillators A and B do not allow to distinguish between the phase angle of the drive and its polar opposite. For any Ω_A and g_{AB}, only the phase distribution of oscillator B uniquely reflects the phase of the drive.

This behavior can be traced back to the destructive interference of various coherences that build up. In short, even if spin A does not show 1:1 phase locking to the drive, the phase of the drive is nevertheless imprinted in the coherences of the full density matrix. Therefore, spin B can exhibit 1:1 phase locking. The contributions of the coherences to the first moment of the synchronization measure of spin A cancel but not for spin B.

For a detailed explanation, we note that the choice of equal gain and damping rates introduces a symmetry: the master equation defined in Eq. (8.2.1) with the Hamiltonian Eq. (8.3.1) is invariant under the transformation that effectively exchanges the states $|j\rangle \leftrightarrow |-j\rangle$,

$$S_j^{\pm} \to \mathcal{Z} S_j^{\pm} \mathcal{Z}^{\dagger} = S_j^{\mp}, \;\; S_j^z \to \mathcal{Z} S_j^z \mathcal{Z}^{\dagger} = -S_j^z \,, \tag{8.3.13}$$

where

$$\mathcal{Z} = \exp(\mathrm{i}\pi(S_A^x + S_B^x)), \;\; S_j^x = (S_j^+ + S_j^-)/2 \,. \tag{8.3.14}$$

We find $\mathcal{L}(\mathcal{Z}\rho\mathcal{Z}^{\dagger}) = \mathcal{Z}\mathcal{L}(\rho)\mathcal{Z}^{\dagger}$, which implies $\rho_{\mathrm{ss}} = \mathcal{Z}\rho_{\mathrm{ss}}\mathcal{Z}^{\dagger}$. Using the invariance of the steady state under the symmetry transformation defined in Eq. (8.3.13), it follows that $\langle S_A^+\rangle = \langle S_A^-\rangle$ and $\langle S_A^+ S_B^-\rangle = \langle S_A^- S_B^+\rangle$, hence $m_A^{(1)} \propto \langle S_A^+\rangle$ and $m_{AB}^{(1)} \propto \langle S_A^+ S_B^-\rangle$ are real. Since the master equation Eq. (8.2.1) only consists of real parameters and $\rho^{(0)}$ is real, even orders $\rho^{(2n)}$ of the perturbation expansion of the steady state are real and odd orders $\rho^{(2n+1)}$ are purely imaginary, see Eq. (8.3.9). At least up to a combined fourth order in Ω_A and g_{AB}, both $m_A^{(1)}$ and $m_{AB}^{(1)}$ only depend on $\rho^{(2n+1)}$, so they must be purely imaginary. Taking into account the symmetry arguments from above, they must vanish in the *interference blockade*: the individual coherences do

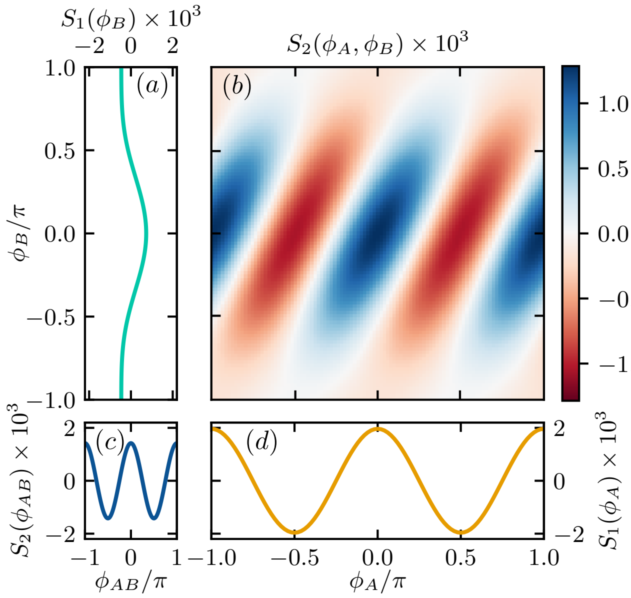

Figure 8.2: Synchronization measures S_1 and S_2, see Eqs. (8.2.3) and (8.2.14), for $\gamma_d^j = \gamma_d^j = \gamma$, $\Omega_A/\gamma = 0.1$, and $g_{AB}/\gamma = 0.15$. (b) Combined synchronization measure $S_2(\phi_A, \phi_B)$. (a),(d) Single synchronization measures $S_1(\phi_A)$ and $S_1(\phi_B)$ as marginals of (b). (c) Combined synchronization measure $S_2(\phi_{AB})$. Both $S_2(\phi_{AB})$ and $S_1(\phi_A)$ exhibit two maxima, whereas $S_1(\phi_B)$ of the undriven spin in panel (a) is characterized by only one maximum.

not vanish but they interfere destructively, $\langle |1\rangle\langle 0| \otimes \mathbb{1}\rangle = -\langle |0\rangle\langle -1| \otimes \mathbb{1}\rangle$, implying $\langle S_A^+\rangle = 0$.

Spin A can be intuitively interpreted as an effective drive acting on spin B mediated by the spin-spin coupling. Because of the additional coupling, $m_B^{(1)}$ depends on $\rho^{(2n)}$, and is therefore real. Thus, the above arguments that explain the interference blockade of spin A do not apply, and spin B is able to synchronize to the external drive. For $m_B^{(1)}$, only the terms of order $g_{AB}\Omega_A$ interfere destructively but terms of order $g_{AB}^3\Omega_A$ survive which we discuss in more detail in Sec. 8.3.2.

In Fig. 8.2, we plot the individual synchronization measures $S_1(\phi_A)$ and $S_1(\phi_B)$ as well as the combined measures $S_2(\phi_A, \phi_B)$ and $S_2(\phi_{AB} = \phi_A - \phi_B)$, that are defined in Sec. 8.2, evaluated for the numerically exact steady state of Eq. (8.2.1). As expected from Eqs. (8.3.10) to (8.3.12), both $S_1(\phi_A)$ and $S_2(\phi_{AB})$ show two maxima, see Figs. 8.2(c) and 8.2(d). These two distributions imply that spin A locks with two preferred phases to the drive and spin B locks with two preferred phases to spin A. Therefore, one could naively conclude that spin B also exhibits two maxima in its phase distribution. However, this is not true in general. Figure 8.2(b) shows that the maxima of the combined quantum synchronization measure lie at $(\phi_A, \phi_B) \in \{(0, 0), (\pi, 0)\}$, leading to the single maximum of $S_1(\phi_B)$, see Fig. 8.2(a).

In Fig. 8.3, we show moments that reflect the synchronization behavior, see Eqs. (8.2.15) and (8.2.16), for various drive and coupling strengths. As predicted by Eqs. (8.3.10) to (8.3.12), $S_1(\phi_B)$ exhibits a first moment, see Fig. 8.3(c). In contrast, the first moment vanishes for $S_1(\phi_A)$ and $S_2(\phi_{AB})$, see Figs. 8.3(a) and 8.3(b). All

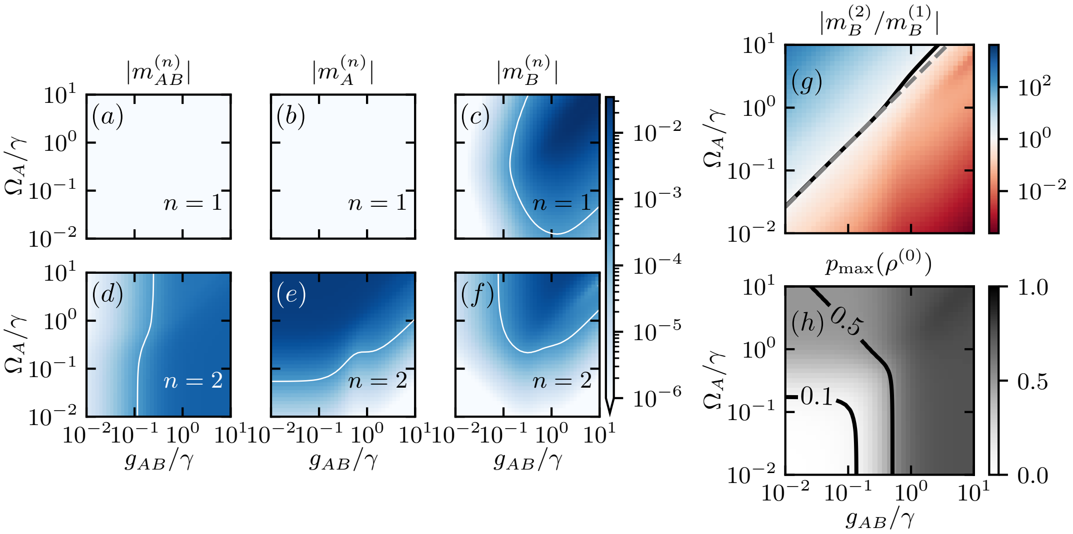

Figure 8.3: Synchronization in detail. (a)–(f) First ($n = 1$) and second ($n = 2$) moments indicating one and two maxima in the corresponding synchronization measures. The white curves are contour lines of the moments at 5×10^{-4}. (g) Ratio of the second and first moment of spin B. The black curve indicates $|m_B^{(2)}/m_B^{(1)}| = 1$ and the gray dashed lines denote the corresponding theoretical prediction $\Omega_A = 5\pi g_{AB}/6$ based on Eq. (8.3.12). (h) Maximum change of state populations, see Eq. (8.3.15).

synchronization measures show a two-maxima contribution, see Figs. 8.3(d) to 8.3(f). In Fig. 8.3(g), we plot the ratio of the second and first moment of the undriven spin B indicating that $S_1(\phi_B)$ exhibits predominantly two maxima if $\Omega_A \gg g_{AB}$ and one maximum if $\Omega_A \ll g_{AB}$. In Fig. 8.3(h), we show the maximum change in populations between the numerically obtained density matrix ρ^{ss} and a reference state $\rho = \rho^{(0)} = |0,0\rangle\langle 0,0|$ [Koppenhöfer and Roulet (2019)]

$$p_{\max}(\rho) = \max_n \left|\rho^{\mathrm{ss}}_{n,n} - \rho_{n,n}\right| . \tag{8.3.15}$$

It can be used to identify the regime of synchronization in which the limit-cycle state is only weakly perturbed, i.e., $p_{\max} \lesssim 0.1$, which we find to be $g_{AB}, \Omega_A \lesssim 0.1\gamma$. In this region, the fourth-order approximation agrees with the numerical results presented in Figs. 8.3(a) to 8.3(g). Moreover, entanglement measures are small below $g_{AB}/\gamma \lesssim 0.1$, see Sec. 8.5. The relation between quantum synchronization and entanglement has been studied for, e.g., spins [Roulet and Bruder (2018b), Chepelianskii and Shepelyansky (2024)] and harmonic oscillators [Mari et al. (2013), Lee et al. (2014), Garg et al. (2023)].

Note that if the gain and damping rates are chosen such that only one of either a drive-spin or a spin-spin interference blockade exists, this blockade does not persist up to large drive and coupling strengths: the drive-spin blockade is lifted by the spin-spin interaction and vice versa. Since in these cases $m_A^{(1)}$ and $m_{AB}^{(1)}$ are not zero, it is not surprising that also $m_B^{(1)}$ is not zero. Only when imposing both blockades simultaneously by equal gain and damping rates for all spins, as described in this section, the blockades persist.

8.3.2 Outside the Interference Blockade

In the previous section, synchronization is blockaded perfectly. We now discuss the behavior of the two-spin system for inverted gain and damping rates $\gamma_g^A = \gamma_d^B = \gamma_g$ and $\gamma_d^A = \gamma_g^B = \gamma_d$ close to the blockade. Here, both $m_A^{(1)}$ and $m_{AB}^{(1)}$ do not vanish. Considering the drive that acts on spin A as a small perturbation leads to the following leading-order contributions in Ω_A/γ,

$$\begin{aligned} m_A^{(1)} =& \mathrm{i}\frac{3\Omega_A}{16}\frac{\gamma_g-\gamma_d}{\gamma_g\gamma_d}\left(1-4g_{AB}^2\frac{(\gamma_g^2+4\gamma_g\gamma_d+\gamma_d^2)}{\gamma_g^2\gamma_d^2}+\mathcal{O}\left(\frac{g_{AB}^4}{\gamma_d^4}\right)\right), \qquad (8.3.16)\\ m_B^{(1)} =& \frac{3\Omega_A g_{AB}}{8\gamma_g\gamma_d}\left(\frac{(\gamma_d-\gamma_g)^2}{\gamma_g\gamma_d}+\mathcal{O}\left(\frac{g_{AB}^4}{\gamma_d^4}\right)\right.\\ &\left.+\, g_{AB}^2\frac{320\gamma_g^3\gamma_d^3+23(\gamma_g^4\gamma_d^2+\gamma_g^2\gamma_d^4)-32(\gamma_g^6+\gamma_d^6)-106(\gamma_g^5\gamma_d+\gamma_g\gamma_d^5)}{3\gamma_g^3\gamma_d^3(2\gamma_g+\gamma_d)(\gamma_g+2\gamma_d)}\right). \end{aligned}$$
(8.3.17)

The first moment of the combined synchronization measure,

$$\begin{aligned} m_{AB}^{(1)} =& \frac{\mathrm{i}9\pi g_{AB}(\overbrace{2(\gamma_d-\gamma_g)g_{AB}^2\gamma_g\gamma_d}^{\text{from }|0,1\rangle\langle 1,0|}+\overbrace{2(\gamma_d-\gamma_g)g_{AB}^2\gamma_g\gamma_d}^{\text{from }|-1,0\rangle\langle 0,-1|})/256}{32g_{AB}^6+\gamma_g^3\gamma_d^3+4g_{AB}^4(2\gamma_g^2+7\gamma_g\gamma_d+2\gamma_d^2)+g_{AB}^2\gamma_g\gamma_d(4\gamma_g^2+5\gamma_g\gamma_d+4\gamma_d^2)}\\ &\times\frac{(4g_{AB}^2+\gamma_g\gamma_d)(\overbrace{(g_{AB}^2+\gamma_g^2)\gamma_d}^{\text{from }|0,0\rangle\langle 1,-1|}-\overbrace{(g_{AB}^2+\gamma_d^2)\gamma_g}^{\text{from }|-1,1\rangle\langle 0,0|})}{32g_{AB}^6+\gamma_g^3\gamma_d^3+4g_{AB}^4(2\gamma_g^2+7\gamma_g\gamma_d+2\gamma_d^2)+g_{AB}^2\gamma_g\gamma_d(4\gamma_g^2+5\gamma_g\gamma_d+4\gamma_d^2)}\\ =& \frac{\mathrm{i}9\pi g_{AB}(\gamma_d-\gamma_g)(4g_{AB}^4+g_{AB}^2\gamma_g\gamma_d-\gamma_g^2\gamma_d^2)/256}{32g_{AB}^6+\gamma_g^3\gamma_d^3+4g_{AB}^4(2\gamma_g^2+7\gamma_g\gamma_d+2\gamma_d^2)+g_{AB}^2\gamma_g\gamma_d(4\gamma_g^2+5\gamma_g\gamma_d+4\gamma_d^2)}, \end{aligned}$$
(8.3.18)

is approximately constant in Ω_A/γ. The known interference blockades for $m_A^{(1)}$, $m_{AB}^{(1)}$, and the leading order of $m_B^{(1)}$ arise for $\gamma_g = \gamma_d$, see [Roulet and Bruder (2018a), Roulet and Bruder (2018b)] and Sec. 8.3.1. Note that the absolute values of the first moments $m_A^{(1)}$, $m_B^{(1)}$, and $m_{AB}^{(1)}$ are invariant under the exchange of the gain and damping rates. The contributions of the coherences $|i,j\rangle\langle k,l|$ to $m_{AB}^{(1)}$ are highlighted in the first line of Eq. (8.3.18). Terms originating from both $|0,1\rangle\langle 1,0|$ and $|-1,0\rangle\langle 0,-1|$ vanish individually, whereas terms proportional to $|0,0\rangle\langle 1,-1|$ and $|-1,1\rangle\langle 0,0|$ cancel in this interference blockade. For $m_B^{(1)}$, the coherences $|0,-1\rangle\langle 0,0|$ and $|0,0\rangle\langle 0,1|$ cancel with the coherences $|-1,0\rangle\langle -1,1|$ and $|1,-1\rangle\langle 1,0|$. Note that contributions to $m_B^{(1)}$ of order $g_{AB}^3\Omega_A$ and higher do not vanish for equal gain and damping rates, see Sec. 8.3.1. There, additional coherences $|1,0\rangle\langle 1,1|$ and $|-1,-1\rangle\langle -1,0|$ appear. The remaining terms of $m_B^{(1)}$ in the interference blockade can be interpreted as first-order

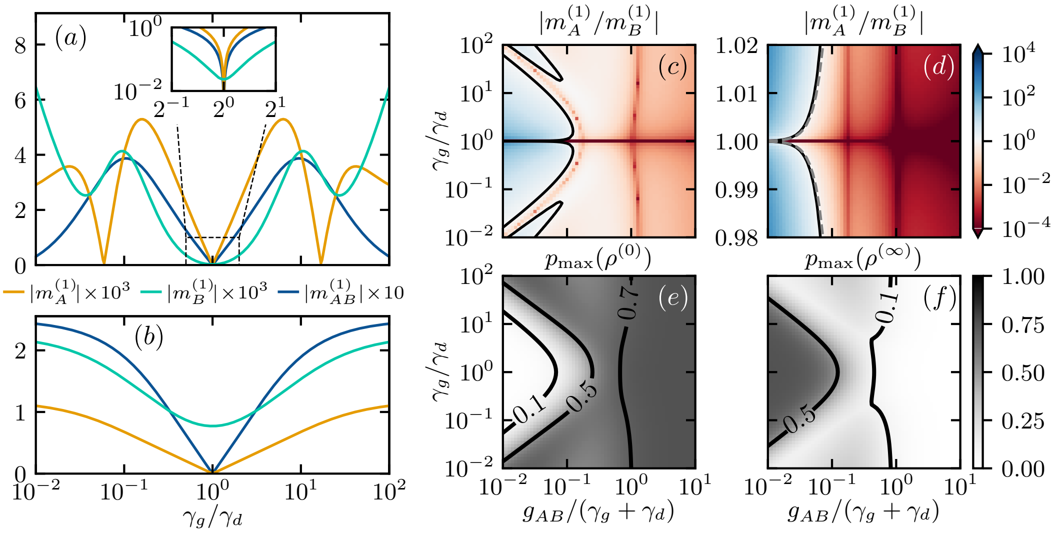

Figure 8.4: Synchronization of two spins 1 for inverted rates $\gamma_g^A = \gamma_d^B = \gamma_g$ and $\gamma_d^A = \gamma_g^B = \gamma_d$. (a), (b) First moments of the individual and combined synchronization measures for $\Omega_A/(\gamma_g+\gamma_d) = 10^{-3}$ and $g_{AB}/(\gamma_g+\gamma_d) = 0.05, 0.5$ (from top to bottom). The inset highlights the region close to the interference blockade $\gamma_g = \gamma_d$. (c), (d) Ratio of the first moments of spin A and B. The gray line corresponds to Eq. (8.3.19). (e), (f) Maximum change of state populations, see Eq. (8.3.15).

synchronization $\propto \Omega_A$ of the undriven spin B to the drive that acts on spin A mediated by a third-order spin-spin interaction $\propto g_{AB}^3$.

We show $m_A^{(1)}$, $m_B^{(1)}$, and $m_{AB}^{(1)}$ in Fig. 8.4. Whenever $\gamma_g \neq \gamma_d$, the symmetry defined by Eq. (8.3.13) is broken and the interference blockades disappear such that 1:1 drive-spin and spin-spin phase locking exist. Nevertheless, there is a regime in which $|m_A^{(1)}| < |m_B^{(1)}|$, see Fig. 8.4(d). Its width can be estimated by expanding the ratio of the first moments of spin A and spin B to first order in $\gamma_g/\gamma_d - 1$. This expansion can be used to approximately solve $|m_A^{(1)}/m_B^{(1)}| = 1$ by

$$\frac{\gamma_g}{\gamma_d} = 1 \pm \frac{20 g_{AB}^3}{3\gamma_d^3} + \mathcal{O}(g_{AB}^5/\gamma_d^5) \approx 1 \pm \frac{160 g_{AB}^3}{3(\gamma_g+\gamma_d)^3}\,. \tag{8.3.19}$$

The region in which the undriven spin B exhibits a stronger 1:1 phase locking to the drive than the driven spin A has an approximate width $\propto g_{AB}^3/\gamma_d^3$ in terms of the ratio of gain and damping rates γ_g/γ_d.

In addition to the interference blockade, i.e., vanishing $m_A^{(1)}$ and $m_{AB}^{(1)}$, between spin A and its drive as well as between both spins we find another synchronization blockade that is induced by the coupling. This new and additional blockade appears at zeros of $m_{AB}^{(1)}$ and $m_A^{(1)}$ for values of γ_g/γ_d depending on g_{AB}. The solution of $m_{AB}^{(1)} = 0$ for $g_{AB}, \gamma_g \ll \gamma_d$ can be obtained analytically,

$$\frac{\gamma_g}{\gamma_d} = \frac{1}{2}(1+\sqrt{17})\frac{g_{AB}^2}{\gamma_d^2} \approx \frac{1}{2}(1+\sqrt{17})\frac{g_{AB}^2}{(\gamma_g+\gamma_d)^2}\,. \tag{8.3.20}$$

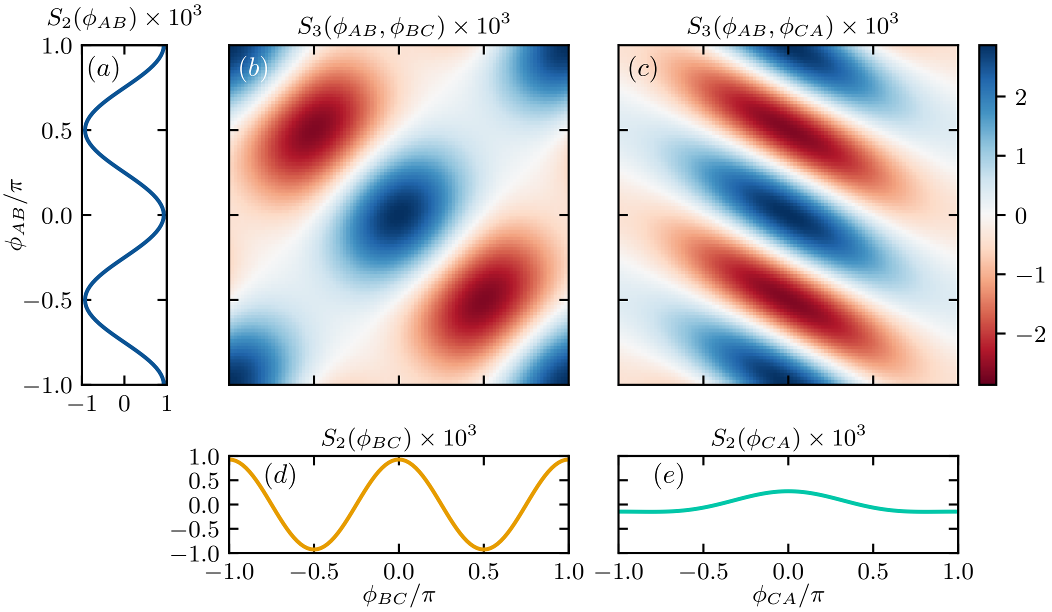

Figure 8.5: Synchronization measures S_2 and S_3, for $\gamma_g^j = \gamma_d^j = \gamma$ and $g_{AB} = g_{BC} = 0.12\gamma$. (b), (c) Combined measures S_3 for three coupled spin-1 oscillators, see Eqs. (8.2.12) and (8.2.13). (a), (d), (e) Combined measures S_2 for pairs of two spins 1, see Eq. (8.2.14). Even if both $S_2(\phi_{AB})$ and $S_2(\phi_{BC})$ exhibit two maxima, $S_2(\phi_{CA})$ only shows one maximum.

The approximate solution of $m_A^{(1)} = 0$ is obtained for (a) small $\gamma_g \ll \gamma_d$ and for (b) both small $g_{AB}, \gamma_g \ll \gamma_d$,

$$\frac{g_{AB}}{\gamma_g + \gamma_d} \overset{\text{(a)}}{\approx} 1.323\,, \tag{8.3.21}$$

$$\frac{\gamma_g}{\gamma_d} \overset{\text{(b)}}{\approx} \frac{2}{\sqrt{1+\sqrt{10}}} \frac{g_{AB}}{\gamma_g + \gamma_d}\,, \tag{8.3.22}$$

see Fig. 8.4(c). In the interference blockade $\gamma_g = \gamma_d = \gamma$, contributions to $m_{AB}^{(1)}$ originating from both $|0,1\rangle\langle 1,0|$ and $|-1,0\rangle\langle 0,-1|$ vanish individually up to first order in Ω_A/γ, whereas terms proportional to $|0,0\rangle\langle 1,-1|$ and $|-1,1\rangle\langle 0,0|$ cancel. In the coupling-induced blockade, these coherences cancel collectively.

The coupling-induced blockades occur for rather large coupling strengths for which the steady state of the system deviates significantly from $\rho^{(0)}$. In the regime $g_{AB} \gtrsim \gamma_g + \gamma_d$ one obtains $p_{\max}(\rho^{(\infty)}) \lesssim 0.1$, i.e., the steady state is close to $\rho^{(\infty)}$, see Fig. 8.4.

8.4 Three Undriven Spins

We now consider a chain of three undriven coupled spin-1 oscillators labeled A, B, and C,

$$H = \frac{g_{AB}}{2} S_A^+ S_B^- + \frac{g_{BC}}{2} S_B^+ S_C^- + \text{H.c.}\,, \tag{8.4.1}$$

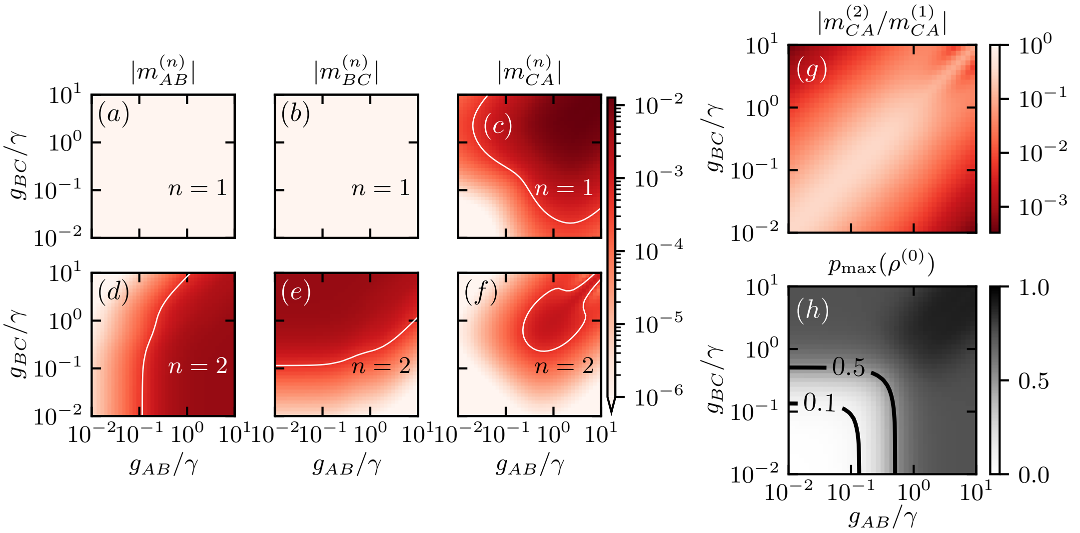

Figure 8.6: Synchronization in detail. (a)–(f) First ($n = 1$) and second ($n = 2$) moments indicating one and two maxima in the corresponding synchronization measures. The white curves are contour lines of the moments at 5×10^{-4}. (g) Ratio $|m_{CA}^{(2)}/m_{CA}^{(1)}| < 1$ of the second and first moment of the combined measure $S_2(\phi_{CA})$ of spins A and C. (h) Maximum change of a state populations, see Eq. (8.3.15).

where g_{AB} (g_{BC}) is the coupling strength between spins A and B (B and C). Similar to Sec. 8.3.1, all gain and damping rates are set equal to $\gamma_g^j = \gamma_d^j = \gamma$. In Fig. 8.5, we show both synchronization measures $S_3(\phi_{AB}, \phi_{BC})$ and $S_3(\phi_{AB}, \phi_{CA})$ evaluated for the numerically exact steady state of Eq. (8.2.1) for three spins. These measures are defined in Eqs. (8.2.12) and (8.2.13). Moreover, we present the synchronization measures S_2 between all three pairs of spins as marginals. As expected, $S_2(\phi_{AB})$ and $S_2(\phi_{BC})$ of both pairs of coupled spins exhibit two maxima due to the quantum interference synchronization blockade, see Figs. 8.5(a) and 8.5(d). However, similar to the single-maximum locking of the undriven spin B in Fig. 8.2(a), the synchronization measure between the spins A and C that are not directly coupled exhibits a single maximum in the phase difference ϕ_{CA}, see Fig. 8.5(e). This contradicts the naive expectation that if $S_2(\phi_{AB})$ and $S_2(\phi_{BC})$ exhibit two maxima, $S_2(\phi_{CA})$ will also exhibit two maxima. In fact, the synchronization measures $S_3(\phi_{AB}, \phi_{BC})$ and $S_3(\phi_{AB}, \phi_{CA})$ exhibit maxima at $(\phi_{AB}, \phi_{BC}, \phi_{CA}) \in \{(0, 0, 0), (\pi, \pi, 0)\}$ revealing the true locking behavior: the phases of neighboring spins are either aligned or anti-aligned.

In analogy to Fig. 8.3, we display relevant moments of the three-spin system in Fig. 8.6. Figures 8.6(a) and 8.6(b) show vanishing 1:1 phase locking between directly coupled spins. In contrast, Fig. 8.6(c) shows 1:1 phase locking between the spins A and C that are not directly coupled. Similar to what was found for the undriven spin B discussed in Sec. 8.3, the quantum synchronization measure between the uncoupled spins A and C exhibits both non-vanishing first and second moments. All synchronization measures exhibit a two-maxima contribution, see Figs. 8.6(d) to 8.6(f). Interestingly, in contrast to the setup of two spin-1 oscillators, Fig. 8.6(g) shows that the first moment always dominates, i.e., $|m_{CA}^{(2)}| < |m_{CA}^{(1)}|$. For $g_{AB}, g_{BC} \lesssim 0.1\gamma$, the maximum change of state populations $p_{\max} \lesssim 0.1$ is small, see Fig. 8.6(h).

8.5 Entanglement Measures

In this final section of this chapter, we look at entanglement measures for both cases described in Secs. 8.3 and 8.4: (i) two coherently coupled spin-1 oscillators, one of which is driven, and (ii) a chain of three coherently coupled spin-1 oscillators. We compute correlations

$$C_{ij}^{(n)} = \frac{\mathrm{COV}_{ij}^{(n)}}{\sqrt{\mathrm{COV}_{ii}^{(n)}\mathrm{COV}_{jj}^{(n)}}}\,, \tag{8.5.1}$$

$$\mathrm{COV}_{ij}^{(n)} = \langle (S_i^- S_j^+)^n \rangle - \langle S_i^{-n} \rangle \langle S_j^{+n} \rangle\,, \tag{8.5.2}$$

and entanglement measures

$$I_{ij} = S(\rho_i) + S(\rho_j) - S(\rho_{ij})\,, \tag{8.5.3}$$

$$\mathcal{N}_j(\rho) = \frac{||\rho^{T_j}||_1 - 1}{2} = \sum_k \frac{|\lambda_k| - \lambda_k}{2}\,, \tag{8.5.4}$$

where I_{ij} is the quantum mutual information, $S(\rho)$ is the von Neumann entropy, and $\mathcal{N}_j$ is the negativity. The eigenvalues of ρ^{T_j} are denoted by λ_k, where T_j indicates the partial transpose that only acts on subsystem j. Note that in a two-partite system, ρ^{T_A} and $\rho^{T_B} = (\rho^{T_A})^T$ have the same eigenvalues and therefore $\mathcal{N}_A = \mathcal{N}_B$. For quantum systems of dimensions larger than 2×3, a necessary condition of separability is zero negativity [Peres (1996), Horodecki et al. (1996)]. Therefore, $\mathcal{N}_j > 0$ implies entanglement. For mixed states, both entanglement and classical correlations contribute to the quantum mutual information I_{ij}.

We want to highlight the following features of correlations between both spins in the two-spin setup. In Figs. 8.7(b) and 8.7(c), both I_{AB} and $\mathcal{N}_A$ exhibit a local maximum between $0.1\gamma < g_{AB} < \gamma$ and below the gray dashed line that indicates the theoretical prediction $\Omega_A = 5\pi g_{AB}/6$ of $|m_B^{(2)}/m_B^{(1)}| = 1$. In this region, the first moment $m_B^{(1)}$ of the synchronization measure of spin B is larger than the second moment $m_B^{(2)}$, indicating 1:1 phase locking, and $p_{\max}(\rho^{(0)})$ exhibits a strong change, see Figs. 8.3(g) and 8.3(h). Therefore, the phase locking through the blockades corresponds to stronger correlations between the spins. Comparing all three panels Figs. 8.7(a) to 8.7(c), in this system, the mutual information I_{AB} appears to be a combination of correlations, e.g., $C_{AB}^{(2)}$, and entanglement.

In Figs. 8.7(d) to 8.7(l), we present the correlations, quantum mutual information, and negativity between pairs of spin-1 oscillators in the three-spin case. We define $\mathcal{N}_{ij}$ as the negativity of spin i evaluated for the reduced density matrix of the subsystem of spin i and j. The correlations, mutual information, and negativity of subsystem AB (BC) exhibit similar qualitative features, e.g., a local maximum of I_{ij} and $\mathcal{N}_{ij}$

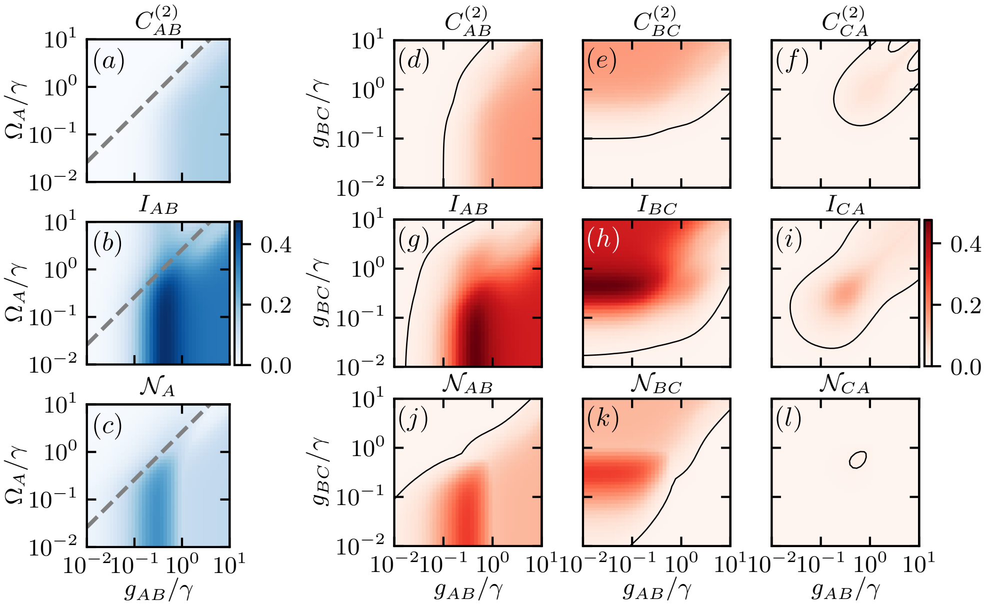

Figure 8.7: Correlation measures for two spins 1 (a)–(c) and three spins 1 (d)–(l). (a) Correlations $C_{AB}^{(2)}$ related to Figs. 8.3(d) to 8.3(f), see Eq. (8.5.2). (b) Quantum mutual information of spin A and B defined in Eq. (8.5.3). (c) Negativity of spin A, see Eq. (8.5.4). The gray dashed line denotes the theoretical prediction $\Omega_A = 5\pi g_{AB}/6$ of $|m_B^{(2)}/m_B^{(1)}| = 1$, see Fig. 8.3. (d)–(f) Correlations related to Figs. 8.6(d) to 8.6(f). (g)–(i) Quantum mutual information of pairs of spins. (j)–(l) Negativity $\mathcal{N}_{ij}$ of spin i evaluated for the reduced density matrix of the subsystem of spin i and j. The black curves are contour lines at 0.01. All measures are evaluated for the steady state of the Lindblad master equation.

between $0.1\gamma < g_{AB}$ $(g_{BC}) < \gamma$, like in the two-spin case. The measures of subsystem CA exhibit local maxima at $0.1\gamma < g_{AB}, g_{BC} < \gamma$. Here, qualitatively, the measures of the other two subsystems overlap.

8.6 Conclusion

In this chapter, we have analyzed setups of two and three coupled spin-1 oscillators in the parameter regime of equal gain and damping rates. In the case of three spins 1, this choice of rates leads to (spin-spin) quantum interference blockades between all coupled oscillators. In the case of two spins, a drive acting on spin A results in a second type of a (drive-spin) quantum interference blockade. Both blockades persist for arbitrarily large drive and coupling strengths.

In the two-spin setup, the blockades manifest themselves in the form of vanishing first moments of (i) the quantum synchronization measure of spin A as well as of (ii) the combined synchronization measure of both spins. Spin A synchronizes with equal probability in and out of phase with the drive with a magnitude proportional to the square of the drive strength Ω_A. Similarly, spin B locks in and out of phase to spin A with a magnitude proportional to the square of the coupling strength g. The naive expectation that spin B will therefore also lock with two preferred phases to the drive fails in general: the undriven spin B exhibits a 1:1 phase locking to the drive *through* both blockades without lifting them. The magnitude of this 1:1 phase locking is proportional to $g_{AB}^3\Omega_A$ corresponding to a first-order locking to the drive mediated by a third-order spin-spin interaction. Remarkably, the driven spin A exhibits no 1:1 phase locking. If the parameters are chosen such that only one of either a drive-spin or a spin-spin interference blockade exists, this blockade does not persist up to large drive and coupling strengths. The drive-spin blockade is lifted by the spin-spin interaction and vice versa. Only when imposing both blockades simultaneously by equal gain and damping rates for all spins, the blockades persist. The quantum synchronization effect described here is not observed for two quantum van der Pol oscillators since these oscillators do not exhibit the drive-spin blockade. Thus, the blockade between the oscillators is lifted by the drive, see Sec. 9.3. In the next chapter, we will study quantum synchronization between two quantum van der Pol oscillators, one of which is driven.

In a three-spin chain, the combined quantum synchronization measures of both pairs of directly coupled spins exhibit two maxima. However, similar to the two-spin case discussed in the previous paragraph, we observe a 1:1 phase locking behavior between the two not directly coupled spins A and C. Analogously, this locking exists without lifting the quantum interference blockades in the other two subsystems AB and BC.

Quantum synchronization thus provides a rich set of interesting features. Even for systems whose building blocks are the simplest possible quantum limit-cycle oscillators, unexpected properties arise like the locking of two not directly coupled spins mediated by an intermediate spin that is itself not locked. An intriguing question for the future is the study of the competition of single-maximum (indirect coupling) and two-maxima locking (direct coupling) in geometrically frustrated configurations of spin-1 oscillators. Another future research topic is to study quantum synchronization in a chain of three identical quantum van der Pol oscillators. Since in this case two blockades between both pairs of coupled oscillators exist, a similar effect of synchronization through the blockades might be observed.

The results and figures of this chapter have been published in parts in [Kehrer et al. (2024b)].

Chapter 9

Quantum Synchronization of Nonreciprocally Coupled Quantum van der Pol Oscillators

This chapter is based on the results published in:

T. Kehrer and C. Bruder,
Quantum synchronization blockade induced by nonreciprocal coupling,
Physical Review A **112**, 012223 (2025)

9.1 Motivation

In 1687, Newton's laws of motion have been published. The third law reads:

> "*Lex III: Actioni contrariam semper & æqualem esse reactionem: sive corporum duorum actiones in se mutuo semper esse æquales & in partes dirigi.*" [Newton (1687)] (latin for "Law III: To every Action there is always opposed an equal Reaction: or the mutual actions of two bodies upon each other are always equal, and directed to contrary parts." [Newton (1729)]).

In this sentence, so-called reciprocal interactions are described. In contrast, interactions between two agents A and B are called *nonreciprocal* if the response of A to an action of B differs from the response of B to an action of A. Nonreciprocal interactions can only appear in nonequilibrium systems [Ivlev et al. (2015)]. In particular, in active matter, i.e., systems composed of active agents [Ramaswamy (2010), Schweitzer (2019)], nonreciprocal interactions have been intensively studied in classical models. Prime examples of such active states are the so-called traveling-wave states. In nonreciprocal models like the Lotka-Volterra predator-prey model [Lotka (1920), Volterra (1926), Bacaër (2011)] these states are associated to two different agents, one of which (predator) is hunting the other (prey). More recently, phase transitions [Fruchart et al. (2021)] and frustration [Hanai (2024)] in systems of nonreciprocal oscillators

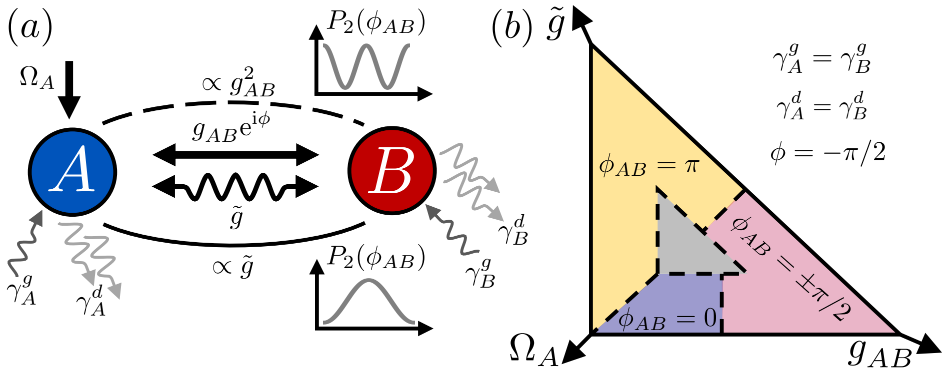

Figure 9.1: Schematic overview of two coherently and dissipatively coupled, driven oscillators A and B. (a) Each oscillator is subject to single-phonon gain and two-phonon loss. The coherent coupling $g_{AB}\mathrm{e}^{\mathrm{i}\phi}$ is denoted by a solid double arrow and the dissipative coupling $\tilde{g}$ by a wavy double arrow. An external drive Ω_A represented by a solid arrow is applied to A. The solid (dashed) arc visualizes (bistable) locking between the oscillators. The insets are qualitative plots of the combined synchronization measure P_2, an effective probability distribution of the relative phase ϕ_{AB}. (b) Schematic regions labeled by the steady-state values of ϕ_{AB} at which P_2 exhibits a maximum. Each corner/arrow head corresponds to the regime in which this parameter is large compared to the others. Dashed lines indicate approximate transitions.

have been investigated. First steps toward nonreciprocity in quantum systems have been taken, e.g., in non-Hermitian quantum mechanics [Hatano and Nelson (1996)], cascaded networks [Roth and Hammerer (2016), Lorenzo et al. (2022)], and topological networks [Wanjura et al. (2020), Wächtler and Platero (2023)]. Lately, investigations of the effects of nonreciprocal interactions on quantum synchronization have started [Nadolny et al. (2025a)].

In this chapter, we consider systems of two coupled quantum limit-cycle oscillators and study the interplay of three competing quantum synchronization mechanisms: phase locking, antiphase locking, and bistable locking. These three effects are induced by an external coherent drive that acts on one of the two quantum oscillators as well as by a coherent and dissipative coupling that yield an effective nonreciprocal interaction between the oscillators. The two couplings can be tuned such that the nonreciprocal interaction even becomes unidirectional [Metelmann and Clerk (2015)]. A schematic overview of the phase-locking regimes is presented in Fig. 9.1. To quantify quantum synchronization, we employ a common measure. We show that the effective interaction leads to synchronization blockades. One blockade occurs between the undriven oscillator and the external drive in the unidirectional case when oscillator A does not influence oscillator B. The second blockade occurs between both oscillators when the effective interaction is close to being unidirectional. A mean-field analysis reproduces this behavior. To understand this blockade in the quantum case, we make use of the quantum synchronization measure evaluated for a perturbation expansion of the steady state.

This chapter is structured as follows. In Sec. 9.2, we introduce the Lindblad master equation which describes the gain and damping processes that stabilize the quantum limit cycles and define suitable quantum synchronization measures. We start our analysis by considering two coherently coupled oscillators, one of which is driven externally, in Sec. 9.3. Then, we introduce a dissipative coupling and study its effect both in the absence and in the presence of the external drive in Sec. 9.4. After studying frequency synchronization in Sec. 9.5 we simulate quantum trajectories in Sec. 9.6. In Sec. 9.7, we analyze the blockades induced by the nonreciprocal interactions. In the last section, Sec. 9.8, we compare the phase diagram of our quantum model to the ones of classical analogues that are defined by the corresponding mean-field equations.

9.2 Model and Quantum Synchronization Measure

We consider two limit-cycle oscillators A and B, stabilized by single-phonon gain at rate γ_g^j and two-phonon damping at rate γ_d^j [Lee and Sadeghpour (2013)],

$$\frac{\mathrm{d}}{\mathrm{d}t}\rho = \dot{\rho} = \mathcal{L}(\rho) = -\mathrm{i}[H,\rho] + \tilde{\mathcal{L}}(\rho)\,, \tag{9.2.1}$$

$$\tilde{\mathcal{L}}(\rho) = \frac{\gamma_g^A}{2}\mathcal{D}[a^\dagger](\rho) + \frac{\gamma_g^B}{2}\mathcal{D}[b^\dagger](\rho) + \frac{\gamma_d^A}{2}\mathcal{D}[a^2](\rho) + \frac{\gamma_d^B}{2}\mathcal{D}[b^2](\rho)\,. \tag{9.2.2}$$

The operators $a^{(\dagger)} = a_A^{(\dagger)}$ and $b^{(\dagger)} = a_B^{(\dagger)}$ denote the annihilation (creation) operators of system A and B. The Hamiltonian H will be defined in the individual sections below and contains coherent drive and coupling terms. Later, we will introduce an additional dissipative coupling between both oscillators to create an effective unidirectional coupling. A schematic overview of the system is given in Fig. 9.1.

To study quantum synchronization phenomena in this model, we have to choose an appropriate quantitative measure of synchronization. In previous works, several measures have been defined [Ludwig and Marquardt (2013), Ameri et al. (2015), Hush et al. (2015), Weiss et al. (2016), Roulet and Bruder (2018a), Jaseem et al. (2020a)]. In the present study, we will follow [Hush et al. (2015), Weiss et al. (2016)] and consider effective probability distributions of phases of quantum oscillators. These distributions are based on the phase states [Barak and Ben-Aryeh (2005)], see also Eq. (7.1.6),

$$|\phi\rangle = \frac{1}{\sqrt{2\pi}}\sum_{n=0}^{\infty} \mathrm{e}^{\mathrm{i}n\phi}\,|n\rangle\ . \tag{9.2.3}$$

For a single oscillator, the measure P_1 is given by

$$\begin{aligned} P_1(\phi) &= \langle\phi|\,\rho\,|\phi\rangle - \frac{1}{2\pi} = \frac{1}{2\pi}\sum_{n,m=0}^{\infty} \mathrm{e}^{\mathrm{i}(m-n)\phi}\rho_{n,m} - \frac{1}{2\pi} \\ &= \frac{1}{2\pi}\sum_{k=1}^{\infty}\sum_{n=0}^{\infty}(\mathrm{e}^{\mathrm{i}k\phi}\rho_{n,n+k} + \mathrm{e}^{-\mathrm{i}k\phi}\rho_{n+k,n})\,, \end{aligned} \tag{9.2.4}$$

where $\rho_{n,m} = \langle n|\,\rho\,|m\rangle$. The sum over n in the last line of Eq. (9.2.4) covers all matrix elements that lie on the kth off-diagonal. The contribution for $m - n = 0$ reduces to $\mathrm{Tr}[\rho]/2\pi = 1/2\pi$ and cancels the second term in the first row of Eq. (9.2.4). The remaining matrix elements $\rho_{n+k,n} = \mathrm{Tr}\big[\tilde{a}^k\rho\big]$ and $\rho_{n,n+k} = \mathrm{Tr}\big[\tilde{a}^{\dagger k}\rho\big]$ in Eq. (9.2.4) are identified as expectation values of an operator $\tilde{a}$,

$$\tilde{a} = \sum_{n=0}^{\infty} |n\rangle\langle n+1| \,, \quad \tilde{a}^k = \sum_{n=0}^{\infty} |n\rangle\langle n+k| \,, \tag{9.2.5}$$

which is related to the Susskind-Glogower operator [Susskind and Glogower (1964)]. Therefore, this synchronization measure can be rewritten in a compact form,

$$P_1(\phi) = \mathrm{Tr}[p(\phi)\rho] - \frac{1}{2\pi} = \langle p(\phi)\rangle - \frac{1}{2\pi} = \frac{1}{2\pi}\sum_{k=1}^{\infty} \mathrm{e}^{-\mathrm{i}k\phi}\langle\tilde{a}^k\rangle + \mathrm{H.c.} \,, \tag{9.2.6}$$

where

$$p(\phi) = \frac{1}{2\pi}\mathbb{1} + \frac{1}{2\pi}\sum_{k=1}^{\infty}(\mathrm{e}^{-\mathrm{i}k\phi}\tilde{a}^k + \mathrm{H.c.}) \tag{9.2.7}$$

is similar to Eqs. (8.2.7) and (8.2.8). The moments of P_1,

$$m^{(n)} = \int_0^{2\pi} \mathrm{d}\phi\, P_1(\phi)\mathrm{e}^{\mathrm{i}n\phi} = \langle\tilde{a}^n\rangle \,, \tag{9.2.8}$$

that are linked to the discrete Fourier transformation of the phase distribution, are expectation values of powers of $\tilde{a}$. In Ch. 8, we have seen that moments are very useful for classifying different types of phase locking since they quantify the weight of the n-maxima term in the phase distribution. Therefore, they can be used to identify switches between e.g., phase locking and bistable phase locking.

In the following paragraphs, we want to gain a better understanding of the operator $\tilde{a}$. As an introductory example, let us study the expectation value of $\tilde{a}$ for an oscillator in a coherent state $|\alpha\rangle$,

$$\begin{aligned}\langle\alpha|\,\tilde{a}^k\,|\alpha\rangle &= \mathrm{e}^{-|\alpha|^2}\sum_{n,m,j=0}^{\infty}\frac{\alpha^{*n}\alpha^m}{\sqrt{n!m!}}\,\langle n|j\rangle\,\langle j+k|m\rangle = \mathrm{e}^{-|\alpha|^2}\sum_{n=0}^{\infty}\frac{\alpha^{*n}\alpha^{n+k}}{\sqrt{n!(n+k)!}}\\ &= \alpha^k\,\mathrm{e}^{-|\alpha|^2}\sum_{n=0}^{\infty}\frac{|\alpha|^{2n}}{n!\sqrt{(n+1)\dots(n+k)}} \,.\end{aligned} \tag{9.2.9}$$

Without the square root in the denominator, the series in Eq. (9.2.9) would equal the exponential function of $|\alpha|^2$. The expression for coherent states close to the origin, i.e., in the limit $|\alpha| \ll 1$, follows directly from a Taylor expansion,

$$\langle\alpha|\,\tilde{a}^k\,|\alpha\rangle \overset{|\alpha|\ll 1}{\approx} \frac{\alpha^k}{\sqrt{k!}} \,. \tag{9.2.10}$$

In this limit, $\tilde{a}$ effectively becomes a phase operator that measures the phase of a coherent state. In contrast to $S' = \langle a \rangle / \sqrt{\langle a^\dagger a \rangle}$, see Eq. (7.1.5), the expectation value $\langle \alpha | \, \tilde{a}^k \, | \alpha \rangle$ vanishes for coherent states located at the origin that are considered to show no form of quantum synchronization, i.e., no phase preference.

The limit of large $|\alpha| \gg 1$ is more subtle. From the inequality

$$\frac{\mathrm{e}^{|\alpha|^2} - 1}{|\alpha|^2} = \sum_{n=0}^{\infty} \frac{|\alpha|^{2n}}{n!(n+1)} \leq \sum_{n=0}^{\infty} \frac{|\alpha|^{2n}}{n!\sqrt{n+1}} \leq \sum_{n=0}^{\infty} \frac{|\alpha|^{2n}}{n!} = \mathrm{e}^{|\alpha|^2} , \tag{9.2.11}$$

one can naively guess that the expression in the center scales like $\propto \mathrm{e}^{|\alpha|^2}/|\alpha|$. For large $|\alpha| \gg 1$, terms of small n become less relevant. Using Stirling's approximation of the Gamma function $\Gamma(n+1) = n!$, see Eq. (8.327.2) of [Gradshteyn and Ryzhik (2015)],

$$\Gamma(n+1) \overset{n \gg 1}{\approx} \sqrt{2\pi n} \left(\frac{n}{\mathrm{e}} \right)^n , \tag{9.2.12}$$

we see that

$$\lim_{n\to\infty} \frac{\Gamma\left(n + \frac{k}{2} + 1\right)}{\Gamma(n+1)\sqrt{(n+1)\ldots(n+k)}} = \lim_{n\to\infty} \frac{\left(n + \frac{k}{2}\right)^{n+\frac{k}{2}}}{n^n \mathrm{e}^{\frac{k}{2}} n^{\frac{k}{2}}} = \lim_{n\to\infty} \frac{\mathrm{e}^{\frac{k}{2}}}{\left(1 + \frac{k}{2n}\right)^{n+\frac{k}{2}}} = 1 . \tag{9.2.13}$$

Therefore, the denominator in the last line of Eq. (9.2.9) can be replaced by $\Gamma(n + k/2 + 1)$,

$$\langle \alpha | \, \tilde{a}^k \, | \alpha \rangle \overset{|\alpha| \gg 1}{\approx} \alpha^k \, \mathrm{e}^{-|\alpha|^2} \sum_{n=0}^{\infty} \frac{|\alpha|^{2n}}{\Gamma\left(n + \frac{k}{2} + 1\right)} = \left(\frac{\alpha}{|\alpha|} \right)^k , \tag{9.2.14}$$

where in the last step the index shift $n \to n - k/2$ was used. Thus, for coherent states, the absolute value of $\langle \alpha | \, \tilde{a}^k \, | \alpha \rangle$ is upper bounded by S'. In conclusion, $\langle \alpha | \, \tilde{a} \, | \alpha \rangle$ measures the phase of coherent states. For large $|\alpha| \gg 1$, it is similar to S' and for small $|\alpha| \ll 1$ it vanishes linearly in α which is a more adequate behavior than S'.

Similar to Eq. (8.2.9), for a system containing N quantum oscillators, we consider the following synchronization measure,

$$P_N(\vec{\phi}) = \left\langle \vec{\phi} \middle| \, \rho \, \middle| \vec{\phi} \right\rangle - \frac{1}{(2\pi)^N} = \left\langle \bigotimes_{j=1}^{N} p(\phi_j) \right\rangle - \frac{1}{(2\pi)^N} , \tag{9.2.15}$$

that is based on tensor products of phase states

$$\left| \vec{\phi} \right\rangle = \bigotimes_{j=1}^{N} |\phi_j\rangle . \tag{9.2.16}$$

In Eq. (9.2.15), this measure is rewritten as tensor products of $p(\phi_j)$ defined in Eq. (9.2.7). Therefore, P_N contains terms with various combinations of $\mathrm{e}^{-\mathrm{i}k\phi_j} \tilde{a}_j^k$ and their Hermitian conjugates that act on the jth oscillator. Thus, the moments of the phase distributions P_N are given by expectation values of products of $\tilde{a}_j^{(\dagger)k_j}$.

The phase distribution measure $P_2(\phi_{AB})$ of the relative phase $\phi_{AB} = \phi_A - \phi_B$ of two oscillators reads

$$P_2(\phi_{AB}) = \int_0^{2\pi} \mathrm{d}\phi_B \, P_2(\phi_{AB} + \phi_B, \phi_B) = \frac{1}{2\pi} \sum_{k=1}^{\infty} \mathrm{e}^{-\mathrm{i}k\phi_{AB}} \langle (\tilde{a}_A \tilde{a}_B^\dagger)^k \rangle + \text{H.c.}\,, \tag{9.2.17}$$

similar to Eq. (8.2.11). Due to the operator structure of P_N mentioned above, we can define the moments of these phase distributions for individual phases ϕ_j and relative phases ϕ_{ij} as

$$m_j^{(n)} = \langle \tilde{a}_j^n \rangle\,, \tag{9.2.18}$$

$$m_{ij}^{(n)} = \langle (\tilde{a}_i \tilde{a}_j^\dagger)^n \rangle\,. \tag{9.2.19}$$

9.3 Coherently Coupled Oscillators

In previous work [Lee and Sadeghpour (2013)], two distinct cases have been studied: (i) a single driven limit-cycle oscillator and (ii) two coherently coupled identical limit-cycle oscillators, i.e, with gain and damping rates $\gamma_g^A = \gamma_g^B$ and $\gamma_d^A = \gamma_d^B$ but $\gamma_g^A \neq \gamma_d^A$. The single oscillator locks to the phase of the external drive with a phase shift of $-\pi/2$. Note that in the context of quantum synchronization the existence of a single maximum of the synchronization measure at ϕ_0 is referred to as ‘phase locking to ϕ_0’, i.e., this maximum does not need to be infinitely sharp. The two coherently coupled oscillators were found to be in the quantum synchronization blockade and exhibit *bistable* phase locking. These two cases are the harmonic-oscillator-like analogues of [Roulet and Bruder (2018a), Roulet and Bruder (2018b)], see also Sec. 7.2.2.

Here, we first consider the combination of both cases, i.e., two coherently coupled identical limit-cycle oscillators, one of which is driven externally. The spin-1 equivalent is discussed in the previous chapter. In the majority of the following sections, all gain and damping rates are set to be equal $\gamma_d^A = \gamma_d^B = \gamma_g^A = \gamma_g^B = \gamma$. For this choice, the oscillators are in the blockade and neither in the classical limit $\gamma_d^j \ll \gamma_g^j$ nor in the quantum limit $\gamma_d^j \gg \gamma_g^j$. The system is described by Eq. (9.2.1) and the Hamiltonian

$$H = \frac{\Omega_A}{2} a^\dagger + \frac{g_{AB}}{2} \mathrm{e}^{\mathrm{i}\phi} a^\dagger b + \text{H.c.}\,. \tag{9.3.1}$$

In the original description of the synchronization behavior of identical quantum limit-cycle oscillators [Lee and Sadeghpour (2013)], two separate locking mechanisms can be identified. First, a driven oscillator A tends to align its phase to the one of the external drive plus a shift of $-\pi/2$. In the limit where another coupled oscillator B identifies the driven oscillator A as an effective drive, the relative phase between both oscillators will be $\phi_{AB} = \phi_A - \phi_B = \phi + \pi/2$. The parameter ϕ is the complex phase of the coherent coupling between A and B, defined in Eq. (9.3.1). Second, the

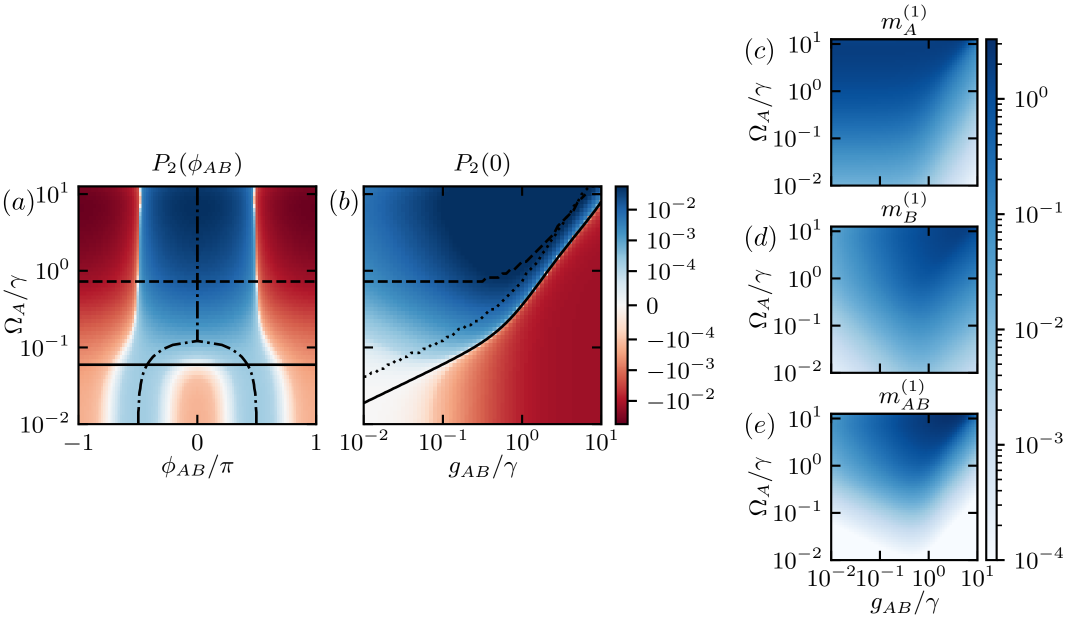

Figure 9.2: Probability distribution of the relative phase of two identical oscillators for $\phi = -\pi/2$ and $\tilde{g} = 0$. (a) Fixed interaction strength $g_{AB} = 0.1\gamma$. The dash-dotted black curve denotes the maxima of P_2. (b) $P_2(0)$ as a function of g_{AB}. The dotted black curve denotes the transition from two maxima to one maximum. In both panels (a) and (b), the color is scaled linear in the interval $[-10^{-4}, 10^{-4}]$ and logarithmic elsewhere. The dashed black curves indicate where $m_{AB}^{(2)} = 0$ and the solid black curves indicate where $|m_{AB}^{(1)}| = |m_{AB}^{(2)}|$. (c)–(e) First moments of the phase distributions $P_1(\phi_A)$, $P_1(\phi_B)$, and $P_1(\phi_{AB})$ showing lifting of the blockade.

probability distribution of the relative phase for two coherently coupled *undriven* oscillators will exhibit two maxima at different values $\phi_{AB} = \phi, \phi + \pi$. Therefore, these two locking mechanisms compete in the following sense: depending on the ratio of drive strength and coupling strength, the combined synchronization measure either exhibits one maximum or two maxima.

In Fig. 9.2, the transition from two maxima to one maximum of the combined synchronization measure for $\phi = -\pi/2$ is visualized. For small drive strengths, P_2 exhibits two maxima at $\phi_{AB} = \pm\pi/2$ that merge into a single maximum at $\phi_{AB} = 0$ for a sufficiently large drive strength. In Fig. 9.2(a) the dash-dotted black curve highlights local maxima of P_2, whereas in Fig. 9.2(b), the dotted curve indicates the point of transition from two maxima to one maximum. The maxima merge at values of Ω_A between the dashed black line where $m_{AB}^{(2)} = 0$ and the solid black line that indicates $|m_{AB}^{(1)}| = |m_{AB}^{(2)}|$. In Figs. 9.2(c) to 9.2(e), the non-vanishing first moments of $P_1(\phi_A)$, $P_1(\phi_B)$, and $P_1(\phi_{AB})$ are shown. An analogue of the drive-spin blockade of Ch. 8 does not exist for quantum van der Pol oscillators. Therefore, $m_A^{(1)}$ is not zero here. Moreover, the blockade between both oscillators $m_{AB}^{(1)} = 0$ only exists for small drive strengths, i.e., it is lifted by the drive. The effect that single blockades are lifted by another interaction has been mentioned in Sec. 8.3.1 for spin-1 oscillators.

9.4 Coherently and Dissipatively Coupled Oscillators

We now add a dissipative coupling $\tilde{g}\,\mathcal{D}[a+b](\rho)$ between the two oscillators to the Lindblad master equation Eq. (9.2.1). This dissipative coupling can be realized by introducing an auxiliary rapidly decaying cavity [Metelmann and Clerk (2015)], see Sec. 2.3.2. The Lindblad master equation of the full three-oscillator model reads

$$\begin{aligned}\dot{\rho} = &-\mathrm{i}\left[\frac{\Omega_A}{2}a^\dagger + \frac{g_{AB}}{2}\mathrm{e}^{\mathrm{i}\phi}a^\dagger b + \frac{g}{2}(b^\dagger c + c^\dagger a) + \text{H.c.}, \rho\right] + \frac{\kappa}{2}\mathcal{D}[c](\rho) \\ &+ \frac{\gamma_g^A}{2}\mathcal{D}[a^\dagger](\rho) + \frac{\gamma_g^B}{2}\mathcal{D}[b^\dagger](\rho) + \frac{\gamma_d^A}{2}\mathcal{D}[a^2](\rho) + \frac{\gamma_d^B}{2}\mathcal{D}[b^2](\rho)\,. \end{aligned} \tag{9.4.1}$$

Like in the previous section, the two quantum van der Pol oscillators that are denoted by the annihilation operators a and b are coherently coupled with strength g_{AB} and phase ϕ. Their gain and damping rates are defined as γ_g^j and γ_d^j. Oscillator A is driven by an external drive Ω_A. Furthermore, both oscillators are coherently coupled with strength g to a rapidly decaying cavity that is characterized by the operator c. The decay rate κ of the cavity is significantly larger than any other timescale of the system.

The Heisenberg equation of motion of the cavity operator c reads

$$\frac{\mathrm{d}}{\mathrm{d}t}c = -\mathrm{i}\frac{g}{2}(a+b) - \frac{\kappa}{4}c\,. \tag{9.4.2}$$

For $\kappa \gg \gamma_d^j, \gamma_g^j$ we can assume that the cavity reaches its steady state much faster than oscillator A and B. Therefore, we replace $c \to -2\mathrm{i}(a+b)g/\kappa$ obtained from Eq. (9.4.2) with $\mathrm{d}c/\mathrm{d}t = 0$ in Eq. (9.4.1) leading to

$$\frac{g}{2}(b^\dagger c + c^\dagger a) + \text{H.c.} \to 0\,, \tag{9.4.3}$$

$$\frac{\kappa}{2}\mathcal{D}[c](\rho) \to 2\frac{g^2}{\kappa}\mathcal{D}[a+b](\rho)\,. \tag{9.4.4}$$

In this limit, the system can be described effectively by two quantum van der Pol oscillators interacting dissipatively. The resulting Heisenberg equations of motion are

$$\frac{\mathrm{d}}{\mathrm{d}t}a = -\mathrm{i}\frac{\Omega_A}{2}\mathbb{1} - \frac{\mathrm{i}g_{AB}\mathrm{e}^{\mathrm{i}\phi} + \tilde{g}}{2}b + \frac{\gamma_g^A - 2\tilde{g}}{4}a - \frac{\gamma_d^A}{2}a^\dagger a^2\,, \tag{9.4.5}$$

$$\frac{\mathrm{d}}{\mathrm{d}t}b = -\frac{\mathrm{i}g_{AB}\mathrm{e}^{-\mathrm{i}\phi} + \tilde{g}}{2}a + \frac{\gamma_g^B - 2\tilde{g}}{4}b - \frac{\gamma_d^B}{2}b^\dagger b^2\,. \tag{9.4.6}$$

A cumulant expansion to lowest order yields the mean-field equations

$$\langle\dot{a}\rangle = -\mathrm{i}\frac{\Omega_A}{2} - \frac{\mathrm{i}g_{AB}\mathrm{e}^{\mathrm{i}\phi} + \tilde{g}}{2}\langle b\rangle + \frac{\gamma_g^A - 2\tilde{g} - 2\gamma_d^A|\langle a\rangle|^2}{4}\langle a\rangle\,, \tag{9.4.7}$$

$$\langle\dot{b}\rangle = -\frac{\mathrm{i}g_{AB}\mathrm{e}^{-\mathrm{i}\phi} + \tilde{g}}{2}\langle a\rangle + \frac{\gamma_g^B - 2\tilde{g} - 2\gamma_d^B|\langle b\rangle|^2}{4}\langle b\rangle\,. \tag{9.4.8}$$

The coupling between A and B depends on the two possible directions

$$g^{\mathrm{eff}}_{A\rightharpoonup B} = -\mathrm{i} g_{AB} \mathrm{e}^{-\mathrm{i}\phi} - \tilde{g}\,, \tag{9.4.9}$$

$$g^{\mathrm{eff}}_{A\leftharpoondown B} = -\mathrm{i} g_{AB} \mathrm{e}^{\mathrm{i}\phi} - \tilde{g}\,, \tag{9.4.10}$$

and becomes unidirectional for $g_{AB} = \tilde{g}$ and $\phi = \pm\pi/2$. The influence of oscillator B on A (A on B) vanishes for $g_{AB} = \tilde{g}$ and $\phi = (-)\pi/2$, i.e., the effective coupling becomes unidirectional.

The equations of motion of the amplitude and phase of the oscillators are obtained by using $\langle a_j \rangle = r_j \mathrm{e}^{\mathrm{i}\phi_j}$,

$$\dot{r}_A = -\frac{\Omega_A}{2}\sin(\phi_A) + \frac{\gamma_g^A - 2\tilde{g}}{4} r_A - \frac{\gamma_d^A}{2} r_A^3 - \frac{r_B}{2}\left(g_{AB}\sin(\phi_{AB}-\phi) + \tilde{g}\cos(\phi_{AB})\right), \tag{9.4.11}$$

$$\dot{r}_B = \frac{\gamma_g^B - 2\tilde{g}}{4} r_B - \frac{\gamma_d^B}{2} r_B^3 + \frac{r_A}{2}\left(g_{AB}\sin(\phi_{AB}-\phi) - \tilde{g}\cos(\phi_{AB})\right), \tag{9.4.12}$$

as well as

$$\dot{\phi}_A = -\frac{\Omega_A}{2r_A}\cos(\phi_A) - \frac{r_B}{2r_A}\left(g_{AB}\cos(\phi_{AB}-\phi) - \tilde{g}\sin(\phi_{AB})\right), \tag{9.4.13}$$

$$\dot{\phi}_B = -\frac{r_A}{2r_B}\left(g_{AB}\cos(\phi_{AB}-\phi) + \tilde{g}\sin(\phi_{AB})\right) \tag{9.4.14}$$

The dynamics of the relative phase obey

$$\dot{\phi}_{AB} = -\frac{\Omega_A}{2r_A}\cos(\phi_A) + \frac{\tilde{g}}{2}\left(\frac{r_A}{r_B} + \frac{r_B}{r_A}\right)\sin(\phi_{AB}) + \frac{g_{AB}}{2}\left(\frac{r_A}{r_B} - \frac{r_B}{r_A}\right)\cos(\phi_{AB}-\phi)\,. \tag{9.4.15}$$

9.4.1 No External Drive

In [Walter et al. (2015)], it has been shown that two dissipatively coupled quantum limit-cycle oscillators lock to a relative phase $\phi_{AB} = \pi$. This synchronization behavior is different to the one induced by a coherent coupling with complex phase $\phi = -\pi/2$, see Sec. 9.3. In Fig. 9.3(a), we present the combined synchronization measure for a fixed coherent coupling strength, whereas in Fig. 9.3(b), we vary both the coherent and dissipative coupling strengths to study the transition between both locking mechanisms at $\Omega_A = 0$. For increasing g_{AB} at fixed $\tilde{g}$, four consecutive changes occur that are shown in Fig. 9.3(b): the effective coupling becomes unidirectional (solid gray line), the second moment vanishes $m^{(2)}_{AB} = 0$ (dashed black curve), the two maxima of the combined synchronization measure originally at $\phi_{AB} = \pm\pi/2$ turn into a single maximum at $\phi_{AB} = \pi$ (dotted black curve), and the first and second moment become equal $|m^{(1)}_{AB}| = |m^{(2)}_{AB}|$ (solid black curve). Counterintuitively, the second moment does not vanish when the effective coupling becomes unidirectional; this feature will be studied in more detail in Sec. 9.7. For small g_{AB}, we recognize that the

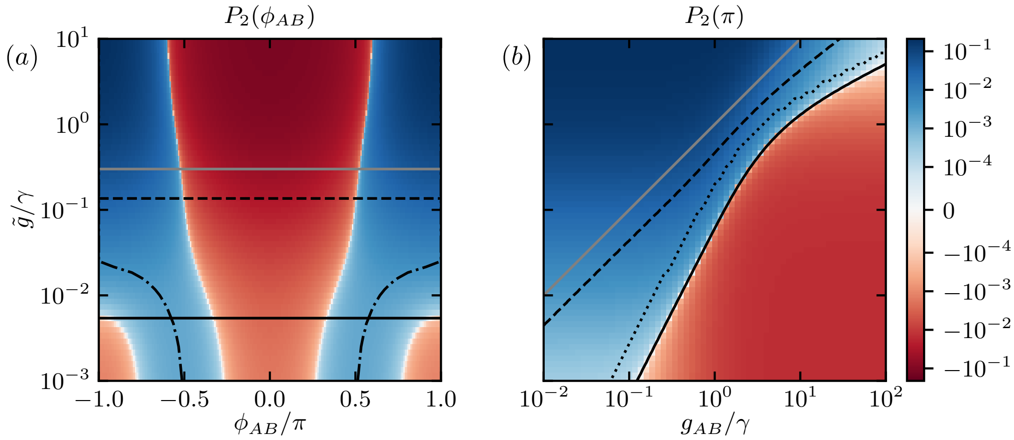

Figure 9.3: Combined synchronization measure P_2 for $\phi = -\pi/2$ and $\Omega_A = 0$. (a) Fixed interaction strength $g_{AB} = 0.3\gamma$. The dash-dotted black curves denote the maxima of P_2. (b) $P_2(\pi)$ as a function of g_{AB}. Here, the dotted curve denotes the transition from two maxima to one maximum of P_2. In both panels, the solid gray lines denote $\tilde{g} = g_{AB}$. The dashed black curves indicate where $m_{AB}^{(2)} = 0$ and the solid black curves indicate where $|m_{AB}^{(1)}| = |m_{AB}^{(2)}|$. The color is scaled linear in the interval $[-10^{-4}, 10^{-4}]$ and logarithmic elsewhere.

boundary between one and two locking phases follows the scaling $\tilde{g} \propto g_{AB}^2/\gamma$. This behavior is reproduced by the mean-field approximation presented in the following. The perturbative solution of the steady-state radii

$$r_j = r_j^{(0)} + \epsilon r_j^{(1)} = \sqrt{\frac{\gamma_g^j}{2\gamma_d^j}} + \epsilon r_j^{(1)}\,, \tag{9.4.16}$$

for $\Omega_A = 0$ reads

$$\epsilon r_A^{(1)} = -\frac{\tilde{g}}{\gamma_g^A}\left(r_A^{(0)} + r_B^{(0)}\cos(\phi_{AB})\right) - \frac{g_{AB}}{\gamma_g^A} r_B^{(0)} \sin(\phi_{AB} - \phi)\,, \tag{9.4.17}$$

$$\epsilon r_B^{(1)} = -\frac{\tilde{g}}{\gamma_g^B}\left(r_B^{(0)} + r_A^{(0)}\cos(\phi_{AB})\right) + \frac{g_{AB}}{\gamma_g^B} r_A^{(0)} \sin(\phi_{AB} - \phi)\,. \tag{9.4.18}$$

For equal rates $\gamma_g^A = \gamma_g^B = \gamma_d^A = \gamma_d^B = \gamma$, this leads to

$$\dot{\phi}_{AB} = \tilde{g}\sin(\phi_{AB}) - \frac{g_{AB}^2}{\gamma}\sin(2(\phi_{AB} - \phi))\,. \tag{9.4.19}$$

If $\tilde{g} \gg g_{AB}^2/\gamma$, a single stable solution $\phi_{AB} = \pi$ exists. If $\tilde{g} \ll g_{AB}^2/\gamma$, the system experiences bistable locking to $\phi_{AB} = \phi, \phi + \pi$. For $\phi = \pm\pi/2$, there are two stable solutions $\phi_{AB} = \pm\arccos\left(-\tilde{g}\gamma/2g_{AB}^2\right)$ if $\tilde{g} < 2g_{AB}^2/\gamma$ and there is a single stable solution $\phi_{AB} = \pi$ if $\tilde{g} > 2g_{AB}^2/\gamma$.

In the configuration of vanishing drive strength, the system exhibits several symmetries. First, a global U(1) symmetry, i.e., the invariance of the Liouvillian $\mathcal{L}$ under the transformation $a_j \to e^{i\theta} a_j$. The interaction term $a^\dagger b \to e^{-i\theta} a^\dagger e^{i\theta} b = a^\dagger b$ as well as the Lindblad dissipators $\mathcal{D}[L] \to \mathcal{D}[\mathrm{e}^{\mathrm{i}k\theta}L] = |\mathrm{e}^{\mathrm{i}k\theta}|\mathcal{D}[L] = \mathcal{D}[L]$ are independently invariant under this transformation. Second, for $\phi = 0, \pi$, the Liouvillian is invariant under the transformation $a \to \mathrm{e}^{\mathrm{i}\phi}b, b \to \mathrm{e}^{-\mathrm{i}\phi}a$. Here, $\mathrm{e}^{\mathrm{i}\phi}a^\dagger b + \mathrm{e}^{-\mathrm{i}\phi}ab^\dagger \to \mathrm{e}^{\mathrm{i}\phi}\mathrm{e}^{-\mathrm{i}\phi}b^\dagger\mathrm{e}^{-\mathrm{i}\phi}a + \mathrm{e}^{-\mathrm{i}\phi}\mathrm{e}^{\mathrm{i}\phi}a^\dagger\mathrm{e}^{\mathrm{i}\phi}b = \mathrm{e}^{\mathrm{i}\phi}a^\dagger b + \mathrm{e}^{-\mathrm{i}\phi}ab^\dagger$ as well as $\mathcal{D}[L]$ are invariant. Note that $a + b \to \mathrm{e}^{\mathrm{i}\phi}(a + \mathrm{e}^{-2\mathrm{i}\phi}b) = \mathrm{e}^{\mathrm{i}\phi}(a + b)$ for $\phi = 0, \pi$. Third, for $\phi = \pm\pi/2$, the Liouvillian is real $\mathcal{L} = \mathcal{L}^*$ which implies that the steady state $\rho_0 = \rho_0^*$ is also real. Following [Fruchart et al. (2021), Nadolny et al. (2025a)], this invariance can be interpreted as a generalized $\mathcal{PT}$ symmetry. In our setup, this symmetry is defined as the invariance under the consecutive transformations $a \leftrightarrow b$ and $g_{AB} \to -g_{AB}$. In other words, if the oscillators are exchanged, we arrive again at the same physics if the sign of g_{AB} is flipped too.

9.4.2 With External Drive

Here, we consider all three parameters Ω_A, g_{AB}, and $\tilde{g}$ to be nonzero. There are three competing synchronization effects: First, as described in Sec. 9.3, the external drive defines a preferred phase to which oscillator A locks with a phase shift of $-\pi/2$. If the coherent coupling with complex phase ϕ is small compared to the drive, it leads to a locking of oscillator B such that the relative phase results in $\phi_{AB} = \phi + \pi/2$. Second, the coherent coupling itself leads to a bistable locking of the relative phase to $\phi_{AB} = \phi, \phi + \pi$. Third, the dissipative coupling induces locking to $\phi_{AB} = \pi$.

Two cuts through the three-dimensional phase diagram at $\Omega_A = 0.2\gamma$ and $\Omega_A = 0.5\gamma$ are presented in Figs. 9.4(a) and 9.4(b). Three regions of the maxima $\pm\phi_{\max}$ of P_2 can be identified. First, the bottom left corner corresponds to a dominant drive where the ratio between $\tilde{g}$ and g_{AB} determines the relative phase ϕ_{AB}, i.e., 0 or π as explained in the beginning of this section and visualized in Fig. 9.1. Second, in the bottom right corner, in which the coherent coupling g_{AB} dominates, the combined synchronization measure experiences two maxima at $\phi_{AB} = \pm\pi/2$. Third, in the top left corner, where the dissipative coupling dominates, the relative phase reaches $\phi_{AB} = \pi$. Figures 9.4(c) and 9.4(d) show the combined synchronization measure along two line cuts in Fig. 9.4(b) where Fig. 9.4(c) corresponds to the dashed gray line and Fig. 9.4(d) corresponds to the solid gray line. In Fig. 9.4(e) we present the line cut shown in Fig. 9.4(d) as well as a fit of a model for $\phi_{\max}$. This model is defined as the maximum of P_m,

$$P_m(\phi_{AB}) = \left(u_1 \frac{g_{AB}\Omega_A^2}{\gamma^3} - u_3 \frac{\tilde{g}}{\gamma}\right)\cos(\phi_{AB}) + \frac{u_2\tilde{g}^2 - u_4 g_{AB}^2}{\gamma^2}\cos(2\phi_{AB})\,, \tag{9.4.20}$$

with $u_i > 0$. The parameter u_1 (u_3) corresponds to a maximum at 0 (π) and the parameter u_2 (u_4) corresponds to maxima at 0 and π (at $\pm\pi/2$). The powers of the parameters in P_m were obtained by a perturbation expansion of the steady state in the parameters g_{AB}, $\tilde{g}$, and Ω_A with respect to the equal gain and damping rates $\gamma_d^j = \gamma_g^j = \gamma$. For each of the two cosine terms in Eq. (9.4.20), we only consider the leading order of each parameter up to a combined third order. Since in this

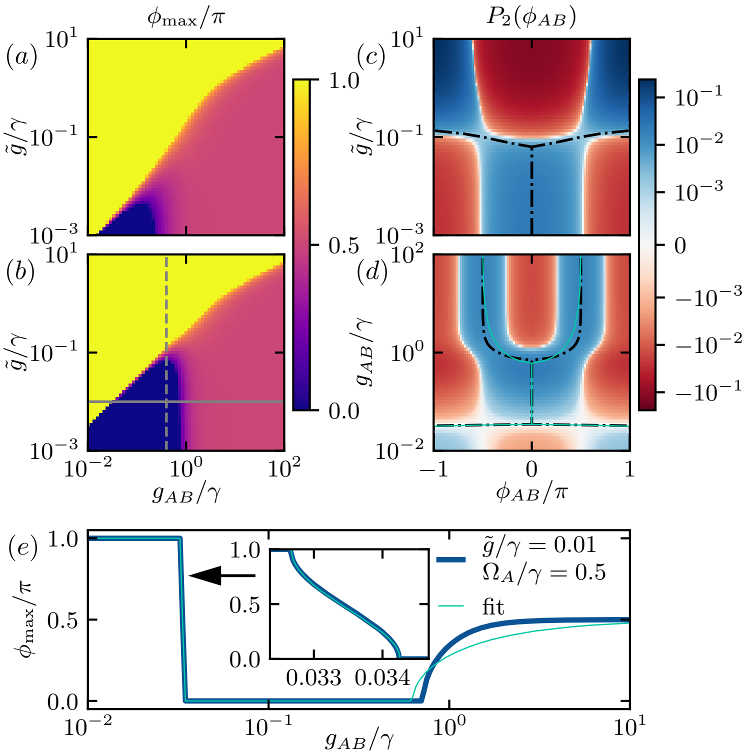

Figure 9.4: Visualization of different regimes of phase locking. The maxima of the combined synchronization measure P_2 are located at $\pm\phi_{\max}$. (a) $\Omega_A = 0.2\gamma$. (b) $\Omega_A = 0.5\gamma$. The dashed gray line indicates the line cut at $g_{AB} = 10^{-0.4}\gamma$ shown in (c) and the solid gray line indicates the line cut at $\tilde{g} = 0.01\gamma$ shown in (d). (c), (d) Combined synchronization measures along line cuts highlighted in (b). The dash-dotted black curves highlight the maxima of P_2. The thin light blue curve corresponds to a fit of the maximum of Eq. (9.4.20) to data of (d). (e) The thick blue curve corresponds to the line cut in (b) indicated by the solid gray line, i.e., the dash-dotted black curves in (d). The inset shows a zoom to the step-like change of $\phi_{\max}$.

calculation we truncate the Fock space at a finite occupation number, the values of u_j cannot be obtained. To get a rough estimate of these values, we fit the maximum of P_m to Fig. 9.4(e) at $\tilde{g}/\gamma = 0.01$. The fit $(u_1, u_2, u_3) \approx (11, 6.0, 8.8)u_4$ shows a good match with the numerical data for $g_{AB} \ll \gamma$. Note that this simple model is only suitable for small $\tilde{g}$ and g_{AB}. For large g_{AB}/γ, the transition of $\phi_{\max}$ from 0 to $\pi/2$ is captured qualitatively. The linear dependence $\tilde{g} \propto g_{AB}$ for which the second moment in Eq. (9.4.20) vanishes, see the dashed black curve in Fig. 9.3(b), appears to be valid even slightly above $g_{AB} = \gamma$. Moreover, for $\Omega_A = 0$, the equality of the first and second moment in Eq. (9.4.20) follows $\tilde{g} \propto g_{AB}^2/\gamma$ for small parameter values up to slightly above $g_{AB} = \gamma$, see the solid black curve in Fig. 9.3(b). For $\tilde{g} = 0$, the equality of the first and second moment implies $\Omega_A \propto \sqrt{g_{AB}}$ for small parameter values up to slightly below $g_{AB} = \gamma$, see Fig. 9.2.

9.5 Frequency Synchronization

Another perspective on these synchronization phenomena is provided by the study of frequency synchronization. In contrast to before, where we studied the phase synchronization of oscillators, we now compute their oscillation frequencies. The power spectrum

$$\mathcal{S}_{ij\ldots}(\omega) = \lim_{t\to\infty} \int_{-\infty}^{\infty} \mathrm{d}\tau \, C_{ij\ldots}(t,\tau) \mathrm{e}^{\mathrm{i}\omega\tau} \,, \tag{9.5.1}$$

is the Fourier transform of the two-time correlations

$$C_{AA}(t,\tau) = \langle a^\dagger(t+\tau) a(t) \rangle \,, \tag{9.5.2}$$

$$C_{BB}(t,\tau) = \langle b^\dagger(t+\tau) b(t) \rangle \,, \tag{9.5.3}$$

$$C_{ABAB}(t,\tau) = \langle b^\dagger(t+\tau) a(t+\tau) a^\dagger(t) b(t) \rangle \,, \tag{9.5.4}$$

in the steady-state limit $t \to \infty$. To approximate $\mathcal{S}_{AA}$ and $\mathcal{S}_{BB}$, we rewrite the Heisenberg equations of motion for $\Omega_A = 0$ of the τ-dependent operators as $\mathrm{d}\vec{v}/\mathrm{d}\tau = M\vec{v}$ where

$$M \approx \frac{1}{4} \begin{pmatrix} \gamma_g^A - 2\tilde{g} - 4\gamma_d^A n_A & 2(\mathrm{i} g_{AB} \mathrm{e}^{-\mathrm{i}\phi} - \tilde{g}) \\ 2(\mathrm{i} g_{AB} \mathrm{e}^{\mathrm{i}\phi} - \tilde{g}) & \gamma_g^B - 2\tilde{g} - 4\gamma_d^B n_B \end{pmatrix} \,, \tag{9.5.5}$$

$$\vec{v} = (\langle a^\dagger(t+\tau) a(t) \rangle, \langle b^\dagger(t+\tau) a(t) \rangle) \,, \tag{9.5.6}$$

and $n_j = \langle a_j^\dagger(t+\tau) a_j(t+\tau) \rangle$. Here, we approximate $\langle a^{\dagger 2}(t+\tau) a(t+\tau) a(t) \rangle \approx 2\langle a^\dagger(t+\tau) a(t+\tau) \rangle \langle a^\dagger(t+\tau) a(t) \rangle$ using a cumulant expansion of second order and the fact that in the limit $t \to \infty$, i.e., evaluating the expectation values in the steady state, $\langle a^{(\dagger)n}(t+\tau) \rangle = \langle a^{(\dagger)n}(t) \rangle = 0$. For equal rates $\gamma_g^j = \gamma_d^j = \gamma$, the two eigenvalues $\lambda_\pm$ of M read

$$\lambda_\pm = \frac{1}{4}(\gamma(1 - 2n_A - 2n_B) - 2\tilde{g}) \pm \frac{1}{2}\sqrt{\tilde{g}^2 - g_{AB}^2 + (n_A - n_B)^2 \gamma^2} \,. \tag{9.5.7}$$

For $n_A \approx n_B$, we can approximate the imaginary part of $\lambda_\pm$ by

$$\omega_\pm = \mathrm{Im}[\lambda_\pm] \approx \pm\sqrt{g_{AB}^2 - \tilde{g}^2}/2 \,. \tag{9.5.8}$$

The correlations $C_{AA}(t,\tau)$ and $C_{BB}(t,\tau)$ effectively measure the time evolution of the phases of the individual oscillators A and B. The correlation $C_{ABAB}(t,\tau)$ is used to obtain the time evolution of the relative phase between both oscillators. Fourier transforms of these three correlations can be used to distinguish between static and active steady states. In Figs. 9.5(a) to 9.5(f), we present $\mathcal{S}_{AA}(\omega_A)$, $\mathcal{S}_{BB}(\omega_B)$, and $\mathcal{S}_{ABAB}(\omega_{AB})$ for fixed $\tilde{g} = 0.01\gamma$ as a function of g_{AB}. The dashed curves denote the approximation $\omega_\pm$ and the dotted curves in Figs. 9.5(e) and 9.5(f) denote $2\omega_\pm$. For $\Omega_A = 0.5\gamma$ (bottom row), the individual spectra $\mathcal{S}_{AA}$ and $\mathcal{S}_{BB}$ exhibit an additional

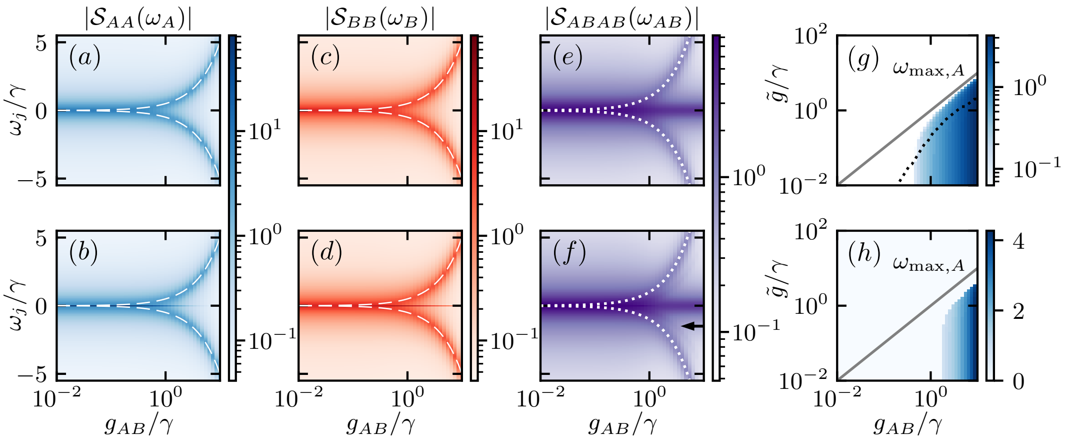

Figure 9.5: Power spectra defined in Eq. (9.5.1) for $\tilde{g} = 0.01\gamma$ as well as $\Omega_A = 0$ (top row) and $\Omega_A = 0.5\gamma$ (bottom row). (a)–(d) The white dashed curves correspond to $\omega_\pm$ of Eq. (9.5.8). (e), (f) The white dotted curves correspond to $2\omega_\pm$ and the arrow in (f) points at a local maximum that is close to $\omega_\pm$. (g), (h) Location of maxima of $\mathcal{S}_{AA}$. The black dotted curve in (g) equals the one in Fig. 9.3(b) and indicates the transition between a single maximum and two maxima in P_2.

local maximum at $\omega_j = 0$ ($j = A, B$) that fades out for $g_{AB} \gg \tilde{g}$. This maximum corresponds to the possibility that the oscillators lock to the frequency of the drive. In Fig. 9.5(f) a local maximum at $\omega_\pm$ is visible (black arrow) which can be interpreted as follows: one of the oscillators locks to the drive while the other one is oscillating at frequency $\omega_\pm$. Similar situations will be discussed for classical oscillators in Sec. 9.8.1.

We show the location of the maxima of $\mathcal{S}_{AA}$ in Figs. 9.5(g) and 9.5(h). The dotted curve in Fig. 9.5(g) is identical to the one in Fig. 9.3(b) and indicates the transition between a single maximum and two maxima in P_2. Below this curve, the relative phase between the oscillators locks to $\phi_{AB} \approx \pm\pi/2$. This region of bistable phase locking partially overlaps with the region of frequency locking to nonvanishing ω_j while the spectrum of the relative frequency has a dominating maximum at $\omega_{AB} = 0$. This partial overlap may be related to the fact that quantum states lock their phase and frequency only probabilistically: therefore, both effects can occur independently. In classical systems, states that exhibit a vanishing relative frequency also exhibit locking of their relative phase. States that feature both frequency locking to $\omega_j \neq 0$ and a vanishing relative frequency $\omega_{AB} = 0$ simultaneously are known as *traveling-wave* states. We will present exemplary time evolutions of such states and the phase diagram of the mean-field equations of multiple such oscillators in Sec. 9.8. Moreover, in Sec. 9.6, quantum trajectories of two coherently coupled and undriven oscillators that exhibit antiphase locking and traveling waves are shown.

The relation between phase and frequency locking of traveling-wave states is also analyzed in systems of nonreciprocally coupled groups of multiple spins 1/2 [Nadolny et al. (2025a)].

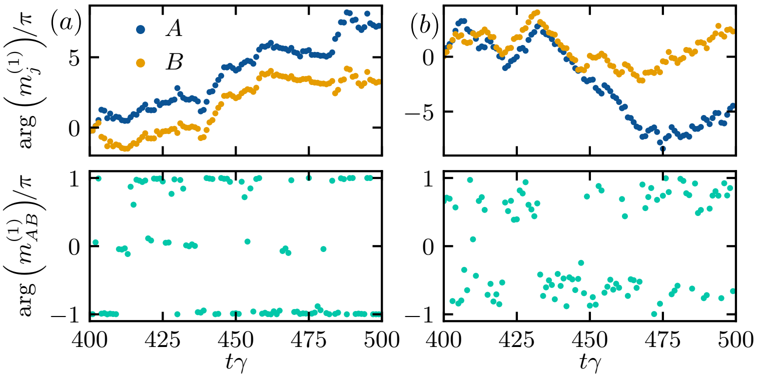

Figure 9.6: Quantum trajectories of two coherently coupled oscillators corresponding to Fig. 9.3. We set $\Omega_A = 0$ and $\tilde{g} = 0.01\gamma$. (a) Antiphase locking to $\phi_{AB} \approx \pi$ for $g_{AB} = 0.1\gamma$. (b) Bistable phase locking to $\phi_{AB} \approx \pm\pi/2$ for $g_{AB} = 2\gamma$. In the upper row, the complex phases are unwrapped: the difference between subsequent values never exceeds $\pm\pi$ due to added shifts of $\pm 2\pi$.

9.6 Quantum Trajectories

In addition to the steady-state analysis of the density matrix presented in Fig. 9.3, we simulate individual quantum trajectories. Following [Wiseman and Milburn (2009)], the stochastic quantum master equation reads

$$\begin{aligned} \mathrm{d}\rho_m = & -\mathrm{i}[H, \rho_m]\mathrm{d}t + \tilde{\mathcal{L}}(\rho_m)\mathrm{d}t + \tilde{g}\mathcal{D}[a+b](\rho_m)\mathrm{d}t \\ & + \sqrt{\tilde{g}}[(a+b-\mathrm{Tr}[(a+b)\rho_m])\rho_m + \mathrm{H.c.}]\mathrm{d}W\,, \end{aligned} \tag{9.6.1}$$

where the first line describes the deterministic part with $H = g_{AB}\mathrm{e}^{\mathrm{i}\phi}a^\dagger b/2 + \mathrm{H.c.}$ and $\tilde{\mathcal{L}}$ is defined in Eq. (9.2.2). In the second line, the stochastic part with Wiener increment $\mathrm{d}W$ originates from the dissipative interaction $\tilde{g}\mathcal{D}[a+b]$. As described in Sec. 9.4, this interaction is mediated by a lossy cavity. Monitoring the signal leaking out of this cavity leads to insights about the expectation value $\langle a+b\rangle$ that carries information about the relative phase ϕ_{AB}. The density matrix ρ_m is the state conditioned on the outcome of a measurement of $\langle a+b\rangle$. Numerically, we compute various operator expectation values using ρ_m. For the case $\Omega_A = 0$, we study the first moments $m_j^{(1)}$ of the individual operators as well as the first moment of the combined synchronization measure $m_{AB}^{(2)}$. Their complex argument effectively corresponds to ϕ_j and ϕ_{AB} and is shown in Fig. 9.6 for $\tilde{g} = 0.01\gamma$. For $g_{AB} = 0.1\gamma$ the relative phase locks to $\phi_{AB} \approx \pi$, whereas for $g_{AB} = 2\gamma$, bistable locking to $\phi_{AB} \approx \pm\pi/2$ occurs. In Fig. 9.6(b), one can furthermore identify the traveling-wave character, i.e., linearly increasing/decreasing phases ϕ_j, as well as a correlation between the signs of $\dot{\phi}_j$ and ϕ_{AB}. The quantum trajectories presented in Fig. 9.6 should be compared with the steady-state analysis shown in Figs. 9.3(b) and 9.5(g).

The quantum trajectories of the three cases along the gray line at $\tilde{g} = 0.01\gamma$ in Fig. 9.4(b) are presented in Fig. 9.7. The drive locks at least one of the oscillators close to $\phi_j \approx -\pi/2$. Therefore, (from left to right in Fig. 9.7) (i) antiphase locking

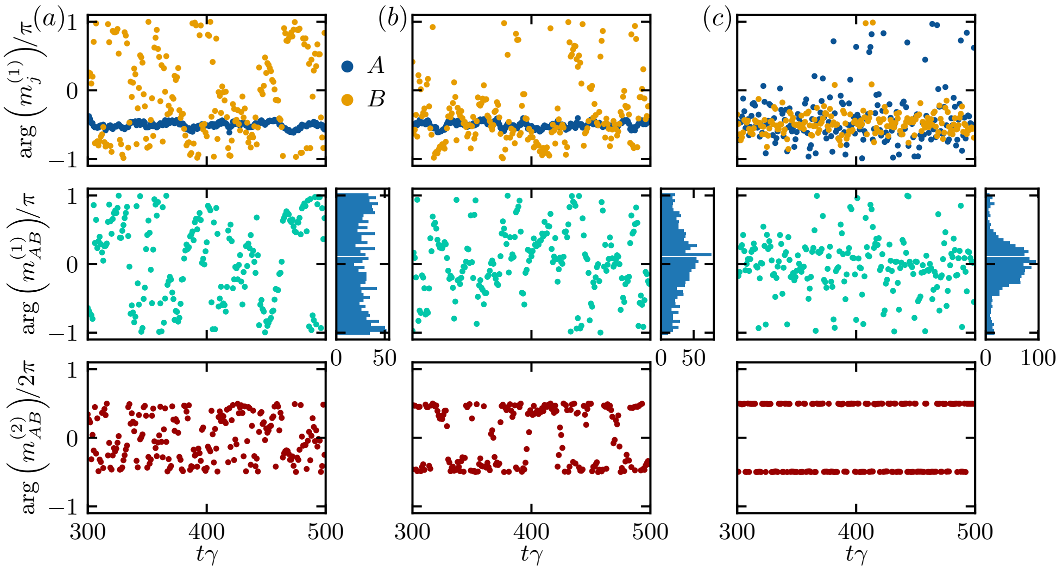

Figure 9.7: Quantum trajectories of two coherently coupled oscillators corresponding to Fig. 9.4(b). We set $\Omega_A = 0.5\gamma$ and $\tilde{g} = 0.01\gamma$. (a) Antiphase locking to $\phi_{AB} \approx \pi$ for $g_{AB} = 0.01\gamma$. (b) Phase locking to $\phi_{AB} \approx 0$ for $g_{AB} = 0.1\gamma$. (c) Both phase locking to $\phi_{AB} \approx 0$ *and* bistable phase locking to $\phi_{AB} \approx \pm\pi/2$ for $g_{AB} = 2\gamma$ can be identified, depending on which moment $m_{AB}^{(n)}$ is studied.

to $\phi_{AB} \approx \pi$, (ii) phase locking to $\phi_{AB} \approx 0$, and (iii) bistable phase locking to $\phi_{AB} \approx \pm\pi/2$ are not that prominent. Moreover, in the regime of bistable phase locking, see Fig. 9.7(c), due to the drive, the first moment $m_{AB}^{(1)}$ does not vanish. Thus, bistable locking can only be identified by analyzing the second moment $m_{AB}^{(2)}$. Here, drive-induced phase locking and bistable locking coexist which we have already seen in Fig. 9.5(f).

The bistable locking of the relative phase and the corresponding traveling-wave states have two configurations: $\phi_{AB} \approx \pm\pi/2$ corresponding to $\dot{\phi}_{AB} \gtrless 0$. Due to quantum fluctuations, the oscillators can switch between these configurations. In classical scenarios of two groups A and B [Fruchart et al. (2021)] as well as for two groups of many spins 1/2 [Nadolny et al. (2025a)], the switching rate depends on the number of agents in one group. For large numbers of agents, the switching is suppressed leading to a so-called nonreciprocal phase transition. In the sense of a finite-component phase transition [Hwang and Plenio (2016), Puebla et al. (2017), Hwang et al. (2018)], we consider the radius of an oscillator to be analogous to the number of agents in one group. The dependence of the number of switches on the radius of identical oscillators $\gamma_g^A = \gamma_g^B$ and $\gamma_d^A = \gamma_d^B$ is presented in Fig. 9.8. Depending on the overall noise strength that increases with both γ_g^A and γ_d^A, the number of jumps between the two configurations can increase or decrease with the theoretical radius $\sqrt{\gamma_g^A/2\gamma_g^A}$ and the measured radius $\langle a^\dagger a\rangle$: in Fig. 9.8, the red (purple) crosses correspond to varying γ_g^A/γ_d^A (γ_d^A/γ_g^A).

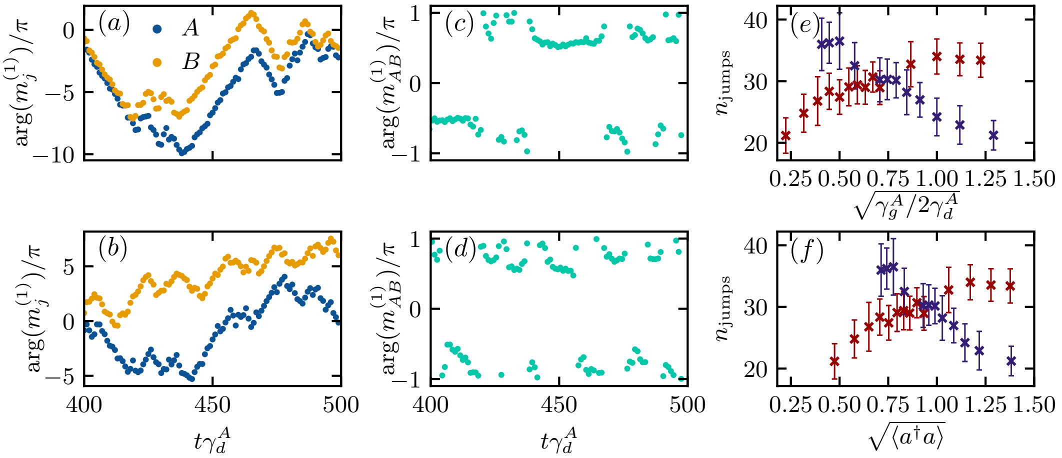

Figure 9.8: Dependence of switching rate for identical oscillators $\gamma_g^A = \gamma_g^B$ and $\gamma_d^A = \gamma_d^B$ without external drive $\Omega_A = 0$. (a), (c) Few switches for $\gamma_g^A = 0.1\gamma_d^A$. (b), (d) More switches for $\gamma_g^A = 3\gamma_d^A$. (e), (f) Vary γ_g^A for fixed $\tilde{g} = 0.1\gamma_d^A$ and $g_{AB} = 2\gamma_d^A$ (red) and vary γ_d^A for fixed $\tilde{g} = 0.1\gamma_g^A$ and $g_{AB} = 2\gamma_g^A$ (purple).

9.7 Blockades

If the first-order contribution to the synchronization measure of the relative phase of two coupled oscillators vanishes and the second-order contribution remains, the oscillators are in the so-called synchronization blockade. Here, since $m_{AB}^{(1)} = 0$, bistable locking of their relative phase corresponding to $m_{AB}^{(2)}$ (see the previous sections) is the leading order. This bistable locking can be interpreted to be mediated by an effective second-order interaction, see Eq. (9.4.19). Intuitively, information is carried back *and* forth between both oscillators. Therefore, we would expect the second moment $m_{AB}^{(2)}$ to vanish when at least one of the effective couplings $g_{A\rightarrow B}^{\text{eff}}$ or $g_{A\leftarrow B}^{\text{eff}}$ of Eqs. (9.4.9) and (9.4.10) vanishes: at $\phi = \pm\pi/2$ and $\tilde{g} = g_{AB}$. However, this is not the case. In Fig. 9.9(a), we show the second moment of the combined synchronization measure P_2. The two zeros of $m_{AB}^{(2)}$ at $\phi = \pm\pi/2$ can be approximated by the dashed gray line that denotes $\tilde{g} = g_{AB}/\sqrt{6}$. This approximation is based on Eq. (9.4.20), where the powers were obtained by a perturbation expansion up to third order in g_{AB}, $\tilde{g}$, and Ω_A. The prefactors were extracted from a fit of the maximum of P_m to numerical data presented in Fig. 9.4(e).

In Fig. 9.9(b), we show the dependence of the zero of $m_{AB}^{(2)}$ on the ratio γ_g^A/γ_d^A. Small values of this ratio correspond to the quantum limit, i.e., small radii of the quantum limit cycle meaning small amplitudes of the oscillator. We expand the steady state of identical oscillators with *different* gain and damping rates $\gamma_g^A = \gamma_g^B$ and $\gamma_d^A = \gamma_d^B$ up to second order in $\tilde{g}/\gamma_d^A$ and g_{AB}/γ_d^A. This leads to an approximation of the value of $\tilde{g}$ at which the second moment of the combined synchronization measure

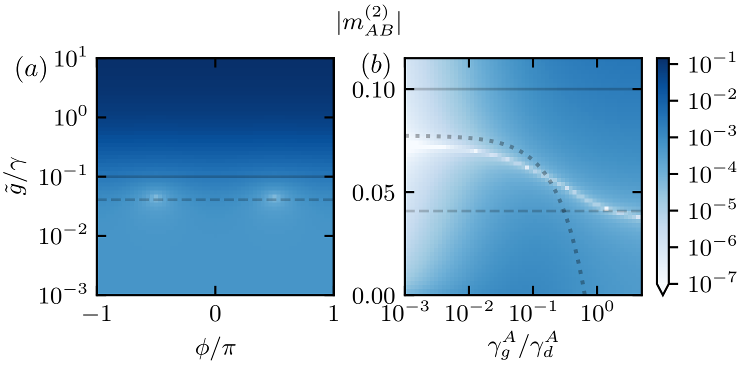

Figure 9.9: Second moment of the combined synchronization measure P_2 for $g_{AB} = 0.1\gamma_d^A$ and $\Omega_A = 0$. (a) Equal rates $\gamma_g^A = \gamma_g^B = \gamma_d^A = \gamma_d^B = \gamma$. (b) Identical oscillators with different rates $\gamma_g^A = \gamma_g^B$ and $\gamma_d^A = \gamma_d^B$ and $\phi = -\pi/2$. The dotted curve corresponds to the approximation defined in Eq. (9.7.1). In both panels, the solid line denotes $\tilde{g} = g_{AB}$ and the dashed line denotes $\tilde{g} = g_{AB}/\sqrt{6}$. The latter expression is obtained from Eq. (9.4.20).

vanishes: for $\gamma_g^A \ll \gamma_d^A$,

$$\tilde{g} \approx \sqrt{\frac{3}{5}} \left(1 - \frac{3\gamma_g^A}{40\gamma_d^A}(12 + 5\sqrt{3})\right) g_{AB} \,. \tag{9.7.1}$$

This approximation is shown in Fig. 9.9(b) as the dotted curve.

More insights into the quantum synchronization mechanisms of unidirectional coupling are obtained by considering an external drive acting on oscillator A. In Fig. 9.10, we show the first two moments of $P_2(\phi_{AB})$ and $P_1(\phi_B)$. For $\phi = -\pi/2$ and $\tilde{g} = g_{AB}$, the effective coupling $g_{A\rightharpoonup B}^{\mathrm{eff}}$ from oscillator A to B is zero, see Eq. (9.4.9). Therefore, naively, the influence of the drive on the undriven oscillator B vanishes. The zero in Fig. 9.10(b) confirms this prediction. This effect can be understood since the Heisenberg equation of motion for b is independent of a,

$$\frac{\mathrm{d}}{\mathrm{d}t} b = \frac{\gamma_g^B - 2\tilde{g}}{4} b - \frac{\gamma_d^B}{2} b^\dagger b^2 \,, \tag{9.7.2}$$

see Eq. (9.4.6). Analogously, Eq. (9.7.2) is invariant under the U(1) transformation $b \to \mathrm{e}^{\mathrm{i}\theta} b$ such that oscillator B shows no phase preference. However, the relative phase between A and B as well as the phase of A is locked. These effects can be understood intuitively by imagining a quantum trajectory of these *unidirectionally* interacting oscillators. Oscillator B evolves independently from A, but A is influenced by (the random jumps of) B. Thus, the relative phase ϕ_{AB} is locked even if ϕ_B is not. In this way, B can be interpreted as an additional noise source acting on A.

At fixed g_{AB}, $\phi = -\pi/2$, and $\Omega_A \neq 0$, increasing $\tilde{g}$ leads to switches from locking ($\phi_{AB} = 0$) to bistable locking and back to locking ($\phi_{AB} = \pi$), see Fig. 9.4(c). At some value close to $\tilde{g} = 5 g_{AB}\Omega_A^2/4$, indicated by the dashed line in Fig. 9.10(a), the relative phase between both oscillators exhibits bistable locking even if both phases lock to a single value individually. This approximation is obtained from Eq. (9.4.20). In

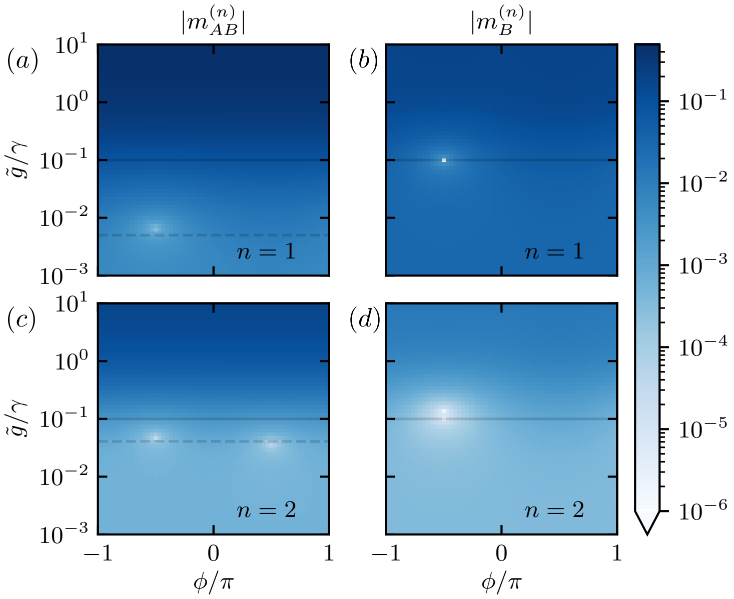

Figure 9.10: Moments of the combined and individual synchronization measures $P_2(\phi_{AB})$ and $P_1(\phi_B)$ for equal rates, $g_{AB} = 0.1\gamma$ and $\Omega_A = 0.2\gamma$. The solid line denotes $\tilde{g} = g_{AB}$. The dashed line in (a) corresponds to the approximation $\tilde{g} = 5g_{AB}\Omega_A^2/4$ and the one in (c) to $\tilde{g} = g_{AB}/\sqrt{6}$. Both lines are obtained from Eq. (9.4.20).

comparison to Fig. 9.9(b), the minima of the second moment $m_{AB}^{(2)}$ shown in Fig. 9.10(c) lie at different values of $\tilde{g}$: in the presence of the external drive the symmetry between $\phi = -\pi/2$ and $\phi = \pi/2$ is broken.

A perturbation expansion of the first and second moment of the synchronization measure of the undriven oscillator B to leading order in g_{AB}, $\tilde{g}$, and Ω_A yields

$$m_B^{(1)} = u_5 \frac{\mathrm{i}\tilde{g} - \mathrm{e}^{-\mathrm{i}\phi} g_{AB}}{\gamma^2} \Omega_A \,, \tag{9.7.3}$$

$$m_B^{(2)} = -(\mathrm{i}u_6\tilde{g} + u_7 \mathrm{e}^{-\mathrm{i}\phi} g_{AB}) \frac{\mathrm{i}\tilde{g} - \mathrm{e}^{-\mathrm{i}\phi} g_{AB}}{\gamma^4} \Omega_A^2 \,. \tag{9.7.4}$$

Both equations suggest a zero at $\tilde{g} = g_{AB}$ and $\phi = -\pi/2$. Within this approximation, the second zero in Fig. 9.10(d) can be explained by opposite signs of u_6 and u_7.

9.8 Classical Analogue

In this section, as a comparison to the phase diagram of the relative phase between the two quantum oscillators shown in Fig. 9.4(b), we will discuss the phase diagrams of the classical analogues of two and three quantum oscillators.

9.8.1 Two Oscillators

The phase diagrams of the relative phase between two quantum oscillators in the mean-field limit are obtained from Eqs. (9.4.7) and (9.4.8). These equations have

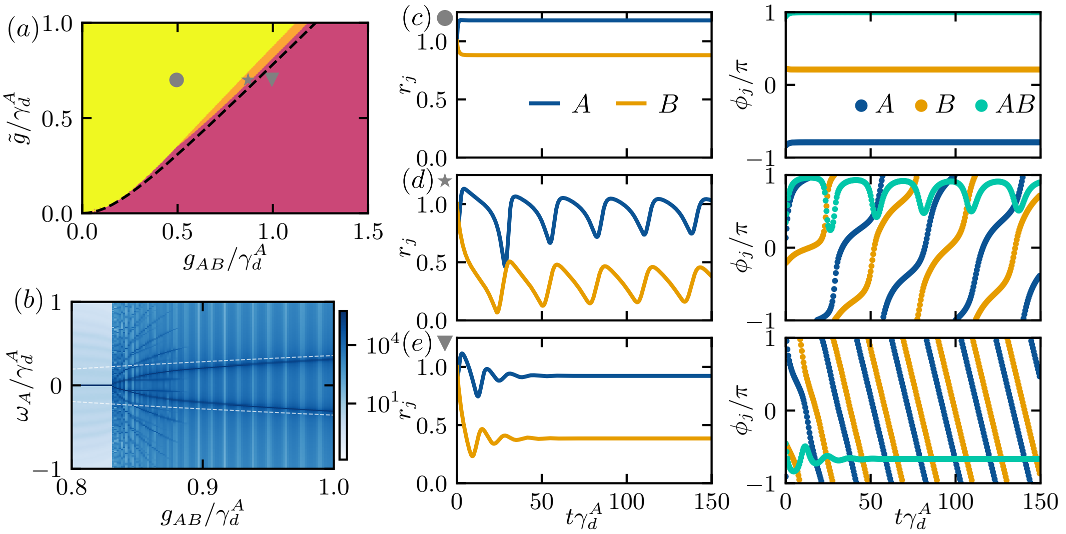

Figure 9.11: Two oscillators without external drive $\Omega_A = 0$ described by Eqs. (9.4.7) and (9.4.8). (a) Phase diagram where each color denotes a different phase. The dashed black curve corresponds to the approximate phase boundary between locking and bistable locking, see Eq. (9.8.1). (b) Spectrum $\mathcal{S}_{AA}(\omega_A)$ for $\tilde{g} = 0.7\gamma_d^A$ (location of symbols in (a)). The dashed white curve corresponds to $\omega_\pm$ defined in Eq. (9.5.8). In the regime of modulated traveling-wave states, i.e., the example presented in (d), several maxima exist. Panels (c) to (e) show the time evolutions of one phase each corresponding to the symbol next to the panel label. The values of g_{AB} and $\tilde{g}$ equal the coordinates of the respective symbol in (a). (c) Phase locking to $\phi_{AB} = \pi$. (d) Modulated traveling-wave states: varying amplitudes and oscillating relative phase around $\phi_{AB} \approx \pm\pi/2$. (e) Traveling-wave states: constantly increasing phases with fixed $\phi_{AB} \approx \pm\pi/2$. A list of rules and thresholds for each class of steady states is given in Sec. 9.8.3.

been studied in the context of exceptional points [Weis et al. (2023)]. The phase diagram for $\Omega_A = 0$ is presented in Fig. 9.11(a). As in the previous sections, we consider identical oscillators $\gamma_g^A = \gamma_g^B$ and $\gamma_d^A = \gamma_d^B$ as well as $\phi = -\pi/2$. To avoid vanishing linear gain that would lead to both oscillators collapsing to zero amplitude, we fix $\gamma_g^A - 2\tilde{g} = \gamma_d^A$. We identify the following regimes: (i) phase locking to $\phi_{AB} = \pi$, (ii) phase locking to $\phi_{AB} = 0$, (iii) traveling-wave states with $\phi_{AB} \approx \pm\pi/2$, and (iv) modulated traveling-wave states. If $g_{AB} = 0$ and $\tilde{g} > 0$, both oscillators want to lock to the other oscillator with $\phi_{AB} = \pi$. For small $g_{AB} \neq 0$ we expect bistable locking for $\tilde{g}$ smaller than $2g_{AB}^2/\gamma_g^A$, see Eq. (9.4.19), resulting in the boundary

$$\tilde{g} = \sqrt{g_{AB}^2 + (\gamma_d^A/4)^2} - \frac{\gamma_d^A}{4}\,. \tag{9.8.1}$$

This boundary corresponds to the dashed black curve in Fig. 9.11(a). The especially interesting so-called (modulated) traveling-wave states are identified by bistable locking of their relative phase and monotonic growing phases of oscillation. Traveling waves exhibit fixed amplitudes and modulated traveling waves exhibit varying amplitudes. Such active states have been studied in the context of nonreciprocal phase transitions [Fruchart et al. (2021), Hanai (2024), Nadolny et al. (2025a)]. The spectra

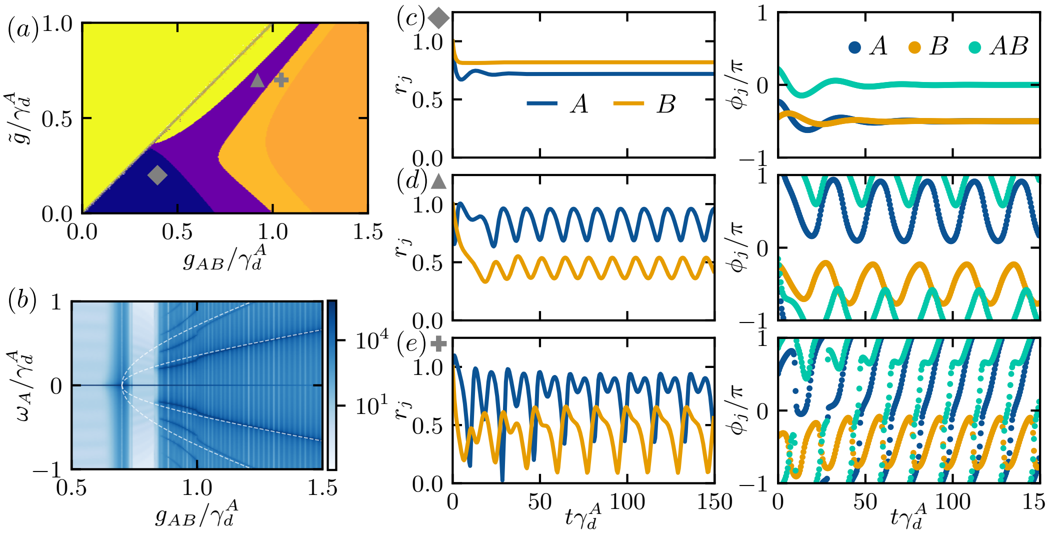

Figure 9.12: Two oscillators with external drive $\Omega_A = 0.5\gamma_g^A$ described by Eqs. (9.4.7) and (9.4.8). (a) Phase diagram where each color denotes a different phase. White pixels were not assigned any phase. The gray line denotes $\tilde{g} = g_{AB}$. (b) Spectrum $\mathcal{S}_{AA}(\omega_A)$ for $\tilde{g} = 0.7\gamma_d^A$ (location of upper symbols in (a)). The dashed white curves indicate $\omega_\pm$ and $2\omega_\pm$ defined in Eq. (9.5.8). Panels (c) to (e) show the time evolutions of one phase each corresponding to the symbol next to the panel label. The values of g_{AB} and $\tilde{g}$ equal the coordinates of the respective symbol in (a). (c) Phase locking to $\phi_A = \phi_B = -\pi/2$. (d) Wobble motion: varying amplitudes and oscillating phases around $\phi_{AB} \approx \pm\pi/2$. (e) Partial traveling-wave states: constantly increasing ϕ_A, oscillating ϕ_B around $-\pi/2$. The yellow phase (top left) corresponds to phase locking to $\phi_{AB} = \pi$, similar to Fig. 9.11(c), where for $\tilde{g} > g_{AB}$ ($\tilde{g} < g_{AB}$) $\phi_A = -\pi/2$ ($\phi_A = \pi/2$). The darker orange phase (center right) hosts modulated traveling-wave states, similar to Fig. 9.11(d). Videos of time evolutions are provided in [Kehrer (2025)]. A list of rules and thresholds for each class of steady states is given in Sec. 9.8.3.

of oscillators in such states show maxima at nonvanishing frequencies, see Fig. 9.11(b). Note that in the regime of modulated traveling waves, maxima at frequencies lower than the expected oscillation frequency appear. These are very likely related to the modulation frequencies of the variation of the amplitude and oscillation frequency.

More classes of steady states are found for nonvanishing drive strength Ω_A. The phase diagram of two oscillators for $\Omega_A = 0.5\gamma_d^A$ is shown in Fig. 9.12(a). Here, in addition to the regions of (i) locking to $\phi_{AB} = \pi$ (yellow, top left) and (ii) modulated traveling-wave states (darker orange, center right) known from Fig. 9.11, we find: (iii) locking to $\phi_A = \phi_B = -\pi/2$, (iv) wobble motion, and (v) partial traveling-wave states. The wobble motion is identified by varying phases ϕ_j within an interval smaller than 2π as well as varying amplitude, see Fig. 9.12(d). Our definition of the wobble motion also includes states that are assigned to the so-called swap phase discussed in [Fruchart et al. (2021)]. In the swap phase, the oscillators are aligned on a line and periodically switch between a static ϕ_j and $\phi_j + \pi$. To distinguish between the wobble motion and traveling waves, we use the following order parameter

$$S_{\mathrm{ori},j} = \frac{1}{\tau} \int\limits_{T}^{T+\tau} \mathrm{d}t \, \mathrm{sign}(\mathrm{Im}[\langle \dot{a}_j \rangle \langle a_j \rangle^*]) \,. \tag{9.8.2}$$

The integrand measures the orientation of rotation which is averaged over a time interval τ when the steady state is reached ($T\gamma_d^A \gg 1$). If the state switches between clockwise and counterclockwise rotation, i.e., varying phase around fixed values (wobble motion), $|S_{\mathrm{ori},j}|$ will be small. However, if a state does not change its orientation of rotation, $|S_{\mathrm{ori},j}|$ will be close to unity. This is the case for (modulated) traveling waves. In Fig. 9.12(e), we present an example trajectory of partial traveling-wave states. Here, only oscillator A performs full rotations ($|S_{\mathrm{ori},A}| \approx 1$), whereas oscillator B is still in a wobble motion ($S_{\mathrm{ori},A} \approx 0$). Remarkably, in this phase and for this choice of nonreciprocal coupling ($\phi = -\pi/2$), the undriven oscillator B is more localized to the phase $\phi_B \approx -\pi/2$ induced by the drive than the driven oscillator which is rotating monotonically. A similar behavior is found in the spectra of the quantum oscillators in Figs. 9.5(b) and 9.5(d), where the peak at $\omega_A = 0$ is less dominant than the peak at $\omega_B = 0$, and the quantum trajectories shown in Fig. 9.7(c). In [Kehrer (2025)][10], we provide videos of time evolutions for each phase that are shown in Figs. 9.12(c) to 9.12(e).

9.8.2 Three Oscillators

We also consider the next more complex system consisting of three oscillators. In Fig. 9.13(a), we present the phase diagram of an open chain of oscillators that obey

$$\langle \dot{a}_j \rangle = \frac{\gamma_g^j - 2\tilde{g} - 2\gamma_d^j |\langle a_j \rangle|^2}{4} \langle a_j \rangle - \frac{G_{j,j+1}}{2} \langle a_{j+1} \rangle - \frac{G_{j,j-1}}{2} \langle a_{j-1} \rangle \,. \tag{9.8.3}$$

Here, we set $\gamma_d^j = \gamma_d^A$ and fix $\gamma_g^j - 2\tilde{g} = \gamma_d^A$. The couplings

$$G_{j,j+1} = G_{j,(j+1)\,\mathrm{mod}\,3} = \tilde{g} + g_- \,, \tag{9.8.4}$$

$$G_{j,j-1} = G_{j,(j-1)\,\mathrm{mod}\,3} = \tilde{g} - g_- \,, \tag{9.8.5}$$

are chosen identical for each oscillator and g_- corresponds to $\mathrm{i}g_{AB}\mathrm{e}^{\mathrm{i}\phi}$ and $\phi = -\pi/2$.

In the open chain, $G_{C,A} = G_{A,C} = 0$ vanish. The phase diagram of the open chain is rich: (i) phase locking to $\Delta\phi_j = \phi_j - \phi_{j+1} = \pi$, (ii) phase locking to $\Delta\phi_j = 0$, (iii) traveling waves, (iv) modulated traveling waves, (v) wobble motion, and (vi) both wobble motion and traveling waves. To distinguish states performing the wobble motion and fully rotating traveling-wave states, in addition to $S_{\mathrm{ori},j}$, we employ the

---

[10] Direct link: https://tobias-kehrer.github.io/thesis/two_classical_nonrecip/ [Accessed: July 26, 2025]

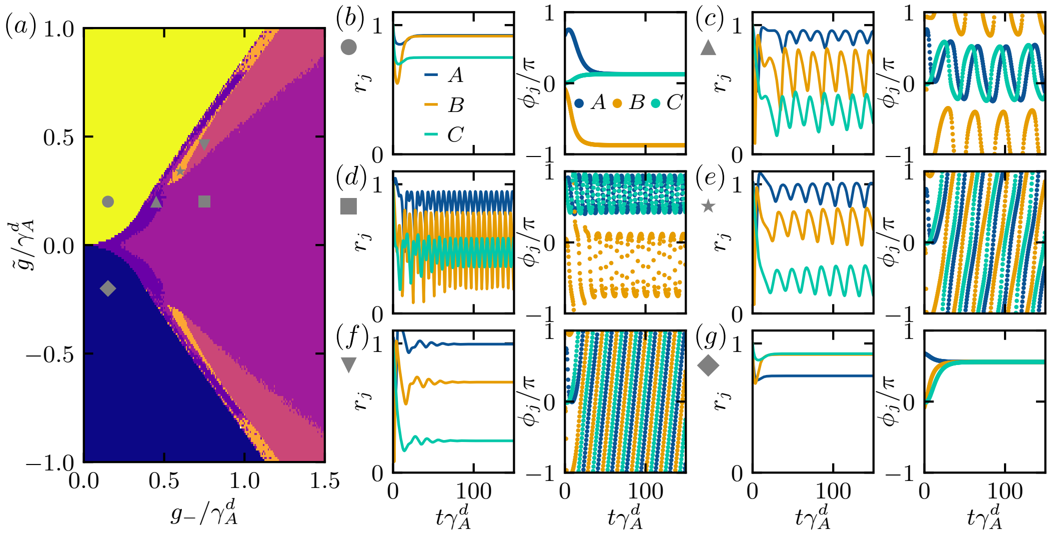

Figure 9.13: Open chain of three oscillators described by Eq. (9.8.3). (a) Phase diagram where each color denotes a different phase. White pixels were not assigned any phase. Panels (b) to (g) show the time evolutions of one phase each corresponding to the symbol next to the panel label. The values of g_- and $\tilde{g}$ equal the coordinates of the respective symbol in (a). (b) Phase locking to $\Delta\phi_j = \phi_j - \phi_{j+1} = \pi$. (c) Wobble motion: varying amplitudes and oscillating phases around $\Delta\phi_j \approx \pi$. (d) Both wobble motion (c) and traveling-wave states (f) exist. (e) Modulated traveling-wave states: varying amplitudes and oscillating phases around $\Delta\phi_j \approx \pm 2\pi/3$. (f) Traveling-wave states: constantly increasing phases with fixed $\Delta\phi_j \approx \pm 2\pi/3$. (g) Phase locking to $\Delta\phi_j = 0$. Videos of time evolutions are provided in [Kehrer (2025)]. A list of rules and thresholds for each class of steady states is given in Sec. 9.8.3.

following order parameter

$$S_{\mathrm{rot},j} = \left| \frac{1}{\tau} \int_{T}^{T+\tau} \mathrm{d}t \, \mathrm{e}^{\mathrm{i}\phi_j} \right| . \tag{9.8.6}$$

It is the magnitude of a time average of the complex phase factors when the steady state is reached ($T\gamma_d^A \gg 1$). The order parameter $S_{\mathrm{rot},j}$ reaches values close to zero for fully rotating (modulated) traveling-wave states, values close to one for static states, and values in between for states performing a wobble motion. For each pixel in Fig. 9.13(a), we generate time evolutions of 100 random initial states $\langle a_j \rangle = \exp(\mathrm{i}\phi_j)$ that are drawn from a uniform distribution over the interval $\phi_j \in [0, 2\pi]$. In [Kehrer (2025)][11], we provide videos of time evolutions for each phase that are shown in Figs. 9.13(b) to 9.13(g).

9.8.3 Order Parameter Thresholds

Here, we list the thresholds and rules to identify the different classes of steady states shown in Figs. 9.11 to 9.13. Other order parameters are: (i) SD_ϕ, the standard

---

[11] Direct link: https://tobias-kehrer.github.io/thesis/three_classical_nonrecip/ [Accessed: July 26, 2025]

deviation of the oscillator phases over time, (ii) SD_a, the standard deviation of the oscillator amplitudes over time. Both order parameters were averaged over all oscillators. The rules for both two-oscillator cases presented in Sec. 9.8.1 are listed in Tab. 9.1.

class	without drive	with drive
static ϕ_A and ϕ_B	$\mathrm{SD}_\phi < 1$	$S_{\mathrm{rot},A} > 0.99 \wedge S_{\mathrm{rot},B} > 0.99$
traveling wave	$\mathrm{SD}_\phi > 1 \wedge \mathrm{SD}_a < 0.01$	-
modulated traveling wave	$\mathrm{SD}_\phi > 1 \wedge \mathrm{SD}_a > 0.01$	$\lvert S_{\mathrm{ori},A}\rvert > 0.9 \wedge \lvert S_{\mathrm{ori},B}\rvert > 0.9$ $\wedge\, S_{\mathrm{rot},A} < 0.99$
partial traveling wave	-	$\lvert S_{\mathrm{ori},A}\rvert > 0.9 \wedge \lvert S_{\mathrm{ori},B}\rvert < 0.9$ $\wedge\, S_{\mathrm{rot},A} < 0.99$
wobble motion	-	$\lvert S_{\mathrm{ori},A}\rvert < 0.9 \wedge \lvert S_{\mathrm{ori},B}\rvert < 0.9$ $\wedge\, S_{\mathrm{rot},A} < 0.99$

Table 9.1: Order parameter rules for two oscillators corresponding to Figs. 9.11 and 9.12.

To distinguish steady states in the three-oscillator case presented in Sec. 9.8.2, we generate time evolutions of 100 random initializations. Out of these time evolutions, a histogram of $|S_{\mathrm{ori},A} + S_{\mathrm{ori},B}|$ with 40 bins in the range $[0, 1]$ is obtained: $S_{\mathrm{hist},k}$, where $k \in [1, 40]$ corresponds to the kth bin. The rules for the three-oscillator case presented in Sec. 9.8.2 are listed in Tab. 9.2.

class	rules
static ϕ_A and ϕ_B	$\mathrm{SD}_a < 10^{-3} \wedge S_{\mathrm{hist},40} > 0$
traveling wave	$\mathrm{SD}_a < 10^{-3} \wedge S_{\mathrm{hist},1} > 99$
modulated traveling wave	$\mathrm{SD}_a > 10^{-3} \wedge S_{\mathrm{hist},1} > 99$
wobble motion	$\mathrm{SD}_a > 10^{-3} \wedge \mathrm{SD}_\phi > 0.1$ $\wedge\, S_{\mathrm{hist},1} = 0$
wobble motion and traveling waves	$0 < S_{\mathrm{hist},1} < 100$

Table 9.2: Order parameter rules for three oscillators corresponding to Fig. 9.13.

9.9 Conclusion

We have investigated the interplay of three phase-locking mechanisms of two quantum limit-cycle oscillators induced by an external drive, a coherent coupling, and a dissipative coupling leading to three different steady-state configurations. In this setup, the effective nonreciprocal interaction can be tuned to be unidirectional. For increasing nonreciprocity at zero drive strength, the following sequence of events occurs: (i) interaction terms in the mean-field equations become unidirectional, (ii) the second moment of the combined quantum synchronization measure vanishes, (iii) a switch from phase locking to bistable locking occurs, and (iv) the first and second moment of the combined quantum synchronization measure become equal. Interestingly, unidirectionality does not coincide with the switch from locking to bistable locking.

Varying all three interaction parameters of the model, i.e., the drive strength of an external signal acting on one of the two oscillators, the magnitude of a coherent coupling, and the strength of a dissipative interaction, we have shown that the steady-state value of the relative phase between the oscillators can be tuned. Making use of the quantum synchronization measure evaluated for a perturbation expansion of the steady state in the three parameters drive strength, coherent coupling, and dissipative interaction, we have qualitatively explained the transitions between the three regimes of phase localization. This perturbation expansion has been used to identify magnitude minima of the second moment of the synchronization measure of the relative phase. Moreover, regions of bistable locking partially overlap with regions in which two-time correlations exhibit a periodic time dependence similar to traveling-wave states. Such traveling-wave states have also been found as steady-state solutions of the mean-field approximation of the master equation of the quantum system. For two and three noreciprocally coupled oscillators in the mean-field limit, we have found highly nontrivial active states by defining suitable order parameters.

Nonreciprocity in (open) quantum systems and their classical analogues is a rapidly emerging field in nonlinear quantum physics. Future research directions include the study of (frustrated) networks of $N \geq 3$ quantum oscillators as well as their (potentially existing) nonreciprocal phase transitions. Their classical analogues exhibit rich phase diagrams too. Future studies might focus, e.g., on the comparison of open and closed chains or on the dependence of the phase diagram on the number of oscillators.

The results and figures of this chapter have been published in parts in [Kehrer and Bruder (2025)].

Chapter 10

Quantum Synchronization of Oscillators Hosting Multiple Limit Cycles

This chapter is based on the results published in:

T. Kehrer, C. Bruder, and P. Solanki,
Quantum Synchronization of Twin Limit-Cycle Oscillators,
Physical Review Letters **135**, 063601 (2025)

10.1 Motivation

All studies of classical and quantum synchronization presented in the previous chapters consider oscillators that host a single limit cycle. While classical systems with multiple limit cycles and distinct basins of attraction, known as Liénard systems [Liénard (1928), Perko (2001), Leonov and Kuznetsov (2013)], have been investigated in detail, synchronization in their quantum analogue has not yet been studied before [Kehrer et al. (2025)]. Their amplitude dynamics can be described by an effective potential $V(r)$, see Fig. 10.1(a), where the number of limit cycles is given by the number of local minima. Depending on the initial state, the system converges to one of the limit cycles unless acted on by a noise source that is strong enough to induce switching events.

While there has been an increasing interest in quantum systems featuring multiple separate limit cycles [Marquardt et al. (2006), Wu et al. (2013), Bhattacharyya et al. (2021), Ruby and Lakshmanan (2024), Kumar et al. (2024), Chia et al. (2025)], their synchronization properties have not been studied before [Kehrer et al. (2025)]. In this chapter, we introduce a quantum Liénard system where two limit cycles *coexist* in a single steady state regardless of the initial conditions and investigate their synchronization behavior. We call this system a twin limit cycle (TLC): it is characterized by a double ring-like structure in phase space as sketched in Fig. 10.1(b). The location of the minima (maxima) of the effective potential of the corresponding

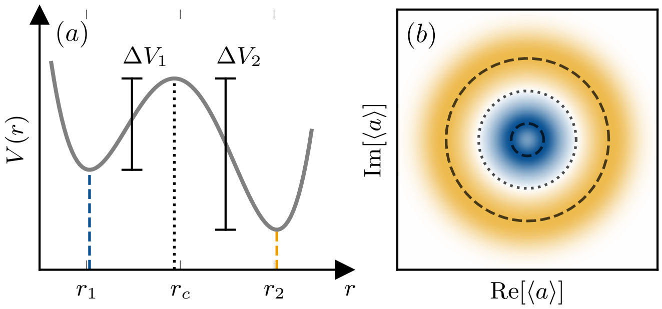

Figure 10.1: Illustration of a system with two limit cycles. (a) Sketch of the effective potential $V(r)$ of a classical Liénard system featuring two basins of attraction separated at r_c. (b) Wigner function of a twin limit cycle, a quantum Liénard system with $\langle a\rangle = r\mathrm{e}^{\mathrm{i}\phi}$. The dashed (dotted) rings with radii r_1 and r_2 (r_c) correspond to the local minima (maximum) of the effective potential obtained from the mean-field equations of motion, see Eq. (10.2.6).

classical Liénard system is indicated by the dashed (dotted) rings. Our setup can be extended to host multiple limit cycles. We examine the synchronization of a single TLC under an external coherent drive and find that the limit cycles exhibit different locking behaviors. Furthermore, for two coupled identical TLCs, both synchronization and blockade effects coexist, an apparent paradoxical interplay unattainable with standard limit cycles. To distinguish the contributions of individual limit cycles of a TLC, we define new finer measures of quantum synchronization. Finally, we outline an experimental setup to implement our model.

This chapter is structured as follows. First, we define the quantum TLC oscillator in Sec. 10.2. Second, in Sec. 10.3, we study the mean-field equations as classical oscillators that host twin limit cycles before considering a single driven TLC oscillator in Sec. 10.4. The complex synchronization between two TLCs is presented in Sec. 10.5. We suggest experimental realizations in Sec. 10.6.

10.2 Model

In the first sections of this chapter, we consider a coherently driven anharmonic quantum oscillator subject to incoherent first and third-order pumping, along with second and fourth-order damping. These dissipative processes stabilize two concentric limit cycles, see Fig. 10.1(b). The dynamics in the rotating frame of the drive is described by the master equation

$$\dot{\rho} = \mathcal{L}(\rho) = -\mathrm{i}[H_0 + H_d, \rho] + \gamma_1\mathcal{D}[a^\dagger](\rho) + \gamma_2\mathcal{D}[a^2](\rho) + \gamma_3\mathcal{D}[a^{\dagger 3}](\rho) + \gamma_4\mathcal{D}[a^4](\rho)\,, \tag{10.2.1}$$

where $\mathcal{D}[L](\rho) = L\rho L^\dagger - (L^\dagger L\rho + \rho L^\dagger L)/2$ is the Lindblad dissipator, $H_0 = \Delta a^\dagger a + K a^{\dagger 2} a^2$, $H_d = \Omega(a + a^\dagger)$, and a ($a^\dagger$) denote the annihilation (creation) operators of the oscillator. The detuning between the TLC and the drive is denoted by Δ, K parametrizes the Kerr nonlinearity, and Ω denotes the strength of the drive. The rates γ_j correspond to incoherent gain (odd j) and damping (even j). For $\gamma_3 = \gamma_4 = 0$, the model simplifies to the paradigmatic quantum van der Pol oscillator with a single limit cycle. Additional incoherent processes of higher order, $\mathcal{D}[a^{\dagger n}](\rho)$ and $\mathcal{D}[a^m](\rho)$, with n (m) being odd (even), can be included to obtain multiple limit cycles.

We obtain the Heisenberg equation of motion of the annihilation operator using Eq. (10.2.1),

$$\frac{\mathrm{d}}{\mathrm{d}t}a = -\mathrm{i}\Omega - \mathrm{i}\Delta a - \mathrm{i}2Ka^\dagger a^2 + \sum_{j=1,3}\gamma_j\frac{j}{2}a^j a^{\dagger(j-1)} - \sum_{j=2,4}\gamma_j\frac{j}{2}a^{\dagger(j-1)}a^j\,. \tag{10.2.2}$$

We begin by examining the semiclassical limit to obtain an approximation to the steady state of the quantum system. The mean-field equation of the effective classical Liénard model can be derived by performing a cumulant expansion to first order

$$\dot{\langle a\rangle} = -\mathrm{i}\Omega - \mathrm{i}\Delta\langle a\rangle - \mathrm{i}2K|\langle a\rangle|^2\langle a\rangle + \langle a\rangle\left(\frac{\gamma_1}{2} - \gamma_2|\langle a\rangle|^2 + \frac{3\gamma_3}{2}|\langle a\rangle|^4 - 2\gamma_4|\langle a\rangle|^6\right)\,. \tag{10.2.3}$$

Setting $\langle a\rangle = r\mathrm{e}^{\mathrm{i}\phi}$, the mean-field equation can be split into equations of motion of the amplitude r and the phase ϕ,

$$\dot{r} = r\left(\frac{\gamma_1}{2} - \gamma_2 r^2 + \frac{3\gamma_3}{2}r^4 - 2\gamma_4 r^6\right) - \Omega\sin(\phi)\,, \tag{10.2.4}$$

$$\dot{\phi} = -\Delta - 2Kr^2 - \frac{\Omega}{r}\cos(\phi)\,. \tag{10.2.5}$$

Since we are interested in the case of two stable limit cycles, we choose γ_j such that the right-hand side of Eq. (10.2.4) exhibits three real zeros $r_1 < r_c < r_2$ at vanishing drive $\Omega = 0$,

$$\dot{r} = r(r_1^2 - r^2)(r_c^2 - r^2)(r_2^2 - r^2)2\gamma_4 \equiv -\partial_r V(r)\,. \tag{10.2.6}$$

Here, r_1 and r_2 are the stable solutions, and r_c is the unstable solution of the mean-field equations, and $V(r)$ is the effective potential, see Fig. 10.1(a). In a classical system, r_c separates the two basins of attraction. An initial state with $r < r_c$ ($r > r_c$) will therefore converge to r_1 (r_2).

To explore the corresponding quantum TLC, we examine the Wigner function associated with the steady state of Eq. (10.2.1). The Wigner function exhibits two coexisting concentric limit cycles, as illustrated in Fig. 10.1(b), regardless of the initial state. In this figure, the dashed and dotted rings represent the stable and unstable solutions of the classical mean-field equation for the oscillator amplitude, respectively, as defined in Eq. (10.2.6). The radius of the outer ring aligns closely with the mean-field prediction r_2, while the inner ring shows a notable deviation from r_1.

In a classical Liénard system of two limit cycles, both basins of attraction are separated at r_c. However, if extrinsic noise is added, trajectories can cross this boundary. In the language of the effective potential shown in Fig. 10.1(a), noise-induced jumps in r have to overcome the potential barriers ΔV_j to “tunnel” between

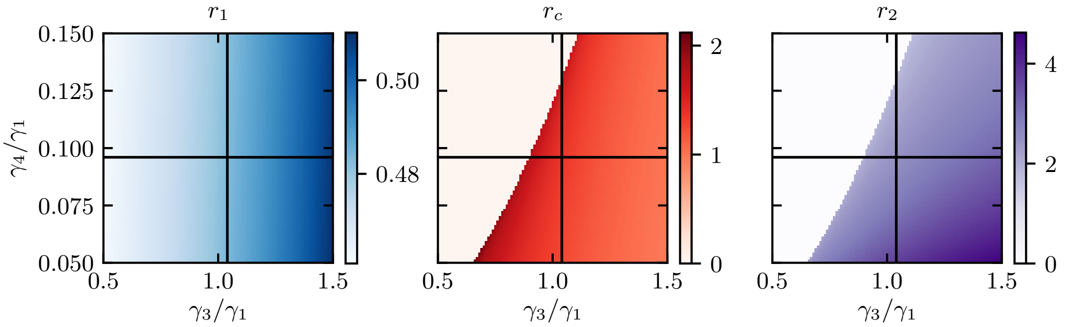

Figure 10.2: Values of real-valued solutions to Eq. (10.2.6) for $\gamma_2 = 2.5\gamma_1$. The black lines indicate $\gamma_3 = 1.04\gamma_1$ and $\gamma_4 = 0.096\gamma_1$, the values that will be used in the quantum case.

both limit cycles. In our quantum setup, the steady state is a combination of two distinct quantum limit cycles. Considering quantum trajectories, the system tunnels between the two limit cycles due to inherent quantum noise, see Sec. 10.4.3 for a detailed discussion.

10.3 Classical Multi-Limit-Cycle Oscillators

Before we study synchronization of quantum TLC oscillators, we want to focus on their classical analogue in the form of their mean-field equations, see Eq. (10.2.3). Already this classical version of such multi-limit-cycle oscillators is showing interesting features presented in the following. Intuitively, it is not surprising that in complex systems like living matter oscillators with multiple limit cycles have been found, e.g., [Laurent and Kellershohn (1999), Enjieu Kadji et al. (2007), Feillet et al. (2014), Goldbeter and Yan (2022)].

The mean-field equations shown in Eqs. (10.2.5) and (10.2.6) can be interpreted as a modified Stuart-Landau oscillator that features higher-order gain and damping leading to multiple stabilized limit cycles. The parameters γ_3 and γ_4 are the rates of additional nonlinear gain and damping terms. Depending on their value, up to two stable radii are possible, see Fig. 10.2. Example trajectories and spectra of several random initializations of a classical TLC are shown in Fig. 10.3. The range of detuning $|\Delta| < \Omega/r$ in which frequency locking occurs depends on the value of the drive strength Ω and the radius r of the limit cycle, see Eq. (10.2.5). Therefore, this range is different for both limit cycles. The three cases in which frequency locking occurs for (i) both limit cycles, (ii) only the outer limit cycle, and (iii) no limit cycle, are presented in Figs. 10.3(a) to 10.3(c). In the spectra, contributions from both limit cycles at the frequencies $\nu_A(\Delta, \Omega, r)$ defined in Eq. (6.2.9) are visible. In Figs. 10.3(d) to 10.3(f), 20 random realizations for different detunings at $\Omega = 0.1\gamma_1$ are shown. For $\Delta = 0.02\gamma_1$, both limit cycles are frequency-locked and lock to $\phi \approx -\pi/2$. For $\Delta = 0.15\gamma_1$, only the inner limit cycle is locked and for $\Delta = 0.5\gamma_1$, none of the limit cycles is locked. Furthermore, states in the attractor of the inner limit cycle exhibit modulations of their radii. The peaks in the spectra Figs. 10.4(b) and 10.4(c) at

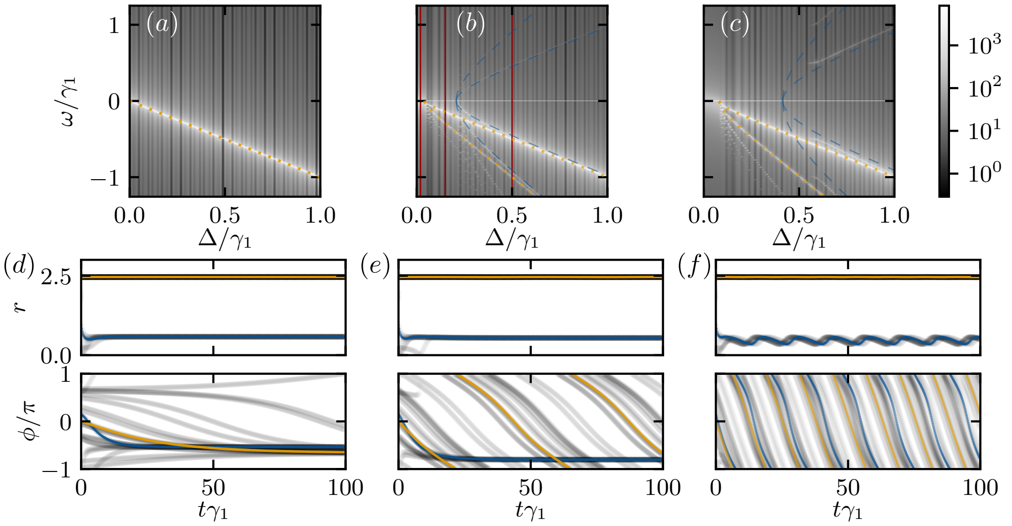

Figure 10.3: Frequency locking of a classical TLC for $\gamma_2 = 2.5\gamma_1$, $\gamma_3 = 1.04\gamma_1$, and $\gamma_4 = 0.096\gamma_1$. (a), (b), (c) Spectra for drive strengths $\Omega/\gamma_1 = 0, 0.1, 0.2$ (from left to right) averaged over 100 random initializations. The blue dashed (orange dotted) curves correspond to the approximation $\omega = \sqrt{\Delta^2 - \Omega^2/r^2}$ defined in Eq. (6.2.9) for the inner (outer) limit cycle with radius r_1 (r_2). (d), (e), (f) Time evolutions of 20 random initializations (gray dots) for drive strength $\Omega = 0.1\gamma_1$ and for detunings $\Delta/\gamma_1 = 0.02, 0.15, 0.5$ (from left to right), corresponding to the three red lines in panel (b). Two evolutions are highlighted in blue (inner limit cycle) and orange (outer limit cycle). Depending on the value of Δ either both limit cycles lock their frequency to the one of the drive, only the inner limit cycle, or no limit cycle.

$\omega = n\nu_A > 0$ correspond to the varying radius of trajectories of the inner limit cycle, see Fig. 10.4(f). The spectra of the radius oscillations exhibit maxima at integer multiples of $\pm\nu_A$.

We now consider Gaussian noise with standard deviation σ that induces jumps between both attractors. Following [Fruchart et al. (2021)], the expected number of jumps in a fixed time interval is proportional to the inverse tunneling time

$$n_{\text{jumps}} \propto \exp\left(-\Delta V/\sigma^2\right), \tag{10.3.1}$$

where ΔV is the barrier of the effective potential V, see Fig. 10.1(a). The larger the noise, the more jumps occur in a fixed time interval, see Figs. 10.4(c) to 10.4(f). In the time evolutions, the correlation between the amplitude of the oscillator and phase locking, as described in the previous paragraph, is visible. If the state is close to r_1, the phase ϕ is locked. In contrast, if the state is close to r_2, no phase locking occurs. For increasing noise, the spectra in Figs. 10.4(a) and 10.4(b) are smoothed and higher-frequency peaks that correspond to the fluctuations of the oscillation frequency, see Eq. (6.2.8), disappear.

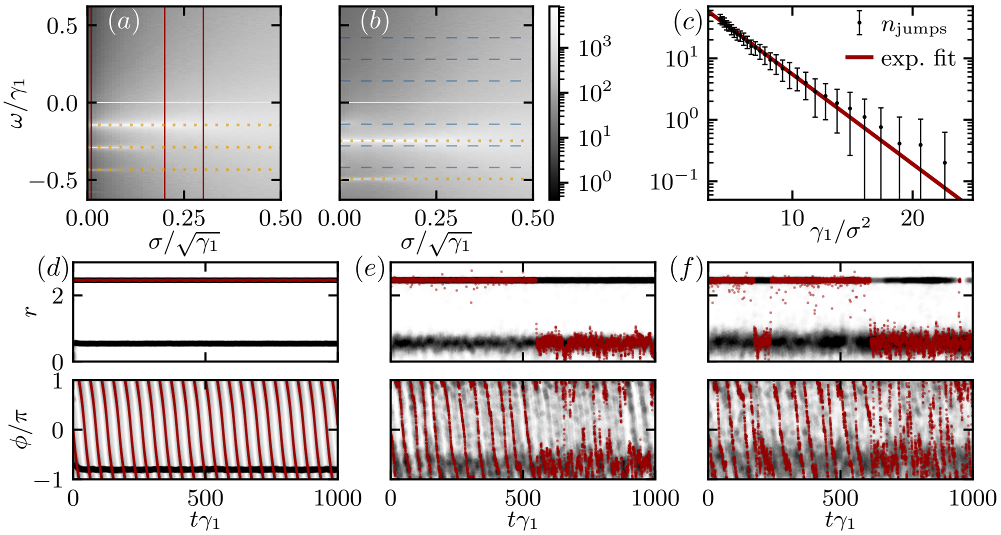

Figure 10.4: Frequency locking of a classical TLC with noise for $\gamma_2 = 2.5\gamma_1$, $\gamma_3 = 1.04\gamma_1$, and $\gamma_4 = 0.096\gamma_1$. (a), (b) Spectra for drive strength $\Omega = 0.1\gamma_1$ and detunings $\Delta/\gamma_1 = 0.15, 0.25$ (from left to right) averaged over 100 random initializations. The blue dashed (orange dotted) lines correspond to the approximation defined in Eq. (6.2.9) for the inner (outer) limit cycle with radius r_1 (r_2). (c) Number of jumps n_{jumps} that occur in a time interval of duration $1000/\gamma_1$ with standard deviations obtained from averaging over 100 realizations. The red curve corresponds to a fit of Eq. (10.3.1). The larger the noise σ, the more jumps occur. (d), (e), (f) Time evolutions of 10 random initializations (overlapping transparent gray dots) for drive strength $\Omega = 0.1\gamma_1$, detuning $\Delta = 0.15\gamma_1$, and for noises $\sigma/\sqrt{\gamma_1} = 0.01, 0.2, 0.3$ (from left to right), corresponding to the three red lines in panel (a). One evolution is highlighted in red.

10.4 One Driven Twin Limit Cycle

We now focus on the synchronization properties of the corresponding quantum Liénard system. First, we discuss phase locking of a TLC to an external drive.

10.4.1 Phase Synchronization

In Fig. 10.5(a), we present the Wigner function corresponding to the steady state of a driven TLC, which exhibits phase localization near $\phi = \arg(\langle a\rangle) = \arg(\Omega) - \pi/2 = -\pi/2$ indicating the synchronization of both limit cycles to the external drive. To characterize and quantify the amount of synchronization, we define a phase localization measure. Various measures of quantum synchronization have been proposed in the literature [Barak and Ben-Aryeh (2005), Ludwig and Marquardt (2013), Hush et al. (2015), Weiss et al. (2016), Roulet and Bruder (2018a), Jaseem et al. (2020a)]. In this work, we use the synchronization measure based on phase states $|\phi\rangle = \sum_{n=0}^{\infty} \mathrm{e}^{in\phi}\,|n\rangle\,/\sqrt{2\pi}$ [Barak and Ben-Aryeh (2005)] where $|n\rangle$ are Fock states. Identical to Eq. (9.2.6),

$$P_1(\phi) = \langle\phi|\,\rho\,|\phi\rangle - \frac{1}{2\pi} = \frac{1}{2\pi}\sum_{k=1}^{\infty} \mathrm{e}^{-\mathrm{i}k\phi}\langle\tilde{a}^k\rangle + \text{H.c.}\,, \tag{10.4.1}$$

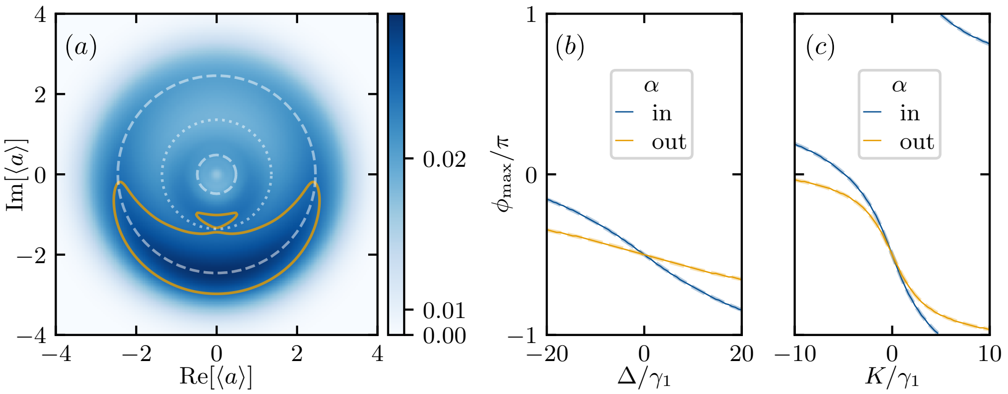

Figure 10.5: Drive-induced phase locking of a TLC. (a) Wigner function for $\Omega = 8\gamma_1$ and $\Delta = K = 0$ showing phase localization of both limit cycles, i.e., a maximum at $\phi = \arg(\langle a\rangle) = \arg(\Omega) - \pi/2 = -\pi/2$. Here, dashed (dotted) rings correspond to stable (unstable) solutions of the mean-field equations of the undriven limit cycles, see Eq. (10.2.6). The solid orange curves are contour lines at 0.0225. Note the power-law color scale. In panels (b) and (c), solid curves denote the maximum of P_1^α with $\alpha \in \{\text{in}, \text{out}\}$, dashed curves denote $\arg(\langle \tilde{a}_\alpha\rangle)$. Varying Δ and K, the inner limit cycle exhibits a larger phase shift than the outer one. This is opposite to the behavior of a standard quantum van der Pol oscillator, see Sec. 7.1.3. Here, $\Omega = 0.25\gamma_1$ for both (b) $K = 0$ and (c) $\Delta = 0$. The dissipation rates for all panels are $\gamma_2 = 2.5\gamma_1$, $\gamma_3 = 1.04\gamma_1$, and $\gamma_4 = 0.096\gamma_1$.

where the operator powers $\tilde{a}^k = \sum_{n=0}^{\infty} |n\rangle\langle n+k|$ capture information about the coherence generation and phase localization. This measure can be interpreted as a probability distribution of phases ϕ from which a uniform distribution is subtracted. If a state shows no phase preference, this measure will be flat and equal to zero. For phase-locked oscillators, a single maximum will appear. Two maxima will be visible for oscillators that exhibit bistable phase locking.

To resolve the phase information of the two limit cycles individually, we define truncated operators $\tilde{a}_\alpha$, with $\alpha \in \{\text{in}, \text{out}\}$, as

$$\tilde{a}_{\text{in}} = \sum_{n=0}^{n_c-1} |n\rangle\langle n+1| \,, \quad \tilde{a}_{\text{out}} = \sum_{n=n_c}^{\infty} |n\rangle\langle n+1| \,. \tag{10.4.2}$$

These are an approximation of operators that only act on the respective subspace of each ring. The cutoff Fock number n_c is chosen to be the integer closest to r_c^2. We use powers of these $\tilde{a}_\alpha$ to define the phase distributions P_1^{in} of the inner and P_1^{out} of the outer ring of a TLC,

$$P_1^\alpha(\phi) = \frac{1}{2\pi\langle \mathcal{I}^\alpha\rangle} \sum_{k=1}^{\infty} \mathrm{e}^{-\mathrm{i}k\phi} \langle \tilde{a}_\alpha^k\rangle + \text{H.c.}\,, \tag{10.4.3}$$

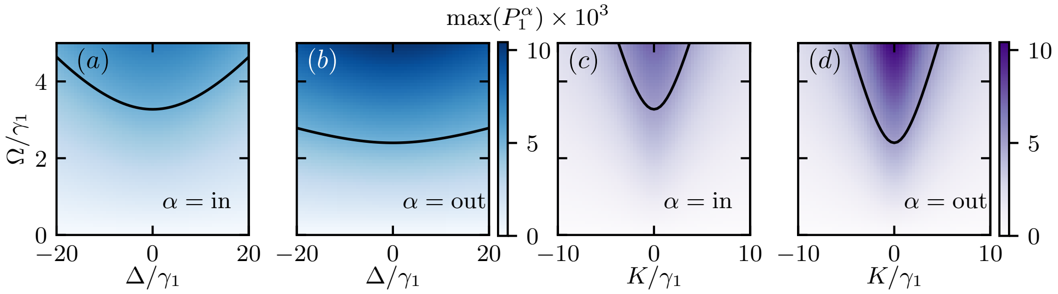

Figure 10.6: Arnold tongues of a driven TLC using P_1^α defined in Eq. (10.4.3). (a), (b) $\Delta = 0$. (c), (d) $K = 0$. The black curves are contour lines at 5. The dissipation rates for all panels are $\gamma_2 = 2.5\gamma_1$, $\gamma_3 = 1.04\gamma_1$, and $\gamma_4 = 0.096\gamma_1$. Compare this plot to Figs. 7.4 and 7.8.

where $\alpha \in \{\text{in}, \text{out}\}$. Here $\mathcal{I}^\alpha$ represents the unit matrix in the subspace α,

$$\mathcal{I}^{\text{in}} = \sum_{n=0}^{n_c} |n\rangle\langle n| \,, \quad \mathcal{I}^{\text{out}} = \sum_{n=n_c+1}^{\infty} |n\rangle\langle n| \,, \tag{10.4.4}$$

and is used to properly normalize the phase distribution.

We use the measure P_1^α to characterize the synchronization properties of the two limit cycles. In Figs. 10.5(b) and 10.5(c), the locking phase angle of a driven TLC is shown for fixed drive strength $\Omega = 0.25\gamma_1$, varying detuning Δ, and Kerr nonlinearity K. Remarkably, for nonzero Δ and K, each limit cycle locks to a distinct phase. Notably, the inner limit cycle responds more strongly to the external drive compared to the outer limit cycle. This deviates from the steady state solution of the mean-field Eq. (10.2.5), which predicts a stronger phase sensitivity of the outer limit cycle. The slopes of the solution $\phi_{\max}$ for $\dot{\phi} = 0$ at $\Delta = K = 0$,

$$\partial_\Delta \phi_{\max} = -\frac{r}{\Omega} \,, \tag{10.4.5}$$

$$\partial_K \phi_{\max} = -\frac{2r^3}{\Omega} \,, \tag{10.4.6}$$

reveal that the value of the locked phase depends stronger on both Δ and K for larger radii. This feature is consistent with standard single-limit-cycle oscillators with $\gamma_3 = \gamma_4 = 0$, see Sec. 7.1.3. The higher-order gain and damping channels lead to features that are unique to TLCs. The overlap of the inner and outer limit cycles of a TLC leads to tunneling and leakage of information between them. This is a qualitatively different behavior compared with the classical analogue following the mean-field equations. Note that quantum limit cycles stabilized by third-order gain and fourth-order damping, see Sec. 7.1.5, that exhibit smaller radii are reacting stronger to detuning Δ than the ones that exhibit larger radii.

We furthermore present Arnold tongues of the inner and outer limit cycles for varying drive strength Ω versus Δ and K in Fig. 10.6. To achieve the same value of P_1^α, the inner limit cycle needs to be driven with a stronger drive similar to the standard quantum van der Pol oscillator presented in Fig. 7.4. This is the opposite behavior

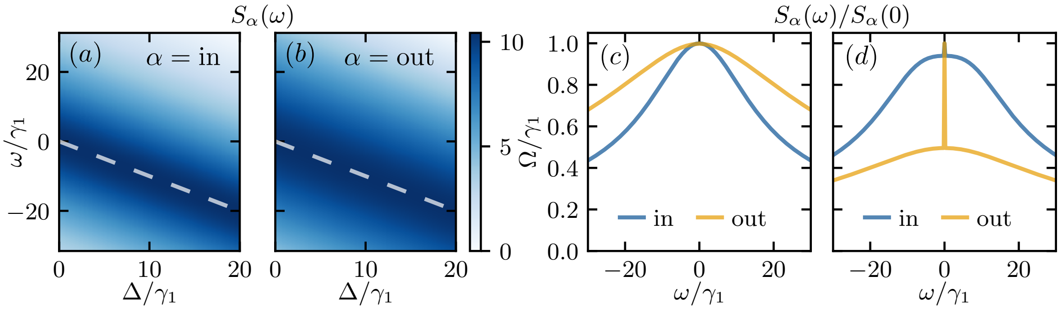

Figure 10.7: Frequency synchronization of a driven TLC with $\gamma_2 = 2.5\gamma_1$, $\gamma_3 = 1.04\gamma_1$, and $\gamma_4 = 0.096\gamma_1$. (a), (b) Power spectra $S_\alpha(\omega)$ for a weak drive $\Omega = 0.25\gamma_1$. The dashed white line corresponds to $\omega = \Delta$. No frequency locking plateau visible. (c), (d) Normalized power spectra $S_\alpha(\omega)/S_\alpha(0)$ corresponding to $\Omega\gamma_1 = 0.25, 5$ (from left to right) and $\Delta = 0$. The power spectra are based on the truncated annihilation operators defined in Eq. (10.4.8) and exhibit a peak at $\omega = 0$ due to injection locking.

compared to quantum limit cycles stabilized by third-order gain and fourth-order damping, see Fig. 7.8.

10.4.2 Frequency Synchronization

In addition to the locking of the two limit cycles of a driven TLC to distinct phases shown in the previous section, we discuss their frequency synchronization below. To analyze the frequency entrainment of the TLC, we utilize the power spectrum which is defined as

$$\mathcal{S}_\alpha(\omega) = \lim_{t\to\infty} \int_{-\infty}^{\infty} \mathrm{d}\tau \langle a_\alpha^\dagger(t+\tau) a_\alpha(t)\rangle \mathrm{e}^{\mathrm{i}\omega\tau} \,, \tag{10.4.7}$$

where $\alpha \in \{\text{in}, \text{out}\}$. The power spectrum defined above is based on two-time correlations of the truncated annihilation operators, which we define as

$$a_{\text{in}} = \sum_{n=0}^{n_c-1} \sqrt{n+1}\, |n\rangle\langle n+1| \,, \quad a_{\text{out}} = \sum_{n=n_c}^{\infty} \sqrt{n+1}\, |n\rangle\langle n+1| \;. \tag{10.4.8}$$

Note the difference to Eq. (10.4.2), where the factor $\sqrt{n+1}$ is not included. The power spectrum is well-defined for both limit cycles for small values of Ω. One such example is shown in Fig. 10.7(c) where $\Omega = 0.25\gamma_1$ and $\Delta = 0$. However, no frequency locking occurs when $\Delta \neq 0$ for such smaller drive strength, see Figs. 10.7(a) and 10.7(b). In regions of stronger drive, where a significant degree of phase synchronization is observed, the spectrum of the inner limit cycles broadens considerably, as illustrated in Fig. 10.7(d) for $\Omega = 8\gamma_1$. Such spectral broadening results from changes in the population distribution within the inner limit cycle, shifting toward the critical radius for higher Ω values. With a further increase in Ω, the population increasingly overlaps with the outer limit cycle, expected to lead to further broadening of the power spectrum. Therefore, the phase synchronization measure is more sensitive and applicable even at

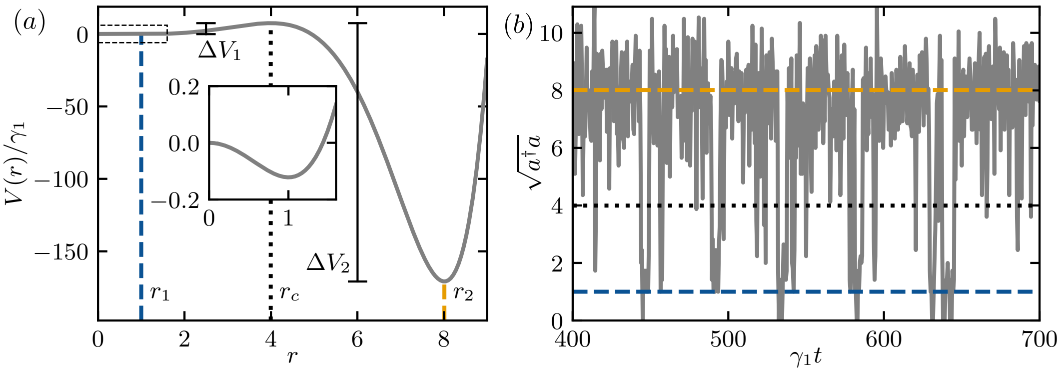

Figure 10.8: Quantum trajectories of the undriven TLC for $\Delta = K = 0$ and the rates that lead to $(r_1, r_c, r_2) = (1, 4, 8)$: $(\gamma_2, \gamma_3, \gamma_4) \approx (0.539, 0.0264, 2.44 \times 10^{-4})\gamma_1$. (a) Effective potential of the mean-field equations along the radial direction, defined in Eq. (10.2.6). Here ΔV_1 (ΔV_2) is the potential difference between the stable minimum at r_1 (r_2) and the unstable maximum at r_c. The inset shows the minimum of $V(r)$ at r_1, see the dashed box in the top left. (b) Single trajectory based on Monte Carlo simulation of Eq. (10.2.1). Jump probabilities between r_1 and r_2 are clearly asymmetric.

higher drive strengths for the TLC oscillators.

10.4.3 Quantum Trajectories

In this section, we briefly examine the coexistence of limit cycles by analyzing the dynamics of a single quantum trajectory in a quantum Liénard system. In Fig. 10.8, we choose the dissipation rates that lead to $(r_1, r_c, r_2) = (1, 4, 8)$: $(\gamma_2, \gamma_3, \gamma_4) \approx (0.539, 0.0264, 2.44 \times 10^{-4})\gamma_1$. The minima of $V(r)$ are sufficiently separated to facilitate the observation of the transition from one stable radius to the other due to intrinsic quantum noise. As shown in Fig. 10.8(a), the noise has to overcome a smaller potential difference, ΔV_1, when transitioning from r_1 to r_2, in contrast to the larger potential difference, ΔV_2, for the reverse direction. This asymmetry in the potential differences is evident in the time evolution of a single trajectory presented in Fig. 10.8(b), where the system spends more time in the outer limit cycle at r_2 compared to the inner limit cycle at r_1. The density matrix of a steady-state can be interpreted as the long-time average of many such quantum trajectories, which results in the two-ring-like structures found in the corresponding Wigner function, similar to Fig. 10.5(a).

10.5 Two Coupled Twin Limit Cycles

We now focus on the synchronization between two coherently coupled TLCs that are depicted schematically in Fig. 10.9. Intuitively, we expect to find *both* locking and bistable locking of the relative phase in this setup. We imagine synchronization to occur between limit cycles of different radius and blockades to emerge between limit cycles of equal radius. In other words, we expect the coexistence of synchronization and blockade, two distinct scenarios described in Sec. 7.1.4. The dynamics of two

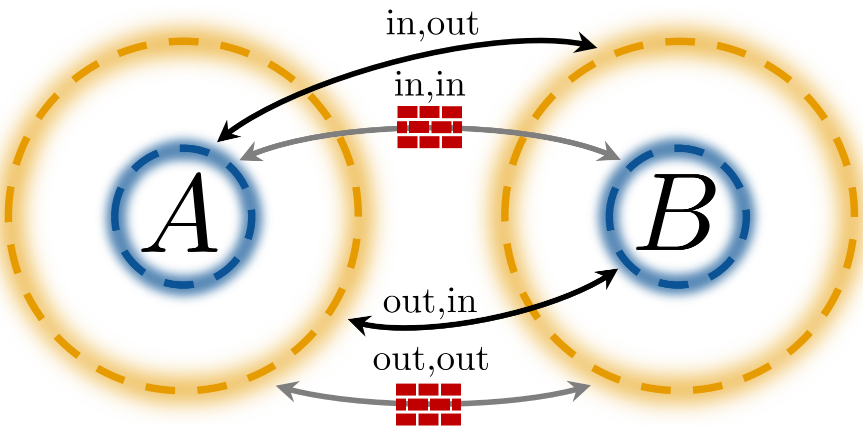

Figure 10.9: Schematic representation of the phase locking behavior of two coherently coupled TLCs. Limit cycles of unequal radius exhibit phase locking. In contrast, for limit cycles of equal radius bistable phase locking is found.

TLCs are described by the Lindblad master equation

$$\dot{\rho} = -\mathrm{i}[g_{AB} a_A^\dagger a_B + \text{H.c.}, \rho] + \mathcal{L}_A(\rho) + \mathcal{L}_B(\rho)\,. \tag{10.5.1}$$

Here, the first term is the coherent coupling between the two TLCs with strength g_{AB}. The Liouvillians $\mathcal{L}_j$ describe the independent dynamics of each TLC similar to Eq. (10.2.1), where the operators a_j act on oscillator j. In the following, we fix $\Omega_A = \Omega_B = 0$, $\delta = \Delta_A - \Delta_B$, and $K = K_A = K_B$.

10.5.1 Phase Locking

Similar to Eq. (9.2.17), the phase distribution of two oscillators is obtained by projecting the density matrix onto the tensor products of phase states $|\phi_A, \phi_B\rangle$ and is defined as

$$\begin{aligned} P_2(\phi_{AB}) &= \int_0^{2\pi} \mathrm{d}\phi \, \langle \phi_{AB} + \phi, \phi | \, \rho \, | \phi_{AB} + \phi, \phi \rangle - \frac{1}{2\pi} \\ &= \frac{1}{2\pi} \sum_{k=1}^{\infty} \mathrm{e}^{-\mathrm{i}k\phi_{AB}} \langle (\tilde{a}_A \tilde{a}_B^\dagger)^k \rangle + \text{H.c.}\,. \end{aligned} \tag{10.5.2}$$

We integrate over the phase ϕ to obtain the synchronization measure for the relative phase $\phi_{AB} = \phi_A - \phi_B$. In analogy to Eq. (10.4.3), we define the combined phase distribution $P_2^{\alpha,\beta}$ of two TLCs as

$$P_2^{\alpha,\beta}(\phi_{AB}) = \frac{1}{2\pi \langle \mathcal{I}_A^\alpha \mathcal{I}_B^\beta \rangle} \sum_{k=1}^{\infty} \mathrm{e}^{-\mathrm{i}k\phi_{AB}} \langle (\tilde{a}_{A,\alpha} \tilde{a}_{B,\beta}^\dagger)^k \rangle + \text{H.c.}\,, \tag{10.5.3}$$

where $\tilde{a}_{j,\alpha}$ and $\mathcal{I}_j^\alpha$ are the truncated operators $\tilde{a}_\alpha$ and the unit operators $\mathcal{I}^\alpha$ that act on the jth oscillator. The measure above allows us to investigate the synchronization between the limit cycles of both oscillators since (α, β) can take various combinations:

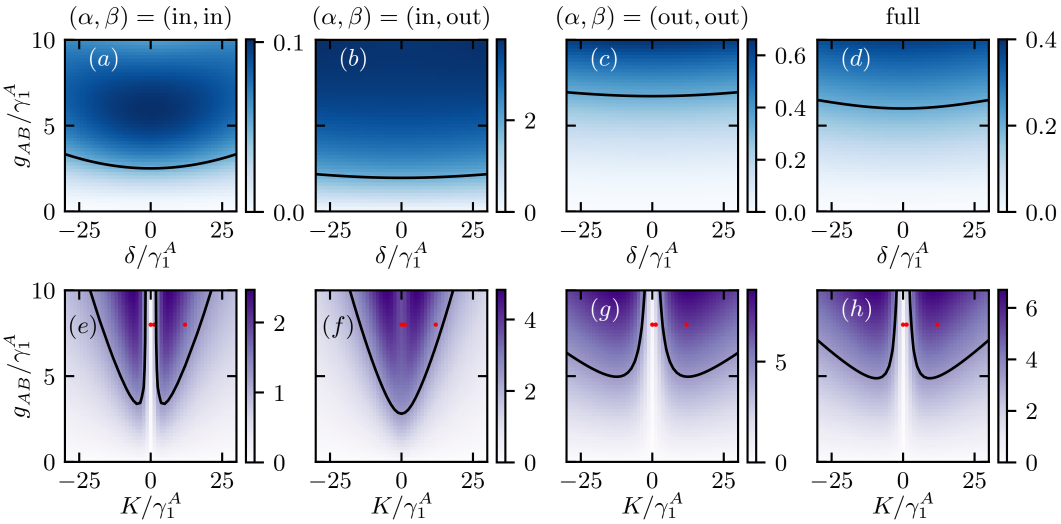

Figure 10.10: Arnold tongues of two identical coupled twin limit cycles with rates $\gamma_j^A = \gamma_j^B$, $\gamma_2^A = 2.5\gamma_1^A$, $\gamma_3^A = 1.04\gamma_1^A$, and $\gamma_4^A = 0.096\gamma_1^A$ for $\Omega_j = 0$ and $n_c = 2$. (a)–(c) Maximum of $P_2^{\alpha,\beta} \times 10^3$ of Eq. (10.5.3) as a function of coupling strength g_{AB} and detuning δ at $K = 0$. (d) Maximum of the full synchronization measure P_2 of Eq. (10.5.2) for $K = 0$. (e)–(g) Maximum of $P_2^{\alpha,\beta} \times 10^3$ as a function of g_{AB} and Kerr nonlinearity K at $\delta = 0$. (h) Maximum of the full synchronization measure P_2 of Eq. (10.5.2) for $\delta = 0$. The black curves denote contour lines at half the maximum value of the color scale. The red dots correspond to the example plots shown in Fig. 10.11.

(in, in), (in, out), (out, in), and (out, out).

We now set the dissipation rates $\gamma_j^A = \gamma_j^B$ equal, such that the radii of the inner limit cycles of both TLCs are identical as well as the radii of the outer limit cycles. In Figs. 10.10(a) to 10.10(d), we plot the maxima of the combined synchronization measures $P_2^{\alpha,\beta}$ and P_2 as a function of g_{AB} and δ for $K = 0$. For $\delta = 0$ and $K = 0$, both oscillators have the same frequencies, and hence, we expect a maximum amount of synchronization. In these four panels, Arnold tongues centered at $\delta = 0$ are visible. The measure $P_2^{\mathrm{in,in}}$ even exhibits a local maximum. This fact can be interpreted as: above $g_{AB} \gtrsim 5/\gamma_1^A$, phase synchronization outside the perturbative regime is found, see the clearly asymmetric Wigner function in Fig. 10.5(a).

In Figs. 10.10(e) to 10.10(h), we plot the maxima of the combined synchronization measures $P_2^{\alpha,\beta}$ and P_2 as a function of g_{AB} and K for $\delta = 0$. Interestingly, the synchronization measure for $(\alpha,\beta) = (\mathrm{in},\mathrm{in})$ and $(\alpha,\beta) = (\mathrm{out},\mathrm{out})$, shown in Figs. 10.10(e) and 10.10(g), is highly suppressed around $K = 0$. This is a signature of the synchronization blockade, where the contribution from the first-order locking vanishes ($\langle \tilde{a}_{A,\alpha}\tilde{a}_{B,\alpha}^\dagger \rangle = 0$) due to the cancellation of coherences. Only second-order phase locking can be observed, as indicated by the two maxima in Fig. 10.11(a). This

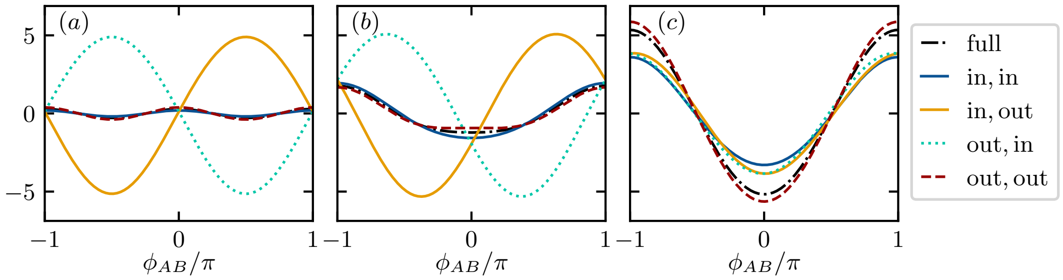

Figure 10.11: Synchronization measures $P_2^{\alpha,\beta}(\phi_{AB}) \times 10^3$ (colored curves) and P_2 (black dash-dotted curve) corresponding to the red dots in Figs. 10.10(e) to 10.10(h) at $g_{AB} = 8\gamma_1^A$ and $K/\gamma_1^A = 0, 1.2, 12$ (from left to right).

blockade can also be understood using the mean-field equations of Eq. (10.5.1),

$$\dot{r}_j = r_j \left(\frac{\gamma_1^j}{2} - \gamma_2^j r_j^2 + \frac{3\gamma_3^j}{2} r_j^4 - 2\gamma_4^j r_j^6 \right) + g_{AB} r_i \sin(\phi_i - \phi_j) - \Omega_j \sin(\phi_j) \,, \tag{10.5.4}$$

$$\dot{\phi}_j = -\Delta_j - 2K_j r_j^2 - g_{AB} \frac{r_i}{r_j} \cos(\phi_i - \phi_j) - \frac{\Omega_j}{r_j} \cos(\phi_j) \,, \tag{10.5.5}$$

where $i, j \in \{A, B\}$ and $i \neq j$. The equation of motion of the relative phase for $\Omega_j = 0$ is

$$\dot{\phi}_{AB} = -\delta - 2K(r_A^2 - r_B^2) + g_{AB} \frac{r_A^2 - r_B^2}{r_A r_B} \cos(\phi_{AB}) \,, \tag{10.5.6}$$

where the coupling term vanishes for limit cycles with equal radii. The limit cycles with different radii exhibit an Arnold tongue, see Figs. 10.10(b) and 10.10(f), signifying synchronization between the (in, out) limit cycles. Thus, both synchronization and blockade effects occur simultaneously in the coupled identical TLC oscillators, a behavior not known in classical analogues in the absence of noise. For our choice of parameters $n_c = 2$ and $\tilde{a}_{\text{out}} \approx \tilde{a}$, $P_2^{\text{out,out}}$ shown in Fig. 10.10(g) behaves qualitatively similar to the standard synchronization measure P_2 defined in Eq. (10.5.2). The existence of the blockade at $K = 0$ is therefore also confirmed by P_2, see Fig. 10.10(h) and Fig. 10.11(a).

The synchronization blockade is lifted for $K \neq 0$ [Lörch et al. (2017)], as shown in Figs. 10.10(e) and 10.10(g). For $\delta = 0$ and $K > 0$ ($K < 0$) the relative phase of both oscillators locks to $\phi_{AB} = \pi$ ($\phi_{AB} = 0$), see Fig. 10.11(c). To understand this behavior, we investigate the mean-field equations in more detail. We examine the phase-locking behavior by expanding Eq. (10.5.6) about the radii r_1 and r_2 of the limit cycles for the two cases: (i) equal radii $r_A, r_B \approx r_\alpha$ and (ii) different radii $r_A \approx r_\alpha$ and $r_B \approx r_\beta$, where $j \in \{A, B\}$, $\alpha, \beta \in \{1, 2\}$, and $\alpha \neq \beta$. For equal radii, we choose

$r_j = r_\alpha + r_{j,1} g_{AB}/\gamma_1 + r_{j,2}(g_{AB}/\gamma_1)^2$,

$$r_{A,1} = -\frac{\sin(\phi_{AB})}{4r_\alpha(r_\alpha^2 - r_\beta^2)(r_\alpha^2 - r_c^2)}\frac{\gamma_1}{\gamma_4} = -r_{B,1}\,, \tag{10.5.7}$$

$$r_{A,2} = \sin^2(\phi_{AB})\frac{9r_\alpha^2(r_\beta^2 + r_c^2) - 5r_\beta^2 r_c^2 - 13r_\alpha^4}{32r_\alpha^3(r_\alpha^2 - r_\beta^2)^3(r_\alpha^2 - r_c^2)^3}\frac{\gamma_1^2}{\gamma_4^2} = r_{B,2}\,. \tag{10.5.8}$$

Note that since $r_1 < r_c < r_2$, the product $(r_\alpha^2 - r_\beta^2)(r_\alpha^2 - r_c^2) > 0$ in the denominators is always positive. The resulting equation of motion of the relative phase ϕ_{AB} when expanding both twin limit cycles about r_α, see Figs. 10.10(e) and 10.10(g), reads

$$\dot{\phi}_{AB} = -\,\delta + \frac{4g_{AB}Kr_\alpha^2\sin(\phi_{AB}) - g_{AB}^2\sin(2\phi_{AB})}{2r_\alpha^2(r_\alpha^2 - r_\beta^2)(r_\alpha^2 - r_c^2)\gamma_4}\,. \tag{10.5.9}$$

If $\delta = K = 0$, bistable locking to $\phi_{AB} = 0, \pi$ occurs, which corresponds to the synchronization blockade due to the absence of first-order phase locking. Thus, the system is in the synchronization blockade between the limit cycles of the same type of the TLCs at $K = 0$. For $\delta = 0$ and $K > 0$ ($K < 0$), the relative phase between both inner or outer limit cycles locks to a single value $\phi_{AB} = \pi$ ($\phi_{AB} = 0$). Thus, for $K \neq 0$, the blockade is lifted. In the case of equal radii, the mean-field prediction coincides with the quantum results.

For different radii $r_A = r_\alpha + r_{A,1}g_{AB}/\gamma_1$ and $r_B = r_\beta + r_{B,1}g_{AB}/\gamma_1$, we obtain

$$r_{A,1} = -\frac{r_\beta\sin(\phi_{AB})}{4r_\alpha^2(r_\alpha^2 - r_\beta^2)(r_\alpha^2 - r_c^2)}\frac{\gamma_1}{\gamma_4}\,, \tag{10.5.10}$$

$$r_{B,1} = -\frac{r_\alpha\sin(\phi_{AB})}{4r_\beta^2(r_\alpha^2 - r_\beta^2)(r_\beta^2 - r_c^2)}\frac{\gamma_1}{\gamma_4}\,. \tag{10.5.11}$$

The equation of motion for the relative phase reads

$$\begin{aligned}\dot{\phi}_{AB} = &-\delta - 2K(r_\alpha^2 - r_\beta^2) + g_{AB}\frac{r_\alpha^2 - r_\beta^2}{r_1 r_2}\cos(\phi_{AB})\\ &+ g_{AB}K\frac{r_1^2 + r_2^2 - r_c^2}{r_1 r_2(r_c^2 - r_1^2)(r_2^2 - r_c^2)\gamma_4}\sin(\phi_{AB})\,.\end{aligned} \tag{10.5.12}$$

For $\delta = K = 0$, these mean-field equations lead to locking to a single value of the relative phase. In contrast to the quantum case, the relative phase in Eq. (10.5.12) locks to $\phi_{AB} = -\pi/2$ for $(\alpha, \beta) = (1, 2) \leftrightarrow (\text{in}, \text{out})$ and to $\phi_{AB} = \pi/2$ for $(\alpha, \beta) = (2, 1) \leftrightarrow (\text{out}, \text{in})$. Choosing $\delta = 0$ and $K > 0$ ($K < 0$) in Eq. (10.5.12) leads to a shift of the locking phase toward $\phi_{AB} = 0$ ($\phi_{AB} = \pi$). This shift contradicts the quantum result too, see Fig. 10.11(c). In conclusion, the mean-field analysis performed here is suitable to predict the locking of the relative phases of (i) equal limit cycles $(\alpha, \beta) = (\text{in}, \text{in}), (\text{out}, \text{out})$ of two coupled TLCs but fails to describe the locking of (ii) different limit cycles $(\alpha, \beta) = (\text{in}, \text{out}), (\text{out}, \text{in})$. An explanation might be that in the quantum Liénard system, both limit cycles are not strictly separated like the basins of

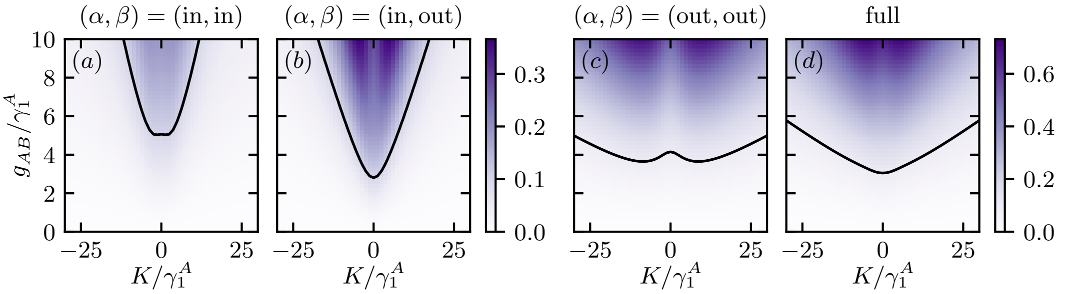

Figure 10.12: Mutual information $I(\rho_{\alpha,\beta}) \times 10^3$ for identical TLCs with $\delta = 0$ and $\gamma_j^A = \gamma_j^B$. (a)–(c) Evaluated for truncated density matrices $\rho_{\alpha,\beta}$, see Eq. (10.5.14). (d) Evaluated for the full density matrix ρ. The black curves denote contour lines at 0.1. The blockade at $K = 0$ is not as prominent as in $P_2^{\alpha,\beta}$, see Fig. 10.10.

attraction in the classical analogue. Therefore, locking mechanisms of different pairs of limit cycles of two TLC oscillators interplay.

10.5.2 Quantum Mutual Information

Another measure of quantum synchronization is the quantum mutual information [Ameri et al. (2015)],

$$I(\rho) = S(\rho_A) + S(\rho_B) - S(\rho)\,, \tag{10.5.13}$$

where S is the von Neumann entropy and ρ_j are reduced density matrices. For mixed states, the quantum mutual information contains both classical and quantum correlations. To quantify the correlation between different limit cycles of the TLC oscillators, we truncate the density matrices as follows

$$\rho_{\alpha,\beta} = \mathrm{Tr}\left[\mathcal{I}_A^{\alpha}\mathcal{I}_B^{\beta}\rho\right]. \tag{10.5.14}$$

In Fig. 10.12, we show the mutual information for truncated density matrices as well as the full density matrix. The behavior of the mutual information is qualitatively similar to that of $P_2^{\alpha,\beta}$ shown in Fig. 10.10. It exhibits a dip around the blockade region at $K = 0$ for the limit cycles (in, in) and (out, out), although it does not vanish completely. In contrast, the mutual information evaluated for the full density matrix contains information about synchronization between different limit cycles and also the blockade effect between similar limit cycles. Hence, the mutual information is not reduced significantly around the blockade. Therefore, even if the mutual information reflects the blockade at $K = 0$, it does not capture the blockade as much as $P_2^{\alpha,\beta}$.

10.5.3 Persistence of the Quantum Synchronization Blockade

In this section, we compare the stability of the synchronization blockade of coupled TLCs with the one of standard limit cycles, i.e., the range of dissipation rates γ_j^A for which the blockade (bistable locking) persists. If there are two equally high maxima in $P_2^{\alpha,\beta}$ at a given value of the ratio γ_j^A/γ_j^B, the blockade (bistable locking) occurs. In the

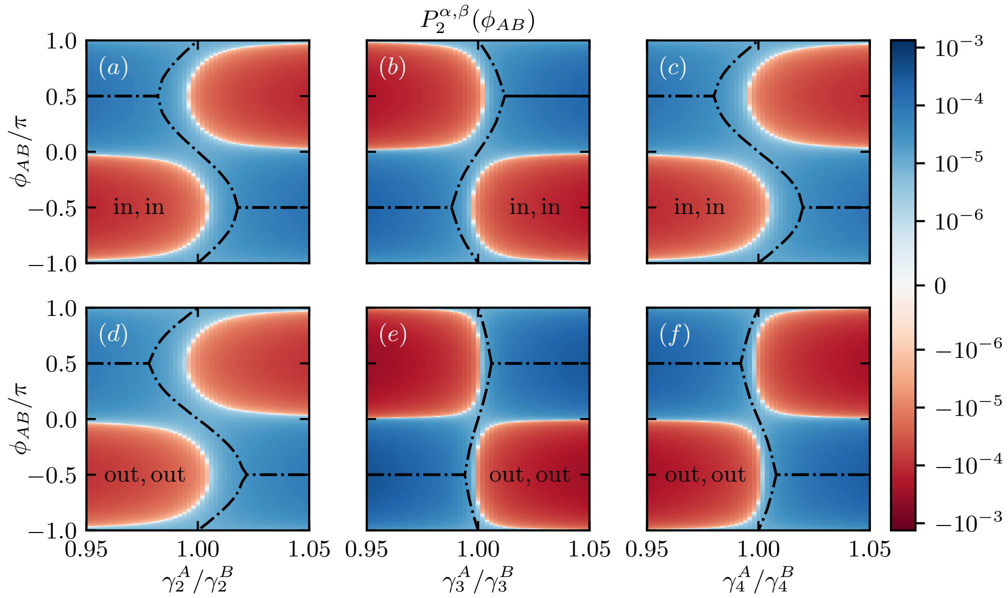

Figure 10.13: Regions of the quantum synchronization blockade of two TLCs for $g_{AB} = \gamma_1^A$, $\gamma_1^A = \gamma_1^B$, $\gamma_2^B = 2.5\gamma_1^A$, $\gamma_3^B = 1.04\gamma_1^A$, and $\gamma_4^B = 0.096\gamma_1^A$. In each column, only a single ratio γ_j^A/γ_j^B is varied. (a)–(c) $P_2^{\text{in,in}}$. (d)–(f) $P_2^{\text{out,out}}$. In all panels, maxima in ϕ_{AB} are denoted by dash-dotted lines. The color scale is linear in the interval $[-10^{-6}, 10^{-6}]$ and logarithmic elsewhere.

mean-filed equations, the equality of the radii seem to be sufficient to lead to vanishing interactions at $K = 0$, see Eq. (10.5.6). When coupling a standard limit-cycle oscillator A to a TLC oscillator B and varying the ratio γ_2^A/γ_2^B while keeping γ_j^B fixed, no blockade emerges between the standard limit cycle and neither of the limit cycles in the TLC. Thus, to show the synchronization blockade effect between two quantum oscillators, the states need to be identical and not only the radii of their limit cycles. Naively, based on the mean-field equations, one could have guessed that when the radius of the standard limit cycle matches one of the radii of the TLC a blockade occurs.

In a system of two coupled TLC oscillators, we vary the rates γ_2^A, γ_3^A, and γ_4^A individually by keeping $\gamma_1^A = \gamma_1^B$, $\gamma_2^B = 2.5\gamma_1^A$, $\gamma_3^B = 1.04\gamma_1^A$, and $\gamma_4^B = 0.096\gamma_1^A$ fixed. The resulting blockades are illustrated in Fig. 10.13 and exist in a narrower range of $\gamma_j^A/\gamma_j^B \in [0.97, 1.03]$ compared to the system of two standard limit cycles presented in Fig. 7.6(a). Thus, the blockade in a pair of TLCs is more susceptible to variations in gain and damping rates than that of two standard limit cycles.

10.6 Experimental Realization

The effects discussed here can be potentially observed in a trapped-ion experiment similar to [Behrle et al. (2023)] that demonstrated quantum synchronization of a phonon laser to an external signal. The setup consists of a calcium and a beryllium ion in a radio-frequency trap that share a common harmonic mode of motion which is

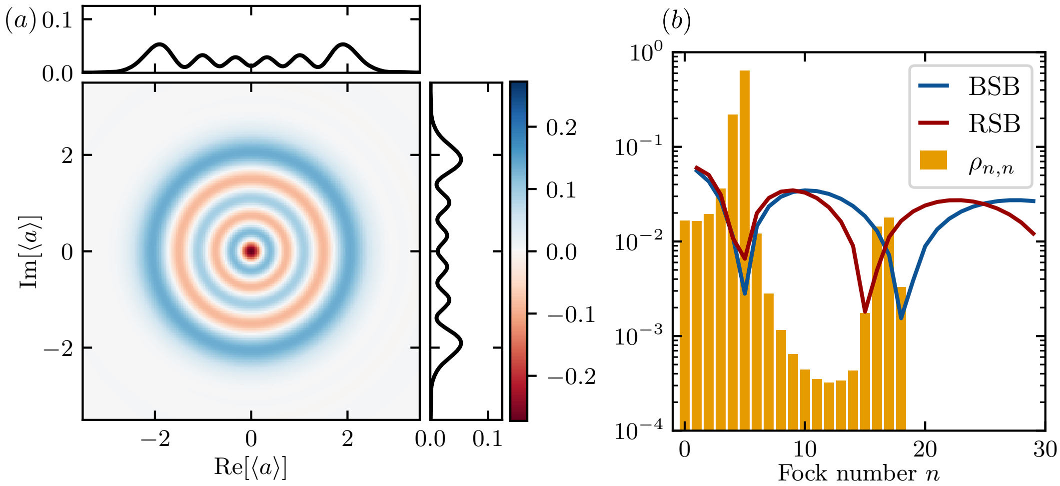

Figure 10.14: Preliminary data showing that a multi-limit-cycle oscillator can be realized by the nonlinear phonon-ion interaction described in Eq. (10.6.1). The parameters are $s_{\mathrm{BSB}} = -s_{\mathrm{RSB}} = 1$, $\Omega_0^{\mathrm{BSB}} = \Omega_0^{\mathrm{RSB}} = 0.1\kappa$, $\eta_{\mathrm{BSB}} = 0.8$, and $\eta_{\mathrm{RSB}} = 0.9$. (a) Wigner function and marginals of the final state of a time evolution of duration $\kappa t = 10^3$ starting from a coherent state $|\alpha = 2\rangle$. (b) Populations $\rho_{n,n}$ of the final state. The curves correspond to the heating $\Omega^{\mathrm{BSB}}_{n,n+1}$ and cooling $\Omega^{\mathrm{RSB}}_{n,n-1}$ sidebands, see Eq. (10.6.1). Populations of Fock numbers $n \geq 19$ are smaller than 10^{-4}. A video of the time evolution can be found at [Kehrer (2025)].

denoted by the annihilation operator a. To realize nth-order gain (mth-order damping) in the Lamb-Dicke regime, one has to implement a sideband heating (cooling) laser that is detuned from a particular transition in the ion energy-level scheme [Leibfried et al. (2003)]. If this detuning equals n ($-m$) times the energy of the harmonic mode and assuming fast ion decay with respect to the timescales of the motion in the trap, an effective jump operator $L = a^{\dagger n}$ ($L = a^m$) is realized. For each dissipator in Eq. (10.2.1), a distinct ion transition has to be chosen. Therefore, to realize the four gain and damping channels of a TLC, two spin transitions per ion have to be driven with one of the four red and blue sideband lasers each.

Alternatively, the setup can be operated outside Lamb-Dicke regime [Rojkov et al. (2024)] making use of the higher-order contributions presented in Eq. (3.3.10) of Sec. 3.3.2. Here, one internal transition (first sideband) for each heating and cooling is driven. Both transitions decay at rate κ. The intrinsic nonlinearity of the phonon-ion interaction leads to the stabilization of multiple limit cycles. We recall the equation of the effective Rabi frequencies [Leibfried et al. (2003)],

$$\Omega_{n,n+s} = \Omega_{n+s,n} = \Omega_0 |\langle n+s|\, \mathrm{e}^{\mathrm{i}\eta(a^\dagger + a)}\, |n\rangle| = \Omega_0 \eta^{|s|} \mathrm{e}^{-\eta^2/2} \sqrt{\frac{n_{\mathrm{min}}!}{n_{\mathrm{max}}!}} L^{|s|}_{n_{\mathrm{min}}}(\eta^2)\,, \tag{10.6.1}$$

where

$$n_{\mathrm{min}} = \min(n, n+s), \quad n_{\mathrm{max}} = \max(n, n+s)\,, \tag{10.6.2}$$

and $L_n^{|s|}(x)$ are the generalized Laguerre polynomials, see Eq. (3.3.12). In Fig. 10.14, preliminary data for the stabilization of a multi-limit-cycle state is shown for $s_{\mathrm{BSB}} = -s_{\mathrm{RSB}} = 1$, $\Omega_0^{\mathrm{BSB}} = \Omega_0^{\mathrm{RSB}} = 0.1\kappa$, $\eta_{\mathrm{BSB}} = 0.8$, and $\eta_{\mathrm{RSB}} = 0.9$. For Fock states $|n\rangle$ for which $\Omega_0^{\mathrm{BSB}} > \Omega_0^{\mathrm{RSB}}$ ($\Omega_0^{\mathrm{BSB}} < \Omega_0^{\mathrm{RSB}}$), population is moved to higher (lower) n. Therefore, state populations accumulate close to crossing points n^* at which $\Omega_0^{\mathrm{BSB}} = \Omega_0^{\mathrm{RSB}}$ and when the heating dominates for slightly smaller Fock numbers $n \lesssim n^*$. The time evolution of duration $\kappa t = 10^3$, starting from a coherent state $|\alpha = 2\rangle$, results in a state whose Wigner function exhibits multiple local maxima along the radial direction. A video of the time evolution can be found at [Kehrer (2025)][12]. More thorough studies of the various model parameters have to be performed in the future.

10.7 Conclusion

We have presented a quantum Liénard system whose steady state hosts two coexisting limit cycles. This is qualitatively different in the classical analogue without noise, where the phase space of the oscillator splits in distinct basins of attraction for each limit cycle. Due to the coexistence of both limit cycles, the quantum system exhibits surprising synchronization behavior: coherently driving this quantum twin limit cycle (TLC) oscillator, each of the two limit cycles locks to a distinct phase when the oscillator is detuned from the drive or in the presence of a Kerr nonlinearity. Varying the detuning or the Kerr nonlinearity, the inner limit cycle exhibits a larger phase shift than the outer one. In contrast, the induced phase shift of a standard quantum van der Pol oscillator increases monotonically with its radius. A pair of coherently coupled identical TLC oscillators shows an apparent paradoxical effect: the relative phase of two *equal-sized* limit cycles of oscillators A and B exhibits bistable locking, i.e., the oscillators are in the quantum synchronization blockade. Simultaneously, two limit cycles of *different* radius lock to a single value of the relative phase. Therefore, in a pair of TLCs, both synchronization and blockade *coexist* within the same steady state. Moreover, the range of the gain and damping rates in which the blockades exist is smaller than in the case of standard quantum limit-cycle oscillators. In conclusion, TLCs exhibit synchronization properties that differ in a qualitative way from those of conventional limit cycle oscillators. They provide a foundation for exploring complex collective dynamics and enable the understanding of quantum synchronization in more general systems with multiple coexisting attractors.

Our setup can be extended by incorporating higher-order gain and damping channels, leading to multiple local minima in the effective potential and, therefore, multiple limit cycles. Another choice of dissipation channels that are more localized in Fock space has been studied in [Rips et al. (2012)]. Employing such channels will lead to multiple effective few-level limit cycles in Fock space centered at various Fock numbers. Future directions also include the study of minimal examples, e.g., spin-2 oscillators where both $|\pm 1\rangle$ are stabilized, as well as networks of TLCs. The study of classical

---

[12] Direkt link: https://tobias-kehrer.github.io/thesis/twin_limit_cycles/ [Accessed: July 26, 2025]

multi-limit-cycle oscillators in the framework of synchronization and nonreciprocity appears to be another path of research with rich physics. The analysis of multiple limit cycles within a single quantum steady state opens a promising avenue within the field of quantum synchronization with potential applications in quantum sensing and entanglement generation.

The results and figures of this chapter have been published in parts in [Kehrer et al. (2025)].

Part III

Conclusion

Chapter 11

Conclusion and Outlook

In the recent years, impressive progress of quantum computing hardware has been made. A precursor of fault-tolerant quantum computers are quantum simulators. As an analogy, a fault-tolerant quantum computer can be used to perform quantum simulations in a digital way whereas quantum simulators implement an analog simulation of a quantum system. Including incoherent processes like gain and damping in quantum simulation is of great interest. This thesis has presented contributions to both hardware-oriented modeling of transmon qudits and theoretical studies of unique quantum features of synchronization. Please consult the individual conclusions of each chapter for a more detailed summary.

Part I: Quantum Computing on Superconducting Hardware

Summary

In the current noisy intermediate-scale quantum era, where fault-tolerant quantum computing is not yet achieved, I believe studying quantum computing platforms as a quantum simulator is the most promising avenue. Moreover, to unlock the full potential of the physical implementation of a qubit, higher-excited *qudit* states of its physical Hilbert space have to be taken into account.

In the example of a superconducting transmon qudit on IBM Quantum hardware, in Ch. 4, we have presented a readout model that is used to compare the performance of two proposed measurement strategies. The default strategy to measure two-level qubit states is to maximize the distinguishability of both states. Applying this strategy to qudits, i.e., multiple states, is in general not optimal since more than two states have to be distinguished properly. One strategy we have proposed operates, similar to the default strategy, at a single readout frequency that minimizes the misclassification error of all relevant qudit states simultaneously. Moreover, we have identified the parameter regime in which another strategy, i.e., combining the outcomes of multiple measurements at distinct readout frequencies, outperforms the single-frequency strategy. To prepare the Fock states of a ququart, i.e., the four lowest eigenstates of a qudit, we have employed higher-order X gates by driving two-photon transitions. One of the advantages of such gates is the speed-up of certain qudit operations.

In order to enable the simulation of open quantum systems, e.g., quantum synchronization that has been discussed in the second part of this thesis, on quantum computing hardware that is optimized to realize unitary time evolutions, we have investigated a strategy to engineer an effective incoherent gain. The model that has been presented in Ch. 5, makes use of echo-sequence-like gate operations combined with decay periods to map the native decay to both effective gain and damping. By making the echo sequence asymmetric in time, the ratio of the effective gain and damping rates can be tuned.

In this first part of the thesis, we have improved the default readout of a transmon qudit. Considering it as a noisy quantum computing platform, we have shown that native decay can be used to simulate an effective incoherent gain.

Outlook

The readout model studied in Ch. 4 inspires other measurement schemes. Further improvements of qudit state readout can potentially be achieved by an adaptive measurement scheme in which the readout frequency is updated sequentially between bunches of data in the spirit of Bayesian inference, e.g., see [Granade et al. (2017), García-Pérez et al. (2021)]. Partial information about the quantum state that is gained after a fraction of the measurement might be used to improve the distinguishability of the following parts of the measurement. Other schemes based on adapting readout frequencies might involve neural networks that have already been used for improved readout [Quek et al. (2021), Wang et al. (2025)].

Similar to our implementation of two-photon transitions for higher-order X gates, multiphoton transitions can be utilized to improve other gate operations, even two-qubit gates [Roth et al. (2017), Li et al. (2024)]. Future research involves to identify further feasible higher-order-gate extensions of the universal qudit gate set [Gottesman (1999), Fischer et al. (2023)].

To improve the quantum simulation of open multilevel models, the echo-sequences presented in Ch. 5 have to be extended to qudits. In the three-level qutrit case, new transitions including two-photon processes can be used to generate mixed states by effective incoherent gain. A question that will be worthwhile to answer is: which effective gain and damping operators can be realized in qutrit or qudit models using such echo-sequence-like gate operations? Moreover, the faster decay of higher excited transmon states [Fischer et al. (2022)] can be used to engineer a speed-up mixed-state preparation in comparison to using qubit states only.

Part II: Quantum Synchronization of Oscillating Systems

Summary

In the second part of this thesis, we have focused on one family of open quantum systems we would like to implement on a quantum simulator: limit-cycle oscillators that show quantum synchronization. Here, gain and damping stabilize a limit-cycle state that exhibits a free phase that can be synchronized to an external signal or the phase of other oscillators.

In Ch. 8, using an efficient operator representation of the synchronization measure, we have studied two scenarios of coherently coupled spin-1 oscillators: (i) two oscillators, one of which is driven coherently, and (ii) a chain of three oscillators. Between pairs of oscillators a synchronization blockade occurs that suppresses standard first-order locking of the relative phase of these oscillators such that only second-order bistable locking remains. Here, the pair of spins locks in and out of phase with each other. Another synchronization blockade between the drive and the driven spin exists. Surprisingly, the two spins at both ends of the three-oscillator chain synchronize similar to the undriven spin in the two-oscillator case that synchronizes to the external drive. Since the mentioned synchronization blockades between directly coupled spins persist, i.e., they are not lifted, we refer to this effect as locking *through* the blockades.

A similar interplay of synchronization mechanisms leading to (i) standard locking to a single value of the relative phase between two oscillators and (ii) bistable locking has been presented in Ch. 9. Here, three interactions compete in a setup of two harmonic-oscillator-like modes. A dissipative interaction between both oscillators induces antiphase locking in contrast to a coherent coupling that nurtures bistable phase locking. A coherent drive that acts on one of the oscillators leads to in-phase or antiphase locking depending on the ratio of the dissipative and coherent interaction strength. The resulting phase diagram as well as emerging synchronization blockades have been understood by a perturbation expansion of the steady state. Quantum analogues of traveling-wave states originating from an effective nonreciprocal interaction have been identified by maxima in the Fourier transforms of two-time correlations as well as by quantum trajectory simulations. The classical analogues of two and three oscillators based on their mean-field equations feature many highly nontrivial active states.

In the last publication discussed in Ch. 10 of this thesis, a new avenue of quantum synchronization has been identified: the study of multi-limit-cycle oscillators, i.e., quantum Liénard systems. We have proposed a model whose steady state hosts two *coexisting* limit cycles, which we call a "twin limit cycle". In contrast, in its classical analogue without noise, the phase space of the oscillator splits into two separated basins of attraction, one for each limit cycle. Due to the coexistence in the quantum case, surprising synchronization effects have been found. We have proposed refined quantum synchronization measures to access the locking behavior of the individual limit cycles. The individual limit cycles of a single coherently driven twin limit cycle lock to distinct phases. Moreover, a pair of coherently coupled twin limit-cycle oscillators exhibits *both* synchronization and synchronization blockades in the same steady state.

In this second part of the thesis, we have identified unique quantum effects of synchronization in both spin-1 and harmonic-oscillator-like models. Moreover, a new direction, the quantum synchronization of multi-limit-cycle oscillators, has been initiated.

Outlook

In Ch. 8, we have introduced an operator expression of the common synchronization measure for multiple spins. Answering the question which operator products contribute to the measure for larger spins will improve the study of quantum synchronization in these setups. The drive-spin blockade occurring in spin-1 models of quantum synchronization has no counterpart in harmonic-oscillator-like models. However, an inter-oscillator blockade exists in both cases. This raises the question whether quantum synchronization through the blockades that has been presented in Ch. 8 also exists in a chain of three harmonic-oscillator-like oscillators.

Another set of future topics is related to squeezing and its impact on quantum synchronization [Sonar et al. (2018), Shen et al. (2023)]. In Figs. 7.3(c) and 7.3(d), steady states of models including higher-order squeezing have been shown. The number of visual maxima in the Wigner functions corresponds to the order of squeezing. What are the implications of this higher-order squeezing for the synchronization of single driven oscillators and coupled oscillators? There might be frustration effects emerging when coupling a second-order squeezed oscillator with a third-order squeezed oscillator. Moreover, higher-order squeezing of a limit-cycle state might be studied in the context of multifurcations, i.e., generalized bifurcations [Strogatz (2024), Chia et al. (2025)].

The squeezing of twin limit cycles might also lead to interesting behavior if both limit cycles react differently to the squeezing drive as they do for a standard coherent drive. Can the limit cycles be significantly off-centered and what are the consequences for defining phases of a limit cycle in the sense of the quantum asymptotic phase [Kato and Nakao (2022), Kato and Nakao (2023)]? In analogy of a driven spin-1 oscillator [Roulet and Bruder (2018a)] as the minimal example of a driven quantum oscillator [Lee and Sadeghpour (2013)], what is the minimal example of a twin limit cycle? One candidate is a spin-2 oscillator, where both states with magnetic quantum number plus or minus one are stabilized. In this regard, interesting questions are: (i) what are suitable synchronization measures to resolve the individual limit cycles, (ii) which choices of Lindblad operators can be considered, and (iii) does a new class of blockades between multi-limit-cycles and a coherent drive exist?

In general, one could choose different dissipators that stabilize multiple limit cycles that exhibit better effective control parameters of the size and width of each limit cycles than those presented in Ch. 10. One example is dissipators with a Lorentzian distribution of gain and damping rates in Fock space discussed in [Rips et al. (2012), Lörch et al. (2017)]. Adjusting the center position and width of two of such Lorentzian gain and damping channels will likely lead to easier control of twin limit-cycle states. The proposal of a physical implementation of multi-limit-cycles presented in Sec. 10.6 makes use of the highly nonlinear interaction between the internal degrees of freedom of a trapped ion and its motional modes outside the Lamb-Dicke regime [Leibfried et al. (2003)]. Moreover, the resulting state space of a related scenario in which both gain and damping channels are engineered by blue and red sidebands driven on the same ion transition, see Sec. 3.3.2, can be explored in the context of dissipative phase transitions [Minganti et al. (2023), Beaulieu et al. (2025)]. Does the combination of both setups, i.e., each of two independent ion transitions is used to implement both gain and damping, feature squeezed limit-cycle states?

Another topic besides squeezing is nonreciprocity [Fruchart et al. (2021)]. Taking the setup described in Ch. 9 as an inspiration, i.e, coherent and dissipative coupling, are there also active steady states of nonreciprocally coupled twin limit-cycles? Moving on from two to many twin limit-cycle oscillators, it will be worthwhile to study networks of many multi-limit-cycle oscillators. Since large quantum many-body systems are difficult to simulate, one might start with their classical mean-field equations. Even in this classical description, interesting nontrivial active states might be found, e.g., traveling-wave states where oscillators jump between stable amplitude configurations.

Classical multi-limit-cycles are known in biochemistry [Laurent and Kellershohn (1999), Enjieu Kadji et al. (2007), Feillet et al. (2014), Goldbeter and Yan (2022)]. An arguably highly speculative question is whether quantum synchronization of multi-limit-cycle oscillators has implications for quantum chemistry. Another exploratory project is the investigation of a quantum analogue of swarmalators that have been mentioned in Sec. 6.6 as quantum active matter. A simple scenario to start with might consider two spins 1 that are coupled via a harmonic oscillator. Interpreting these oscillators as ions in a common trap [Behrle et al. (2023)], the coupling-mediating mode corresponds to their relative motion. Extending this setup to multiple spins and oscillators in a 2D trap, a special case of quantum swarmalators would be realized.

More physical implementations of quantum synchronization than the ones mentioned in Ch. 7 can be expected in the near future. Several platforms like superconducting circuits [Grimm et al. (2020)] or trapped ions [Behrle et al. (2023)] offer promising control. The development of new approaches to realizing quantum synchronization can work in both directions: (i) new architectures might be needed to implement known quantum limit cycles and (ii) hardware limitations and hardware features could inspire new ways of limit-cycle-state stabilization.

Bibliography

J. A. Acebrón, L. L. Bonilla, C. J. Pérez Vicente, F. Ritort, and R. Spigler, “The Kuramoto model: A simple paradigm for synchronization phenomena”, Rev. Mod. Phys. **77**, 137–185 (2005).

R. Adler, “A Study of Locking Phenomena in Oscillators”, Proceedings of the IRE **34**, 351–357 (1946).

M. Aifer, J. Thingna, and S. Deffner, “Energetic Cost for Speedy Synchronization in Non-Hermitian Quantum Dynamics”, Phys. Rev. Lett. **133**, 020401 (2024).

T. Alexander, N. Kanazawa, D. J. Egger, L. Capelluto, C. J. Wood, et al., “Qiskit pulse: programming quantum computers through the cloud with pulses”, Quantum Science and Technology **5**, 044006 (2020).

E. Altman, K. R. Brown, G. Carleo, L. D. Carr, E. Demler, et al., “Quantum Simulators: Architectures and Opportunities”, PRX Quantum **2**, 017003 (2021).

V. Ameri, M. Eghbali-Arani, A. Mari, A. Farace, F. Kheirandish, et al., “Mutual information as an order parameter for quantum synchronization”, Phys. Rev. A **91**, 012301 (2015).

E. Amitai, N. Lörch, A. Nunnenkamp, S. Walter, and C. Bruder, “Synchronization of an optomechanical system to an external drive”, Phys. Rev. A **95**, 053858 (2017).

A. P. Antonov, Y. Zheng, B. Liebchen, and H. Löwen, “Engineering active motion in quantum matter”, Phys. Rev. Res. **7**, 033008 (2025).

V. I. Arnol’d, “Small denominators. I. Mapping the circle onto itself”, Izv. Akad. Nauk SSSR Ser. Mat. **25**, 21–86 (1961).

N. Bacaër, *A Short History of Mathematical Population Dynamics* (Springer London, 2011).

A. Balanov, N. Janson, D. Postnov, and O. Sosnovtseva, *Synchronization - From Simple to Complex* (Springer Science & Business Media, Berlin Heidelberg, 2008).

W. Band and J. L. Park, “A general method of empirical state determination in quantum physics: Part II”, Foundations of Physics **1**, 339–357 (1971).

R. Barak and Y. Ben-Aryeh, “Non-orthogonal positive operator valued measure phase distributions of one- and two-mode electromagnetic fields”, Journal of Optics B: Quantum and Semiclassical Optics **7**, 123 (2005).

J. Bardeen and W. H. Brattain, “The Transistor, A Semi-Conductor Triode”, Phys. Rev. **74**, 230–231 (1948).

A. Barenco, C. H. Bennett, R. Cleve, D. P. DiVincenzo, N. Margolus, et al., “Elementary gates for quantum computation”, Phys. Rev. A **52**, 3457–3467 (1995).

R. Barends, J. Kelly, A. Megrant, D. Sank, E. Jeffrey, et al., “Coherent Josephson Qubit Suitable for Scalable Quantum Integrated Circuits”, Phys. Rev. Lett. **111**, 080502 (2013).

J. T. Barreiro, M. Müller, P. Schindler, D. Nigg, T. Monz, et al., “An open-system quantum simulator with trapped ions”, Nature **470**, 486–491 (2011).

V. M. Bastidas, I. Omelchenko, A. Zakharova, E. Schöll, and T. Brandes, “Quantum signatures of chimera states”, Phys. Rev. E **92**, 062924 (2015).

G. Beaulieu, F. Minganti, S. Frasca, V. Savona, S. Felicetti, et al., “Observation of first- and second-order dissipative phase transitions in a two-photon driven Kerr resonator”, Nature Communications **16**, 1954 (2025).

T. Behrle, T. L. Nguyen, F. Reiter, D. Baur, B. de Neeve, et al., “Phonon Laser in the Quantum Regime”, Phys. Rev. Lett. **131**, 043605 (2023).

L. Ben Arosh, M. C. Cross, and R. Lifshitz, “Quantum limit cycles and the Rayleigh and van der Pol oscillators”, Phys. Rev. Res. **3**, 013130 (2021).

P. Benioff, “The computer as a physical system: a microscopic quantum mechanical hamiltonian model of computers as represented by turing machines”, Journal of Statistical Physics **22**, 563–591 (1980).

E. Bernstein and U. Vazirani, “Quantum Complexity Theory”, SIAM Journal on Computing **26**, 1411–1473 (1997).

S. Bhattacharyya, A. Ghosh, and D. S. Ray, “Microscopic quantum generalization of classical Linard oscillators”, Phys. Rev. E **103**, 012118 (2021).

R. Bianchetti, S. Filipp, M. Baur, J. M. Fink, C. Lang, et al., “Control and Tomography of a Three Level Superconducting Artificial Atom”, Phys. Rev. Lett. **105**, 223601 (2010).

A. Blais, A. L. Grimsmo, S. M. Girvin, and A. Wallraff, “Circuit quantum electrodynamics”, Rev. Mod. Phys. **93**, 025005 (2021).

A. Blais, R.-S. Huang, A. Wallraff, S. M. Girvin, and R. J. Schoelkopf, “Cavity quantum electrodynamics for superconducting electrical circuits: An architecture for quantum computation”, Phys. Rev. A **69**, 062320 (2004).

N. Blum, A. Li, K. O’Keeffe, and O. Kogan, “Swarmalators with delayed interactions”, Phys. Rev. E **109**, 014205 (2024).

N. Bohr, “I. On the constitution of atoms and molecules”, The London, Edinburgh, and Dublin Philosophical Magazine and Journal of Science **26**, 1–25 (1913a).

N. Bohr, “LXXIII. On the constitution of atoms and molecules”, The London, Edinburgh, and Dublin Philosophical Magazine and Journal of Science **26**, 857–875 (1913b).

N. Bohr, "XXXVII. On the constitution of atoms and molecules", The London, Edinburgh, and Dublin Philosophical Magazine and Journal of Science **26**, 476–502 (1913c).

H. Bombin and M. A. Martin-Delgado, "Topological Quantum Distillation", Phys. Rev. Lett. **97**, 180501 (2006).

H. Bombin and M. A. Martin-Delgado, "Topological Computation without Braiding", Phys. Rev. Lett. **98**, 160502 (2007).

J. E. Bourassa, R. N. Alexander, M. Vasmer, A. Patil, I. Tzitrin, et al., "Blueprint for a Scalable Photonic Fault-Tolerant Quantum Computer", Quantum **5**, 392 (2021).

S. Bravyi, S. Sheldon, A. Kandala, D. C. Mckay, and J. M. Gambetta, "Mitigating measurement errors in multiqubit experiments", Phys. Rev. A **103**, 042605 (2021).

C. D. Bruzewicz, J. Chiaverini, R. McConnell, and J. M. Sage, "Trapped-ion quantum computing: Progress and challenges", Applied Physics Reviews **6**, 021314 (2019).

B. Buča, C. Booker, and D. Jaksch, "Algebraic theory of quantum synchronization and limit cycles under dissipation", SciPost Physics **12**, 097 (2022).

J. B. Buck, "Synchronous Rhythmic Flashing of Fireflies", The Quarterly Review of Biology **13**, 301–314 (1938).

G. Burkard, T. D. Ladd, A. Pan, J. M. Nichol, and J. R. Petta, "Semiconductor spin qubits", Rev. Mod. Phys. **95**, 025003 (2023).

A. Cabot, G. L. Giorgi, F. Galve, and R. Zambrini, "Quantum Synchronization in Dimer Atomic Lattices", Phys. Rev. Lett. **123**, 023604 (2019).

A. Cabot, G. L. Giorgi, and R. Zambrini, "Nonequilibrium Transition between Dissipative Time Crystals", PRX Quantum **5**, 030325 (2024).

A. Cabot, G. Luca Giorgi, and R. Zambrini, "Synchronization and coalescence in a dissipative two-qubit system", Proceedings of the Royal Society A **477**, 20200850 (2021).

H. J. Carmichael, *Statistical Methods in Quantum Optics 1 - Master Equations and Fokker-Planck Equations* (Springer, Berlin Heidelberg, 1999).

A. Cervera-Lierta, M. Krenn, A. Aspuru-Guzik, and A. Galda, "Experimental High-Dimensional Greenberger-Horne-Zeilinger Entanglement with Superconducting Transmon Qutrits", Phys. Rev. Appl. **17**, 024062 (2022).

E. Champion, Z. Wang, R. W. Parker, and M. S. Blok, "Efficient Control of a Transmon Qudit Using Effective Spin-7/2 Rotations", Phys. Rev. X **15**, 021096 (2025).

D. M. Chapin, C. S. Fuller, and G. L. Pearson, "A New Silicon p-n Junction Photocell for Converting Solar Radiation into Electrical Power", Journal of Applied Physics **25**, 676–677 (1954).

H.-B. Chen, C. Gneiting, P.-Y. Lo, Y.-N. Chen, and F. Nori, "Simulating open quantum systems with hamiltonian ensembles and the nonclassicality of the dynamics", Phys. Rev. Lett. **120**, 030403 (2018).

L. Chen, H.-X. Li, Y. Lu, C. W. Warren, C. J. Križan, et al., “Transmon qubit readout fidelity at the threshold for quantum error correction without a quantum-limited amplifier”, npj Quantum Information **9**, 26, 26 (2023).

A. D. Chepelianskii and D. L. Shepelyansky, “Quantum Synchronization and Entanglement of Dissipative Qubits Coupled to a Resonator”, Entropy **26**, 415 (2024).

A. Chia, L. C. Kwek, and C. Noh, “Relaxation oscillations and frequency entrainment in quantum mechanics”, Phys. Rev. E **102**, 042213 (2020).

A. Chia, W.-K. Mok, L.-C. Kwek, and C. Noh, “Quantization of nonlinear non-Hamiltonian systems”, arXiv:2503.06939 (2025).

C.-U. Choe, T. Dahms, P. Hövel, and E. Schöll, “Controlling synchrony by delay coupling in networks: from in-phase to splay and cluster states”, Phys. Rev. E **81**, 025205 (2010).

A. Ciavarella, N. Klco, and M. J. Savage, “Trailhead for quantum simulation of SU(3) Yang-Mills lattice gauge theory in the local multiplet basis”, Phys. Rev. D **103**, 094501, 094501 (2021).

I. Couzin, “Collective minds”, Nature **445**, 715–715 (2007).

S. Danilin, A. Vepsäläinen, and G. S. Paraoanu, “Experimental state control by fast non-Abelian holonomic gates with a superconducting qutrit”, Physica Scripta **93**, 055101 (2018).

C. Davis-Tilley and A. D. Armour, “Synchronization of micromasers”, Phys. Rev. A **94**, 063819 (2016).

L. De Broglie, “Recherches sur la théorie des Quanta”, Ann. Phys. **10**, 22–128 (1925).

L. Del Re, B. Rost, A. F. Kemper, and J. K. Freericks, “Driven-dissipative quantum mechanics on a lattice: Simulating a fermionic reservoir on a quantum computer”, Phys. Rev. B **102**, 125112 (2020).

D. Deutsch and R. Jozsa, “Rapid solution of problems by quantum computation”, Proceedings of the Royal Society of London. Series A: Mathematical and Physical Sciences **439**, 553–558 (1992).

D. Deutsch and R. Penrose, “Quantum theory, the Church–Turing principle and the universal quantum computer”, Proceedings of the Royal Society of London. A. Mathematical and Physical Sciences **400**, 97–117 (1985).

P. A. M. Dirac and R. H. Fowler, “The fundamental equations of quantum mechanics”, Proceedings of the Royal Society of London. Series A, Containing Papers of a Mathematical and Physical Character **109**, 642–653 (1925).

P. A. M. Dirac and R. H. Fowler, “The physical interpretation of the quantum dynamics”, Proceedings of the Royal Society of London. Series A, Containing Papers of a Mathematical and Physical Character **113**, 621–641 (1927).

J. J. Duistermaat and J. A. C. Kolk, *Lie Groups* (Springer Berlin Heidelberg, 2000).

M. F. Dumas, B. Groleau-Paré, A. McDonald, M. H. Muñoz-Arias, C. Lledó, et al., "Measurement-induced transmon ionization", Phys. Rev. X **14**, 041023 (2024).

A. Duncan and M. Janssen, *Constructing Quantum Mechanics: Volume 1: The Scaffold: 1900-1923* (Oxford University PressOxford, Aug. 2019).

D. J. Egger, M. Werninghaus, M. Ganzhorn, G. Salis, A. Fuhrer, et al., "Pulsed Reset Protocol for Fixed-Frequency Superconducting Qubits", Phys. Rev. Appl. **10**, 044030 (2018).

A. Einstein, "Über einen die Erzeugung und Verwandlung des Lichtes betreffenden heuristischen Gesichtspunkt", Ann. Phys. (Berlin) **322**, 132–148 (1905).

A. Einstein, "Zur Quantentheorie der Strahlung", Phys. Z. **18**, 121–128 (1917).

S. S. Elder, C. S. Wang, P. Reinhold, C. T. Hann, K. S. Chou, et al., "High-Fidelity Measurement of Qubits Encoded in Multilevel Superconducting Circuits", Phys. Rev. X **10**, 011001 (2020).

H. G. Enjieu Kadji, R. Yamapi, and J. B. Chabi Orou, "Synchronization of two coupled self-excited systems with multi-limit cycles", Chaos: An Interdisciplinary Journal of Nonlinear Science **17**, 033113 (2007).

N. Es'haqi-Sani, G. Manzano, R. Zambrini, and R. Fazio, "Synchronization along quantum trajectories", Phys. Rev. Res. **2**, 023101 (2020).

L. Essen and J. V. L. Parry, "An Atomic Standard of Frequency and Time Interval: A Cæsium Resonator", Nature **176**, 280–282 (1955).

A. Fedorov, L. Steffen, M. Baur, M. da Silva, and A. Wallraff, "Implementation of a Toffoli Gate with Superconducting Circuits", Nature **481**, 170 (2012).

C. Feillet, P. Krusche, F. Tamanini, R. C. Janssens, M. J. Downey, et al., "Phase locking and multiple oscillating attractors for the coupled mammalian clock and cell cycle", Proceedings of the National Academy of Sciences **111**, 9828–9833 (2014).

R. C. Fetecau, Y. Huang, and T. Kolokolnikov, "Swarm dynamics and equilibria for a nonlocal aggregation model", Nonlinearity **24**, 2681–2716 (2011).

R. P. Feynman, "Simulating physics with computers", International Journal of Theoretical Physics **21**, 467–488 (1982).

L. E. Fischer, A. Chiesa, F. Tacchino, D. J. Egger, S. Carretta, et al., "Universal Qudit Gate Synthesis for Transmons", PRX Quantum **4**, 030327 (2023).

L. E. Fischer, D. Miller, F. Tacchino, P. K. Barkoutsos, D. J. Egger, et al., "Ancilla-free implementation of generalized measurements for qubits embedded in a qudit space", Phys. Rev. Res. **4**, 033027 (2022).

M. Fruchart, R. Hanai, P. B. Littlewood, and V. Vitelli, "Non-reciprocal phase transitions", Nature **592**, 363 (2021).

G. García-Pérez, M. A. C. Rossi, and S. Maniscalco, “IBM Q Experience as a versatile experimental testbed for simulating open quantum systems”, npj Quantum Information **6**, 1 (2020).

G. García-Pérez, M. A. Rossi, B. Sokolov, F. Tacchino, P. K. Barkoutsos, et al., “Learning to Measure: Adaptive Informationally Complete Generalized Measurements for Quantum Algorithms”, PRX Quantum **2**, 040342 (2021).

D. Garg, Manju, S. Dasgupta, and A. Biswas, “Quantum synchronization and entanglement of indirectly coupled mechanical oscillators in cavity optomechanics: A numerical study”, Physics Letters A **457**, 128557 (2023).

C. Gerry and P. Knight, *Introductory Quantum Optics* (Cambridge University Press, Oct. 2004).

G. L. Giorgi, F. Galve, G. Manzano, P. Colet, and R. Zambrini, “Quantum correlations and mutual synchronization”, Phys. Rev. A **85**, 052101 (2012).

L. Glass, “Synchronization and rhythmic processes in physiology”, Nature **410**, 277–284 (2001).

R. J. Glauber, “Coherent and Incoherent States of the Radiation Field”, Phys. Rev. **131**, 2766–2788 (1963).

A. Goldbeter and J. Yan, “Multi-synchronization and other patterns of multi-rhythmicity in oscillatory biological systems”, Interface Focus **12**, 20210089 (2022).

D. Gottesman, “Fault-Tolerant Quantum Computation with Higher-Dimensional Systems”, in Quantum Computing and Quantum Communications, edited by C. P. Williams (1999), pp. 302–313.

D. Gottesman, “Fault-tolerant quantum computation with constant overhead”, Quantum Info. Comput. **14**, 1338–1372 (2014).

D. Gottesman, A. Kitaev, and J. Preskill, “Encoding a qubit in an oscillator”, Phys. Rev. A **64**, 012310 (2001).

I. S. Gradshteyn and I. M. Ryzhik, *Table of Integrals, Series, and Products (Eighth Edition)*, edited by D. Zwillinger and V. Moll (Academic Press, Boston, 2015).

C. Granade, C. Ferrie, and S. T. Flammia, “Practical adaptive quantum tomography”, New Journal of Physics **19**, 113017 (2017).

A. Grimm, N. E. Frattini, S. Puri, S. O. Mundhada, S. Touzard, et al., “Stabilization and operation of a Kerr-cat qubit”, Nature **584**, 205–209 (2020).

L. K. Grover, “A fast quantum mechanical algorithm for database search”, in Proceedings of the Twenty-Eighth Annual ACM Symposium on Theory of Computing, STOC ’96 (1996), pp. 212–219.

S.-Y. Ha and D. Kim, “Emergence of synchronous behaviors for the Schrödinger–Lohe model with frustration”, Nonlinearity **32**, 4609 (2019).

A. Haase, J. Frahm, D. Matthaei, W. Hänicke, and K.-D. Merboldt, “FLASH imaging: Rapid NMR imaging using low flip-angle pulses”, Journal of Magnetic Resonance **213**, 533–541 (2011).

E. L. Hahn, “Spin Echoes”, Phys. Rev. **80**, 580–594 (1950).

M. Hajdušek, P. Solanki, R. Fazio, and S. Vinjanampathy, “Seeding Crystallization in Time”, Phys. Rev. Lett. **128**, 080603 (2022).

R. Hanai, “Nonreciprocal Frustration: Time Crystalline Order-by-Disorder Phenomenon and a Spin-Glass-like State”, Phys. Rev. X **14**, 011029 (2024).

S. Haroche and J.-M. Raimond, *Exploring the Quantum: Atoms, Cavities, and Photons* (Oxford University Press, Aug. 2006).

N. Hatano and D. R. Nelson, “Localization Transitions in Non-Hermitian Quantum Mechanics”, Phys. Rev. Lett. **77**, 570–573 (1996).

S.-W. He, Z. J. Deng, Y. Xie, Y.-Y. Wang, and P.-X. Chen, “Entanglement signatures for quantum synchronization with single-ion phonon laser”, Opt. Express **32**, 13998–14009 (2024).

G. Heinrich, M. Ludwig, J. Qian, B. Kubala, and F. Marquardt, “Collective Dynamics in Optomechanical Arrays”, Phys. Rev. Lett. **107**, 043603 (2011).

W. Heisenberg, “Über quantentheoretische Umdeutung kinematischer und mechanischer Beziehungen.”, Zeitschrift für Physik **33**, 879–893 (1925).

J. Hennig, A. Nauerth, and H. Friedburg, “RARE imaging: A fast imaging method for clinical MR”, Magnetic Resonance in Medicine **3**, 823–833 (1986).

N. Holonyak and S. F. Bevacqua, “Coherent (Visible) Light Emission From Ga(As1-xPx) Junctions”, Applied Physics Letters **1**, 82–83 (1962).

T. Holstein and H. Primakoff, “Field Dependence of the Intrinsic Domain Magnetization of a Ferromagnet”, Phys. Rev. **58**, 1098–1113 (1940).

H. Hong and S. H. Strogatz, “Kuramoto Model of Coupled Oscillators with Positive and Negative Coupling Parameters: An Example of Conformist and Contrarian Oscillators”, Phys. Rev. Lett. **106**, 054102 (2011a).

H. Hong and S. H. Strogatz, “Conformists and contrarians in a Kuramoto model with identical natural frequencies”, Phys. Rev. E **84**, 046202 (2011b).

M. Horodecki, P. Horodecki, and R. Horodecki, “Separability of mixed states: necessary and sufficient conditions”, Physics Letters A **223**, 1–8 (1996).

G. N. Hounsfield, “Computerized transverse axial scanning (tomography): Part 1. Description of system”, British Journal of Radiology **46**, 1016–1022 (2014).

B. J. H. Hughes, “Pseudo-Force Extension of the Swarmalator Model”, Supervisors: T. Kehrer and C. Bruder, Project Thesis (University of Basel, Department of Physics, 2024).

M. R. Hush, W. Li, S. Genway, I. Lesanovsky, and A. D. Armour, “Spin correlations as a probe of quantum synchronization in trapped-ion phonon lasers”, Phys. Rev. A **91**, 061401(R) (2015).

K. Husimi, “Some Formal Properties of the Density Matrix”, Proceedings of the Physico-Mathematical Society of Japan. 3rd Series **22**, 264–314 (1940).

C. Huygens, *Oeuvres complètes. Tome V. Correspondance 1664-1665*, edited by D. B. de Haan (Société Hollandaise Des Sciences, Martinus Nijhoff, Den Haag, 1893).

M.-J. Hwang and M. B. Plenio, “Quantum Phase Transition in the Finite Jaynes-Cummings Lattice Systems”, Phys. Rev. Lett. **117**, 123602 (2016).

M.-J. Hwang, P. Rabl, and M. B. Plenio, “Dissipative phase transition in the open quantum Rabi model”, Phys. Rev. A **97**, 013825 (2018).

IBM Quantum., https://quantum.ibm.com/ (2023).

IBM Quantum., https://quantum.cloud.ibm.com/ (2025).

A. V. Ivlev, J. Bartnick, M. Heinen, C.-R. Du, V. Nosenko, et al., “Statistical Mechanics where Newton’s Third Law is Broken”, Phys. Rev. X **5**, 011035 (2015).

M. Janssen and A. Duncan, *Constructing Quantum Mechanics Volume Two: The Arch, 1923-1927* (Oxford University Press Oxford, Aug. 2023).

N. Jaseem, M. Hajdušek, P. Solanki, L.-C. Kwek, R. Fazio, et al., “Generalized measure of quantum synchronization”, Phys. Rev. Res. **2**, 043287 (2020a).

N. Jaseem, M. Hajdušek, V. Vedral, R. Fazio, L.-C. Kwek, et al., “Quantum synchronization in nanoscale heat engines”, Phys. Rev. E **101**, 020201 (2020b).

A. Javadi-Abhari, M. Treinish, K. Krsulich, C. J. Wood, J. Lishman, et al., “Quantum computing with Qiskit”, arXiv:2405.08810 (2024).

E. Jaynes and F. Cummings, “Comparison of quantum and semiclassical radiation theories with application to the beam maser”, Proceedings of the IEEE **51**, 89–109 (1963).

M. Jerger, P. Macha, A. R. Hamann, Y. Reshitnyk, K. Juliusson, et al., “Realization of a Binary-Outcome Projection Measurement of a Three-Level Superconducting Quantum System”, Phys. Rev. Appl. **6**, 014014 (2016).

T. H. Johnson, S. R. Clark, and D. Jaksch, “What is a quantum simulator?”, EPJ Quantum Technology **1**, 10 (2014).

B. Josephson, “Possible new effects in superconductive tunnelling”, Physics Letters **1**, 251–253 (1962).

A. Kandala, A. Mezzacapo, K. Temme, M. Takita, M. Brink, et al., “Hardware-efficient variational quantum eigensolver for small molecules and quantum magnets”, Nature **549**, 242–246 (2017).

G. Karpat, İ. Yalçınkaya, and B. Çakmak, “Quantum synchronization of few-body systems under collective dissipation”, Phys. Rev. A **101**, 042121 (2020).

Y. Kato and H. Nakao, “A definition of the asymptotic phase for quantum nonlinear oscillators from the Koopman operator viewpoint”, Chaos: An Interdisciplinary Journal of Nonlinear Science **32**, 063133 (2022).

Y. Kato and H. Nakao, “Quantum asymptotic phases reveal signatures of quantum synchronization”, New Journal of Physics **25**, 023012 (2023).

Y. Kato and H. Nakao, “Quantum spin van der Pol oscillator – a spin-based limit-cycle oscillator exhibiting quantum synchronization”, arXiv:2409.08791 (2024).

T. Kehrer, *Personal Website*, https://tobias-kehrer.github.io/thesis/ [Accessed: July 26, 2025], 2025.

T. Kehrer and C. Bruder, “Quantum synchronization blockade induced by nonreciprocal coupling”, Phys. Rev. A **112**, 012223 (2025).

T. Kehrer, C. Bruder, and P. Solanki, “Quantum Synchronization of Twin Limit-Cycle Oscillators”, Phys. Rev. Lett. **135**, 063601 (2025).

T. Kehrer, T. Nadolny, and C. Bruder, “Improving transmon qudit measurement on IBM Quantum hardware”, Phys. Rev. Res. **6**, 013050 (2024a).

T. Kehrer, T. Nadolny, and C. Bruder, “Quantum synchronization through the interference blockade”, Phys. Rev. A **110**, 042203 (2024b).

Y. Kim, A. Eddins, S. Anand, K. X. Wei, E. van den Berg, et al., “Evidence for the utility of quantum computing before fault tolerance”, Nature **618**, 500–505 (2023).

A. Y. Kitaev, “Quantum computations: algorithms and error correction”, Russian Mathematical Surveys **52**, 1191–1249 (1997).

J. Koch, T. M. Yu, J. Gambetta, A. A. Houck, D. I. Schuster, et al., “Charge-insensitive qubit design derived from the Cooper pair box”, Phys. Rev. A **76**, 042319 (2007).

M. Koppenhöfer, C. Bruder, and A. Roulet, “Quantum synchronization on the IBM Q system”, Physical Review Research **2**, 023026 (2020).

M. Koppenhöfer and A. Roulet, “Optimal synchronization deep in the quantum regime: Resource and fundamental limit”, Phys. Rev. A **99**, 043804 (2019).

S. Kotz, N. Balakrishnan, and N. L. Johnson, “Dirichlet and Inverted Dirichlet Distributions”, in *Continuous multivariate distributions*, edited by W. A. Shewhart and S. S. Wilks (John Wiley & Sons, Ltd, 2000) Chap. 49, pp. 485–527.

P. Krantz, M. Kjaergaard, F. Yan, T. P. Orlando, S. Gustavsson, et al., “A quantum engineer’s guide to superconducting qubits”, Applied Physics Reviews **6**, 021318 (2019).

V. R. Krithika, P. Solanki, S. Vinjanampathy, and T. S. Mahesh, “Observation of quantum phase synchronization in a nuclear-spin system”, Phys. Rev. A **105**, 062206 (2022).

C. M. Kropf, C. Gneiting, and A. Buchleitner, “Effective dynamics of disordered quantum systems”, Phys. Rev. X **6**, 031023 (2016).

R. Kumar, M. K. Singh, S. Mahajan, and A. B. Bhattacherjee, "Study of optical bistability/multistability and transparency in cavity-assisted-hybrid optomechanical system embedded with quantum dot molecules", Opt Quant Electron **56**, 91 (2024).

Y. Kuramoto, "Self-entrainment of a population of coupled non-linear oscillators", in *International symposium on mathematical problems in theoretical physics* (Springer, Berlin, Heidelberg, 1975).

Y. Kuramoto, *Chemical Oscillations, Waves, and Turbulence* (Springer Berlin Heidelberg, 1984).

W. Kutta, "Beitrag zur näherungsweisen Integration totaler Differentialgleichungen", Zeitschrift für Mathematik und Physik **46**, 435–453 (1901).

L. D. Landau, "52 - On The Problem Of Turbulence", in *Collected Papers of L.D. Landau*, edited by D. ter Haar (Pergamon, 1965), pp. 387–391.

L. D. Landau and E. M. Lifshitz, *Quantum Mechanics: Non-Relativistic Theory* (Elsevier, 1977).

A. W. Laskar, P. Adhikary, S. Mondal, P. Katiyar, S. Vinjanampathy, et al., "Observation of Quantum Phase Synchronization in Spin-1 Atoms", Phys. Rev. Lett. **125**, 013601 (2020).

M. Laurent and N. Kellershohn, "Multistability: a major means of differentiation and evolution in biological systems", Trends in Biochemical Sciences **24**, 418–422 (1999).

P. C. Lauterbur, "Image Formation by Induced Local Interactions: Examples Employing Nuclear Magnetic Resonance", Nature **242**, 190–191 (1973).

T. E. Lee, C.-K. Chan, and S. Wang, "Entanglement tongue and quantum synchronization of disordered oscillators", Phys. Rev. E **89**, 022913 (2014).

T. E. Lee and H. R. Sadeghpour, "Quantum Synchronization of Quantum van der Pol Oscillators with Trapped Ions", Phys. Rev. Lett. **111**, 234101 (2013).

D. Leibfried, R. Blatt, C. Monroe, and D. Wineland, "Quantum dynamics of single trapped ions", Rev. Mod. Phys. **75**, 281–324 (2003).

G. A. Leonov and N. V. Kuznetsov, "Hidden Attractors in Dynamical Systems: from Hidden Oscillations in Hilbert-Kolmogorov, Aizerman, and Kalman Problems to Hidden Chaotic Attractor in Chua Circuits", International Journal of Bifurcation and Chaos **23**, 1330002 (2013).

J. Leppäkangas, N. Vogt, K. R. Fratus, K. Bark, J. A. Vaitkus, et al., "Quantum algorithm for solving open-system dynamics on quantum computers using noise", Phys. Rev. A **108**, 062424 (2023).

B. Li, T. Calarco, and F. Motzoi, "Experimental error suppression in Cross-Resonance gates via multi-derivative pulse shaping", npj Quantum Information **10**, 66 (2024).

S. Li, B.-J. Liu, Z. Ni, L. Zhang, Z.-Y. Xue, et al., “Superrobust Geometric Control of a Superconducting Circuit”, Phys. Rev. Appl. **16**, 064003 (2021).

A. Liénard, “Etude des oscillations entretenues”, Revue générale de l’électricité **23**, 901–912, 946–954 (1928).

J. U. F. Lizarraga and M. A. M. de Aguiar, “Synchronization and spatial patterns in forced swarmalators”, Chaos: An Interdisciplinary Journal of Nonlinear Science **30**, 053112 (2020).

N. Lörch, E. Amitai, A. Nunnenkamp, and C. Bruder, “Genuine Quantum Signatures in Synchronization of Anharmonic Self-Oscillators”, Phys. Rev. Lett. **117**, 073601 (2016).

N. Lörch, S. E. Nigg, A. Nunnenkamp, R. P. Tiwari, and C. Bruder, “Quantum Synchronization Blockade: Energy Quantization Hinders Synchronization of Identical Oscillators”, Phys. Rev. Lett. **118**, 243602 (2017).

N. Lörch, J. Qian, A. Clerk, F. Marquardt, and K. Hammerer, “Laser Theory for Optomechanics: Limit Cycles in the Quantum Regime”, Phys. Rev. X **4**, 011015 (2014).

S. Lorenzo, B. Militello, A. Napoli, R. Zambrini, and G. M. Palma, “Quantum synchronisation and clustering in chiral networks”, New Journal of Physics **24**, 023030 (2022).

A. J. Lotka, “Analytical Note on Certain Rhythmic Relations in Organic Systems”, Proceedings of the National Academy of Sciences **6**, 410–415 (1920).

A. J. Lotka, *Elements of Physical Biology* (Williams & Wilkins, 1925).

S. Luccioli, S. Olmi, A. Politi, and A. Torcini, “Collective dynamics in sparse networks”, Phys. Rev. Lett. **109**, 138103 (2012).

M. Ludwig and F. Marquardt, “Quantum Many-Body Dynamics in Optomechanical Arrays”, Phys. Rev. Lett. **111**, 073603 (2013).

T. H. Maiman, “Stimulated Optical Radiation in Ruby”, Nature **187**, 493–494 (1960).

Y. Makhlin, G. Schön, and A. Shnirman, “Quantum-state engineering with Josephson-junction devices”, Rev. Mod. Phys. **73**, 357–400 (2001).

R. Mandelbaum, A. D. Córcoles, and J. Gambetta, “IBM’s Big Bet on the Quantum-Centric Supercomputer: Recent Advances Point the Way to Useful Classical-Quantum Hybrids”, IEEE Spectrum **61**, 24–33 (2024).

M. M. Mano and M. D. Ciletti, *Digital Design: With a introduction to the Verilog HDL* (Pearson Prentice Hall, 2013).

V. E. Manucharyan, J. Koch, L. I. Glazman, and M. H. Devoret, “Fluxonium: Single Cooper-Pair Circuit Free of Charge Offsets”, Science **326**, 113–116 (2009).

G. Manzano, F. Galve, G. L. Giorgi, E. Hernández-García, and R. Zambrini, “Synchronization, quantum correlations and entanglement in oscillator networks”, Scientific Reports **3**, 1439 (2013).

A. Mari, A. Farace, N. Didier, V. Giovannetti, and R. Fazio, “Measures of Quantum Synchronization in Continuous Variable Systems”, Phys. Rev. Lett. **111**, 103605 (2013).

F. Marquardt, J. G. E. Harris, and S. M. Girvin, “Dynamical Multistability Induced by Radiation Pressure in High-Finesse Micromechanical Optical Cavities”, Phys. Rev. Lett. **96**, 103901 (2006).

J. M. Martinis, S. Nam, J. Aumentado, and C. Urbina, “Rabi Oscillations in a Large Josephson-Junction Qubit”, Phys. Rev. Lett. **89**, 117901 (2002).

D. C. McKay, T. Alexander, L. Bello, M. J. Biercuk, L. Bishop, et al., “Qiskit Backend Specifications for OpenQASM and OpenPulse Experiments”, arXiv:1809.03452 (2018).

D. C. McKay, I. Hincks, E. J. Pritchett, M. Carroll, L. C. G. Govia, et al., “Benchmarking Quantum Processor Performance at Scale”, arXiv:2311.05933 (2023).

D. C. McKay, C. J. Wood, S. Sheldon, J. M. Chow, and J. M. Gambetta, “Efficient Z gates for quantum computing”, Phys. Rev. A **96**, 022330 (2017).

A. Metelmann and A. A. Clerk, “Nonreciprocal Photon Transmission and Amplification via Reservoir Engineering”, Phys. Rev. X **5**, 021025 (2015).

K. C. Miao, M. McEwen, J. Atalaya, D. Kafri, L. P. Pryadko, et al., “Overcoming leakage in quantum error correction”, Nature Physics **19**, 1780–1786 (2023).

M. H. Michael, M. Silveri, R. T. Brierley, V. V. Albert, J. Salmilehto, et al., “New Class of Quantum Error-Correcting Codes for a Bosonic Mode”, Phys. Rev. X **6**, 031006 (2016).

A. Miessen, D. J. Egger, I. Tavernelli, and G. Mazzola, “Benchmarking Digital Quantum Simulations Above Hundreds of Qubits Using Quantum Critical Dynamics”, PRX Quantum **5**, 040320 (2024).

F. Minganti, V. Savona, and A. Biella, “Dissipative phase transitions in n-photon driven quantum nonlinear resonators”, Quantum **7**, 1170 (2023).

M. Mirrahimi, Z. Leghtas, V. V. Albert, S. Touzard, R. J. Schoelkopf, et al., “Dynamically protected cat-qubits: a new paradigm for universal quantum computation”, New Journal of Physics **16**, 045014 (2014).

T. Nadolny and C. Bruder, “Macroscopic Quantum Synchronization Effects”, Phys. Rev. Lett. **131**, 190402 (2023).

T. Nadolny, C. Bruder, and M. Brunelli, “Nonreciprocal Synchronization of Active Quantum Spins”, Physical Review X **15**, 011010 (2025a).

T. Nadolny, M. Brunelli, and C. Bruder, “Nonreciprocal Interactions Induce Frequency Shifts in Superradiant Lasers”, Phys. Rev. Lett. **134**, 193603 (2025b).

C. Nayak, S. H. Simon, A. Stern, M. Freedman, and S. Das Sarma, “Non-Abelian anyons and topological quantum computation”, Rev. Mod. Phys. **80**, 1083–1159 (2008).

J. von Neumann, “First draft of a report on the EDVAC”, IEEE Annals of the History of Computing **15**, 27–75 (1993).

J. von Neumann, “Mathematische Begründung der Quantenmechanik”, Königliche Gesellschaft der Wissenschaften zu Göttingen. Mathematisch-physikalische Klasse, Nachrichten 1–57 (1927a).

J. von Neumann, “Wahrscheinlichkeitstheoretischer Aufbau der Quantenmechanik”, Königliche Gesellschaft der Wissenschaften zu Göttingen. Mathematisch-physikalische Klasse, Nachrichten 245–272 (1927b).

J. von Neumann, “Thermodynamik quantenmechanischer Gesamtheiten”, Königliche Gesellschaft der Wissenschaften zu Göttingen. Mathematisch-physikalische Klasse, Nachrichten 273–291 (1927c).

I. Newton, *Philosophiæ Naturalis Principia Mathematica* (Jussu Societatis Regiæ ac Typis Joseph Streater. Prostat apud plures bibliopola, Londini, 1687).

I. Newton, *The Mathematical Principles of Natural Philosophy*, Translated into English by Andrew Motte (Printed for Benjamin Motte, at the Middle-Temple-Gate, in Fleetstreet, London, 1729).

M. A. Nielsen and I. L. Chuang, *Quantum Computation and Quantum Information - 10th Anniversary Edition* (Cambridge University Press, Cambridge, 2010).

K. O’Keeffe and H. Hong, “Swarmalators on a ring with distributed couplings”, Phys. Rev. E **105**, 064208 (2022).

K. P. O’Keeffe, H. Hong, and S. H. Strogatz, “Oscillators that sync and swarm”, Nature Communications **8**, 1504 (2017).

N. Ofek, A. Petrenko, R. Heeres, P. Reinhold, Z. Leghtas, et al., “Extending the lifetime of a quantum bit with error correction in superconducting circuits”, Nature **536**, 441–445 (2016).

H. M. Oliveira and L. V. Melo, “Huygens synchronization of two clocks”, Scientific Reports **5**, 11548 (2015).

E. Ott and T. M. Antonsen, “Low dimensional behavior of large systems of globally coupled oscillators”, Chaos: An Interdisciplinary Journal of Nonlinear Science **18**, 037113 (2008).

D. B. Owen, “A table of normal integrals”, Communications in Statistics - Simulation and Computation **9**, 389–419 (1980).

D. B. Owen, “Tables for Computing Bivariate Normal Probabilities”, The Annals of Mathematical Statistics **27**, 1075–1090 (1956).

Á. Parra-López and J. Bergli, “Synchronization in two-level quantum systems”, Phys. Rev. A **101**, 062104 (2020).

W. Paul, “Electromagnetic traps for charged and neutral particles”, Rev. Mod. Phys. **62**, 531–540 (1990).

W. Pauli, “Über den Zusammenhang des Abschlusses der Elektronengruppen im Atom mit der Komplexstruktur der Spektren”, Zeitschrift für Physik **31**, 765–783 (1925).

I. V. Pechenezhskiy, R. A. Mencia, L. B. Nguyen, Y.-H. Lin, and V. E. Manucharyan, “The superconducting quasicharge qubit”, Nature **585**, 368–371 (2020).

A.-G. Penner, L. Viotti, R. Fazio, L. Arrachea, and F. von Oppen, “Heat-to-motion conversion for quantum active matter”, arXiv:2503.07751 (2025).

F. Penning, “Die Glimmentladung bei niedrigem Druck zwischen koaxialen Zylindern in einem axialen Magnetfeld”, Physica **3**, 873–894 (1936).

A. Peres, “Separability Criterion for Density Matrices”, Phys. Rev. Lett. **77**, 1413–1415 (1996).

L. Perko, *Differential Equations and Dynamical Systems* (Springer New York, 2001).

A. Pikovsky and M. Rosenblum, “Dynamics of globally coupled oscillators: progress and perspectives”, Chaos: An Interdisciplinary Journal of Nonlinear Science **25**, 097616 (2015).

A. Pikovsky, M. Rosenblum, and J. Kurths, *Synchronization: A Universal Concept in Nonlinear Science* (Cambridge University Press, Cambridge, England, 2001).

M. Planck, “Ueber das Gesetz der Energieverteilung im Normalspectrum”, Ann. Phys. (Berlin) **309**, 553–563 (1901).

B. van der Pol, “A Theory of the Amplitude of Free and Forced Triode Vibrations”, The Radio Review **1**, 701–710 (1920).

B. van der Pol, “VII. Forced oscillations in a circuit with non-linear resistance. (Reception with reactive triode)”, The London, Edinburgh, and Dublin Philosophical Magazine and Journal of Science **3**, 65–80 (1927).

J. F. Poyatos, J. I. Cirac, and P. Zoller, “Quantum Reservoir Engineering with Laser Cooled Trapped Ions”, Phys. Rev. Lett. **77**, 4728–4731 (1996).

J. Preskill, “Quantum Computing in the NISQ era and beyond”, Quantum **2**, 79 (2018).

R. Puebla, M.-J. Hwang, J. Casanova, and M. B. Plenio, “Probing the Dynamics of a Superradiant Quantum Phase Transition with a Single Trapped Ion”, Phys. Rev. Lett. **118**, 073001 (2017).

Qiskit contributors, *Qiskit: an open-source framework for quantum computing*, 2023.

Y. Quek, S. Fort, and H. K. Ng, “Adaptive quantum state tomography with neural networks”, npj Quantum Information **7**, 105 (2021).

S. Ramaswamy, “The Mechanics and Statistics of Active Matter”, Annual Review of Condensed Matter Physics **1**, 323 (2010).

N. F. Ramsey, “A Molecular Beam Resonance Method with Separated Oscillating Fields”, Phys. Rev. **78**, 695–699 (1950).

S. Rips, M. Kiffner, I. Wilson-Rae, and M. J. Hartmann, “Steady-state negative Wigner functions of nonlinear nanomechanical oscillators”, New Journal of Physics **14**, 023042 (2012).

D. Ristè, C. C. Bultink, M. J. Tiggelman, R. N. Schouten, K. W. Lehnert, et al., "Millisecond charge-parity fluctuations and induced decoherence in a superconducting transmon qubit", Nature Communications **4**, 1913 (2013).

R. L. Rivest, A. Shamir, and L. Adleman, "A method for obtaining digital signatures and public-key cryptosystems", Commun. ACM **21**, 120–126 (1978).

M. Rohden, A. Sorge, M. Timme, and D. Witthaut, "Self-Organized Synchronization in Decentralized Power Grids", Phys. Rev. Lett. **109**, 064101 (2012).

I. Rojkov, M. Simoni, E. Zapusek, F. Reiter, and J. Home, "Stabilization of cat-state manifolds using nonlinear reservoir engineering", arXiv:2407.18087 (2024).

B. Rost, B. Jones, M. Vyushkova, A. Ali, C. Cullip, et al., "Simulation of Thermal Relaxation in Spin Chemistry Systems on a Quantum Computer Using Inherent Qubit Decoherence", arXiv:2001.00794 (2020).

A. Roth and K. Hammerer, "Synchronization of active atomic clocks via quantum and classical channels", Phys. Rev. A **94**, 043841 (2016).

M. Roth, M. Ganzhorn, N. Moll, S. Filipp, G. Salis, et al., "Analysis of a parametrically driven exchange-type gate and a two-photon excitation gate between superconducting qubits", Phys. Rev. A **96**, 062323 (2017).

A. Roulet and C. Bruder, "Synchronizing the Smallest Possible System", Phys. Rev. Lett. **121**, 053601 (2018a).

A. Roulet and C. Bruder, "Quantum Synchronization and Entanglement Generation", Phys. Rev. Lett. **121**, 063601 (2018b).

C. Ruby and M. Lakshmanan, "Liénard type nonlinear oscillators and quantum solvability", Physica Scripta **99**, 062004 (2024).

C. Runge, "Ueber die numerische Auflösung von Differentialgleichungen", Mathematische Annalen **46**, 167–178 (1895).

M. Saffman, "Quantum computing with atomic qubits and Rydberg interactions: progress and challenges", Journal of Physics B Atomic Molecular Physics **49**, 202001 (2016).

C. Schäfer, M. G. Rosenblum, J. Kurths, and H.-H. Abel, "Heartbeat synchronized with ventilation", Nature **392**, 239–240 (1998).

A. W. Schlimgen, K. Head-Marsden, L. M. Sager, P. Narang, and D. A. Mazziotti, "Quantum Simulation of Open Quantum Systems Using a Unitary Decomposition of Operators", Phys. Rev. Lett. **127**, 270503 (2021).

E. Schrödinger, "Quantisierung als Eigenwertproblem", Annalen der Physik **384**, 361–376 (1926a).

E. Schrödinger, "Quantisierung als Eigenwertproblem", Annalen der Physik **384**, 489–527 (1926b).

E. Schrödinger, "Quantisierung als Eigenwertproblem", Annalen der Physik **385**, 437–490 (1926c).

E. Schrödinger, “Quantisierung als Eigenwertproblem”, Annalen der Physik **386**, 109–139 (1926d).

E. Schrödinger, “Über das Verhältnis der Heisenberg-Born-Jordanschen Quantenmechanik zu der meinen”, Annalen der Physik **384**, 734–756 (1926e).

F. Schwabl, *Quantum Mechanics* (Springer, Berlin Heidelberg New York, 2007).

F. Schweitzer, “An agent-based framework of active matter with applications in biological and social systems”, European Journal of Physics **40**, 014003 (2019).

Y. Shen, H. Y. Soh, W. Fan, and L.-C. Kwek, “Enhancing quantum synchronization through homodyne measurement, noise, and squeezing”, Phys. Rev. E **108**, 024204 (2023).

A. Shnirman, G. Schön, and Z. Hermon, “Quantum Manipulations of Small Josephson Junctions”, Phys. Rev. Lett. **79**, 2371–2374 (1997).

P. W. Shor, “Scheme for reducing decoherence in quantum computer memory”, Phys. Rev. A **52**, R2493–R2496 (1995).

P. W. Shor, “Polynomial-Time Algorithms for Prime Factorization and Discrete Logarithms on a Quantum Computer”, SIAM Journal on Computing **26**, 1484–1509 (1997).

M. M. Shulaker, G. Hills, N. Patil, H. Wei, H.-Y. Chen, et al., “Carbon nanotube computer”, Nature **501**, 526–530 (2013).

D. R. Simon, “On the Power of Quantum Computation”, SIAM Journal on Computing **26**, 1474–1483 (1997).

S. Slussarenko and G. J. Pryde, “Photonic quantum information processing: A concise review”, Applied Physics Reviews **6**, 041303 (2019).

P. Solanki, N. Jaseem, M. Hajdušek, and S. Vinjanampathy, “Role of coherence and degeneracies in quantum synchronization”, Phys. Rev. A **105**, L020401 (2022).

P. Solanki, M. Krishna, M. Hajdušek, C. Bruder, and S. Vinjanampathy, “Exotic Synchronization in Continuous Time Crystals Outside the Symmetric Subspace”, Phys. Rev. Lett. **133**, 260403 (2024).

P. Solanki, F. M. Mehdi, M. Hajdušek, and S. Vinjanampathy, “Symmetries and synchronization blockade”, Phys. Rev. A **108**, 022216 (2023).

A. Sommerfeld, “Zur Quantentheorie der Spektrallinien”, Ann. Phys. (Berlin) **356**, 1–94 (1916a).

A. Sommerfeld, “Zur Quantentheorie der Spektrallinien”, Ann. Phys. (Berlin) **356**, 125–167 (1916b).

S. Sonar, M. Hajdušek, M. Mukherjee, R. Fazio, V. Vedral, et al., “Squeezing Enhances Quantum Synchronization”, Phys. Rev. Lett. **120**, 163601 (2018).

K. Sone, Y. Ashida, and T. Sagawa, “Topological synchronization of coupled nonlinear oscillators”, Phys. Rev. Res. **4**, 023211 (2022).

H. L. Stover and W. H. Steier, “Locking of Laser Oscillators by Light Injection”, Applied Physics Letters **8**, 91–93 (1966).

F. W. Strauch, S. K. Dutta, H. Paik, T. A. Palomaki, K. Mitra, et al., “Strong-Field Effects in the Rabi Oscillations of the Superconducting Phase Qubit”, IEEE Transactions on Applied Superconductivity **17**, 105–108 (2007).

S. H. Strogatz, *Nonlinear Dynamics and Chaos: With Applications to Physics, Biology, Chemistry, and Engineering* (Chapman and Hall/CRC, Jan. 2024).

S. H. Strogatz, *Sync: The Emerging Science of Spontaneous Order* (Hyperion, New York, 2003).

S. H. Strogatz, D. M. Abrams, A. McRobie, B. Eckhardt, and E. Ott, “Theoretical mechanics: Crowd synchrony on the Millennium Bridge”, **438**, 43–44 (2005).

J. T. Stuart, “On the non-linear mechanics of wave disturbances in stable and unstable parallel flows Part 1. The basic behaviour in plane Poiseuille flow”, Journal of Fluid Mechanics **9**, 353–370 (1960).

D. J. T. Sumpter, *Collective Animal Behavior* (Princeton University Press, Princeton, NJ, Oct. 2010).

S. Sun, L.-C. Shih, and Y.-C. Cheng, “Efficient quantum simulation of open quantum system dynamics on noisy quantum computers”, Physica Scripta **99**, 035101 (2024).

L. Susskind and J. Glogower, “Quantum mechanical phase and time operator”, Physics Physique Fizika **1**, 49–61 (1964).

M. Suzuki, “Generalized Trotter’s formula and systematic approximants of exponential operators and inner derivations with applications to many-body problems”, Communications in Mathematical Physics **51**, 183–190 (1976).

R. Sweke, I. Sinayskiy, D. Bernard, and F. Petruccione, “Universal simulation of Markovian open quantum systems”, Phys. Rev. A **91**, 062308 (2015).

F. Tacchino, A. Chiesa, R. Sessoli, I. Tavernelli, and S. Carretta, “A proposal for using molecular spin qudits as quantum simulators of light–matter interactions”, J. Mater. Chem. C **9**, 10266–10275 (2021).

H. Taher, S. Olmi, and E. Schöll, “Enhancing power grid synchronization and stability through time-delayed feedback control”, Phys. Rev. E **100**, 062306 (2019).

R. Tan, C. Bruder, and M. Koppenhöfer, “Half-integer vs. integer effects in quantum synchronization of spin systems”, Quantum **6**, 885 (2022).

Z. Tao, F. Schmolke, C.-K. Hu, W. Huang, Y. Zhou, et al., “Noise-induced quantum synchronization with entangled oscillations”, Nature Communications **16**, 8457 (2025).

N. Thomas and M. Senthilvelan, “Quantum synchronization in quadratically coupled quantum van der Pol oscillators”, Phys. Rev. A **106**, 012422 (2022).

M. Tolunay, I. Liepuoniute, M. Vyushkova, and B. A. Jones, “Hamiltonian simulation of quantum beats in radical pairs undergoing thermal relaxation on near-term quantum computers”, Physical Chemistry Chemical Physics **25**, 15115–15134 (2023).

H. F. Trotter, “On the product of semi-groups of operators”, Proceedings of the American Mathematical Society **10**, 545–551 (1959).

L. Tumash, A. Zakharova, J. Lehnert, W. Just, and E. Schöll, “Stability of amplitude chimeras in oscillator networks”, EPL (Europhysics Letters) **117**, 20001 (2017).

UNESCO, *International Year of Quantum Science and Technology*, https://quantum2025.org [Accessed: March 15, 2025], 2025.

G. M. Vaidya, S. B. Jäger, and A. Shankar, “Quantum synchronization and dissipative quantum sensing”, Phys. Rev. A **111**, 012410 (2025).

D. Viennot and L. Aubourg, “Quantum chimera states”, Physics Letters A **380**, 678–683 (2016).

V. Volterra, “Fluctuations in the Abundance of a Species considered Mathematically^1”, Nature **118**, 558–560 (1926).

U. Vool and M. Devoret, “Introduction to quantum electromagnetic circuits”, International Journal of Circuit Theory and Applications **45**, 897–934 (2017).

M. te Vrugt and R. Wittkowski, “Metareview: a survey of active matter reviews”, The European Physical Journal E **48**, 12 (2025).

C. W. Wächtler, V. M. Bastidas, G. Schaller, and W. J. Munro, “Dissipative nonequilibrium synchronization of topological edge states via self-oscillation”, Phys. Rev. B **102**, 014309 (2020).

C. W. Wächtler and J. E. Moore, “Topological Quantum Synchronization of Fractionalized Spins”, Phys. Rev. Lett. **132**, 196601 (2024).

C. W. Wächtler and G. Platero, “Topological synchronization of quantum van der Pol oscillators”, Phys. Rev. Res. **5**, 023021 (2023).

S. Walter, A. Nunnenkamp, and C. Bruder, “Quantum Synchronization of a Driven Self-Sustained Oscillator”, Phys. Rev. Lett. **112**, 094102 (2014).

S. Walter, A. Nunnenkamp, and C. Bruder, “Quantum synchronization of two Van der Pol oscillators”, Ann. Phys. (Berlin) **527**, 131–138 (2015).

C. Wang, M.-C. Chen, C.-Y. Lu, and J.-W. Pan, “Optimal readout of superconducting qubits exploiting high-level states”, Fundamental Research **1**, 16–21 (2021).

Y. Wang, Z. Hu, B. C. Sanders, and S. Kais, “Qudits and High-Dimensional Quantum Computing”, Frontiers in Physics **8**, 589504 (2020).

Z. Wang, ed., *Cell-Cycle Synchronization*, Methods in Molecular Biology (Humana New York, NY, 2022).

Z. Wang, R. W. Parker, E. Champion, and M. S. Blok, “High-E_J/E_C transmon qudits with up to 12 levels”, Phys. Rev. Appl. **23**, 034046 (2025).

C. C. Wanjura, M. Brunelli, and A. Nunnenkamp, "Topological framework for directional amplification in driven-dissipative cavity arrays", Nature Communications **11**, 3149 (2020).

H. Weimer, M. Müller, I. Lesanovsky, P. Zoller, and H. P. Büchler, "A Rydberg quantum simulator", Nature Physics **6**, 382–388 (2010).

C. Weis, M. Fruchart, R. Hanai, K. Kawagoe, P. B. Littlewood, et al., *Exceptional points in nonlinear and stochastic dynamics*, 2023.

T. Weiss, A. Kronwald, and F. Marquardt, "Noise-induced transitions in optomechanical synchronization", New Journal of Physics **18**, 013043 (2016).

T. Weiss, S. Walter, and F. Marquardt, "Quantum-coherent phase oscillations in synchronization", Phys. Rev. A **95**, 041802 (2017).

E. P. Wigner, *Group theory: And its application to the quantum mechanics of atomic spectra* (Academic Press, 1959).

A. R. Willms, P. M. Kitanov, and W. F. Langford, "Huygens' clocks revisited", Royal Society Open Science **4**, 170777 (2017).

D. Willsch, D. Rieger, P. Winkel, M. Willsch, C. Dickel, et al., "Observation of Josephson harmonics in tunnel junctions", Nature Physics **20**, 815–821 (2024).

A. T. Winfree, "Biological rhythms and the behavior of populations of coupled oscillators", Journal of Theoretical Biology **16**, 15–42 (1967).

H. M. Wiseman and G. J. Milburn, *Quantum Measurement and Control* (Cambridge University Press, Nov. 2009).

S. A. Wolf, A. Y. Chtchelkanova, and D. M. Treger, "Spintronics—A retrospective and perspective", IBM Journal of Research and Development **50**, 101–110 (2006).

H. Wu, G. Heinrich, and F. Marquardt, "The effect of Landau–Zener dynamics on phonon lasing", New Journal of Physics **15**, 123022 (2013).

M. Xu, D. A. Tieri, E. C. Fine, J. K. Thompson, and M. J. Holland, "Synchronization of Two Ensembles of Atoms", Phys. Rev. Lett. **113**, 154101 (2014).

A. Yadav, K. J, V. K. Chandrasekar, W. Zou, J. Kurths, et al., "Exotic swarming dynamics of high-dimensional swarmalators", Phys. Rev. E **109**, 044212 (2024).

M. Yamagishi, N. Hatano, and H. Obuse, "Proposal of a quantum version of active particles via a nonunitary quantum walk", Scientific Reports **14**, 28648 (2024).

X.-F. Yin, W.-Z. Zhang, and L. Zhou, "The synchronization and entanglement of optomechanical systems", Journal of Modern Optics **64**, 578–582 (2017).

M. A. Yurtalan, J. Shi, M. Kononenko, A. Lupascu, and S. Ashhab, "Implementation of a Walsh-Hadamard Gate in a Superconducting Qutrit", Phys. Rev. Lett. **125**, 180504 (2020).

S. Zeytinoğlu, M. Pechal, S. Berger, A. A. Abdumalikov, A. Wallraff, et al., "Microwave-induced amplitude- and phase-tunable qubit-resonator coupling in circuit quantum electrodynamics", Phys. Rev. A **91**, 043846 (2015).

L. Zhang, Z. Wang, Y. Wang, J. Zhang, Z. Wu, et al., “Quantum synchronization of a single trapped-ion qubit”, Phys. Rev. Res. **5**, 033209 (2023).

O. V. Zhirov and D. L. Shepelyansky, “Quantum synchronization”, The European Physical Journal D **38**, 375–379 (2006).

O. V. Zhirov and D. L. Shepelyansky, “Synchronization and Bistability of a Qubit Coupled to a Driven Dissipative Oscillator”, Phys. Rev. Lett. **100**, 014101 (2008).

B. Zhu, J. Schachenmayer, M. Xu, F. Herrera, J. G. Restrepo, et al., “Synchronization of interacting quantum dipoles”, New Journal of Physics **17**, 083063 (2015).

J. Zou, S. Bosco, B. Pal, S. S. P. Parkin, J. Klinovaja, et al., “Quantum computing on magnetic racetracks with flying domain wall qubits”, Phys. Rev. Res. **5**, 033166 (2023).